May 2019

Chemical Approaches for Nanofabrication Based on Colloidal Lithography with Organosilanes, Nanoparticles and Nickel Films: The Role of Water in Directing Surface Self-Assembly

Neepa Malsi Kumari Kuruppu Arachchige
Louisiana State University and Agricultural and Mechanical College

CHEMICAL APPROACHES FOR NANOFABRICATION BASED ON COLLOIDAL LITHOGRAPHY WITH ORGANOSILANES, NANOPARTICLES AND NICKEL FILMS: THE ROLE OF WATER IN DIRECTING SURFACE SELF-ASSEMBLY

A Dissertation

Submitted to the Graduate Faculty of the
Louisiana State University and
Agricultural and Mechanical College
in partial fulfillment of the
requirements for the degree of
Doctor of Philosophy

in

The Department of Chemistry

by
Neepa Malsi Kumari Kuruppu Arachchige
B.S., University of Colombo, Sri Lanka. 2014
August 2019

ජීවිතය කියාදුන් දයාබර අම්මාටත්,

හිතන්නට, දිනන්නට දිරිය දුන්

තාත්තාටත්, ඒ මතකයන්ටත් ආදරෙන්

To my beloved mother

and

In loving memory of my father

ACKNOWLEDGMENTS

I would like to express my gratitude to Professor Jayne C. Garno for the guidance, encouragement and great mentorship that she provided throughout my graduate career. I will always cherish the research experience of Garno group and many pieces of advice I received from Dr. Garno. I also thank Dr. Megan Macnaughtan, Dr. Justin Ragains, Dr. Revati Kumar and Dr. Kunlun Ding for serving in my committee and providing valuable feedback toward improving my research and dissertation. I was extremely fortunate to have friendly and caring group members who tremendously supported me in every step of the way. I appreciate the support received from all former group members of Garno research group.

My sense of strength, resilience and motivation comes from the great upbringing and nurturing of my family. I am grateful for the unconditional love of my mother and brother, and for supporting me in my time of need. I am forever thankful for the loving memories of my father who always believed in me and showed how to embrace people with equal kindness and respect. I thank them for being a part of my life, sharing stories with me and most importantly allowing me to see a world outside of southern Sri Lanka even when I don't get to see them as much often as I like to. Special thanks must go to Nicole Lemoine, Ms. Kim Mollere and Ms. Gail Acree for heart-warming kindness and thoughtfulness they have shown me throughout my time in Baton Rouge, Louisiana.

TABLE OF CONTENTS

LIST OF TABLES

LIST OF FIGURES

LIST OF SCHEMES

LIST OF ABBREVIATIONS

AC	Alternating Current
AC-AFM	Acoustic- Atomic Force Microscopy
AFM	Atomic Force Microscopy
APTES	3-Aminopropyltriethoxysilane
CVD	Chemical Vapor Deposition
CFM	Chemical Force Microscopy
CP-AFM	Conductive Probe Atomic Force Microscopy
DIPEA	*N, N*-Diisipropylethylamine
DPN	Dip-pen Nanolithography
DMAB	Borane dimethylamine complex
EBL	Electron Beam Lithography
ELD	Electroless Deposition
FMM	Force Modulation Microscopy
HOMO	Highest Occupied Molecular Orbital
LED	Light Emitting Diode
LUMO	Lowest Occupied Molecular Orbital
MAC	Magnetic AC mode
MeCN	Acetonitrile
MFM	Magnetic Force Microscopy
MRFM	Magnetic Resonance Force Microscopy
MSM	Magnetic Sample Modulation
NIL	Nano Imprint Lithography

OEP	2,3,7,8,12,13,17,18-octaethylporphyrin
OTS	Octadecyltrichlorosilane
PES	Photoemission Spectroscopy
PSD	Position Sensitive Detector
SAMs	Self-Assembled Monolayers
SEM	Scanning Electron Microscopy
SET	Single Electron Transfer
SFM	Scanning Force Microscopy
Si-OEP	Si coordinated OEP strands
SPFM	Scanning Polarization Force Microscopy
SPM	Scanning Probe Microscopy
TPP	Tetraphenyl Porphyrin
TSG	Template-stripped Gold
XPS	X-ray Photoelectron Spectroscopy
ZnPc	Zinc Phthalocyanine

ABSTRACT

The capabilities for accomplishing fundamental surface studies with molecular systems are demonstrated in this dissertation using measurement and imaging modes of scanning probe microscopy. Model systems were chosen for investigations of surface self-assembly mechanisms, with an emphasis on understanding the role of interfacial water in surface reactivity. A key strategy for molecular level studies was to prepare nanostructures using protocols with colloidal lithography and scanning probe-based lithography (SPL). Nanofabricated samples were characterized *ex situ* with contact and tapping-mode atomic force microscopy (AFM) after key reaction steps, providing direct views of changes in surface morphology at the nanoscale. Magnetic sample modulation (MSM) combined with contact mode AFM provided a route to detect the vibration of magnetic nanomaterials in response to an externally applied electromagnetic field. Nanoscale measurements of the size-scaling effects for physical properties such as conductance and nanomagnetism are contemporary topics in the field of nanoscience. Protocols of SPL were used for studies with organic thin films; nanoshaving and nanografting experiments provided a means to prepare ultra-small nanostructures.

Nickel-coated nanostructures were constructed on amine-terminated nanorings of aminopropyltriethoxysilane (APTES) using colloidal lithography and chemical steps of electroless deposition (ELD), nickel was deposited by an autocatalytic redox reaction using palladium as a catalyst. Protocols were developed to investigate the role of water in the association and placement of silane molecules on surfaces as a strategy for indirectly tracking the location of water on surfaces. Visible light photocatalysis was used to prepare nanostructured films by immersing surface masks of monodisperse spheres in solutions of an aryl halide and then irradiating the solution with blue light. Films of aryl halide are linked to the surface by C-Au bonds to form robust

films that resist the effects of oxidation. Nanostructured films of octaethylporphyrin (OEP) were prepared with immersion particle lithography by reaction with silicon tetrachloride. Porphyrins bound to the surface through covalent Si-O-surface linkages coordinated to the centers of the macrocycles in a "kebob" arrangement. The Si-O-Si “skewer” strategy was also successful for encapsulating Au nanoparticles with porphyrins to make core-shell nanoparticles. Fundamental studies targeted questions related to controlling surface assembly and interfacial chemistry details.

CHAPTER 1. INTRODUCTION

Molecular-level studies of surface self-assembly reactions at vapor/solid and liquid/solid interfaces are the focus of this dissertation. Characterizations with atomic force microscopy (AFM) were used for *ex situ* studies of successive surface changes after key steps of chemical reactions, providing insight for reaction mechanisms. A premise for all of the described studies is that the nature of the surface has a strong influence on the reaction outcome. Parameters such as structure, composition and wettability of the atomic/molecular interfaces determine the localization, shape and thickness of surface structures. Tools of nanofabrication were applied to prepare patterns of nickel films, porphyrins, aryl halides as well as organosilane and organothiol self-assembled monolayers (SAMs). Well-defined nanostructures were prepared as models to enable analysis of interfacial chemistry with molecular-level sensitivity for a few layers of metal atoms or molecules of SAMs. Manipulation and control of chemical assembly are critical for studies of the size-dependent trends for physical and mechanical properties using the measurement modes of AFM. Conventional contact and tapping-mode AFM images provided 3D digital images of topography with associated chemical maps of nanostructures. Magnetic sample modulation (MSM), force modulation microscopy (FMM) and scanning probe lithography modes of AFM were applied for characterizing samples.

1.1. Experimental Methods with Scanning Probe Microscopy

The primary analytical tool used for surface investigations in this dissertation belongs to a family of surface imaging and measurement modes of scanning probe microscopy (SPM), which are described in Chapter 2. Scanning probe techniques enable ultra-sensitive detection of surface forces and furnish high-resolution images of thin films and nanomaterials at the molecular level. An overview of the historical milestones, operating principles as well as instrument configurations

is presented in Chapter 2 for the SPM modes used in this dissertation. In particular, modes of atomic force microscopy (AFM) provided exquisite details of the morphology of nanostructures prepared with particle lithography. Nanostructures of organosilanes and organothiols were used to build composite nanostructures in combination with processes of ELD and macromolecular assembly. Nanofabrication was used for sample preparation, to generate test platforms for fundamental studies of the surface chemistry, mechanisms of self-assembly as well as physical properties of materials at the nanoscale.

1.2. Nickel Nanorings Prepared using Electroless Deposition: AFM Characterization using Magnetic Sample Modulation

Studies of the surface chemistry for preparing ring-shaped nanostructures of Ni nanorings are presented in Chapter 3.[1] Metal nanostructures were prepared using electroless deposition (ELD) of Ni onto patterned templates of aminosilane. Samples were prepared by chemical approaches with colloidal lithography to investigate surface changes *ex situ* after key points of the reactions using atomic force microscopy (AFM). Ring-shaped nanostructures of 3-aminopropyltriethoxysilane (APTES) were prepared on Si(111) using vapor deposition with a surface mask of silica spheres. The particle mask was removed to reveal ring-shaped nanopatterns presenting amine groups at the interface. Organosilane nanopatterns were then immersed in a solution of Pd catalyst followed by treatment in a Ni plating bath. Changes in surface morphology after each reaction step were characterized *ex situ* using tapping-mode AFM to follow the time course of nanofabrication. Images of the Ni nanorings acquired with AFM were compared with SEM micrographs to further elucidate the morphology of the metal coatings. The magnetic character of the nanostructures was investigated with magnetic sample modulation (MSM-AFM), which is a hybrid of contact mode AFM combined with magnetic actuation of samples. Surface maps of the vibration of diamagnetic Pd and magnetic Ni nanorings were obtained with MSM-

AFM, providing insight on the process of electroless plating. Fine details of the surface corrugation and grain structure of the Ni-coated areas of the sample detected with SEM were sensitively resolved with MSM-AFM that were not apparent in AFM topography frames. Chemistry-based steps with ELD and colloidal lithography provide a practical route for reproducible nanofabrication of highly regular geometries with high-throughput.

1.3. Physical Experiments for Binding Trifunctional Organosilanes at the Vapor/solid Interface

Investigations of the molecular events which occur during the surface self-assembly of organosilanes from vapor are presented in Chapter 4, with a focus on the role of water in forming a discontinuous hydration layer on model surfaces.[2] As a unique strategy for tracking the location of water on surfaces, nanopatterning protocols were developed with colloidal lithography to compare the wettability differences of Si(111) and mica(001). Trace amounts of interfacial water are required to drive hydrosilation reactions with trifunctional organosilanes to form surface assemblies. In essence, trifunctional octadecyltrichlorosilane (OTS) was used as a marker molecule to map out the areas of the surface where water was deposited. The competition between hydrophobic and hydrophilic domains for adsorption and coalescence of water condensed from vapor can be mapped by observing the localization of organosilanes which bind to water at the solid interface. The effect of systematic changes in film thickness and surface coverage of OTS were evaluated at the vapor/solid interface by adding incremental amounts of water to sealed reaction vessels and assessing the outcome after reaction with vapor-phase silane. Colloidal lithography with monodisperse latex was applied to enable the preparation of well-defined interfaces with exquisite control of the spacing and composition of patterned elements at the nanometer level. A film of latex spheres was used to mask and protect discrete areas of the surface from vapor deposition. Small, circular areas of uncovered substrate were exposed when the mask

was removed to provide a baseline for measuring the dimensions of surface assemblies of organosilanes with atomic force microscopy (AFM). Interestingly, confined container sites of a water meniscus which surrounds the base of the sphere mask proved to be hot spots for directing the deposition of OTS to generate multilayered ring nanostructures. Beyond the steps of the initial hydrolysis and subsequent condensation steps of organosilation reactions, these studies address the nature of the interface and wettability factors which influence the association and placement of silane molecules on surfaces.

1.4. Nanopatterning and Surface Characterizations of Photografted Aryl Thin Films

High-resolution AFM and nanolithography protocols were used to characterize the surface structure and properties of photografted aryl thin films in Chapter 5. Preparation of robust organic thin films that are resistant to thermal and oxidative degradation is a requirement for the manufacture of highly efficient organic platforms for applications in molecular electronics. Grafting of carbon-centered radicals produced by visible light catalysis, photografting, was used to produce stable and robust thin films on gold substrates. The photografting approach was combined with particle lithography to produce arrays of nanostructures on Au(111). Robust, photografted films with aryl radicals can be attached to gold by Au-C bond, which are covalent and thus can resist oxidative and chemical degradation. To prepare nanopatterns, discrete regions of a gold substrate were protected with a surface mask of monodisperse silica spheres. Then the masked substrate was exposed to aryl radicals produced by visible light photocatalysis reactions by immersion in dilute solutions containing aryl halide, a photocatalyst and a reducing agent. Visible light irradiation of the mixture formed aryl radicals that eventually grafted onto uncovered areas of the gold substrate. The mask of silica spheres was removed by sonication in ethanolic media to reveals a periodic arrangement of nanoholes formed within the photografted thin film.

The morphology and thickness of the nanopatterned films was characterized with AFM as a strategy to optimize film quality. Protocols with nanoshaving were also applied to measure film thickness and to evaluate the robustness of the photografted aryl films.

1.5. Studies of the Surface Self-assembly of Si-Octaethylporphyrin

The influence of silicon tetrachloride as a coupling agent for the surface assembly of 2,3,7,8,12,13,17,18-octaethylporphyrin (OEP) on Si(111) was investigated using atomic force microscopy (AFM), as described in Chapter 6.[3] Nanopatterned films of porphyrins were prepared using particle lithography to evaluate the morphology, thickness and molecular orientation of Si-OEP films. Porphyrins have a macrocyclic tetrapyrrole structure which may be functionalized with various substituents. Modifications of the macrocycle, peripheral groups or bound metal ions can generate a range of electrical and photoelectrical properties. When preparing surface films, the planar macrocycles of porphyrins spontaneously self-associate to form stacked structures. This natural capability of self-stacking poses a challenge for developing processes for molecular patterning. When preparing films, porphyrins associate by electrostatic interactions between macrocycles as well as physisorption to the substrate to form coplanar arrangements of stacks of molecules, analogous to a stack of coins. The orientation of porphyrins on surfaces is also affected by the nature of the peripheral substituents and their position on the macrocycle. We introduced silicon tetrachloride to the porphyrin reaction vessel to mediate coupling between the surface and porphyrins through covalent interactions. Protocols of particle lithography were used as a nanoscale patterning tool to prepare well-defined surface structures and films of OEP. Our goals are to correlate nanoscale properties (conductance, photocurrent generation) with designed surface structures of porphyrins in which the coupling between the surface and porphyrins is mediated by covalent interactions. Conceptually, by arranging and orienting the macrocycles of porphyrins with

defined orientation, local surface measurements can be address questions about how structure influences properties.

1.6. Synthesis of Gold Nanoparticles Encapsulated with Si-Porphyrin

A new approach for preparing core-shell metal nanoparticles that are encapsulated with porphyrins or phthalocyanines is described in Chapter 7, using strategies based on Si-O coupling with $SiCl_4$. Our protocol for the synthesis of porphyrin encapsulated nanoparticles is based on chemical reactions with silicon tetrachloride in a "one pot" reaction, covalently linking octaethyl porphyrin (OEP) through Si-O bridges directly to the center of the macrocycle. Chromophores such as porphyrins and phthalocyanines provide a way to introduce interesting electrical and photophysical properties to nanomaterials.

1.7. Conclusions and Future Prospects

An overall summary of the dissertation as well as potential directions for future research is provided in Chapter 8. Multiple SPM modes were applied for studying the structure and chemistry of nanopatterns composed of organic thin films, porphyrins, and nanoparticles. To broaden the scope of investigations, further experiments with current sensing and photocurrent modes of SPM can be applied. Such studies will target a molecular-level understanding of chemical structure and processes for material applications. Protocols can be designed to prepare samples on conductive surfaces for characterizations with advanced SPM modes that are not as commonly employed due to technical challenges and experimental difficulties.

CHAPTER 2. EXPERIMENTAL METHODS WITH SCANNING PROBE MICROSCOPY

Scanning probe microscopy (SPM) refers to a family of nanoscale measurement and imaging methods that require the use of a sharp probe to scan samples. Information is obtained of physical and chemical forces which are plotted point-by-point to generate digital maps of 3D morphology and surface chemistry. Multiple channels of information are acquired concurrently, depending on the configuration of the instrument. Development of SPM began with the invention of scanning tunneling microscope (STM) in 1981.[4] The inventors of STM, Gerd Binnig and Heinrich Rohrer of IBM Zurich were awarded a Nobel prize in 1986. The imaging principle of STM is based on electron tunneling between a metal probe and conductive sample over a short gap, typically a distance measuring less than one nanometer. Atomically-resolved images of the electronic structure of surfaces can be achieved in real space with STM for samples that are conductive or semi-conductive. A few years later, a further SPM configuration was introduced for characterizing nonconductive surfaces which is commonly known as atomic force microscopy (AFM) developed by Binnig, Quate and Gerber in 1986.[5] The operation for AFM is based on imaging a surface using forces interacting between a tip and sample, rather than tunneling current. The operating principle of AFM is based on atomic forces (e.g. attractive, repulsive) between the tip and sample, thus AFM is also commonly referred to as scanning force microscopy (SFM) and the terms are synonymous. The experiments presented in this dissertation use SPM modes of AFM for surface characterizations.

2.1. Operational Modes of Scanning Probe Microscopy: Historical Milestones

Unlike optical microscopes which require a lens, the resolution of SPM is not limited by the wavelength of light, no lenses are required to focus light or electron beams. Modes of SPM employ a sharp probe affixed to a cantilever to “feel” the surface. The interactions between the

tip and the sample are recorded and mapped point-by-point to form images of surface structures in real time at scales from microns to nanometers. Experiments with SPM, have been designed to measure conductive,[6] magnetic,[7] thermal,[8] and photochemical,[9] properties for a range of samples by configuring the instrument for selected operational modes. A summary of several SPM imaging and measurement modes are listed in Table 2.1. The modes used for dissertation studies include contact mode, tapping-mode, magnetic sample modulation, force modulation microscopy and SPM-based nanofabrication.

Table 2.1. Milestones with SPM Imaging and Measurement Modes

Mode	Parameters measured	Feedback	Inventors
Scanning tunneling microscopy (STM)	Surface morphology	Magnitude of tunneling current	G.Binnig and H.Rohrer (1981)[4]
Contact mode AFM	Topography, frictional forces	Cantilever deflection	G.Binnig, C.F.Quate and C. Gerber (1986)[5]
Non-contact AFM	Topography	Cantilever deflection	Y. Martin et al. (1987)[10]
Magnetic force Microscopy (MFM)	Topography, relatively long-range magnetic forces	Cantilever deflection	Y. Martin and H.K. Wickramasinghe (1987)[11]
Force modulation microscopy (FMM)	Topography, elastic response	Cantilever deflection	Maivald et al. (1991)[12]
Tapping-mode AFM	Topography, elastic response	Amplitude of tip oscillation	Q. Zhong (1993)[13]
Magnetic AC or MAC-mode	Topography, elastic response	Amplitude of tip oscillation	W. M. Dougherty (1996)[14]
Conductive probe AFM	Topography, local conductivity	Cantilever deflection	T. W. Kelley et al. (1999)[15]
Magnetic sample modulation (MSM)	Topography, vibrational response to magnetic field	Cantilever deflection	J-R. Li, B.R. Lewandowski, S. Xu and J.C Garno (2009)[16]

2.2. Imaging and Measurement Modes of Scanning Probe Microscopy

The modes of SPM can be generally classified into three categories which describe the operation of the probe in contact, non-contact or intermittent-contact.[17] For contact mode, the tip and sample are maintained in continuous contact, physically touching the sample in which the interactions are dominated by van der Waal's attractive as well as short-range repulsive forces. For non-contact mode, the tip is kept at a discrete distance from the surface while measuring long-range forces such as magnetic, electrostatic or van der Waal's forces.[18] In intermittent contact mode, commonly referred to as tapping-mode, the cantilever is driven to oscillate near the resonance frequency as the tip "taps" the surface. With tapping-mode, the stick-slip adhesion and lateral forces between tip and surface are reduced to provide better resolution for imaging soft and sticky samples. The shifts in phase and amplitude of the cantilever motion compared to a driving signal provide mechanical information of elastic response and viscoadhesion.[19-20] The two most commonly used modes of SPM, contact mode AFM (in air and liquid media) and tapping-mode will be described in this chapter, as well as protocols for sample preparation. Two additional modes used for studies in this dissertation will also be presented: magnetic sample modulation (MSM) and force modulation microscopy (FMM).

2.2.1. Operating Principle of Contact Mode Atomic Force Microscopy (AFM)

Contact mode was first utilized by Binning et al. to achieve images of ceramic[5] and graphite[21] surface with atomic corrugations. In contact mode, the tip remains in continuous contact with the surface and variations of the cantilever deflection are detected with a photodetector. Experiments with SPM can be accomplished in ambient air, in liquid[22] or in a vacuum.[23] A common characteristic of all of the methods of SPM is that a probe is scanned over the sample, typically in a square raster pattern. The probe is used as a force sensor to measure interactions

between the tip and sample during scanning at scales from nanometers to microns. For contact mode AFM, the interactive forces produce changes in cantilever deflection that can be detected with a position sensitive detector (PSD). Topographic images are generated point-by-point by to map the changes in tip deflection compared to an initial threshold force setpoint. Continuous changes in tip deflection compared to the setpoint provide a feedback loop for adjusting the z position of the tip during surface scans. Atomic force microscopy provides ultrasensitive measurements in three dimensions, the horizontal X-Y plane and the vertical Z direction, with a lateral resolution of 0.1 nm and a vertical resolution of 0.01 nm.[24] It has been demonstrated that atomic resolution can be achieved with a sharp tip for ultra-flat surface materials such as graphite,[21] molybdenum sulfide,[25] inorganic crystals,[26-27] and metal oxides.[28]

Probes for AFM can be fabricated from any material that can be shaped into a spring-like cantilever. Tips are usually made of silicon (Si) or silicon nitride (Si_3N_4) and measure 10 to 400 μm in width and 0.3 to 2μm in thickness. Tips can also be composed of metals, diamonds or carbon nanotubes. There two basic geometries of AFM cantilevers, rectangular and triangular. A small sharp tip is attached to a cantilever. The force constant and resonant frequency of the cantilever is selected according to requirements for the sample to be studied and imaging mode. A typical soft commercial AFM cantilever for contact mode AFM is made of silicon or silicon nitride (Si_3N_4) with a radius ranging from 5 to 20 nm with spring constants less than 1 N/m.[29] For tapping-mode, the typical resonant frequency of probes ranges from 160 to 400 kHz, however softer cantilevers with resonances below 100 kHz can be used for tapping-mode imaging in liquid environments. Typically, the force constant chosen for vibration of cantilevers in ambient air is greater than 10 N/m.

The basic setup for contact mode AFM is shown in Figure 2.1. To construct AFM images, the vertical and lateral deflection of the cantilever is measured using a position sensitive photodetector (PSD) comprised of four photocells. For contact mode, the beam of a diode laser is focused onto the back of the cantilever. As the beam deflects off the back of the reflective cantilever to the PSD, the laser position shifts in response to changes in deflection that occur as the tip is scanned across a sample to profile topography. The position of the laser spot is used to map changes in both topographical profiles (top minus bottom signals) and frictional forces that

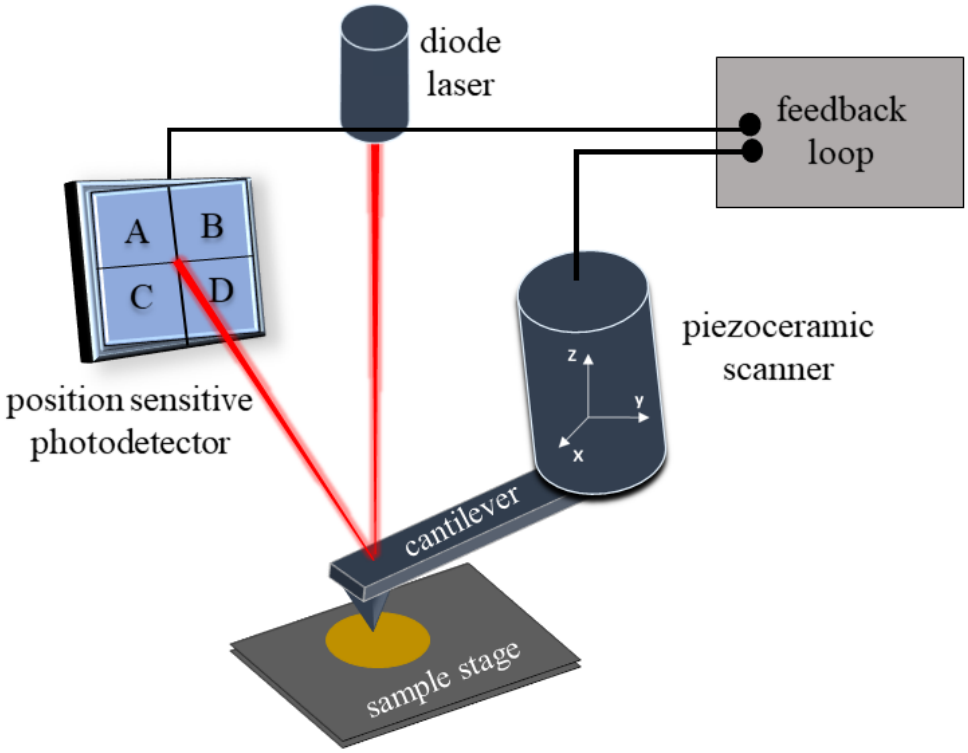

Figure 2.1. Overview of the basic instrument configuration for AFM.

act on the tip (left minus right segments). The PSD signal is part of a positional feedback loop to adjust incremental voltages applied to the scanner. An initial force setpoint is established experimentally to maintain a certain tip deflection. In the "scan-by-tip" configuration shown in Figure 2.1, the AFM probe is mounted on a piezoceramic tube scanner to control the movement of the cantilever. The same feedback mechanism is used for the "scan-by-sample" configuration,

in which the sample is raster scanned against a fixed probe for AFM operation. Control of the force applied to the tip is achieved by three-dimensional expansion or contraction of the piezoceramic scanner. The offset of the tip or sample displacement is proportional to the voltage applied by the feedback loop.[30] To generate images, the changes in voltage are tracked in real time and translated into pixels to form digital frames. For contact mode AFM, surface topography and lateral force channels are acquired simultaneously.

A feedback loop is used to incrementally adjust a certain cantilever deflection and to control the amount of force applied to the tip initially established as a force setpoint. Fluctuations of the surface topography influence the vertical movement of the cantilever to displace the laser spot to move up or down on the photodiode. The frictional forces from the sample influence torque or bow of the cantilever parallel to the scanning direction to cause lateral displacement of the laser spot on the left and right quadrants of the detector. The feedback loop sensitively tracks the changes in tip motion. The feedback loop controls the motion of the piezo scanner in the z-direction to bring the cantilever to its initial deflection and the setpoint force during scans.

The voltage signal measured with the feedback loop is concurrently translated into three imaging frames: topography, deflection and lateral force channels as shown in the example of Figure 2.2. The topography frame maps height changes with a color scale following the contours of the surface; typically, darker colors are assigned to the shallower regions of the sample, and a lighter color corresponds to taller regions. The deflection image shows the raw data in volts that compensates for the changes of laser position controlled with the feedback loop. Deflection images do not correlate with any physical property and are considered as the "error signal" in contact mode imaging. Deflection images are useful for revealing the edges of surface features. The torsional twisting of the tip that occurs due to the frictional forces between the tip and the sample

is used to construct lateral force images.[31-32] Color contrast in lateral force frames provide information about differences in chemical composition and distinctly outline edges of surface domains. A quantitative frictional force image can be obtained by subtracting the trace and retrace lateral force frames

Nanoholes of uncovered Au(111) formed within a film of dodecanethiol were imaged in ambient air using contact mode AFM (Figure 2.2). The sample was prepared using immersion colloidal lithography, in which a film of monodisperse silica spheres were used as a surface mask. After the spheres were rinsed away, the topography frame (Figure 2.2a) reveals 14 dark circles exposing places that had been protected by a surface mask of silica spheres. The surrounding

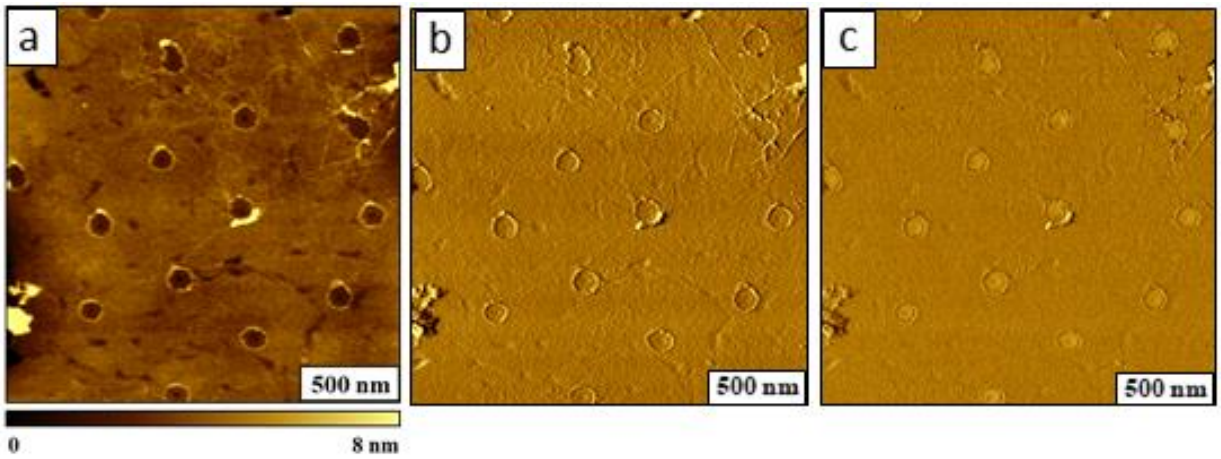

Figure 2.2. Examples of imaging and measurement channels acquired with contact mode AFM. (a) Topography (2×2 μm^2); (b) deflection; (c) lateral force image. Images were acquired for a sample containing nanoholes of uncovered Au(111) substrate within a film of dodecanethiol prepared using colloidal lithography with silica spheres of 500 nm dimeter.

brighter areas are filled with a monolayer of dodecanethiol measuring ~ 1.5 nm in thickness. The thickness of the dodecanethiol film corresponds to a $\sqrt{3}\times\sqrt{3}R30^o$ commensurate structure with a 30^o molecular tilt with respect to surface normal. The raw data in volts that compensate for incremental changes of laser position that were controlled by the feedback loop are mapped in the deflection image, Figure 2.2b. The color contrast in the lateral force image (Figure 2.2c) provides ultra-sensitive maps of the differences in surface chemistry. The lateral force image reveals distinct

outlines of the edges of surface domains and nanoholes. The tip experiences frictional forces as the probe is scanned across the sample according to the functional groups at the interface which enables maps of the chemical composition of thin film samples.

2.2.2. Acquisition and Interpretation of AFM Force-Distance Curves

A force-distance curve can be used to quantitatively measure tip-sample interactions[26, 33] as well as to gather information about additional chemical and physical properties of samples. Ma et al. have reported a method to use the force-distance curve to measure the radial modulus of DNA nanotubes.[34] Force-distance curve measurements were used to obtain the chemical structure of perylene tetracarboxylic dianhydride single molecules adsorbed onto Si(111) surface as reported by Iwata et al.[35] Force spectroscopy with AFM has also been used to probe adhesion and elastic characteristics of polymer[36] and biological samples.[37]

The force interactions between the tip and the sample can be quantitatively measured and profiled with force-distance curves.[38-40] An example force-distance curve acquired in an ambient environment is shown in Figure 2.3 for a sample of nanoholes within a film of dodecanethiol nanoholes prepared on Au(111). The force-distance curve is a plot of the cantilever deflection with respect to the position of the tip during an approach and retract cycle. A triangular waveform voltage is applied to the piezoceramic scanner to enable an approach and retract cycle. The deflection voltage is monitored during the cycle and later converted to force using Hooke's law.[40]

$$F = -kx \qquad \text{Equation 2.1}$$

$$F = k_c Z_c \qquad \text{Equation 2.2}$$

In Hooke's law (equation 2.1), the force (F) applied on a stretched spring is calculated by multiplying the spring constant (k) by the distance (x) to which the spring is stretched from its equilibrium position. To calculate the force experienced by the tip from the sample during the

acquisition of force-distance curve, the spring constant of the probe (k_c) is multiplied by the magnitude of the cantilever deflection (Z_c) as shown in equation 2.2.

The attractive and repulsive forces that tip exerts on the sample can be categorized into regions as indicated in Figure 2.3. When the tip is far away from the sample (I) at the beginning of the approach curve, no interactions are present. As the tip approaches closer to the sample, weak

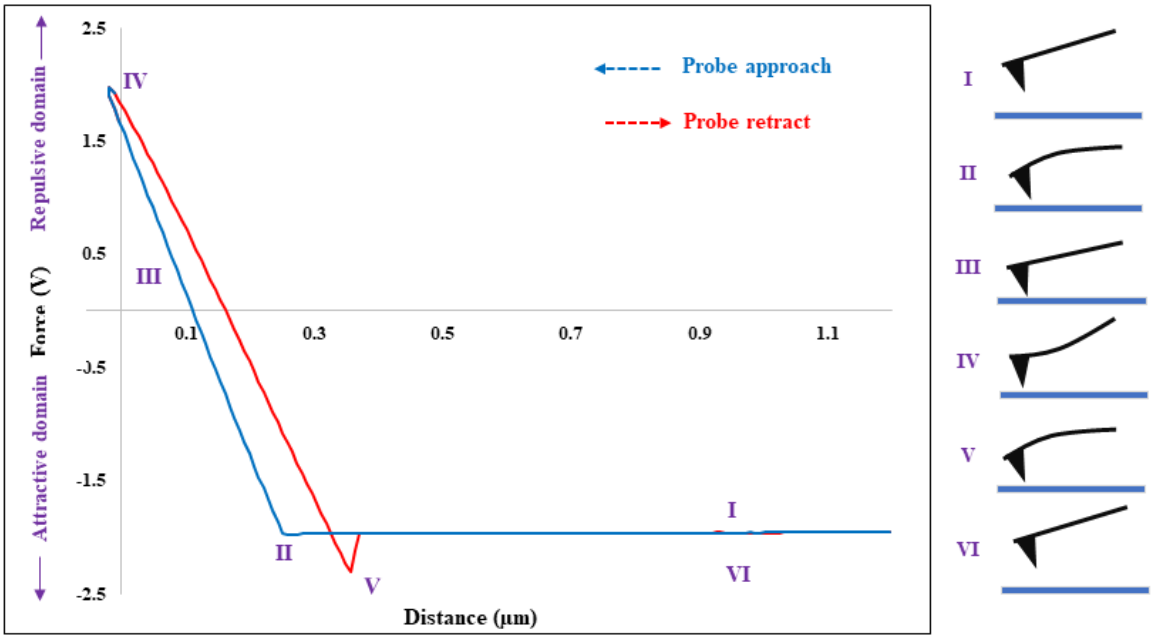

Figure 2.3. Force-distance curve acquired in air with a Si_3N_4 tip (force constant 0.2 N/m) with a sample of nanoholes within a dodecanethiol film on Au(111). The cantilever deflection is represented on the left for points during the approach (blue) and retract (red) cycle.

interactive forces begin to interact with the tip. This first interaction zone is known as the attractive region of the force-distance curve. Upon approaching, the tip snaps on to contact (II) due to the increasing influence of van der Waals as well as electrostatic forces. This produces the small dip of the curve found in region II. The tip is in direct contact with the sample in region III and begins to experience the buildup of repulsive forces. As the tip presses further towards the sample, the strength of repulsive forces will also increase to cause the cantlever to bend. Once the maximum deflection assigned by user setpoint is reached, the retraction cycle begins, indicated at region IV.

The area where repulsive forces are dominant is classified as the repulsive domain. Even though the tip is moving away from the surface, it remains in contact due to adhesive forces (region V) to make the cantilever bend downwards. As the deflection reaches a maximum threshold and the gap between the tip and the sample is far enough, the tip will snap out of the contact. As the tip is moved further away from the sample it shows the flat slope of region VI where there are no forces exerted. During contact mode imaging, the dominant forces occur mainly in the repulsive region of the force-distance curve in which the tip is placed directly on the surface, whereas for the tapping-mode the interaction forces lie in the attractive domain.

2.2.3. Liquid Imaging with AFM

Experiments conducted in liquid media with AFM have enabled improvements for imaging resolution with minimal sample damage by eliminating the capillary and van der Waals forces between the tip and the sample.[39] Both contact[41] and tapping-mode[42-43] AFM experiments have been conducted in liquid media. When the AFM tip is immersed in liquid, the resonance frequency of the cantilever is shifted downfield which reduces the overall vibrational noise that could interfere during imaging.[44-45] Liquid imaging was first introduced by Marti et al. demonstrating that better resolution can be obtained for samples of graphite and NaCl crystals covered with water.[46] The capability of operating in liquid media for AFM studies was employed by Asakawa et al. to image the surface structure of TiO_2 nanoparticles with subnanometer resolution,[47] and Fukuma et al. reported successful imaging of polydiacetylene with molecular resolution.[48] Further advantages of liquid imaging are enabled for studying biological samples under physiological conditions.[49] Experiments can be conducted *in situ* for macromolecules such as fatty acids for studies of self-assembly mechanisms.[44]

The experimental setup for liquid imaging incorporates an uncovered polycarbonate liquid cell which is mounted on the sample stage (Figure 2.4). The sample is placed inside the liquid cell and secured by placing the metal ring on it. A syringe filled with the liquid of interest is connected to the liquid cell through a tube and it maintains a continuous supply of liquid throughout the experiment. A force-distance curve obtained for a contact mode experiment conducted in an

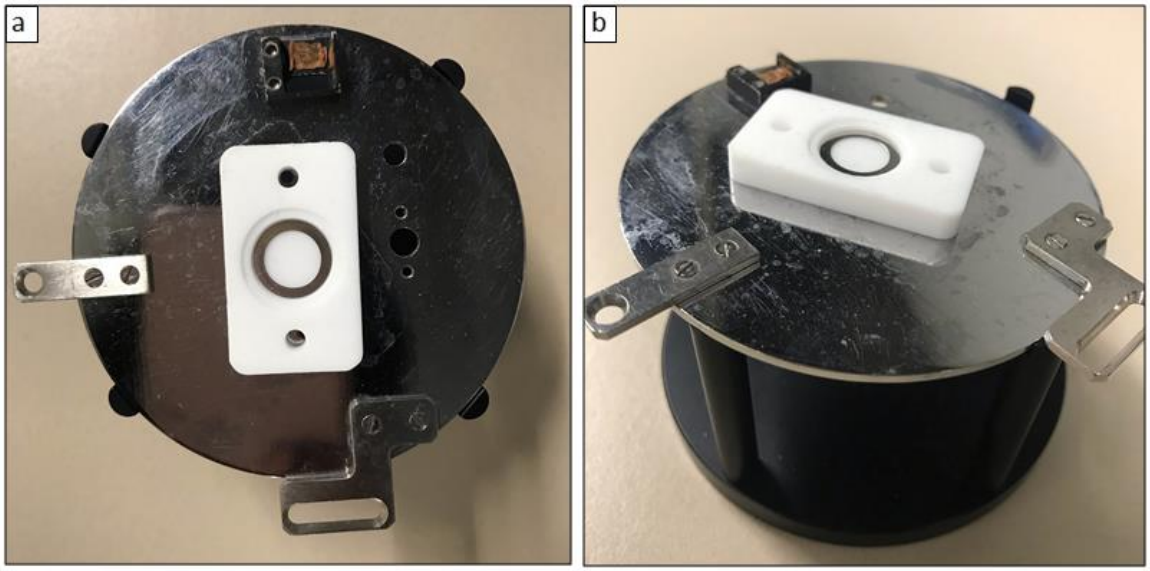

Figure 2.4. Photographs of the liquid cell used for *in situ* AFM studies. (a) Top view and (b) side view.

ethanolic media with a sample of dodecanethiol nanoholes films on Au(111) is shown in Figure 2.5. The attractive capillary forces during a retractive cycle are eliminated by imaging in liquid, comparing the snap out zone (region V) for Figure 2.3 and Figure 2.5. A substantial reduction of adhesive and capillary forces during a retractive cycle can clearly be seen in Figure 2.5 when AFM imaging is done in liquid media.

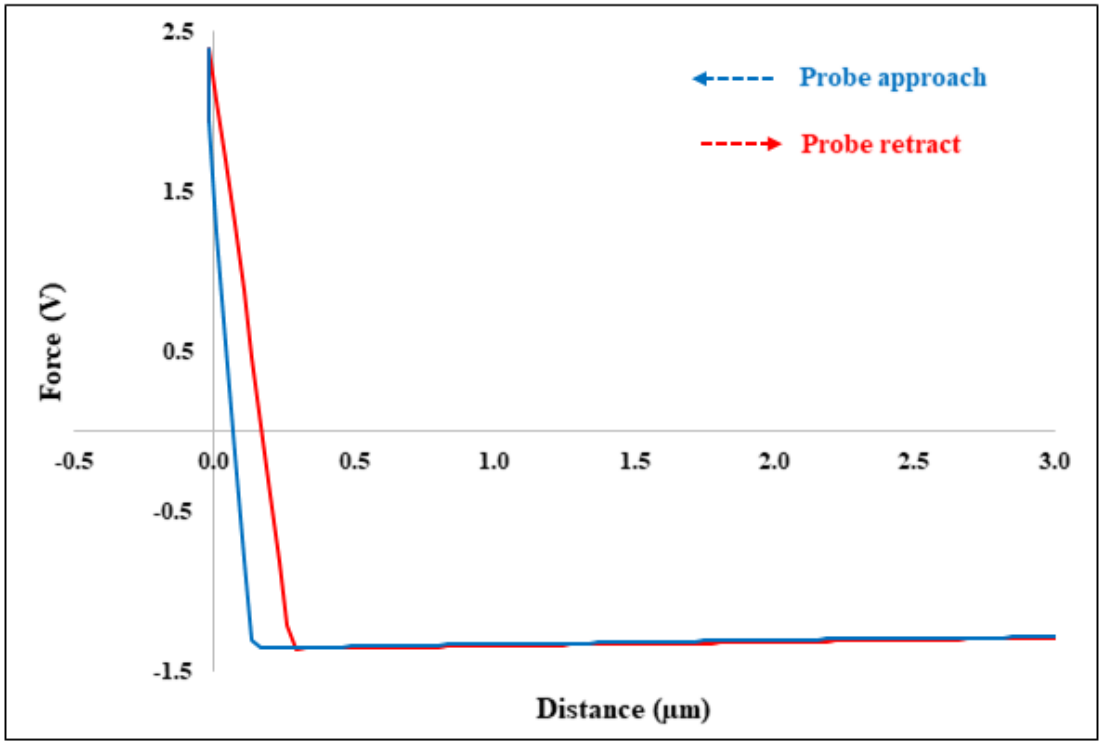

Figure 2.5. Force-distance curve acquired in ethanol with a silicon nitride tip (force constant 0.2 N/m) for a dodecanethiol SAM prepared on Au(111).

2.2.4. Operating principles of Tapping-Mode AFM

Tapping-mode, also known as acoustic AFM (AC-AFM), is a dynamic mode of AFM that is often helpful to improve resolution for imaging delicate or soft and sticky samples. The shear forces and stick-slip adhesion of a probe operated in contact mode can cause perturbation of the surface or may damage soft, fragile samples. Such forces are eliminated with tapping-mode AFM.[13] In tapping-mode, the AFM cantilever is driven to oscillate close to its resonant frequency sufficiently close to the surface such that it intermittently is driven into contact with the surface, and then is disengaged to "*tap*" the surface. A small piezo-actuator element is placed within the cantilever holder or nosecone (Figure 2.6) to drive the tapping of the cantilever. By driving the tip to quickly touch the surface mitigates the problems caused by stick-slip adhesion and transient

interfacial binding of the probe to the surface that is caused by frictional forces. The feedback loop of tapping-mode is configured to maintain a constant amplitude of the cantilever compared to an initial setpoint value of the driving signal. As the tapping tip is scanned across a sample, the topography height changes influence the oscillation of the cantilever. Shifts in the amplitude and phase of the cantilever oscillation are plotted to generate mechanical information of the sample using a lock-in amplifier. The feedback loop controls the tip oscillation, referencing signals from the PSD compared to the driving signal to make incremental adjustments of the tip-sample separation to maintain a constant amplitude.

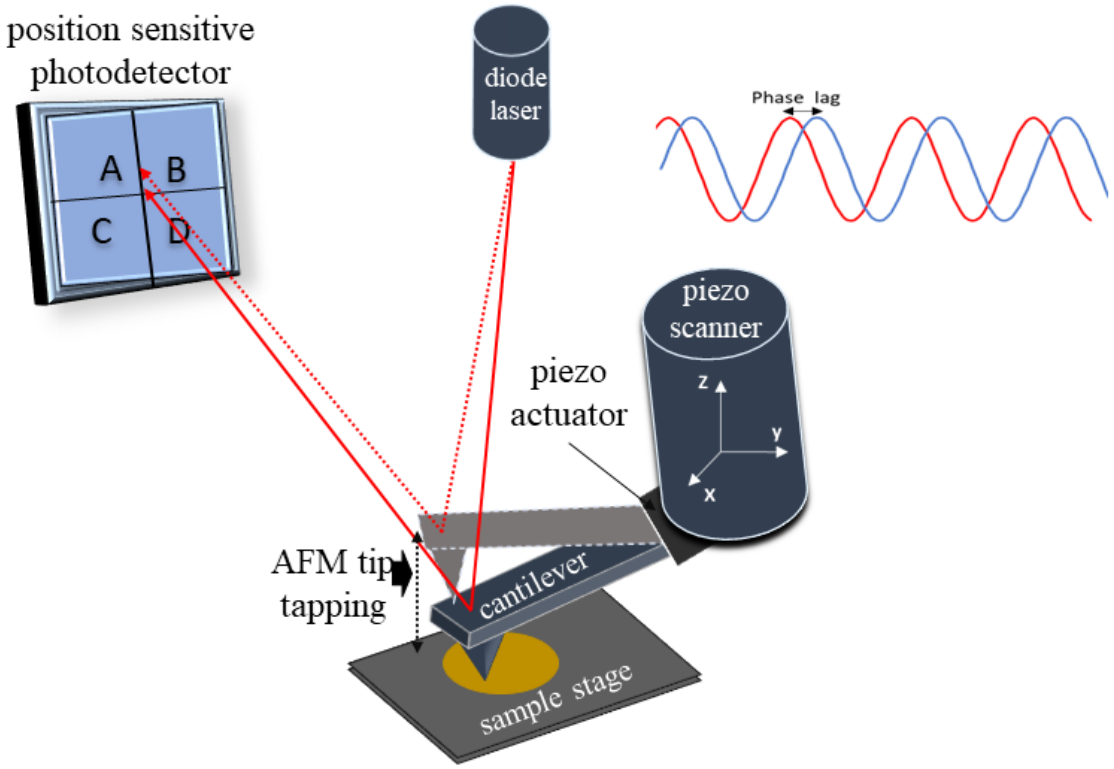

Figure 2.6. Basic set-up for tapping-mode AFM using a scan-by-tip instrument configuration.

With intermittent tapping-mode AFM, the voltage signal adjustments are converted to digital images as topography and phase frames which are concurrently acquired (Figure 2.7). In addition to 3D information of surface morphology obtained with topography images (Figure 2.7a), phase channels are generated with tapping-mode AFM. The phase channel is derived from changes

in the phase angle of tip oscillation, and does not correlate directly with mechanical properties. Since the amplitude signal (Figure 2.7b) is used for positional feedback with tapping-mode, interpretable amplitude frames are not produced for data analysis. Phase images (Figure 2.7c) indicate the shifts in phase angle for the tip motion compared to the driving signal and the actual cantilever oscillation of the probe. Shifts in the phase of tip motion are caused by changes in adhesive and elastic response of the sample. Therefore, phase frames provide sensitive maps of the local chemistry of domains that have differences in surface chemistry to compare side-by-side with topography images.[50-51]

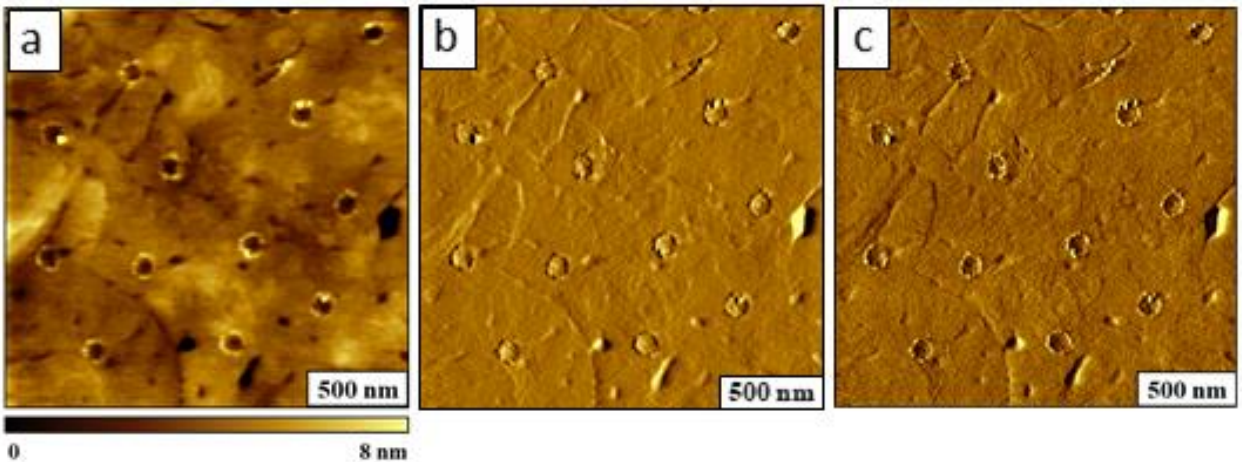

Figure 2.7. Imaging frames acquired with tapping-mode AFM. (a) Topography (2×2 μm^2); (b) amplitude; and (c) phase image. Images were acquired with a sample of nanoholes within a dodecanethiol film on Au(111).

The resonance frequency of Si_3N_4 cantilevers used for tapping-mode is typically between 50-400 kHz. An example amplitude response curve (AC tuning curve) for a frequency sweep using a Si_3N_4 cantilever is shown in Figure 2.8, revealing a prominent resonance peak at 290.5 kHz. The AC tuning curve is acquired at the beginning of a tapping-mode experiment to determine the optimum frequency parameters for imaging when the tip is not engaged with the surface. By scanning through a range of frequencies and monitoring the amplitude of oscillation via the photodiode signal, a peak near the resonance amplitude is selected for imaging. The amplitude of

the cantilever is dampened when the tip is placed in contact with the sample. Therefore, a frequency that is slightly lower than the resonance peak with a lower amplitude value is selected as the actual driving frequency for imaging. The net forces exerted by the tip are considered to occur in the repulsive regime of the force-distance curve for tapping-mode experiments.[52-53]

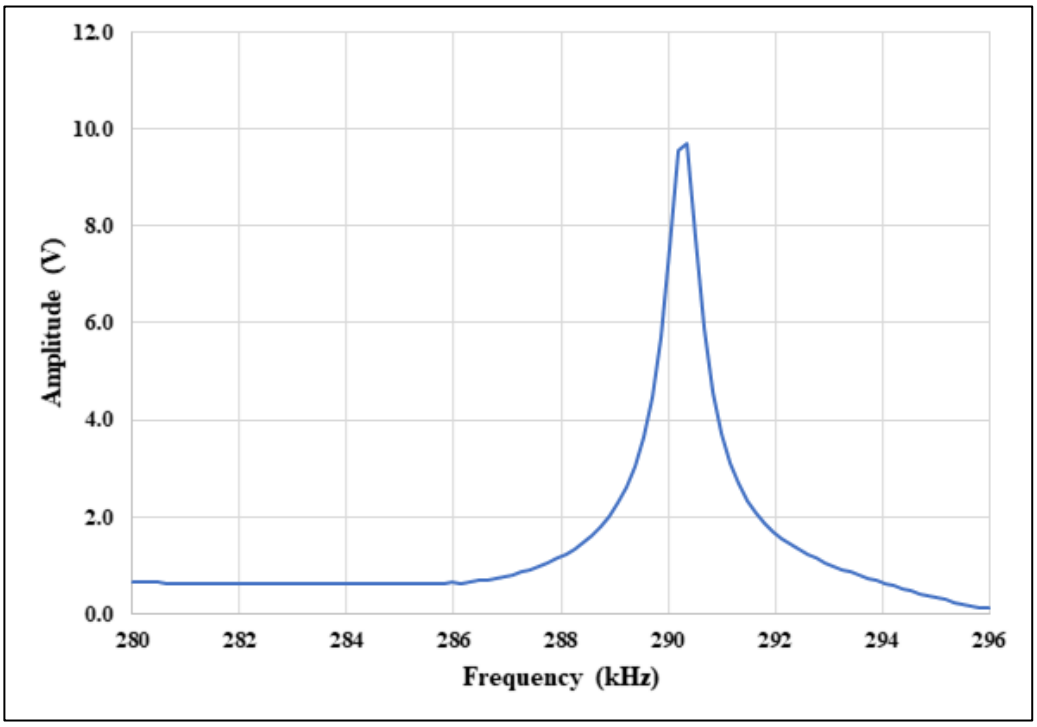

Figure 2.8. Frequency sweep acquired in air with tapping-mode Si_3N_4 tip (force constant 40 N/m) for a sample of nanohole patterns within dodecanethiol on Au(111).

2.2.5. Combining Magnetic Sample Modulation with Contact Mode AFM

Magnetic sample modulation (MSM) AFM is a combination of contact mode atomic force microscopy combined with actuation of magnetic areas of a sample. The MSM mode has been applied for studies of magnetic materials such as ferritin,[54] iron nanoclusters[16, 55] and composite $FeNi_3$ nanoparticles.[56] A non-magnetic probe is required for MSM-AFM, the magnetic areas of the sample are driven to vibrate in response to an external AC electromagnetic field. In contrast, magnetic force microscopy (MFM) requires a tip that is coated with a thin magnetic film of Co, Fe or an alloy for operation in noncontact mode.[57-58] The strength of the magnetic field of the

sample must be sufficiently strong to deflect or attract a micrometer-sized cantilever to enable mapping of the magnetic domains. The magnetic tip is lifted above the surface at discrete distances to sense the relatively weak, long-range forces of magnetic areas. During lift mode operation, the MFM tip will deflect according to the magnetic polarity to map both the strength and polarity of magnetic domains. The bulky underside metal coating produces a relatively blunt probe, which limits the resolution of MFM to around 300-500 nm. Other SPM magnetic modes such as magnetic resonance force microscopy (MRFM), [59-60] and magnetic AC (MAC-mode)[61-63] require the use of tips with a magnetic coating. A key difference for the imaging strategy applied for MSM is that a magnetic tip is not required, instead of measuring magnetism directly, the sample motion is detected by a non-magnetic probe.

For studies with MSM mode, a non-magnetic lever operated in contact mode is combined with sample modulation induced by an oscillating magnetic field. A commercially available MAC-mode sample stage generates an alternating magnetic field with the application of AC current to the wire coil solenoid. When a current carrying wire is formed into several loops to form a coil, a magnetic field develops that flows through the center of the coil along the longitudinal axis and circles back around the outside of the loop or coil, as shown in Figure 2.9. The strength of the magnetic field of the solenoid increases proportionately as the current is increased. The magnetic field lines circling each loop of wire combines with the fields from the other loops to produce a concentrated field down the center of the coil. The AC current generates a magnetic field which alternates in polarity and strength according to the frequency and amplitude parameters of the driving current. With the Mac-mode stage, samples are placed close to one end of the solenoid to experience the strongest flux of the AC electromagnetic field. Magnetic nanostructures are induced to vibrate in the electromagnetic field providing selective contrast for the magnetic areas that are

in motion. The changes in MSM phase and amplitude relative to the driving AC signal are detected and mapped with the MSM to identify areas of the magnetic domains. Example MSM-AFM images are shown in Figure 2.9 for amplitude (Figure 2.9a) and MSM phase (Figure 2.9b) channels which are simultaneously acquired with topographs. During the first half of the scan, vibration of magnetic Ni nanostructures can be mapped out in both frames. However, when the AC current was turned off halfway through image acquisition the vibration of the sample can no longer be detected. No features can be resolved in the lower part of the image with the field turned off. Dynamic changes can be studied by tailoring the magnetic field strength and frequency. With MSM-AFM,

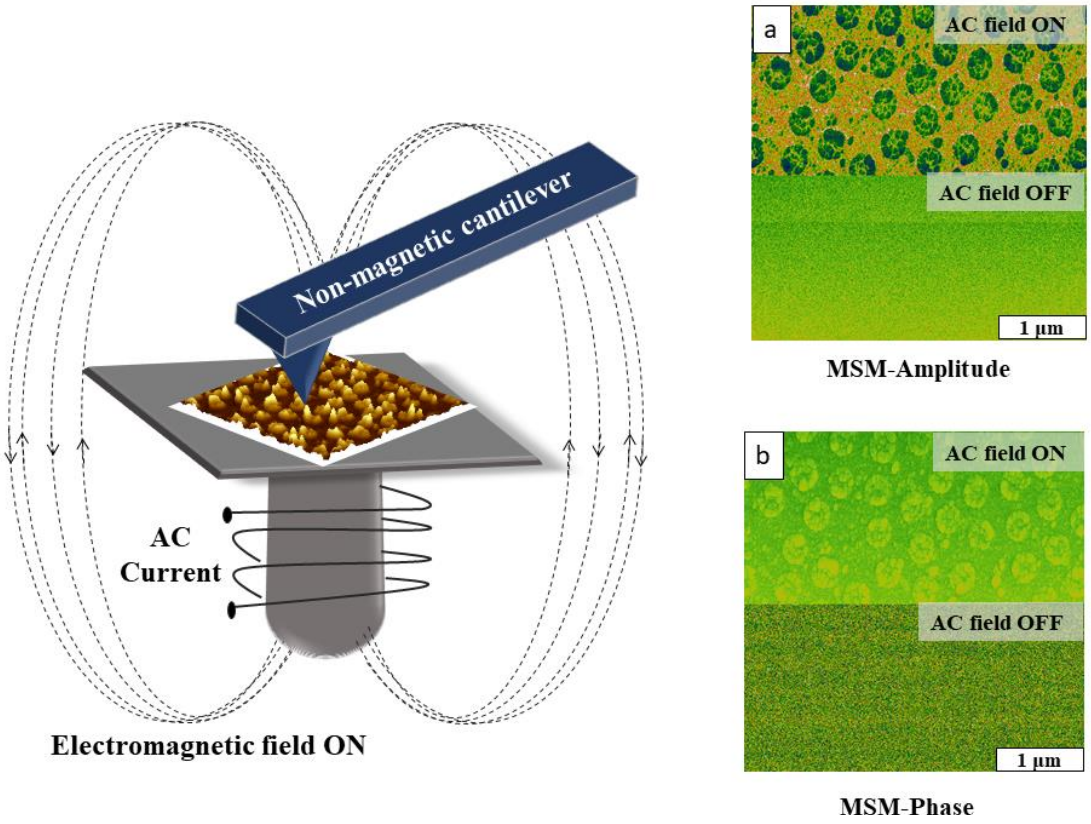

Figure 2.9. Set-up for contact-mode AFM operation with MSM (left). Example results with (a) MSM-amplitude and (b) MSM-phase channels when the AC electromagnetic field was turned on and then turned off halfway through the scan. The sample shows an array of Ni nanorings, acquired with 234 kHz and a field strength of 0.2 T.

extreme sensitivity is achieved for slight changes in tip movement because a lock-in amplifier is used to acquire the amplitude and phase components of the deflection signals. The field strength for MSM is on the order of 0.05 to 0.6 Tesla, and high-field permanent magnets are not required for measurements. For the instrument set-up of MSM, positional feedback for the scanner is not changed and the typical force-deflection settings for scanning in contact mode are used for topographic data acquisition. To obtain amplitude and phase components of the tip motion, an auxiliary output channel from the quadrant photodiode of the AFM scanner is directed to input channels of a lock-in amplifier, using the driving AC waveform as a reference. Thus, the periodic motion of the sample vibration can be tracked by changes in the deflection of the tip. The changes in phase angle and amplitude as the tip interacts with the vibrating sample are plotted as a function of tip position to create MSM phase and amplitude images. With each MSM experiment, control spectra are also acquired to monitor the tip trajectory and its free amplitude as the AC field is ramped when the tip is lifted from the surface, and when the tip is placed at non-magnetic locations of the sample such as for bare areas of the substrate.

2.2.6 AFM Studies with Force Modulation Microscopy (FMM)

Force modulation microscopy (FMM) is a widely used AFM mode for studying the mechanical characteristics of samples, which was introduced by Maivald et al. in 1991.[12] Information of elastic and viscoelastic[64-66] properties as well as quantitative measurements of Young's modulus[67-68] can be investigated at the nanoscale. The FMM mode has been applied to study polymers,[69-70] organic thin films,[71-72] proteins,[73] agar gels,[74] biomolecules,[75] cells,[76] and metal alloys.[77]

For operation with FMM, the tip is held in continuous contact with the surface, similar to contact mode using a force setpoint for feedback (Figure 2.10). The sample is driven to vibrate in

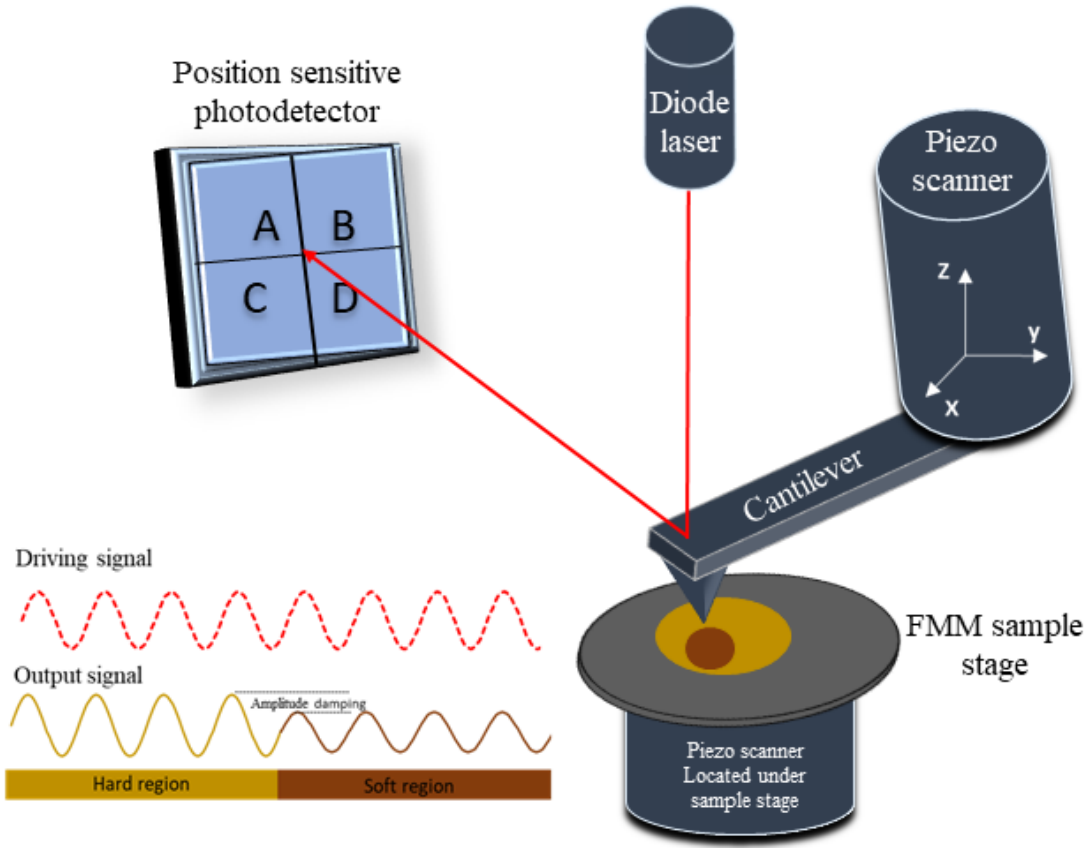

Figure 2.10. Instrument setup for FMM mode of operation.

the z direction by a piezo actuator within the sample stage. As the sample vibrates, the force between tip and sample is modulated resulting in an amplitude and phase shift of the output signal, which is determined by local differences in sample elasticity. As the tip is traced over a hard surface, the amplitude response is slightly greater in magnitude compared to the driving signal. On the other hand, when the tip traces across a soft region, the amplitude is reduced because the oscillation is absorbed or dampened. A feedback loop is used to maintain a constant cantilever deflection during imaging to generate topography frames, in the same manner as with contact-mode AFM. Both the amplitude and phase shifts of the PSD signal are mapped to form digital amplitude and phase images concurrently with topography. Local variations in the elastic properties of samples are mapped with high sensitivity and the nanoscale with FMM amplitude and phase images.

2.3. Protocols for Nanolithography Based on Scanning Probe Microscopy

Nanolithography methods have been applied to fabricate surface patterns with dimensions of nanometers using lithography modes of SPM. In methods of scanning probe lithography (SPL), the AFM probe is used to alter the arrangement of nanomaterials on surfaces to produce designed nanostructures. Examples include dip-pen nanolithography (DPN),[78] nanoimprint lithography (NIL),[79] nanoshaving,[80] and nanografting.[81] Mechanisms used for scanning-probe based nanolithography include molecular diffusion, etching, bias-induced surface oxidation and molecular replacement. Nanoshaving and nanografting protocols with self-assembled monolayers (SAMs) of *n*-alkanethiols were used for studies in this dissertation and will be detailed in this section. After patterning, nanopatterns can be further r functionalized with site-selective chemical reactions to attach molecular adsorbates,[82] DNA,[83-84] proteins,[85] or nanoparticles.[86]

2.3.1. Patterning Surface Films by Nanoshaving

When imaging with AFM probes, typically a minimum force is applied to the sample, to prevent damage to the sample. However, when applying greater forces, the AFM tip can be used as tool for inscribing nanopatterns with a process that is typically referred to as nanoshaving. The displacement of *n*-alkanethiol molecules chemisorbed onto Au(111) surfaces (nanoshaving) was first demonstrated by Liu et al. by using a Si_3N_4 tip with applied force up to 300 nN.[87] Nanoshaving has been accomplished successfully with self-assembled monolayers of alkanethiols,[88] alkylsilanes,[89-90] phospholipids,[91] polymer thin films[92] and photografted aryl thin films.[93]

The main steps of nanografting are shown in Figure 2.11. First, the surface is scanned with low force in contact mode (Figure 2.11a) to locate an area that is relatively flat without surface

defects or contaminants. Next, nanoshaving is accomplished by exerting a high force and sweeping the probe multiple times (Figure 2.11b) across the sample. The sweeping action with high force

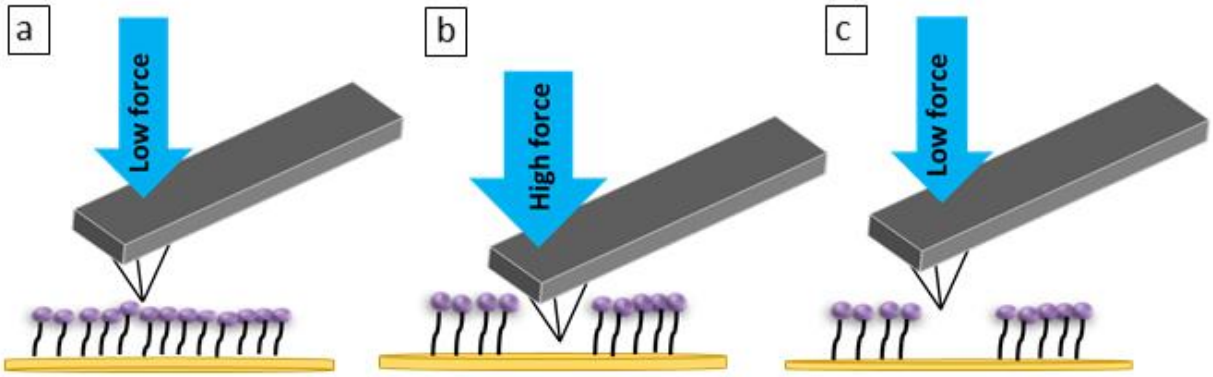

Figure 2.11. Steps of nanoshaving. (a) Initial characterization under low (nonperturbative) force; (b) nanoshaving is accomplished by increasing the force to remove molecules under the probe; (c) returning to low force, the shaved area can be characterized *in situ.*

displaces molecules following the track of the AFM probe to inscribe a nanoscale pattern. The parameters for the amount of force and number of line sweeps need to be tuned for each experiment, depending on the nature of the sample. Nanoshaving can be done in both ambient conditions and in liquid. If the experiment is conducted in air, displaced molecules tend to pile up along the edges of nanoshaved area. However, in liquid media, the shaved molecules are mostly dissolved away to produce clean edges. Complex designs can be generated using lithography automation software.[94] After completing the nanoshaving step, the area can be characterized *in situ* by returning to low, nondestructive force (Figure 2.11c).

An example experiment for nanoshaving is presented in Figure 2.12, showing an arrangement of letter nanopatterns nanoshaved within a film of dodecanethiol on Au(111) under ethanolic media. The darker areas of the nanopatterns within the topography frame (Figure 2.12a) indicate the uncovered gold substrate surrounded by the decanethiol SAM (bright contrast). The local thickness can be measured by placing a cursor profile across the nanopattern. The thickness

measured 1.4 ± 0.4 nm, referencing the uncovered substrate as a baseline (Figure 2.12c). This value matches closely with the expected thickness (1.56 nm) of dodecanethiol/Au, assuming a molecular tilt of 28°.[95]

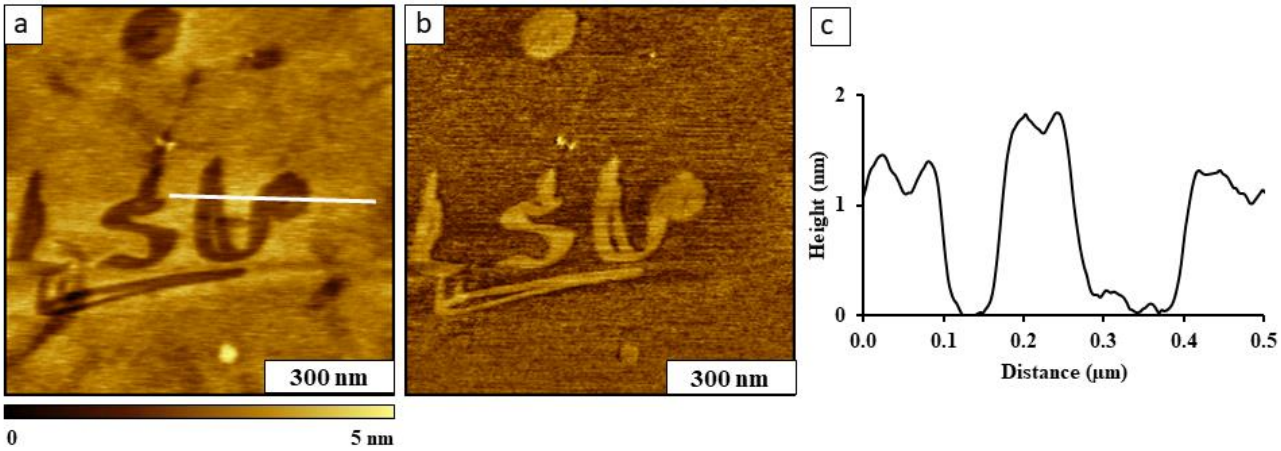

Figure 2.12. Letter patterns nanoshaved within a dodecanethiol SAM. (a) Topograph (0.9×0.9 μm^2), (b) simultaneously acquired lateral force image; (c) cursor profile for the white line in *a*. The experiment was accomplished using contact mode AFM in ethanolic media

2.3.2. Protocols for Nanografting

Nanografting is accomplished in liquid media containing selected "ink" molecules by applying mechanical force to simultaneously shave areas of thiol SAMs and replace with fresh molecules from solution. Nanografting was introduced in 1997 by Xu et al.[88] Since alkanethiols bind through chemisorption to metal substrates, the tip can be used to shave areas of the films by breaking Au-S bonds. Nanografting has not been successful with systems that are not thiolated such as alkylsilanes, which form robust, covalent bonds to substrates. Nanografting has been applied successfully with *n*-alkanethiols,[96-97] certain metalloproteins,[98] and thiolated DNA.[84] Advantages of nanografting are that the same probe can be used *in situ* for successive steps of imaging and characterization, enabling side-by-side characterizations of molecules with selected chemical functionalities. The local structure of proteins that are linked to nanografted patterns has been investigated.[85, 99]

Nanografting is performed in liquid media containing molecules to be patterned (Figure 2.13). The basic steps for nanografting are accomplished *in situ* using the same probe for fabrication and imaging. In the first step, a small force is applied to the tip to enable AFM imaging to locate a suitable area of the sample for patterning (Figure 2.13a). The force is chosen so that surface molecules are not perturbed or damaged. In the second step, a higher force is applied to selectively remove areas of the matrix SAM, while the molecules from solution self-assemble

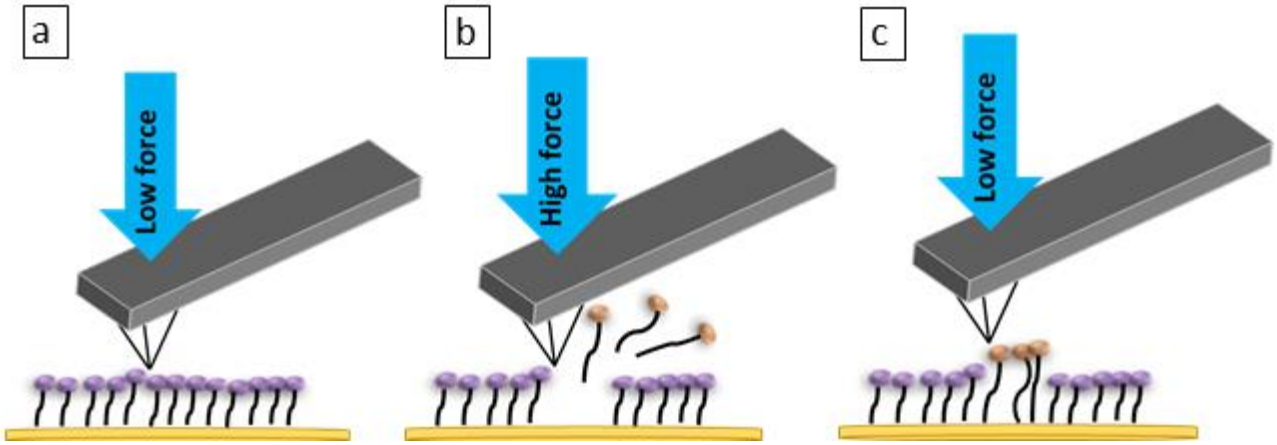

Figure 2.13. Steps of nanografting accomplished in liquid media containing ink molecules for patterning. (a) Initial scans are acquired with low force; (b) with higher force applied to the tip, nanografted patterns are produced by nearly simultaneous removal of surface molecules and replacement with new molecules from solution; (c) returning to low force, the nanopatterns can be characterized *in situ*.

immediately following the scanning track of the probe (Figure 2.13b). Returning to low force in the final step, the nanografted designs can be characterized *in situ* (Figure 2.13c). When selecting a solvent to dissolve the molecules for nanografting experiments, ethanol, butanol and water are suitable to minimize evaporation in the open liquid cell. Solvents which evaporate quickly such as dichloromethane or toluene do not work well for nanografting protocols.

An example nanografting experiment is presented in Figure 2.14 showing a square of octadecanethiol written within a SAM of dodecanethiol on Au(111). A square pattern (150×150 nm^2) was nanoshaved within dodecanethiol using a scan rate of 30 lines/second and an applied

force of 10 Nn. The sample was immersed in a liquid cell filled with a 10^{-3} M solution of octadecanethiol in ethanol. As molecules of dodecanethiol under the tip were shaved away under high force, molecules of octadecanethiol assembled immediately following the scanning path of the probe. The edges of the nanografted area are outlined in the concurrent lateral force image (Figure 2.14b). The height of the nanografted square measured 1.2 ± 0.2 nm taller than the matrix SAM (Figure 2.14c). The theoretical thickness of octadecanethiol and dodecanethiol are 2.22 nm and 1.56 nm respectively.[95] Thus, the overall height of the nanografted molecules would measure (1.2 + 1.56) 2.8 ± 0.6 nm in this example. This value is taller than would be expected, however there are five concentric steps arranged from left-to-right across the pattern, each measuring 0.2 nm. A flatter area of the substrate would be needed for accurate measurements of film thickness.

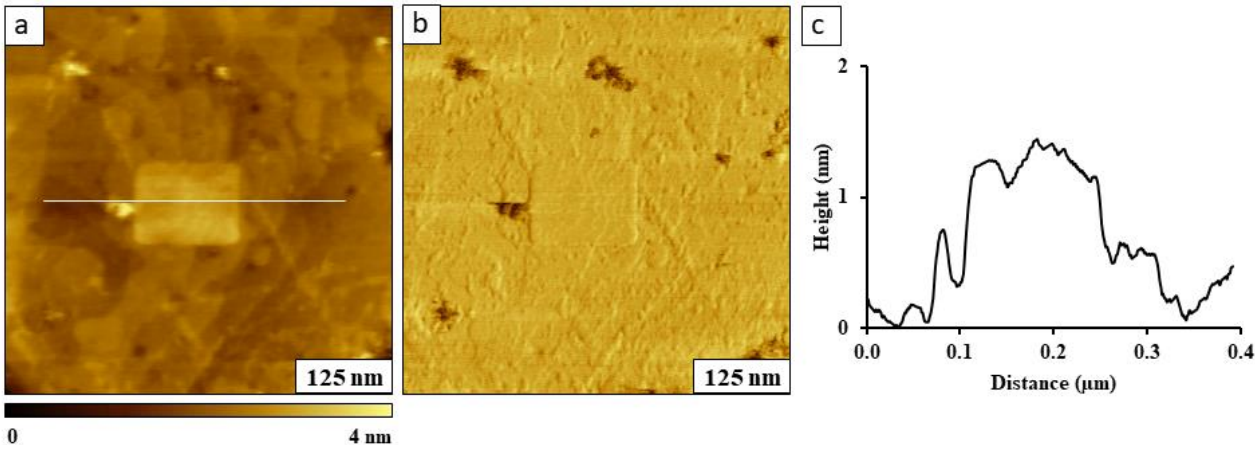

Figure 2.14. Nanografted square of octadecanethiol written within a dodecanethiol film on Au(111) in ethanolic media. (a) Topography frame (150×150 nm^2); (b) lateral force image; (c) cursor profile for the line drawn in *a*.

2.4. Self-Assembled Monolayers (SAMs) of Organosilanes and Organothiols

Self-assembled monolayers (SAMs) are molecular assemblies that form spontaneously on solid surfaces such as glass, semiconductors, metals and metal oxides. Molecular self-assembly has been studied both from gas and liquid phase using a broad range of experimental approaches. The interface of SAMs can be precisely tuned to form the desired chemical functionalities. The

general structure of a SAM consists of three parts: an end group which forms a chemical bond or a strong molecule-substrate link to the surface; a backbone of alkyl or aryl chains that act as a spacer; and a terminal functional group.[100] The terminal groups of the molecules provide chemical functionality to the interface of the SAM. The wettability, adhesion and reactivity of the surface are determined by the choice of terminal groups. The properties of SAMs have been applied for applications which include organic electronic devices,[101] biosensors,[102] corrosion inhibition,[103] and microfabrication.[104]

Molecular classes of SAMs that have been investigated include organosilanes,[105] organothiols,[106] alkylsulfides,[107] xanthates,[108] diamines,[109] arylthiocyanates[110] and peptides.[111] The SAMs used this dissertation are organosilanes and organothiols (Figure 2.15 and 2.16). Well-organized monolayers formed by solution phase adsorption of silane molecules onto glass substrates were first reported and described by Jacob Sagiv in 1980.[112] Surfaces such as glass, quartz, silicon, mica and metal oxides present free hydroxyl groups for generating organosilane SAMs. The covalent network of organosilane bonds is highly stable and robust. Organosilane SAMs are formed by a hydrolysis reaction with the trace amounts of water. The hydrolyzed silanes bind to the surface through a condensation reaction to form Si-O-Si bonds to the substrate as well as forming intermolecular linkages between adjacent silane molecules. Such molecular self-associations lead to branching during polymerization which can produce to disordered films and multilayers.[100, 113] Water and the surface wettability have a direct influence on the resulting density and overall structure of the monolayer. Anhydrous solvents are used for making organosilane SAMs to minimize the presence of water for solution phase reactions with organosilanes, however it can be difficult to control the amount of water for vapor phase processes with organosilanes. Alkane chains of densely packed organosilanes SAMs orient upright from the surface with a tilt

angle of approximately 15° with respect to the surface normal (Figure 2.15).[100] The geometry, surface coverage and the packing of silane SAMs are highly dependent on temperature,[114]

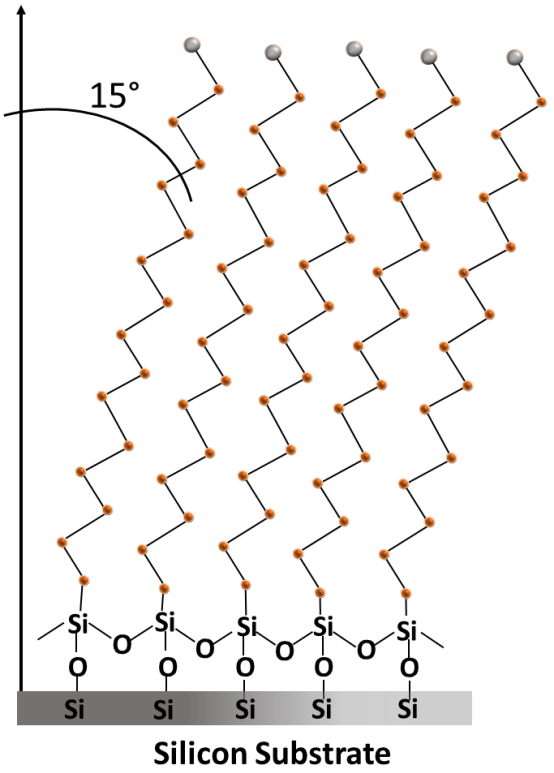

Figure 2.15. General structure for SAMs of organosilanes.

humidity,[115] the nature of the solvent,[116-117] and the amount and the surface distribution of water.[118-119]

The first studies of the self-assembly of organic disulfides on Au(111) through spontaneous absorption was reported by R. G. Nuzzo and coworkers in 1983.[120] Alkanethiols have a strong affinity to bind to noble and coinage metal surfaces such as Au, Ag, Pt, Pd, and Cu through chemisorption. The basic structure of an alkanethiol molecule consists of three parts: the sulfur group, a carbon backbone and the terminal functional group. During surface self-assembly, the sulfur binds to a gold surface through chemisorption to form a commensurate structure. The carbon

chain provides a spacer to design the thickness of the films. Intermolecular (van der Waals) forces between adjacent carbon chains facilitate a high packing density. Functional groups such as methyl, alcohol, esters, carboxylic acids or amides can be used as the terminal group of *n*-alkanethiols. Protocols for preparing SAMs are to immerse the substrate in dilute solutions of alkanethiols to produce highly reproducible, crystalline films. The solution self-assembly of *n*-alkanethiol SAMs on gold surfaces occurs in two steps: a physisorbed, lying-down phase and an upright configuration. The first phase of alkanethiol self-assembly produces a film of physisorbed *n*-alkanethiol molecules lying-down on the gold surface with the carbon backbone aligned parallel to the substrate. A phase transition occurs when the surface coverage is saturated and thiol molecules rearrange to form the crystalline phase with a standing up configuration.[121-122] Within alkanethiol SAMs, the molecular backbone is tilted 30° relative to the surface normal, as shown

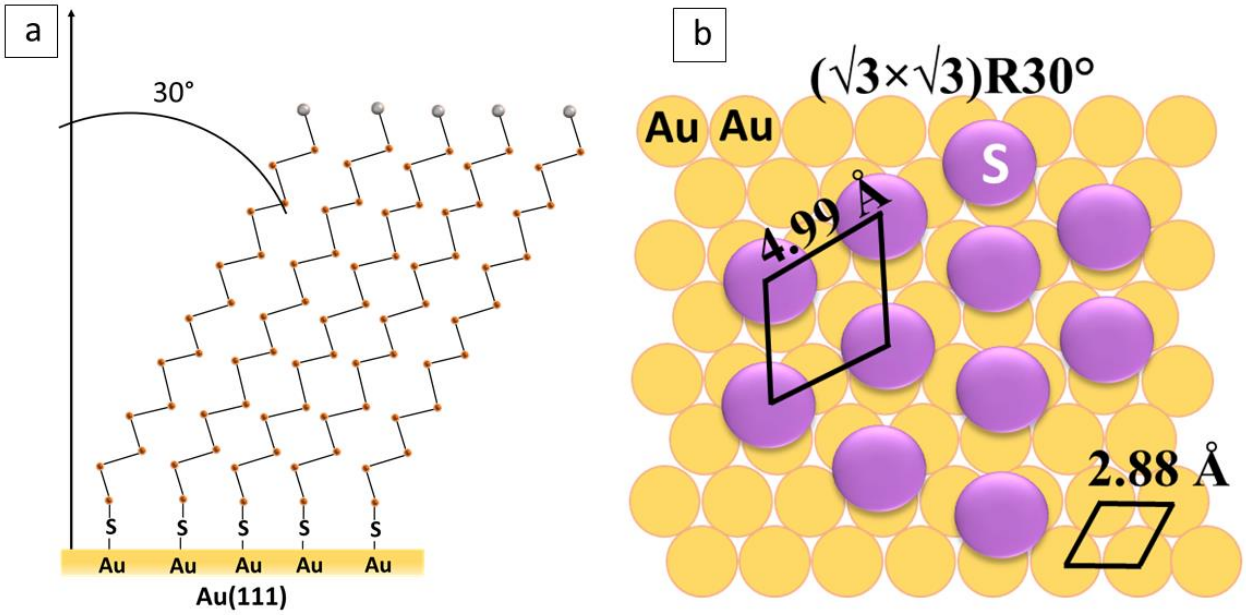

Figure 2.16. Generalized chemical models for SAMs of organosilanes. (a) Side-view and (b) top view of the commensurate lattice structure of alkanethiols formed on Au(111).

in Figure 2.16a. Molecules of alkanethiols spontaneously self-assemble to form a close-packed, commensurate ($\sqrt{3} \times \sqrt{3}$)R30° lattice shown in Figure 2.16b. The sulfur groups are considered to bind at triple hollow sites of Au(111) through chemisorptive Au-S bonds.

Typical surface features of an alkanethiol SAM of dodecanethiol formed on Au(111) acquired with contact mode imaging in ethanolic media are shown in Figure 2.17. Views of multiple irregularly shaped terraces of the underlying gold surface can be visualized in the topography frame of Figure 2.17a. A close-up view of gold terrace steps is shown in the zoom-in topograph of Figure 2.17b, with each step measuring a monoatomic height. The cursor profile in Figure 2.17c indicates close agreement with the expected value for step height measuring ~0.22 nm in height.[123]

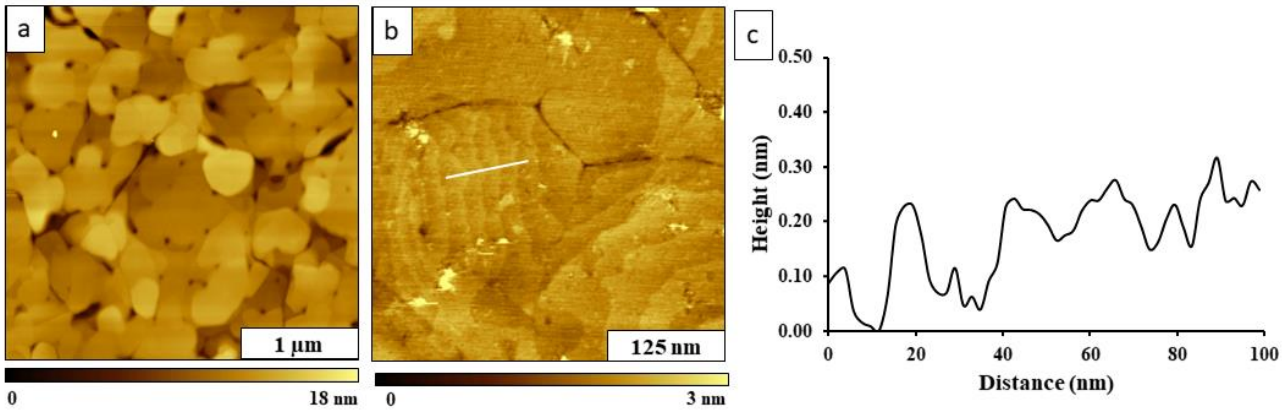

Figure 2.17. Dodecanethiol SAM on atomically flat Au(111) viewed with contact mode AFM, acquired in ethanol. (a) Topograph of 4×4 µm^2 area; (b) gold atomic steps are resolved in a magnified area (0.5×0.5 µm^2); (c) cursor profile for the line profile drawn across a monoatomic gold step shown in *b*.

2.5. Nanostructures Prepared with Particle Lithography

Particle lithography, also referred to as colloidal lithography[124-125] and nanosphere lithography[126-127] has been used to prepare nanopatterns of proteins,[54] silane SAMs,[124] thiol SAMs,[128] metal films,[129] and nanoparticles.[129] Particle lithography was first introduced as "Natural Lithography" by Deckman and Dunsmuir in 1982, in which the authors demonstrated arrays of

densely-packed spheres of polystyrene were formed spontaneously on aluminum substrates.[130] Approaches with particle lithography enable the simultaneous construction of millions of nanopatterns on surfaces to produce uniform geometries over relatively large areas using a few basic chemical steps with colloidal particles.

All of the protocols for colloidal patterning require a surface mask or template of monodisperse silica or latex spheres. A surface mask is prepared by depositing a suspension of monodisperse colloids onto a flat substrate, which is then dried. The mask can also be prepared by spin-coating or Langmuir processes to promote crystallization. During the drying step, hydrodynamic and capillary forces pull the spheres together to form a close-packed layer. Example AFM images of the close-packed arrangement of silica spheres are shown in Figure 2.18, which formed spontaneously by drying an aqueous colloidal suspension in ambient air. The images show

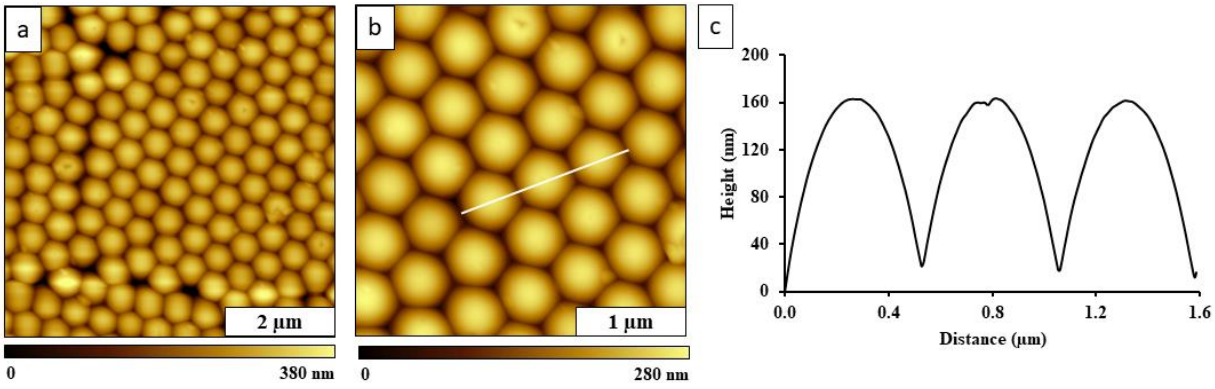

Figure 2.18. The closed-packed arrangement of silica spheres with 500 nm diameter. (a) Topograph (6×6 µm^2) of silica spheres acquired with tapping mode; (b) magnified topograph (3×3 µm^2); (c) cursor profile for the line in *b*.

the uppermost layer of a multilayer film, there are a few imperfections such as vacancies and shifts in registry (Figure 2.18a). In the close-up view of Figure 2.18b, the closed packed hexagonal arrangement of silica spheres is apparent. The cursor profile in Figure 2.18c shows height and distance changes along the line drawn on Figure 2.18b. Eventhough, the diameter of the spheres is 500 nm, the cursor profile doesn't show the true height. This is because the AFM tip cannot

reach to the bottom of the spheres due to the tight packing of the spheres. However, the distance between two adjacent spheres is measured closer to 500 nm. Vapor phase molecules or nanomaterials are deposited through the colloidal mask to form surface patterns. The areas where the spheres are in contact with the surface prevent the deposition of materials at protected sites. Sonicating in a solvent or stripping is used to remove the particle mask to generate nanostructures.

For dissertation experiments, protocols of particle lithography combined with self-assembly of organosilanes and organothiols were used to prepare high-throughput arrays of model surface structures. The areas that were uncovered when the sphere mask was removed were used as nanocontainers for the selective deposition of other molecules and nanomaterials.

Two example experiments with immersion particle lithography are shown in Figure 2.19. A masked substrate was immersed in a dilute solution of ethanol and octadecyltrichlorosilane (OTS) in anhydrous toluene to form patterns of nanoholes. In this example, the masked sample was annealed by heating at 150 °C for 24 h to secure the spheres onto the surface to sustain the attachment of particles of the surface during solvent immersion. Upon immersion, the molecules of alkylthiols or alkylsilanes self-assembled onto the exposed areas on the substrate surrounding the beads of the mask. The spheres were removed by steps of sonication in water and ethanol. The patterns of nanoholes produced by immersion particle lithography are shown for dodecanethiol in Figure 2.19a. The dark circles in the topography frame of Figure 2.19a indicate circular areas of the uncovered gold substrate that had been protected by the spheres of the particle mask. A few dark scars are apparent within the dodecanethiol SAM, which are typical features of an alkanethiol SAM. The features of the underlying substrate can be vaguely resolved, such as gold terraces and step edges. There are 46 nanoholes in the 4×4 μm^2 scan area. The average diameter of the nanoholes measured 100 ± 20 nm (n=40), and the average depth measured the thickness of a

monolayer,1.4 ± 0.3 nm (*n*=40). Frictional contrast is mapped in the concurrently acquired lateral force image of Figure 2.19b. The tip-surface interactions within gold areas of nanoholes have different chemical contrast compared to the surrounding areas of the methyl-terminated SAM.

In the second example (Figure 2.19c), nanoholes were formed within an OTS SAM on Si(111) using immersion particle lithography. There are 40 circular dark holes of Si(111) that were uncovered after rinsing away the surface mask of silica spheres, shown within the 4×4 μm^2

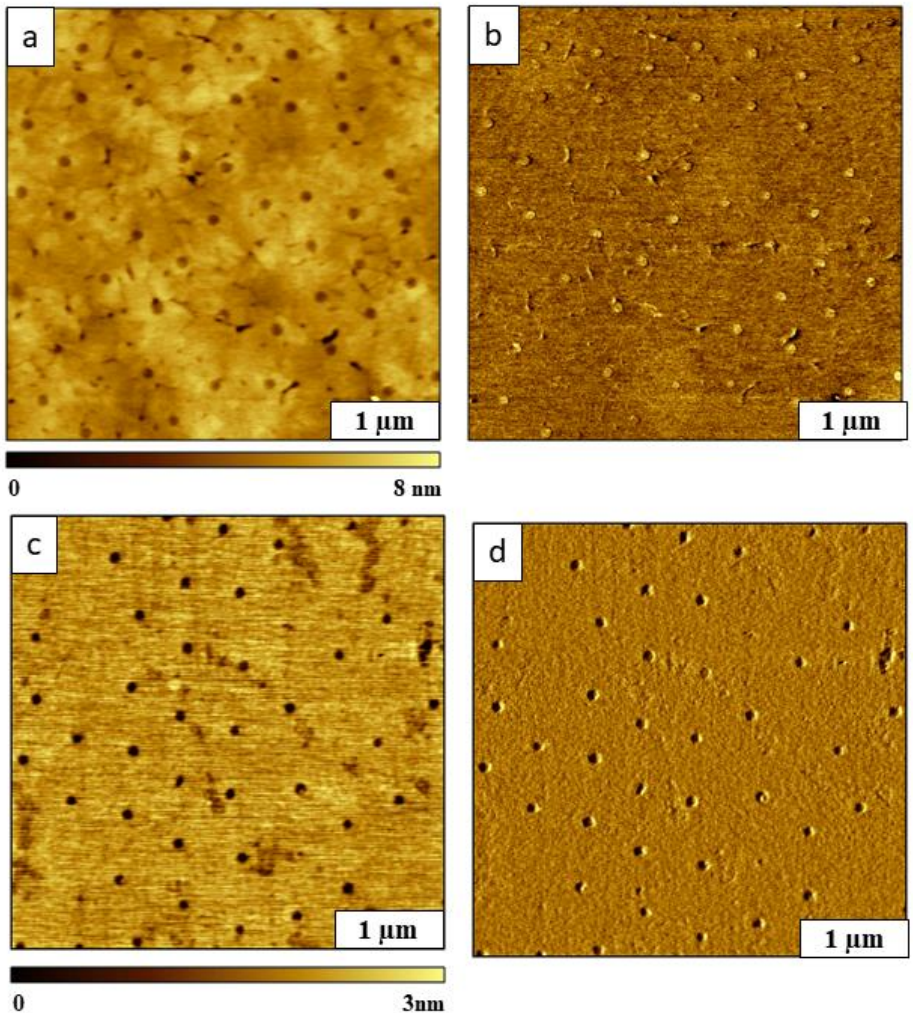

Figure 2.19. Nanoholes within a SAM of dodecanethiol prepared on Au(111) (top row), and within OTS on Si(111) (bottom row). Protocols with immersion particle lithography were used to prepare the samples. (a) Contact mode topography image (4×4 μm^2) of nanoholes within dodecanethiol; (b) corresponding lateral force image of *a*; (c) topography image (4×4 μm^2) of nanoholes within OTS SAM; (d) lateral force image for *c*. Samples were prepared using 500 nm silica spheres as a surface mask.

topography frame of Figure 2.19c. The average diameter and the depth of nanoholes measured 100 ± 30 nm and 2.0 ± 0.3 nm, respectively (n=40). The overall surface coverage of OTS is ~ 91%. Pixel counting with a manual threshold was used for estimating surface coverage. The remaining areas of uncovered substrate can be used for depositing molecules or nanomaterials in further patterning steps. The differences in surface chemistry are mapped in the concurrently acquired lateral force image of Figure 2.19d, disclosing the specificity of patterning for OTS.

When preparing surface masks, slight changes in the drying step will produce distinct surface geometries of holes or ring nanopatterns. The mechanisms of surface wetting are discussed in Chapter 4 for the vapor/solid interface. The surface geometry that is produced by colloidal lithography with organosilanes depends sensitively on the localization of trace amounts of water persisting on the substrate. The confined, narrow regions of meniscus sites at the base of the spherical particles can trap water deposits to form nanorings. Example images of nanoholes and nanorings are demonstrated in Figure 2.20 with OTS. Using particle lithography with immersion in a 0.1 % (v/v) of OTS solution in anhydrous toluene produced nanoholes within a surface film (Figure 2.20a). Heated vapor deposition of OTS generated surface structures of nanorings, shown in Figure 2.20b. The shapes and edges of the surface patterns can be sensitively resolved in the concurrently acquired phase images (Figures 2.20c,d). In essence, the localization of water on the surface drives the surface attachment of organosilanes to self-assemble in wetted areas surrounding the particle mask. A few imperfections are evident in areas with missing spheres, however in the overall view, exquisitely regular, periodic arrangements are apparent which have highly uniform geometries at the nanoscale, for areas spanning microns of the sample.

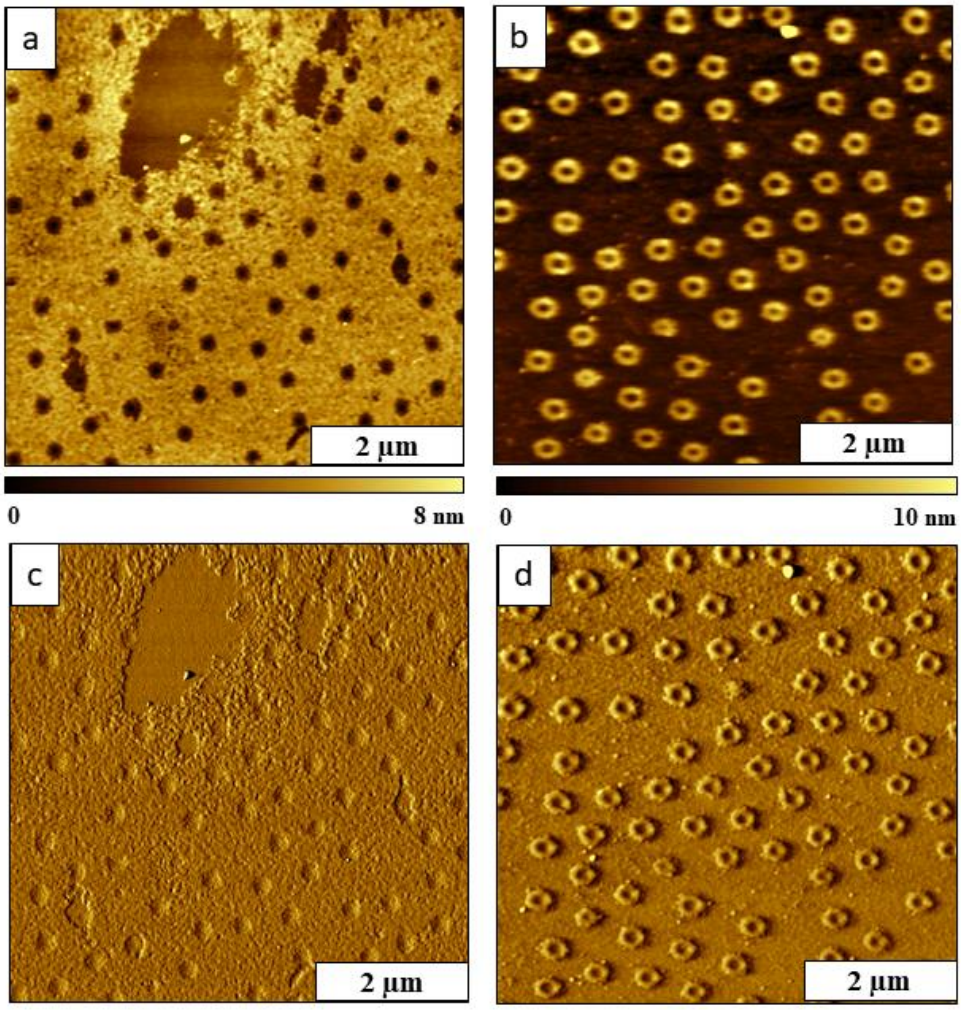

Figure 2.20. Patterns of nanoholes and nanorings of OTS prepared on Si(111) using particle lithography. Tapping-mode topographs of (a) nanoholes within an OTS SAM; (b) nanorings of OTS; (c) phase image simultaneously acquired with *a*; (d) phase frame for *b*. Images were acquired with tapping mode AFM for samples prepared with silica (for nanoholes) and latex (for nanorings) with 500 nm diameter.

2.6. Summary

Nanopatterning protocols furnished a practical strategy for investigating mechanisms of chemical assembly on surfaces, for the experiments described in this dissertation. Protocols with particle lithography were used to prepare model interfaces for the AFM experiments presented in Chapters 3-7. Nickel nanorings were prepared with particle lithography combined with electroless deposition in Chapter 3 for studies with MSM-AFM. Studies of the role of the wettability at the

interface for surface reactions was examined using organosilane as a tracking molecule to map the water distribution on hydrophilic and hydrophobic surfaces in Chapter 4. Scanning probe-based nanolithography and particle lithography protocols were used to study surface films prepared by photografting aryl iodides in Chapter 5. Surface linkage of porphyrins onto planar Si(111) surfaces and nanoparticle surfaces was examined in Chapter 6 and Chapter 7. Particle lithography was applied to nanopattern the porphyrins to facilitate ultrasensitive measurements with scanning probe microscopy. Tapping-mode and contact mode AFM imaging were used to characterize nanopatterns *ex situ* after key reaction steps in each Chapter. Force modulation microscopy was applied to examine differences in elastic properties of phthalocyanine nanostructures in Appendix G.

CHAPTER 3. NICKEL NANOFILMS ELECTROLESSLY DEPOSITED ON ORGANOSILANE NANORINGS AND CHARACTERIZED BY CONTACT MODE AFM COMBINED WITH MAGNETIC SAMPLE MODULATION*

3.1. Introduction

Patterning approaches for preparing ring-shaped nanostructures of metals has become an active area of research, providing models for fundamental studies of the relationship of reduced dimensions with associated size-dependent magnetic[131-133] and optical[134-135] properties. Magnetic states, magnetization reversal and optical properties are strongly dependent on the thickness, diameter and composition of metal nanostructures.[136-137] Nickel coatings offer properties of corrosion resistance, hardness, and wear resistance for commercial applications. In addition, nickel is an element that is ferromagnetic at room temperature which offers capabilities for magnetic separations.[138-139]

Processes for fabricating metal nanorings include electron-beam[140-142] and nanoimprint[143-145] lithography. Chemical approaches for nanofabrication with colloidal lithography (also referred to as particle lithography) have been developed to prepare arrays of Ni nanorings using electrodeposition.[136, 146] For example, an approach using colloidal lithography combined with electrodeposition of Ni, Co, bimetallic Ni/Au, CdSe, and polydopamine was reported by Cho, et al. for preparing metallic, semiconducting and insulating nanorings.[146] With colloidal lithography methods, the use of a mask of size-sorted latex or silica spheres offers architectural control of the dimensions and spacing of nanorings, by selecting the diameters of spheres.[147-148] To prepare a surface mask, suspensions of monodisperse colloidal particles can be dried on flat substrates to naturally form an organized arrangement of spheres. Surface masks have also been prepared by

*Content in this chapter is published as a article in ACS Omega. Reprinted (adapted) with permission from (ACS Appl. Nano Mater 2019, DOI: 10.1021/acsanm.9b00153). Copyright (2019) American Chemical Society (See Appendix C).

steps of solvent evaporation or spin-coating to produce crystalline films with hexagonally packed arrangements of spheres. In further steps, metals can be deposited through the mask to form ring-shaped patterns surrounding the spheres, using strategies such as ELD,[129, 149] electron-beam deposition[150] or electrodeposition.[151]

Electroless deposition (ELD) is a versatile approach for accomplishing metal plating without the use of electrical energy which can be adapted for benchtop chemistry. An advantage of the chemical reduction process of ELD compared to electroplating approaches is that the metal coatings tend to have relatively uniform thickness throughout the plated surface. With ELD, metal films are prepared by an autocatalytic method where metal is deposited in the presence of a catalyst from an aqueous solution of a metal salt in solution with a reducing agent and a complexing agent. The reducing agent supplies electrons for metal ion reduction, whereas the complexing agent prevents metal ions precipitating out as insoluble by-products as well as serves as a buffer to maintain a certain pH and ionic strength.[152-153] Examples of reducing agents include sodium hypophosphite, hydrazine, Pd salts, borohydride and boron-nitrogen compounds. The coatings formed with ELD are actually alloys such as NiP or NiB, depending on the reagents in the plating bath. Methods of ELD have been applied for making Ni coatings for industrial applications and also for micro- and nanofabrication.[154-156]

Both superparamagnetic and ferromagnetic nanostructures of Ni have been prepared with ELD approaches. Arrays of CoNiP nanodots were prepared with ELD on a patterned Si substrate using electron-beam lithography and reactive ion etching.[157] The composite magnetic nanostructures were characterized with magnetometry, electron microscopy and magnetic force microscopy (MFM). Nanorod structures of Ni were synthesized using anodic aluminum oxide as

a template for ELD with Ni.[158-159] As prepared, the nanorods were superparamagnetic but were transformed into ferromagnetic structures when annealed at 400 ^{o}C.

Electroless plating can be used to prepare metal coatings on surfaces of non-conducting substrates such as glass, plastics and ceramics at low temperatures. Surfaces which have an active terminal group for binding Pd catalysts such as organothiols,[160] organosilanes,[161-165] polyelectrolyte layers[166-167] and polymers[168-170] have been applied for ELD. Catalytic Pd nanoparticles bound to nitrogen-bearing polymers[170] or aminosilane layers[171-173] have been used as seeds for subsequent deposition and growth of Ni. The amine-terminated organosilane 3-aminopropyltriethoxysilane (APTES) has been described as a coupling agent, or as a catalyst adhesive layer for selectively binding Pd nanoparticles.

Magnetic force microscopy (MFM) has been applied to investigate the magnetic characteristics of metal nanorings.[126, 174-176] In the traditional approach for magnetic imaging with MFM, the underside of a silicon or silicon-nitride AFM probe is coated with a magnetic alloy such as cobalt and chromium for permanent magnetization of the tip. When scanned with AFM in non-contact mode, the magnetized MFM tip is repelled or attracted to magnetic domains of the sample to map the strength and polarity of magnetic regions. A drawback of the MFM approach is that the tips are not ultra-sharp, the metal coating produces larger, blunt probes. Also, the magnetic forces of samples tend to be fairly relatively weak, which limits resolution to the realm of microns.

In this report, a protocol was developed for preparing Ni nanorings using ELD and colloidal lithography. The successive steps of preparing organosilane nanorings and coating surfaces with Pd catalyst and Ni were evaluated with modes of AFM and electron microscopy. Magnetic sample modulation (MSM) was combined with contact mode atomic force microscopy (AFM) for characterizing samples of Ni nanorings. Our approach with modulation of magnetic samples

requires using a *nonmagnetic* probe to sensitively visualize how nanomaterials vibrate in response to the flux of an AC electromagnetic field, such as metal nanoparticles[56, 149] and ferroproteins.[173] A soft, nonmagnetic AFM probe serves as a vertical motion sensor for mapping areas of the sample which vibrate in response to an alternating magnetic field. With MSM-AFM, selective modulation of magnetic, ferromagnetic, paramagnetic and diamagnetic nanomaterials can be sensitively detected with a conventional AFM probe, by actuating the sample with an externally applied AC magnetic field. The differences for images with and without an applied field can be used to identify magnetic areas of the sample. To achieve selective mapping of Pd and Ni surface features, lock-in detection was used to track changes in the phase and amplitude of the tip motion due to magnetic actuation of the sample relative to the driving AC signal.

3.2. Experimental Section

3.2.1. Materials and Reagents

3-Aminopropyl)triethoxysilane (APTES) was purchased from Gelest (Morrisville, PA) and used as received. Borane dimethylamine complex (DMAB, 97%) was acquired from Beantown Chemical Corporation, (Hudson, NH). Lactic acid and Ni(II) nitrate hexahydrate ($Ni(NO)_3 \bullet H_2O$) were purchased from Alfa Aesar, (Tewksbury, MA). Potassium tetrachloropalladate(II) (K_2PdCl_4, $\geq$ 99.99%) and sodium citrate dihydrate, were obtained from Sigma-Aldrich (St. Louis, MO). Sulfuric acid (98.0 % J.T. Baker, Phillipsburg, NJ), hydrochloric acid (HCl, 37.2%, Fisher Scientific, Hampton, NH), ammonium hydroxide (NH_4OH, 29%, Ward's Science, Rochester, NY) and hydrogen peroxide, (H_2O_2, 30% (VWR) were used as received. Size-sorted, monodisperse silica spheres in water (diameter 496 ± 8 nm) were purchased from Thermo Fisher Scientific (Fremont, CA). Silicon wafers were obtained from Ted Pella (Redding, CA). Ethanol, 200 proof was obtained from Deacon Labs (Prussia, PA). To ensure purity for preparing

solutions, Milli-Q type 1 water, (18 megohm, Millipore, Bedford, MA) was used for preparing solutions and washing samples.

3.2.2. Preparation of a Surface Mask

Pieces of polished silicon wafers, (10×10 mm) were immersed in piranha solution for 1.5 h to remove any organic residues present on the substrate. Piranha solution is a mixture of sulfuric acid and hydrogen peroxide at a ratio of 3:1 (v/v). Caution: piranha solution is highly corrosive and should be handled with great care. After soaking in piranha, substrates were rinsed with copious amounts of ultrapure water and dried with nitrogen. To remove residual surfactants or contaminants, the silica spheres were cleaned by centrifugation in ultrapure water as follows. A portion of 400 μL of the solution of silica spheres and 600 μL ultrapure water was added to a microcentrifuge tube. The suspension was centrifuged at 20 000 rpm for 10 min. The supernatant was removed and the pellet was resuspended in 1 mL water. The centrifugation step was repeated three times. The pellet of the final centrifugation step was resuspended in 400 μL of ultrapure water by vortex mixing. The surface mask for colloidal lithography was prepared by depositing 20 μL of clean silica spheres onto Si(111) substrates. The sample was dried under ambient conditions for 4 h.

3.2.3. Protocol for Colloidal Lithography with Vapor Deposition

Nanopatterns of APTES were prepared using colloidal lithography with a vapor deposition protocol as reported previously with octadecyltrichlorosilane (OTS).[177-178] Vapor phase deposition at elevated temperatures has been reported to produce smooth layers of APTES on Si(111) substrates.[113] Substrates with the dried film of silica spheres were placed on a raised platform inside a sealed jar containing 400 μL of neat APTES. The container was then placed in an oven at 70 C for 18 h. Next, the samples were removed and rinsed with ethanol. The surface mask of

spheres was efficiently removed by sonication in ethanol and then in ultrapure water. The sonication step was repeated three times, then the samples were dried under a flow of nitrogen. The overall steps for nanofabrication are shown in Supporting Information, Figure A.1.

3.2.4. Electroless Deposition of Ni

Electroless deposition of Ni was accomplished using conditions that were previously described for surfaces of polymers[179] and films of APTES.[180] A catalyst solution (5 mM) of Pd (K_2PdCl_4) was prepared in ultrapure water and adjusted to pH 2 with 1 M HCl. The samples with APTES nanorings were immersed in the Pd catalyst solution for 3 h followed by rinsing with ultrapure water. An electroplating bath was prepared with 1.10 g $Ni(NO)_3$, 0.5 g of sodium citrate, 0.05 g of DMAB and 0.25 g of lactic acid in 25 ml water. The pH of the bath was adjusted to 6.5 using 25% NH_4OH. Samples were submerged in the bath for 3 h, then removed and rinsed thoroughly with ultrapure water, followed by nitrogen drying. During the sample immersion steps, the solutions were not actively stirred.

3.2.5. Atomic Force Microscopy (AFM)

A model 5500 scanning probe microscopy system (Keysight, Santa Rosa, CA) was used to characterize samples in ambient air. Silicon AFM probes with an aluminum reflex coating were used to acquire tapping-mode AFM images, which had an average resonance frequency of 300 kHz and force constant of 40 N/m (Budget Sensors, PN Tap300Al-G). Soft silicon probes were used for MSM-AFM (Budget Sensors, PN ContAl-G) with a force constant of 0.2 N/m. For tapping-mode, images were acquired using a tip speed of 2.15 lines/s with 512 lines/frame. Samples were mounted on a magnetic AC (MAC) mode sample stage (Keysight, Santa Rosa, CA) for MSM-AFM studies. Digital images were acquired with PicoView (version 1.20.2). The scan

rate used to acquire MSM-AFM images was 1.9 lines/s and 512 lines/frame. Images were processed and analyzed with Gwyddion (version 2.49) which is freely available online.[181]

3.2.6. Scanning Electron Microscopy (SEM)

Scanning electron micrographs were acquired using an FEG Quanta 3D SEM.

3.3. Results and Discussion

A multi-step approach was used to prepare Ni nanopatterns using ELD and colloidal lithography with organosilanes. With a few basic steps, regular arrangements of millions of metal nanostructures were prepared on templates of organosilane nanopatterns on Si(111). Changes in surface morphology were evaluated *ex situ* after each key step using AFM studies in ambient air.

3.3.1. Construction and AFM Characterization of Ni Nanostructures.

In the first step, organosilane nanostructures were prepared on Si(111) substrates. A surface mask of silica spheres was exposed to a heated vapor of APTES to form ring-shaped nanostructures as shown in Figures 3.1a and 3.1b. The APTES nanorings are apparent after the silica spheres were rinsed away. Since the silica beads of the surface mask were weakly attached to the surface primarily through physisorption, the beads are readily displaced with rinsing steps. However, the film of APTES binds covalently to the substrate and persists on the surface despite multiple steps of solvent rinses and sonication that were used to remove the particle mask.

With vapor deposition of organosilanes the distribution of water on the substrate is not uniform under ambient air; there is a thicker layer of water at meniscus areas at the base of the spheres. The thickness and size of the meniscus sites will vary according to the diameter of the particles and humidity. With organosilanes, the ring geometries pinpoint the location of water meniscus sites where hydrolysis and condensation reactions take place.[177] The bright circles in the topography frames are nanorings where a multilayer of APTES was formed. The dark spots inside

of the center of the rings are the sites of exposed substrate where the spheres of the mask were displaced. There are 260 rings within the 12 × 12 μm^2 frame of Figure 3.1a, which scales to ~10^8 nanopatterns/cm^2. There are a few vacancies where spheres of the surface mask are missing, however the geometry of nanopatterns is relatively uniform over broad areas of the sample,

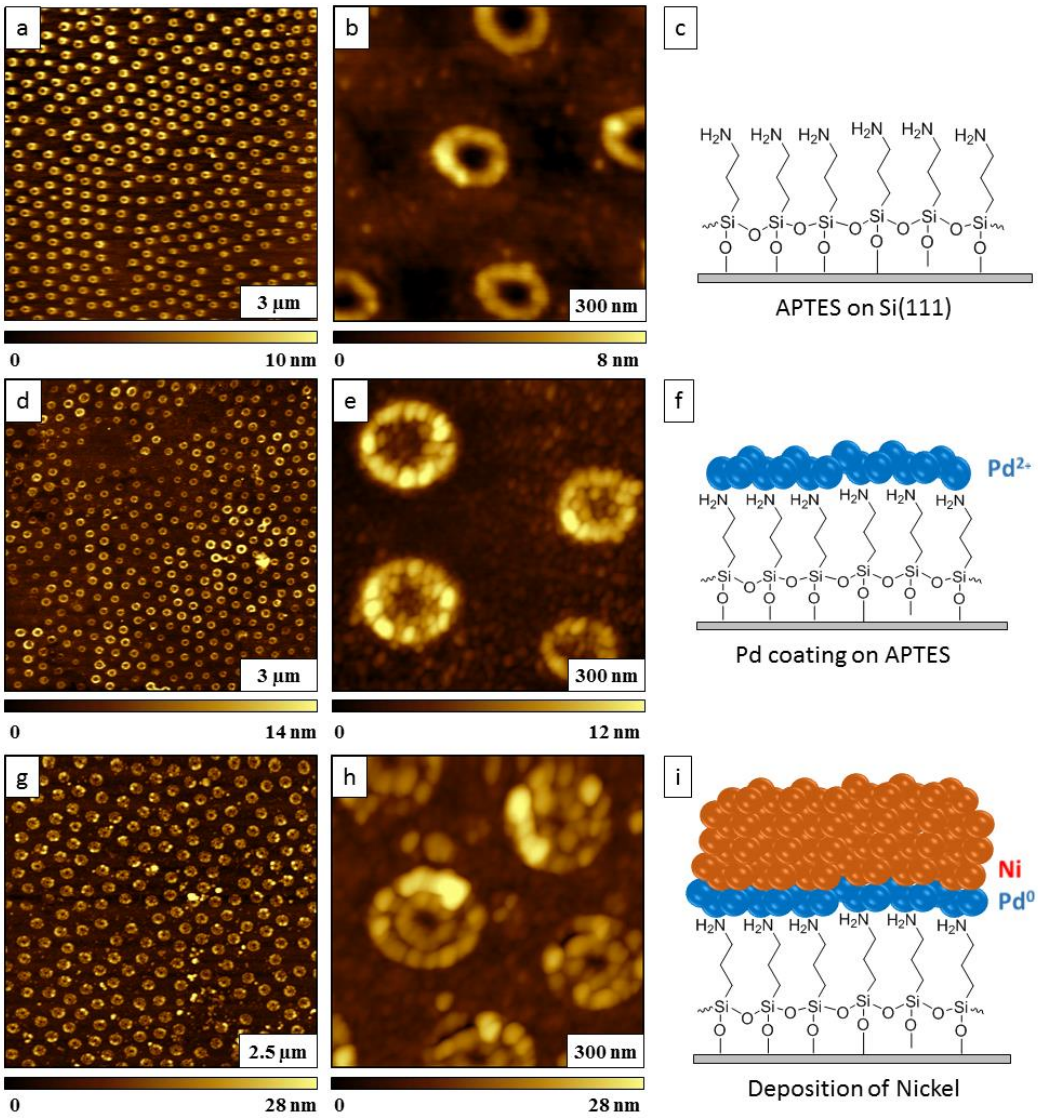

Figure 3.1. Surface changes after key steps for preparing Ni nanostructures using ELD and particle lithography. (a) Nanorings of APTES on Si(111) prepared by particle lithography combined with vapor deposition viewed with a topography image (12 × 12 μm^2); (b) zoom-in topography frame (1.2 × 1.2 μm^2); (c) surface model of APTES monolayer. (d) After deposition of Pd catalyst on APTES nanostructures; (e) close-up view; (f) scheme for addition of catalyst particles. (g) After immersion in the plating bath, nanorings have increased in size (topography image, 10 × 10 μm^2);

(h) Magnified topography image of Ni nanorings (1.2 × 1.2 μm^2); (i) model of Ni nanostructure assembly. Images were acquired in ambient air using tapping-mode AFM.

spanning tens of microns. A close-up view of five nanorings is shown in Figure 3.1b, the areas between the rings appear to be quite flat and free of contaminants, these areas have a monolayer film of APTES. The bright areas of nanorings, where there is a multilayer of APTES, cover ~28% of the surface. The surface coverage of the tallest areas where there is a multilayer of APTES measures ~28% for areas of the bright nanorings. The round shapes of the ring patterns are not perfectly symmetric at the nanoscale for natural self-assembly. The

AFM topography images provide a real space view of the outcome of the molecular assembly process that occurred with a heated vapor of APTES. The interfacial amine groups of APTES will serve as a template for subsequent patterning steps to add catalyst and metal via electroless deposition (Figure 3.1c). In the next step, the substrate with APTES nanorings was immersed in a Pd catalyst solution to activate the surface for electroless plating. In acidic media, K_2PdCl_4 salt forms $PdCl_4^{2-}$ which then undergoes reduction to form Pd(0). After surface treatment with the Pd catalyst, increases in the size and morphology of APTES nanorings are revealed in Figures 3.1d and 3.1e. The nanostructures have become taller and wider, compared to the untreated surface views. There are 285 nanorings within the topography frame of Figure 3.1d, evidencing a hexagonal arrangement with a few vacancies. A close-up view of four nanorings (Figure 3.1e) shows that the structures are comprised of small clusters of particles. Catalyst nanoparticles have also assembled in areas between the nanorings, however with tapping-mode it is difficult to fully resolve the true morphology of the areas in between rings which appear to have a clustered morphology. The surface coverage of the taller areas of the rings has increased to ~35% with the observation that the nanostructures became taller and wider with addition of Pd. Nanoparticles of

Pd^{2+} coalesce to form nanocrystals that attach to the amine groups of APTES, which will provide nucleation sites for the electroless deposition of Ni (Figure 3.1f).

In the final step of nanofabrication, samples were immersed in an electroless plating bath to direct the reduction of Ni onto the sites of catalyst nanoparticles. Representative AFM images of Ni nanorings formed after plating are shown in Figures 3.1g and 3.1h. After metallization, the widths and heights of the nanostructures have become taller and wider. The surface coverage of the areas of the taller Ni nanorings has increased to 41% correspondingly with an increase in the widths of nanorings. A magnified view of 4 nanorings (Figure 3.1h) reveals that an inner and outer ring has formed to produce concentric circles in this example. When preparing replicate samples, we observed that slight changes in the solution conditions (e.g. pH, concentration, age of the solutions) can produce distinct differences in surface morphology of the nanostructures. An experiment which produced a morphology of taller, single rings is shown in Supporting Information, Figure A.2. Clusters of nanoparticles are apparent in between the nanorings. A model for the overall assembly of the nanostructure is shown in Figure 3.1i.

Further information of surface changes after reaction step can be derived from phase images, particularly for the areas in between the nanorings; example frames are shown in Figures 3.2a-3.2c. Phase images were concurrently acquired with tapping-mode frames and provide exquisite details of the edges and shapes of surfaces. Distinct changes are apparent for the three key steps revealed in Figure 3.2. The areas in between the rings of APTES are smooth and flat in Figure 3.2a. After treatment with the catalyst, nanoparticles of Pd are distributed throughout the sample with greater aggregation occurring on areas of the nanorings (Figure 3.2b). The morphology and the size of the Pd crystals are affected by factors such as immersion time, pH and chloride ion concentration.[182] After immersion in the Ni plating bath, the particles in areas between

the nanorings have grown into larger clusters, and the width and height of the rings has increased (Figure 3.2c). From multiple line profiles, the thickness of the Ni rings measures 15 ± 3 nm (*n*=50) taller than the surrounding areas.

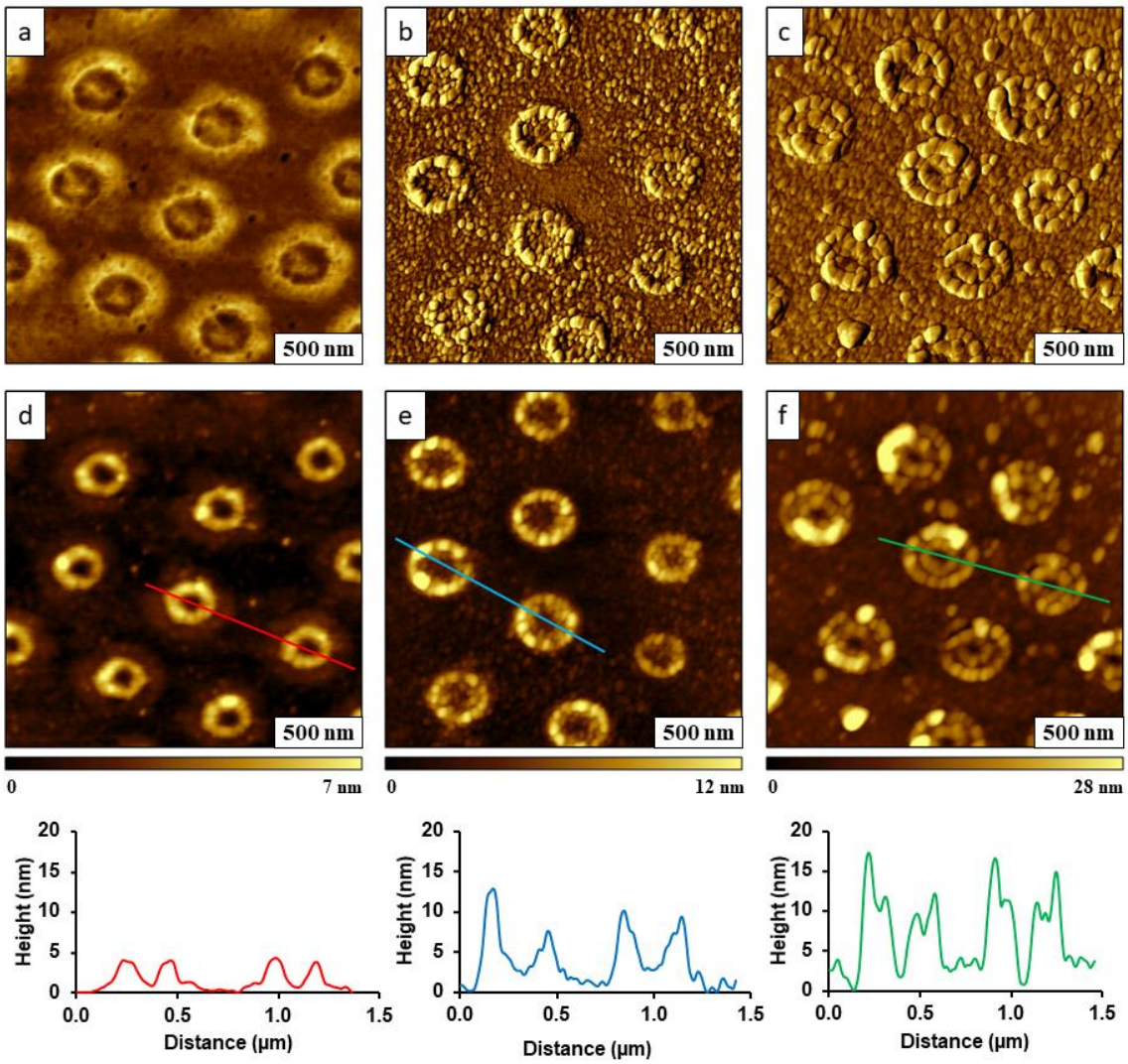

Figure 3.2. Successive changes in surface morphology after each key step. (a) Tapping-mode phase image of APTES nanorings on Si(111); (b) changes after depositing Pd shown with a phase frame; (c) phase channel for Ni nanorings; (d) Topography image of APTES nanorings; (e) topograph after treatment with Pd; (f) Topograph after electroless deposition of Ni. Cursor profiles for the lines drawn across *d, e* and *f* are shown below the topographs. Tapping-mode images were acquired in ambient air for 2 × 2 μm^2 areas.

After each key step, topography frames that were captured simultaneously with the phase images in the top row are presented in Figures 3.2d-3.2f, with an example cursor profile across

two nanostructures below each image. The experiments were conducted *ex situ*, and the frames selected are representative of the morphologies viewed throughout the sample. Each of the frames measure 2 × 2 μm^2 in dimension, enabling a side-by-side comparison of the shapes and arrangement of ten nanorings. Interestingly, the holes in the centers of the nanorings have persisted, however it is not clear from AFM characterizations whether metal was deposited inside the center areas of the nanorings. A greater amount of metal deposition occurred on the ring areas which have a multilayer of APTES, and likely is also present in areas between the rings. The width and the height of the nanorings increased after each step, shown with example cursor profiles below each topograph in Figure 2. With each successive reaction step, the width of the nanorings became taller and broader in dimension, referencing the areas surrounding the rings as a baseline.

A benefit of using colloidal lithography for surface studies is that multiple, replicate nanostructures are produced for systematic quantitative analysis. To more accurately gauge the changes in dimension, 50 measurements were made with cursor profiles of individual structures to assess the increases in size as well as the variability of the shapes of the nanorings. The values of the average and standard deviation are summarized in Table 3.1 after each successive reaction step. The heights were measured at the tallest points of individual nanorings. In the first step of nanofabrication, nanorings of APTES were produced at the sites of water that formed in a meniscus surrounding the silica spheres of the surface mask. The height of the rings measured 5.3 ± 0.8 nm, indicating growth of a multilayer of APTES. Since the theoretical length of APTES is 1.0 nm, the areas of the rings contain 4-6 molecular layers. When preparing films of organosilanes, there is a competition in forming Si-O linkages to the substrate, Si-O-Si bridges between adjacent molecules, and forming free Si-OH hydroxyl groups. A multilayer will form in the presence of

excess water through self-polymerization. The resulting structures of nanorings present amine groups as well as hydroxyl moieties at the interface.

Table 3.1. Dimensions of nanostructures measured from AFM cursor profiles of topography frames.

Nanostructure	Height (nm) (n = 50)	Outer diameter (nm) (n = 50)	Inner diameter (nm) (n = 50)
APTES nanorings	5.3 ± 0.8	273 ± 28	107 ± 14
Nanorings with Pd catalyst	7.3 ± 1.6	315 ± 34	96 ± 28
Nanorings with Ni coating	15 ± 3.4	400 ± 20	68 ± 16

After immersion in the catalyst solution, the thickness of the nanostructures increased from 5.3 to 7.3 nm, indicating that the Pd deposits measured ~ 2 nm in thickness. After treatment in the plating bath, the nanorings changed from 7.3 to 15 nm in height, however the areas in between the ring are also coated with Ni so that the actual size increase is larger. The outer diameter and inner diameter measured 400 ± 20 nm and 68 ± 16 nm, respectively, for the Ni nanorings. The distribution of measurements for the height and diameter of the nanorings is provided in Supporting Information, Figures A.3 and A.4.

For the autocatalytic process of electroless deposition, Pd nanoparticles serve as electron exchange centers for Ni reduction. The initial deposition of Ni takes places with nucleation both on and in between Pd nanoparticles.[183] With ELD, Ni itself is a catalyst for the plating reaction. Therefore, Ni deposition will progress automatically even after Pd sites are coated with metal. As the deposition continues, the deposited Ni islands proceed to grow to form continuous films until reagents are depleted in the plating bath. The role of the Pd catalyst for Ni deposition was tested by immersing samples with APTES nanorings directly in a Ni plating bath, skipping the catalyst step. There was little or no deposition of Ni without the Pd catalyst shown in Supporting Information, Figure A.5.

3.3.2. Investigation of the Magnetic Response of Ni Nanostructures with MSM-AFM

When an AC electromagnetic field is applied to the sample during AFM imaging, ferromagnetic nanostructures will vibrate in response to the flux of the polarity of the field according to selected frequency and field strength parameters. The metal nanostructures are linked to the surface with an organosilane bridge, which serves as a spring for vertical vibration. An AFM probe operated in continuous contact mode can be used to sensitively detect the motion of a vibrating sample (i.e. changes in sinusoidal phase and amplitude of the tip oscillation) with reference to an applied AC waveform signal that drives sample vibration. (Operating procedure of

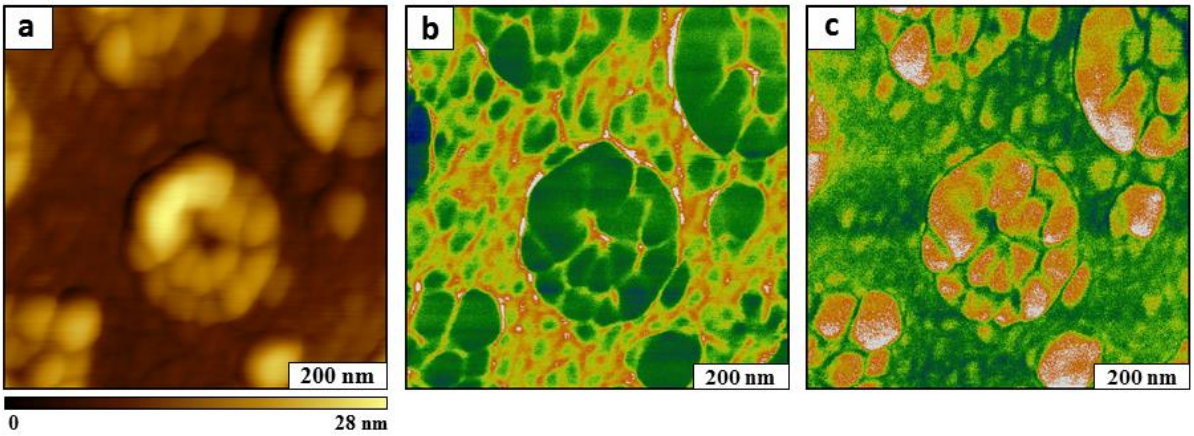

Figure 3.3. Single Ni nanoring imaged with MSM. (a) MSM topography image (800 × 800 nm^2); simultaneously acquired (b) MSM amplitude and (c) MSM phase frames. The driving frequency chosen was 234 kHz with an applied magnetic field strength of ~0.2 T.

MSM is given in Appendix B) With MSM-AFM, the nonmagnetic tip is not actuated, instead the vertical displacement of the vibrating sample can be mapped by contact mode imaging. Example MSM images are presented in Figure 3.3 revealing detailed structural features of an individual Ni nanoring. Essentially, MSM-AFM is a variant of the established instrument configuration for force modulation AFM, except that sample actuation is selective for magnetic domains. Intricate details of the sample morphology and edges of the Ni nanostructures are resolved in the MSM amplitude (Figure 3.3b) and phase (Figure 3.3c) channels. Clusters of Ni

formed a concentric spiral of triangular facets surrounding the circumference of the APTES nanorings. Note that there is an interesting web-like grain structure in areas in between the nanorings that is clearly resolved in Figure 3.3b.

A broader view of a sample area with 15 nanopatterns is presented in Figure 4a with simultaneously acquired MSM amplitude and phase frames. The characteristic spiral shapes and reproducible sizes are apparent for Ni nanorings arranged in a hexagonal pattern across the surface of Si(111) in the topography frame (Figure 3.4a, left). The areas with magnetic response are mapped in the associated MSM amplitude and phase frames for the Ni nanorings (Figure 3.4a, center frames). A resonance peak at 234 kHz was selected for MSM imaging, shown in the frequency spectrum of Figure 3.4a (right). The same imaging parameters were used to acquire images of the sample without metal deposition (Figure 3.4b), as well as after addition of Pd catalyst (Figure 3.4c).

When the resonance parameter of 234 kHz was applied for the sample of APTES without any metal treatment with Ni or Pd, the MSM amplitude and MSM phase images of the nanorings do not have any resolvable features (Figure 3.4b). The topography channel for the untreated APTES nanorings (Figure 3.4b, left) exhibits morphologies of a conventional contact mode image. However samples must contain magnetic materials to enable successful sample modulation with MSM-AFM. Phase and amplitude channels from MSM experiments with APTES nanorings without metal deposition are shown in the center frames of Figure 3.4b, without resolvable detection of any structures. The results were acquired with the proximal peak of 275 kHz detected by a frequency sweep, however there were no successful images for MSM amplitude and MSM phase channels for the nonmagnetic APTES sample. The spectra reveal mainly background peaks in the frequency sweep (Figure 3.4b, right). As might be predicted, characterizations with MSM-

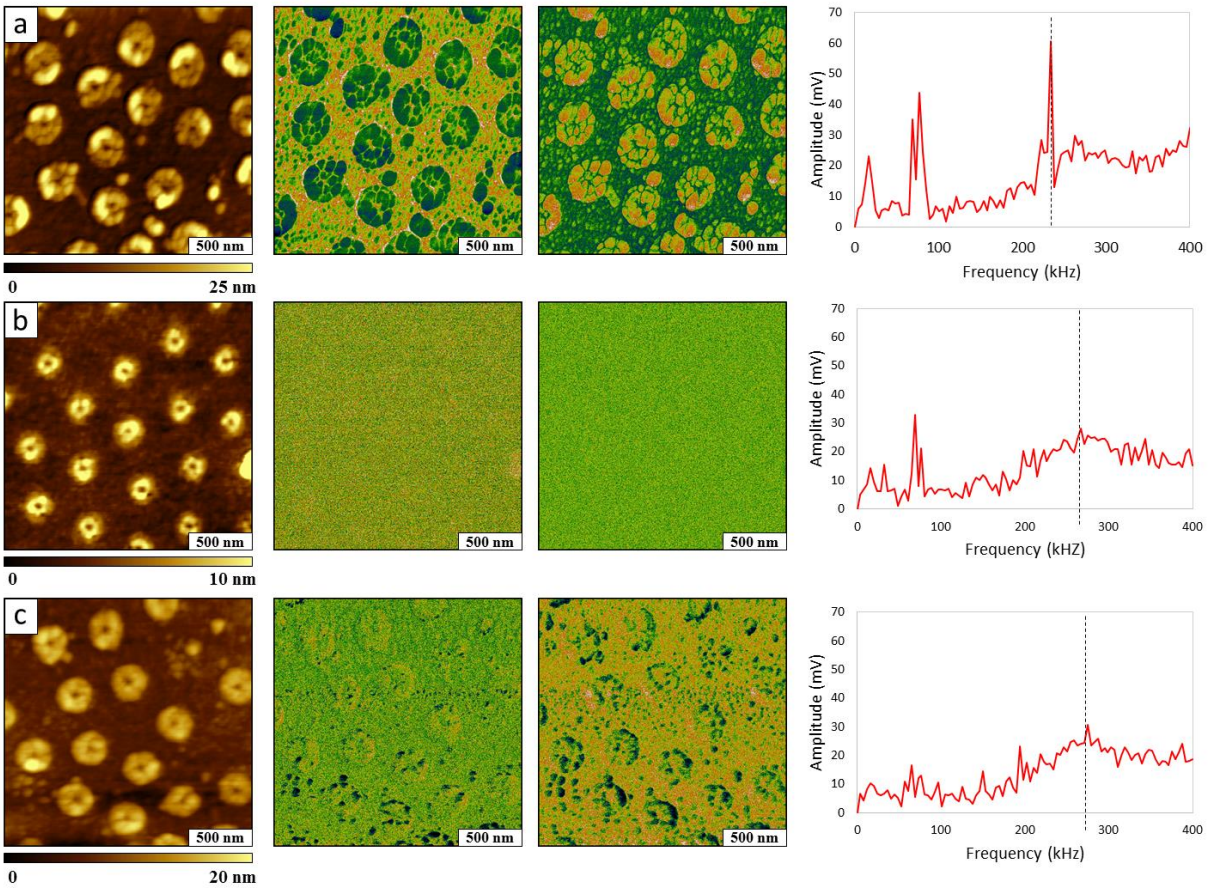

Figure 3.4. Samples of APTES nanorings after treatment with Pd and Ni characterized with MSM-AFM. (a) Top row from left to right: MSM-topography, MSM amplitude, MSM phase channels and frequency spectra obtained for a sample of Ni nanorings acquired at 234 kHz. (b) Middle row: MSM-topography, MSM amplitude, MSM-phase channels and frequency spectra obtained with uncoated APTES nanorings at 275 kHz. (c) Bottom row: MSM-topography, MSM amplitude, MSM-phase channels and frequency spectra for APTES nanorings with Pd deposits obtained at 275 kHz. Images were acquired in air using the same AFM probe for each sample (2×2 μm^2).

AFM could detect surface changes for APTES nanopatterns after treatment with a Pd catalyst, shown in Figure 3.4c (bottom row). The topography image (Figure 3.4c, left) displays an area with 16 nanorings within the 2×2 μm^2 frame, however it is not the same identical area in each example since the experiments were conducted *ex situ*. Since palladium is diamagnetic,[141] areas with the catalyst were shown to vibrate in response to the external AC electromagnetic field in the center frames of Figure 3.4c. With a driving frequency of 234 kHz, little response was detected, so the next nearest peak at 275 kHz was selected for MSM imaging (Figure 3.4c, right). The high

sensitivity of MSM-AFM is apparent, when one considers that only trace amounts of Pd catalyst were bound to the surface. The areas of the surface containing Pd are quite well resolved in the MSM-phase channel of Figure 3.4c, disclosing the particulate shapes of Pd nanoparticles forming nanorings, as well as the attachment of Pd in areas between the APTES nanorings.

During AFM imaging, the frequency of the electromagnetic field can be systematically ramped to evaluate the optimized parameters for acquiring data. A modulation frequency of 234 kHz was chosen for studies with the Ni nanorings (Figures 3.3 and 3.4a) by selecting the peak maxima during a sweep from 0 to 400 kHz. The capability of acquiring frequency spectra provides further information about the dynamics of the actuated particles when changing the parameter of the driving frequency of the field modulation. An example dynamic experiment is shown in Figure 3.5 in which the frequency was ramped at selected intervals of image acquisition using a tip speed of 1.9 lines/s with 512 lines/frame. As the frequency was incrementally increased at selected intervals during imaging, the vibration of the samples was mapped in the concurrently acquired MSM amplitude and MSM phase channels. The amplitude axis of the spectrum in Figure 3.5d correlates directly with the z displacement of the AFM tip, which is on the order of 1-10 nm. The tallest resonance peak at 234 kHz was shown to exhibit sharp color contrast in both the MSM amplitude and MSM phase channels. At 77 kHz, a strong response was detected in the MSM amplitude frame, however the sensitivity of the phase frame was weak. The tallest peaks of the amplitude *vs* frequency spectrum provided the sharpest contrast for imaging. Further example MSM images of Ni nanorings are provided in Supporting Information Figures A.6 and A.7.

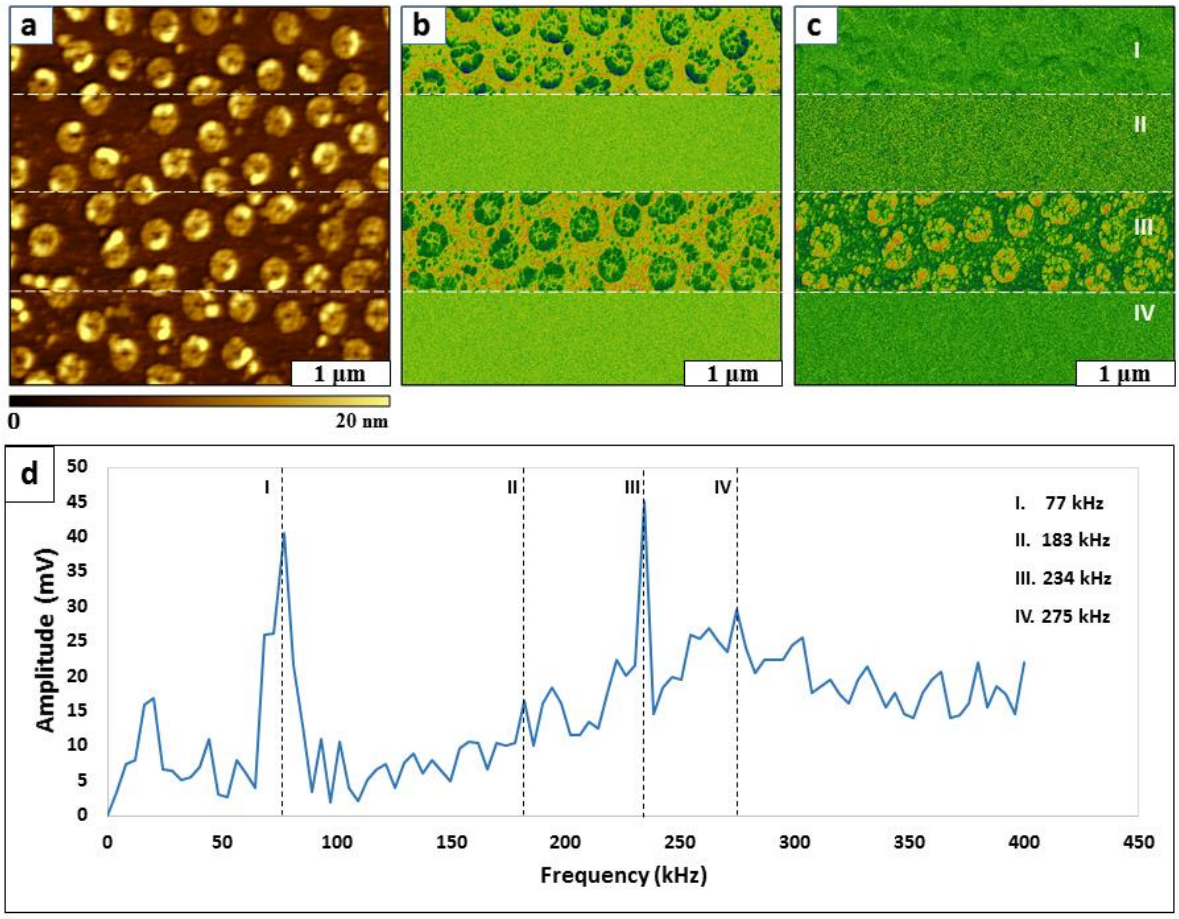

Figure 3.5. Changes of image contrast within a single frame were detected during MSM imaging of Ni nanopatterns using selected resonance frequencies to drive the sample oscillation. (a) MSM topography channel; (b) concurrently acquired MSM amplitude and (c) MSM phase image. (d) Frequency spectra obtained with a field strength of 0.2 T. Images were acquired in ambient air for an area of $4 \times 4\ \mu m^2$.

After choosing a resonance frequency, an analogous dynamic approach can be applied to evaluate the optimized field strength for capturing images by ramping the field strength during image acquisition (Figure 3.6). As the field strength was successively increased at designated increments from the bottom to the top of the frame, the vibrational amplitude of the vertical motion of the Ni nanorings changed accordingly. The topography frame shows no discernable changes in resolution for each section of the image as the field strength was increased (Figure 3.6a). The topographic resolution remains unchanged from section to section because the tip remains in

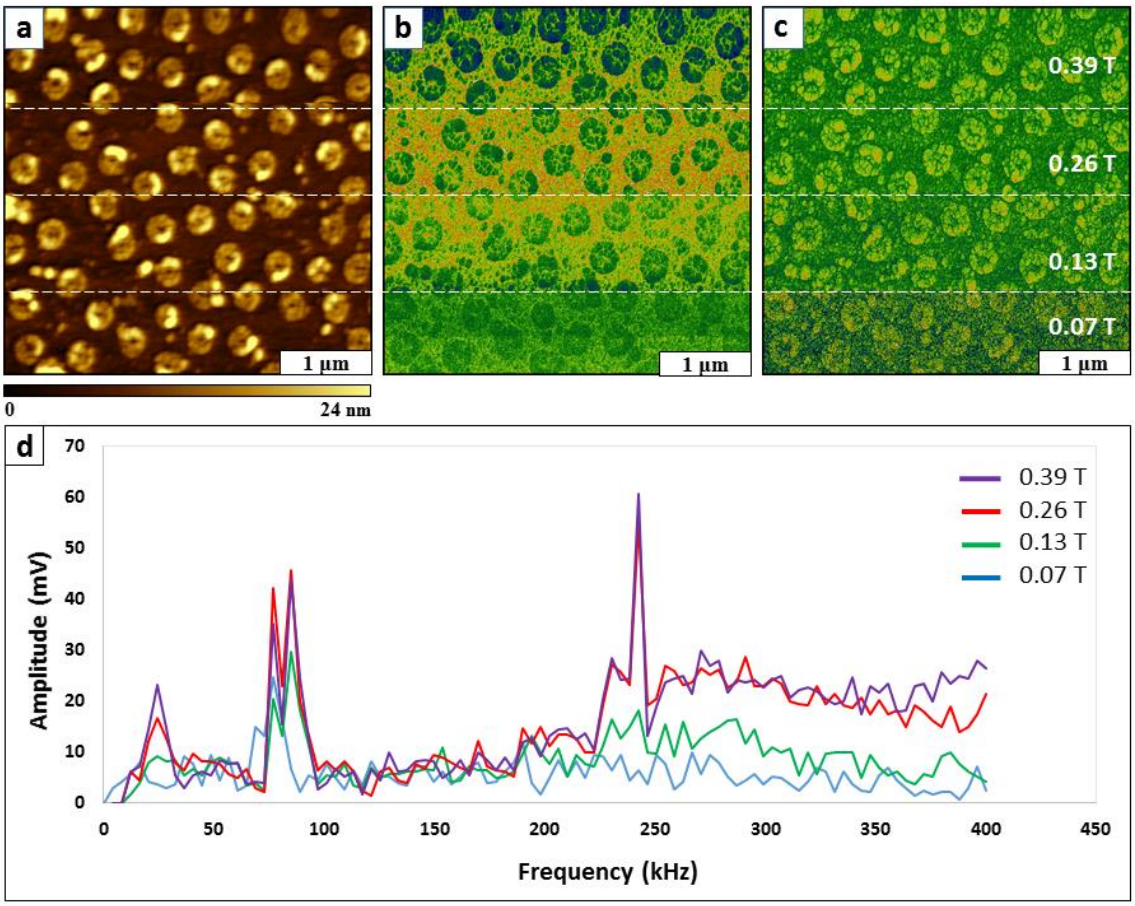

Figure 3.6. Dynamic changes within a single frame for an MSM experiment with Ni nanorings as the applied field is ramped, and the frequency was maintained at 236 kHz. (a) MSM topography channel; (b) simultaneously acquired MSM amplitude and (c) MSM phase frames; (d) frequency profiles acquired with selected drive strengths. Images are 4×4 µm^2 in size.

continuous contact with the vibrating sample for the selected range of driving field strength. In this example, there is no detectable side-to-side movement of the nanopatterns within the surface plane. We have actually observed samples move and vibrate in lateral directions with MSM topography frames for soft protein samples, reported in a previous study of ferritin.[184] With ferritin, the samples were small, protein-encapsulated iron nanoparticles which were able to move in lateral directions as well as vertically in response to the flux of the AC magnetic field. For the Ni nanorings, the surface structures are attached to a Si substrate by a molecular linker (APTES)

which would provide flexibility for vertical movement. The packing of APTES is relatively dense, thus there was no lateral broadening of features detected in the topography frames.

For MSM studies, the up and down motion of the Ni nanorings can be sensitively detected by the AFM tip using a lock-in amplifier, as shown in both the MSM amplitude (Figure 6b) and MSM phase frames (Figure 3.6c). If the sample was securely immobilized or embedded into the substrate, no motion would be detected in response to the modulated electromagnetic field. Since the Ni nanostructures are linked to the surface with organosilanes, APTES provides a molecular spring. The alternating electromagnetic field induces vibration in the vertical direction which can be sensitively mapped in MSM amplitude and MSM phase images. For the experiment of Figure 3.6, as you proceed from section to section from the bottom to top of each frame, the images become sharper with markedly greater contrast as the field was increased. The AFM tip was rastered in a line-by-line fashion from bottom to top across the sample and correspondingly the tip trajectory responded to the increase in vibrational motion of the magnetic nanorings as the field was incrementally ramped between 0.07 and 0.39 T.

By parking the tip on an individual Ni nanostructure and sweeping the frequency, the resonances can be plotted with different applied field strengths. An overlay of the frequency sweeps for selected field strengths is presented in Figure 6d. An amplitude response measuring 50 mV corresponds approximately to a 10 nm deflection of the AFM tip. A prominent peak for the amplitude response at a frequency of 234 kHz was detected at 0.26 T, which were the parameters selected for the driving field strength for MSM experiments shown in Figures 3.3-3.5.

3.3.3. Characterization of Ni Nanostructures with Scanning Electron Microscopy (SEM)

Direct 2D views of the metal nanorings were obtained with SEM for comparison to AFM studies, as a means to assess how images were distorted by tip-sample convolution. Since conductive samples are required for the SEM imaging process, the molecular nanorings of APTES were not characterized with SEM. A regular, hexagonal arrangement of Ni nanorings is revealed in the micrograph of Figure 3.7a, which follows the periodicity of the particle mask used for patterning APTES. The center-to-center distance matches precisely with the 500 nm diameter of the silica spheres of the surface mask. A close-up view of nine Ni nanorings is captured in Figure 3.7b, revealing that metal was deposited throughout areas of the sample, even inside the circumference of the rings. The surface topology is not smooth, rather a discontinuous grain structure was observed which was not detected in AFM topography images. using a standard commercial probe. The fine details of the grain structure of metal films can be resolved with ultra-sharp probes.59 As a further processing step, we annealed several samples of Ni nanorings at temperatures ranging from 50 to 300 oC, however the shapes of the nanorings was not retained after the heating step. After an annealing step, the samples showed random arrangements of irregularly shaped metal aggregates, and the shapes of the nanoring patterns was no longer evident. It is likely that the APTES linker did not persist at high temperature for securing the ELD film to the substrate.

Interesting details can be distinguished when comparing the SEM micrographs of Ni nanorings obtained in Figure 3.7 to the MSM images in Figure 3.3. For the topography frame of Figure 3a, the areas in between the taller Ni nanorings show a clustered morphology. A common imaging artifact of AFM images is that small cracks appear as bumps, reflecting the probe

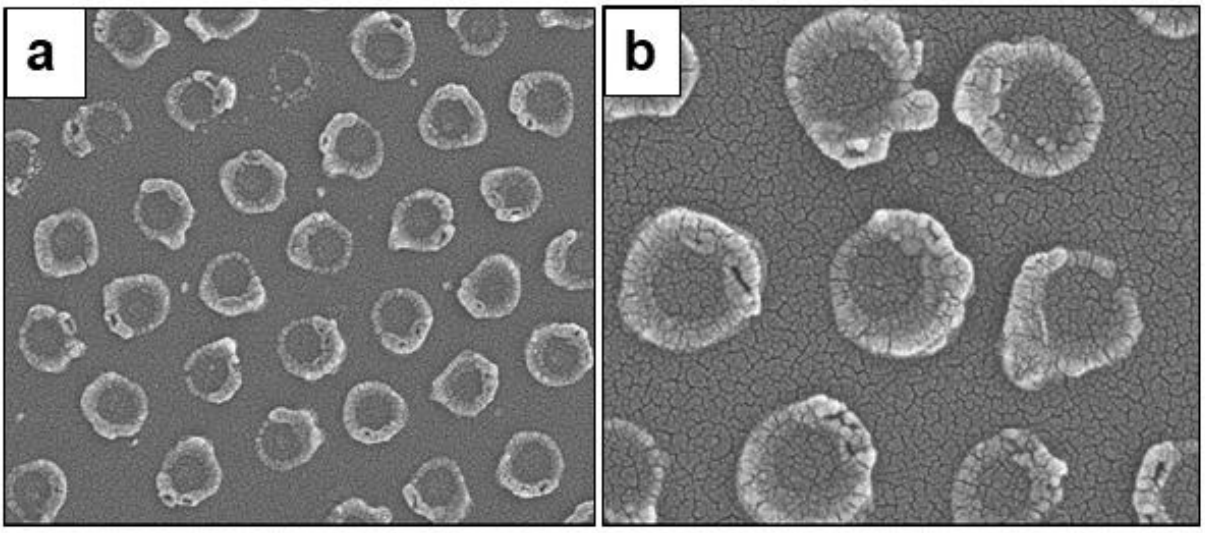

Figure 3.7. Micrographs of Ni nanorings obtained with SEM. (a) SEM view of Ni nanorings fabricated with electroless deposition (3×3 μm^2); (b) magnified image (1.5×1.5 μm^2).

geometry rather than showing the true shape of the surface feature, as shown for areas in between the nanorings for the topograph of Figure 3.3a. However, the fractal grain structure of the Ni coating is sensitively resolved with the corresponding MSM amplitude frame of Figure 3.3b. Sample modulation has previously been reported to improve resolution for detecting fine details of surface structures because stick-slip adhesion between the tip and sample is reduced.[185]

A challenge for nanotechnology will be to improve chemistry-based lithography methods to gain precise control of the shapes and sizes of surface features at ultra-small dimensions. A hallmark for well-resolved AFM studies at the nanoscale is that pristine, impeccable landscapes are not what is viewed. Nearly all surfaces have imperfections such as contaminants, adatoms, defects, and atomic or molecular vacancies. Detecting such defects using AFM is an indicator of high resolution. As an example with colloidal lithography processes, the polydispersity of sphere diameters will correspondingly propagate into imperfections in the periodicity and surface arrangement of nanopatterns. With the advent of new routes to synthesize nanostructures, the capabilities for nanomanufacturing have yet to be fully realized.

3.4. Conclusions

Periodic arrangements of Ni rings with regular and symmetric shapes were prepared with high throughput at the nanoscale using a surface mask of silica particles and electroless plating. The successive fabrication steps of colloidal lithography combined with electroless deposition were evaluated using MSM-AFM for preparing Ni/Pd coatings on APTES nanopatterns. Studies with MSM-AFM and SEM provided direct views of the selectivity of metal patterning protocols by revealing the sites of metal deposits. The domains of both magnetic (Ni) and diamagnetic (Pd) deposits could be sensitively characterized with *ex situ* MSM-AFM studies, revealing that the catalyst and metal had deposited on areas of the APTES rings as well as on areas in between the nanoring structures. The ring morphology of the APTES template persisted throughout the immersion steps of electroless plating, however SEM micrographs clearly revealed that the centers of the rings were also filled with metal deposits. The generic approach for patterning with ELD will likely be applicable to other surfaces, since organosilanes such as APTES can be patterned on a range of substrate materials (e.g. mica, glass, metal oxides).

CHAPTER 4. HETEROGENEOUS ASSEMBLY OF WATER FROM THE VAPOR PHASE – PHYSICAL EXPERIMENTS WITH BINDING TRIFUNCTIONAL ORGANOSILANES AT THE VAPOR/SOLID INTERFACE

4.1. Introduction

Water has a role in many physical and chemical processes at interfaces, however it can be a challenge to directly probe the molecular-scale behavior of water at interfaces for both experimental and theoretical methods. Water at interfaces has been a subject of extensive research since the thickness and structure of the layer of interfacial water has an impact on chemical reactivity. The role of water is understood to initiate reactions of organosilanes to form crosslinked films, however, our understanding of the overall complex molecular mechanism of the surface self-assembly of trifunctional organochlorosilanes is incomplete. The process of chemical vapor deposition (CVD) is widely used for silanization. Hydrosilation reactions of organosilanes are often used for designing the interfacial chemistry of surfaces and have broad applications for the microelectronics industry and for tailoring the surface chemistry of biochips as coupling agents.

It is generally considered that thin layers of water will cover most surfaces in ambient humidity which may measure a few nanometers up to even microns in thickness. There are important differences in the properties and reactivity of the first interfacial layer of water compared to further layers, however it is not clear at which thickness will the properties of the thin film become the same as for bulk water. The physical behavior of confined water has been reported to differ from that of bulk properties.1, 2, 3, 4, 5 The properties of elastic response,6 viscosity,7 dielectric constant,8 and water transport/mobility,9, 10 have been investigated under spatial confinement. When confined, water does not behave in the same manner as it does in the bulk liquid.11 Confinement influences the structure and ordering of water at the solid interface.12, 13 The arrangement of water molecules at a solid boundary are yet to be completely understood. The

roughness and chemical nature of the substrate are also known to affect the binding, structure and properties of the initial water layer at the vapor/solid interface.14, 15, 16, 17 How the hydrophobic or hydrophilic nature of the underlying substrate affects surface wetting has yet to be fully explained.

Water has a direct influence on the mechanism of forming organosilane monolayers and therefore on the resulting structure of the monolayer that can be obtained on a silica surface. Silicon is currently the most important material for the semiconductor industry. The surface of silica is generally silicon oxide (SiO2), and is targeted by many studies as a model system with a very strong hydrophilic nature with certain treatments.18 There is controversy regarding the structure of water on silica to form hydration layers and surface silanol (Si-OH) groups. In a humid atmosphere, water is readily adsorbed on areas of surface silanols to form a monolayer of water molecules, eventually forming a multilayer film on top of the already adsorbed water molecules. The structure of water films on Si was studied in situ at different humidity levels using Kelvin Probe microscopy and X-ray photoemission and electron spectroscopy by Verdaguer et al. showing that water forms a uniform film that is 4-5 layers in thickness for 0-75% relative humidity, reaching 6-7 layers at 90% humidity.19 Macroscopic drops of water formed at 100% humidity. Silicon can be either hydrophilic or hydrophobic depending on surface preparation. The native oxide surface that is terminated with Si−OH is reported to be hydrophilic with a water contact angle < 5° whereas the water contact angle is ~ 83° presenting SiH at the interface when the surface is treated with hydrofluoric acid.15

When freshly cleaved, mica furnishes a pristine surface which is hydrophilic. Although mica surfaces contain relatively few hydroxyl groups, exposure to water vapor has been used to effect surface hydrosilation.20 Muscovite mica is a mineral composed mainly of SiO2, Al2O3,

and K2O which has a complex layer structure held together by electrostatic forces. In comparison to oxidized silicon surfaces, mica has fewer silanol groups for binding organosilanes because one in four silicon atoms in the silicon layer of mica is replaced by an aluminum atom. It has been reported that freshly cleaved mica has about 11% silanol groups.21 The thickness of the adsorbed water layer on mica as a function of relative humidity is not a settled question. It has been reported that mica is completely wetted with a monolayer at 75% to 90% humidity.14, 22 Studies with infrared suggests that the wetting of mica is incomplete,23 and studies with ellipsometry have reported that mica is completely wetted.24 The initial stages of water adsorption have been viewed directly for mica surfaces for submonolayer films using non-contact modes of scanning probe microscopy such as frequency-modulation AFM25, 26, 27, 28 and scanning polarization force microscopy (SPFM).29 Hydration forces between an AFM tip and mica surface have also been probed with AFM,30 and modeled with simulations.28 The mobility of water as well as with the perturbation of an AFM probe prohibit directly imaging water with contact mode AFM configurations.31

The presence of water in the system is one of the most important parameters in silanization reactions. Hydrolysis and condensation steps of organosilane reactions are considered to occur sequentially to produce covalent Si-O-Si linkages to hydroxylated or metal-oxide surfaces. However, competing reactions take place concurrently to either form intramolecular linkages or to make free hydroxyl moieties. Such molecular self-associations can lead to branching polymerization which will generate multilayers and disordered packing. Anhydrous solvents can help to minimize the presence of water for solution phase reactions with organosilanes, however it can be difficult to control the amount of water for vapor phase processes with organosilanes. Chemical vapor deposition has been accomplished with mica surfaces to pattern

octadecyltrichlorosilane (OTS)32, 33 and 3-aminopropyltriethoxysilane (APTES).34, 35, 36, 37 Heated vapor deposition of OTS on Si(111) substrates has been combined with particle lithography to generate nanopatterns of nanopatterns with high throughput.38, 39, 40, 41, 42, 43, 44 The overall process of molecular self-assembly with organosilanes is driven by the location and thickness of water at the vapor/solid interface.40, 45, 46 Residues of water define the placement of organosilanes during successive steps of hydrolysis and condensation reactions.20, 47, 48

In this report, experiments were designed to investigate the role of surface wettability for the water-driven assembly of trifunctional octadecyltrichlorosilane (OTS) from the vapor phase. Studies with atomic force microscopy (AFM) were used to derive a more complete understanding of the interfacial chemistry involving condensation, hydrolysis, and reaction parameters at the vapor/solid interface. Structures which formed at the liquid/solid interface were assessed using planar substrates of Si(111) and mica(0001) as models of hydrophobic and hydrophilic interfaces. One of the three chloro substituents of OTS will bind to the substrate, however the two remaining sites are available either for crosslinking to adjacent surface-bound molecules or to enable self-polymerization reactions to form multilayered assemblies. The side reaction of self-polymerization will take place on surface sites with greater amounts of water. Protocols were developed to track the wetting process in stages of water adsorption from the vapor phase by introducing incremental quantities of water to sealed containers containing a substrate masked with colloidal spheres and heating the reaction vessel. After the surface wetted by condensed water vapor, OTS was then added to bind to the wetted regions of the surface. Silicon and mica interfaces were chosen to compare the water distribution on hydrophobic vs hydrophilic substrates. A curved geometry with spheres of latex on a flat surface was used as a structural template to direct the placement of water. Essentially, molecules of organosilanes will bind at surface sites occupied by water as a marker of

the location and thickness of water deposits. Characterization of the surface assemblies with atomic force microscopy (AFM) accomplished ex situ provided details of the complex interplay of water, surfaces and molecular self-assembly.

4.2. Experimental Section

4.2.1. Materials and Reagents

Octadecyltrichlorosilane (OTS) was obtained from Acros Organics, Thermo Fisher Scientific (New Jersey). Size-sorted latex spheres (diameter 499 ± 40 nm) were obtained from Thermo Scientific (Fremont, CA). Concentrated sulfuric acid (98.0%) was obtained from J. T. Baker, Fisher Scientific. Hydrogen peroxide (30%) was sourced from British Drug Houses (VWR). Ethanol, 200 proof was obtained from Deacon Labs (Prussia, PA). Milli-Q type 1 water,18 megohm, Millipore, Bedford, MA) was used for reactions and for rinsing steps. Precut polished silicon wafers Si(111) (Ted Pella, Inc. Redding, CA) and ruby muscovite mica (Sand J and Trading Co., NY) were used as substrates.

4.2.2. Preparation of a Surface Mask

Pieces of polished silicon wafers, (5×5 mm) were cleaned by immersion in freshly prepared piranha solution for 1.5 h. Piranha is an etching solution used to remove organic contaminants from surfaces that is prepared by sulfuric acid and hydrogen peroxide at a 3:1 ratio. Caution: piranha solution is highly corrosive and should be handled with great care. Next, the substrates were rinsed with copious amounts of ultrapure water and dried under nitrogen. A suspension of latex spheres was cleaned by centrifugation in ultrapure water to remove any residual surfactants or contaminants. A suspension containing 400 μL of latex spheres and 600 μL ultrapure water was placed in a plastic vial and then centrifuged at 20,000 rpm for 10 min. The supernatant was removed and the pellet was resuspended in 1 mL water. The steps were repeated for three cycles.

The pellet of the final centrifugation step was resuspended in 200 μL of ultrapure water. A drop of the latex suspension (20 μL) was deposited onto Si(111) and mica(0001) substrates to prepare the surface masks for protocols with particle lithography. The samples on Si(111) were dried for at least 4 h under ambient conditions. When aqueous suspensions of monodisperse latex spheres are dried on ultra-flat substrates, close-packed spheres within surface films spontaneously form a hexagonal symmetry spanning fairly wide, micron-sized domains. Mica substrates were cleaved immediately before depositing latex, to obtain a pristine and atomically flat surface. The suspensions placed on mica substrates were dried in ambient air for 24 h.

4.2.3. Protocols to Control the Deposition of Water

A general protocol for combining particle lithography with heated vapor deposition of organosilanes has been reported previously.49, 50 In preceding protocols, no water was introduced to the reaction vessel. For this report, the reaction was designed so that the surfaces of masked silicon wafers or mica were first dried in an oven with a desiccant to remove residual water. The surfaces were wetted by introducing certain amounts of water and then letting the system equilibrate before adding the organic vapor. The protocol was selected so that the subsequent introduction of an organic vapor of OTS would provide a way to track the placement of water deposits on hydrophobic or hydrophilic surfaces.

4.2.4. Particle Lithography Protocol with Si(111)

Substrates with a mask of latex spheres were further dried for 1 h at 70oC in an oven containing desiccant, to remove remaining water residues. Polystyrene latex is fairly soft, with a Young's modulus of 2-8 GPa, depending on sphere diameter.51 When dried, latex beads can pack together so tightly through capillary forces of drying that the sphere geometry can be compressed into a hexagonal shape. High temperatures and prolonged heating can deform latex particles, so a

temperature of 70oC was chosen for drying the samples. After the heated drying step, the samples were immediately placed into jars (110 mL volume) with selected volumes of water, and sealed. The reaction vessel was incubated at 70oC to equilibrate for 1 h. Next, a drop of neat OTS (300 mg) was added to the reaction vessel, and the heating step was continued for 18 h at 70oC. After vapor-phase reaction, the samples were cleaned by rinsing with ethanol under sonication to remove the film of latex spheres, then dried with a stream of nitrogen.

4.2.5. Protocol with Mica Substrates

The steps for preparing the samples with mica were the same as with Si(111) except that the exposure to a heated vapor of OTS was terminated after 6 h. After completing the vapor phase reaction, the samples were rinsed with ethanol and water to remove the surface mask. The cleaning of mica substrates was completed carefully and gently to avoid peeling away layers of mica without sonication. Mica substrates were rinsed with a stream of ethanol until the film of spheres was no longer visible on the substrate.

4.2.6. Atomic Force Microscopy (AFM)

Model 5420 (Agilent Technologies, Santa Clara, CA) and 5500 (Keysight, Santa Rosa, CA) scanning probe microscopes were used to characterize samples. Digital images were acquired with PicoView (version 1.20.2). Silicon AFM probes (Budget Sensors, PN Tap300Al-G) with an aluminum reflex coating were used for imaging samples in ambient air with tapping-mode (Figures 4.1, 4.2a, 4.2b, 4.3a, 4.5). The average resonance frequency and force constant of the probes were 300 kHz and of 40 N/m, respectively. Soft silicon probes (Budget Sensors, PN ContAl-G) with a force constant of 0.2 N/m were used for contact mode experiments (Figures 4.2c,d,e, 4.3b, 4.6). Images were processed and analyzed using Gwyddion (version 2.49) which is available online.[181]

4.3. Results and Discussion

Physical experiments were designed to evaluate reaction outcomes at the solid interface resulting from vapor condensation and silanization for two substrates. The model surfaces selected for study were Si(111) and mica(0001), which represent relatively hydrophobic and hydrophilic interfaces, respectively. The substrates were masked with a film of latex particles to generate a curved geometry against the planar surface, also forming narrow meniscus sites for trapping water in confined areas. At a fundamental level, the wettability of surfaces governs the attachment of organosilanes during hydrolysis and condensation reactions. The self-associative, cooperative properties of water influence surface placement during condensation of a vapor. With steps of heated vapor deposition of OTS, molecular assemblies attach to localized areas of water deposits. Areas with greater amounts of water will correspondingly produce multilayered organosilane structures through self-polymerization. With the controlled addition of incremental amounts of water to reaction vessels, the corresponding changes in the surface density of water was tracked by binding OTS from vapor phase. Samples were removed after a certain interval of vapor exposure and then evaluated *ex situ* using AFM studies, to provide an indirect map of the placement of water deposits. The successive evolution of molecular structures provides mechanistic details of surface self-assembly reactions.

4.3.1. Detecting and Mapping the Distribution of Water on Si(111)

The outcome of reactions of surface water with trifunctional OTS on Si(111) are shown in Figure 1. Silicon substrates furnish a model hydrophobic interface for interacting with vapor phase water and OTS. Incremental amounts of water (2 mg, 10 mg, 100 mg, 300 mg) were added to each reaction vessel containing a silicon substrate masked with latex spheres. After equilibration at 70^{o}C, a volume of neat OTS was added to the containers. A control sample was also prepared

without adding water (Figure 4.1a). The first image of the series reveals that trace residues of water persisted at areas near the latex spheres, despite the fact that the masked substrates had been dried in an oven containing desiccant. The meniscus sites at the base of the latex spheres define a 3D confined container for trapping water. Molecules of OTS from vapor phase will deposit exclusively in areas where water is present. In the control sample of Figure 1a, the thickness of the OTS clusters within the circular patterns measure ~ 2 nm, corresponding to the height of a single layer with nearly upright orientation. The thickness of a dense monolayer of OTS has been reported to measure values ranging from 2.26 to 2.76 nm, contingent on parameters of sample preparation. [186-188]

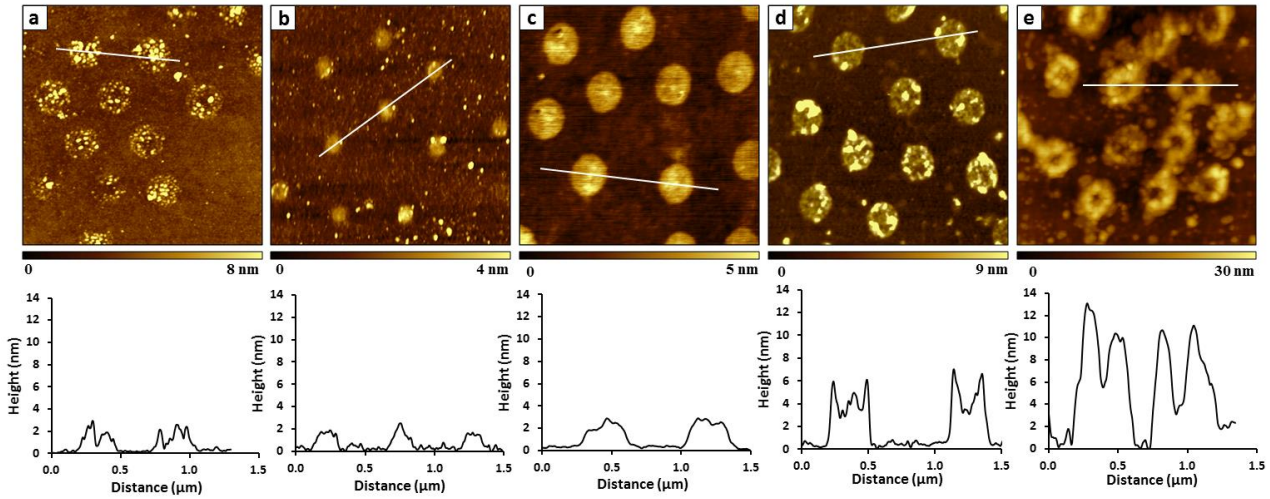

Figure 4.1. Molecules of OTS bind at sites of water deposits on wetted Si(111) surfaces masked with colloidal latex spheres. Topography views acquired with tapping mode of samples prepared (a) without adding water and with water volumes of (b) 2 mg; (c) 10 mg; (d) 100 mg; and (e) 300 mg added to the reaction vessels. The corresponding cursor profiles are shown under each topography image. Each image of the series measures 2 × 2 μm^2 in size, and were acquired with tapping-mode AFM in ambient air.

The fully extended length of an OTS molecule is 3.04 nm. For surfaces masked with latex particles, water tends to collect at the base of latex spheres, forming a circular meniscus. Water also binds in areas in between the spheres as evidenced by sparse, small bright spots in areas between the circle patterns where OTS has bound to ultra-small deposits of water droplets. As

small volumes of water were added incrementally to the reaction vessels, the images of the series correspondingly show greater density of OTS in the circular sites that had surrounded the sphere mask (Figures 4.1b-4.1e). The areas of OTS grow larger and thicker with addition of greater amounts of water. The line profiles underneath each image reveal progressively taller and thicker surface structures, which preferentially localized within the confined areas near the latex spheres.

In the series of images, the circular areas have filled with OTS and form progressively taller and wider structures, as demonstrated with example line profiles in the bottom panels of Figure 4.1. In the first three frames (Figures 4.1a, b, c) the thickness values correspond to a single layer of OTS, whereas with greater amounts of water (Figures 4.1d,e) the height profiles indicate multilayered structures were generated. The height of the circles in Figure 4.1d match the thickness of a bilayer of OTS, whereas the taller ring nanopatterns of Figure 1e measure heights of 5-6 layers of OTS. Filled circles were observed in Figures 4.1c,d,e, which indicates that water permeated surrounding and even underneath the spheres of the latex mask. At the highest water concentration (Figure 1e) multilayered nanostructures are observed, which formed a ring shape surrounding a depression in the center where the spheres were displaced. Initially, there are a few aggregates of OTS that formed in areas between the circles, the density of the OTS nanoislands increased between Figure 4.1a and 4.1b. Further along the series, in Figure 4.1c the surrounding areas do not evidence discrete nanoislands of OTS. In previous studies we have learned that with sufficient water density a continuous monolayer film of OTS forms throughout the substrate and multilayers are only generated in the spatially confined sites of the water meniscus. The height of the multilayer scales with the diameter of the latex spheres so that larger spheres form taller multilayer structures.[186]

4.3.2. Distribution of Water Condensed from Vapor on Mica Detected with AFM

When mica was used as a model substrate which is hydrophilic, the deposition of water and OTS from vapor phase produced markedly different surface structures in comparison to silicon. The outcomes of vapor phase hydrosilation reactions with selected amounts of added water are shown as a series of AFM images captured after reaction with OTS (Figure 4.2). When no water was added to the reaction vessel (Figure 4.2a), tiny ring-shaped nanopatterns of OTS formed

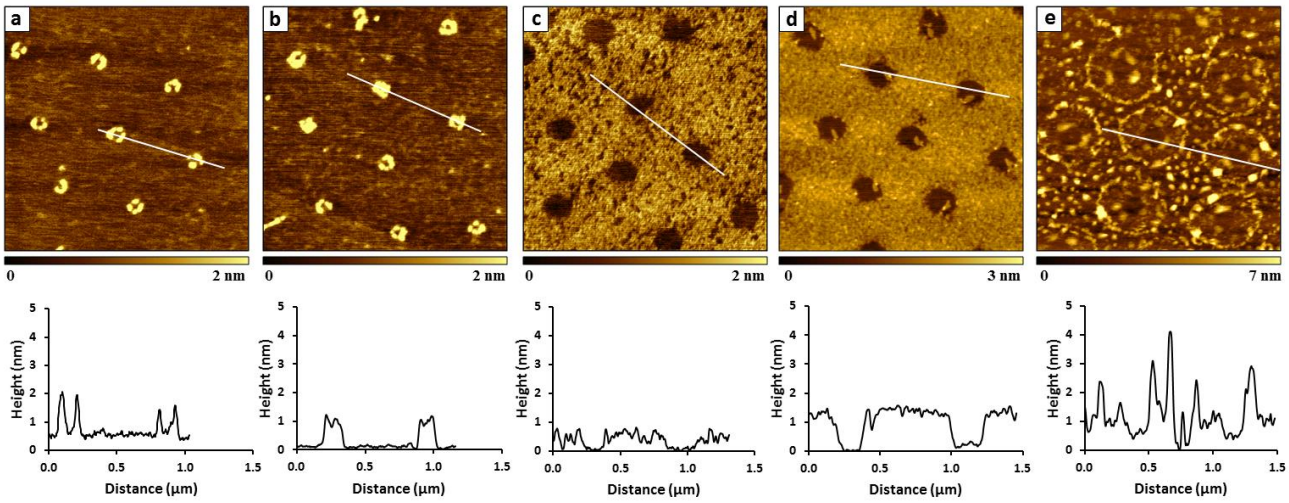

Figure 4.2. Water-directed assembly of OTS surfaces of mica viewed with contact mode AFM in air. Topography images acquired for samples prepared (a) without added water and with water volumes of (b) 2 mg; (c) 10 mg; (d) 100 mg; and (e) 300 mg. Cursor profiles for the lines on each topography frame are shown in the bottom row. Each image of the series measures 2 × 2 μm^2 in size.

which reveal the locations where water persisted in meniscus sites that surrounded the latex particles of the surface mask. However, most of the rings are not intact, forming incomplete circles for the sample prepared without adding water. For the control sample, even though the masked mica substrates were dried in an oven with desiccant, tiny water residues persisted in confined areas near the base of the spheres. The center of the rings indicate the areas of uncovered substrate that had been masked by latex spheres, and the donut shapes of the nanorings map out the areas that contained small residues of water.

As incremental amounts of water were further added to the reaction vessels (Figures 4.2b-e), the corresponding changes in water distribution were detected indirectly in AFM images, by mapping the locations of OTS that had bound to surface sites of water. As the amount of water vapor correspondingly increased along the series, the differences in OTS coverage attributable to the wettability of mica become apparent. With a small amount (2 mg) of water added, the nanorings become slightly wider (Figure 4.2b), however the height of an OTS monolayer is retained. The dimensions of surface features are indicated with an example height profile underneath each image. When further quantities of water were added to the reaction vessel (Figures 4.2c,d,e) the distribution of water is no longer localized at the meniscus regions, instead water spread across areas of the hydrophilic mica surface throughout areas in between spheres of the latex mask. A loosely packed, incomplete film is apparent in Figure 4. 2c, however as the water concentration increased, a dense, continuous monolayer is evident in Figure 4.2d. For thin films at low surface coverage, shorter heights were measured with incomplete filling of the area between the circles of uncovered mica. This suggests that the C18 hydrocarbon backbone of OTS is canted towards the plane, to generate shorter heights. As the surface density of OTS increased, the molecules adopt a nearly upright orientation (Figure 4.2d) measuring ~2 nm in thickness. Saturation coverage was reached with the sample of Figure 2e, which evidences a dense film of OTS without gaps of substrate showing between molecular clusters. Bright islands of OTS are apparent where clusters of multilayers have formed in a scattered arrangement across the sample, particularly at the edges of circles which surrounded the latex spheres.

A close-up view of the sample prepared with 300 mg of water is presented in Figure 4.3. There are clear differences in the surface distribution of OTS in the side-by-side comparison of two samples prepared with the same parameters of water and OTS vapor. With silicon, there are

still uncovered areas of substrate in areas between multilayered nanorings of OTS. Aggregates of OTS assemblies are scattered in between the rings, however a dense assembly of OTS primarily took place at the sites of a water meniscus near the base of the latex spheres. For silicon, the localization of water at the meniscus sites provided a container for self-polymerization of silanols to generate taller structures comprised of OTS multilayers.

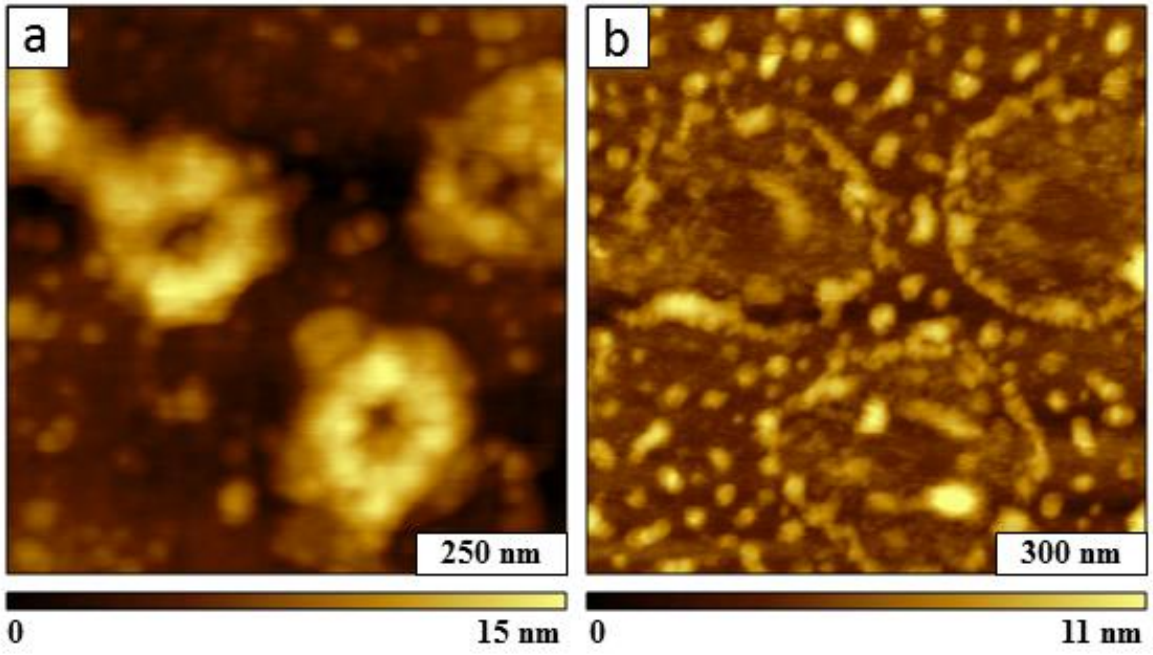

Figure 4.3. Distinct differences in the localization of OTS is apparent with 300 mg of water added to the reaction vessels, determined by the substrate wettability. (a) Multilayer rings were formed on hydrophobic silicon near the base of latex spheres of the surface mask. (b) A monolayer of OTS formed with saturation coverage on mica, with a second layer formed of random island aggregates of multilayered OTS.

In contrast, with mica substrates the water spread to fully cover areas of the substrates between and surrounding the latex beads, and self-polymerization took place after the first layer was formed. Since the colloidal lithography process is a 3D approach, one would expect that the beads of the upper multilayers of latex would also become wetted from vapor phase water, and at higher vapor concentration the moisture would form small droplets that would drip to fall on the surface. The circular outline shown for the OTS patterns likely caused by small droplets of water

that have fallen to the surface to form a circumference surrounding particles of the latex mask. The craters at the center of the circle patterns contain uncovered mica, which pinpoint the locations where the spherical beads of the colloidal mask were made contact with the planar substrate. The differences in wettability correspondingly propagate into differences in the distribution and thickness of OTS assemblies, which form by hydrolysis and condensation reactions with surface-bound water at the vapor/solid interface.

4.3.3. Dimensions of OTS Surface Structures as the Concentration of Water Vapor Increased.

Colloidal lithography provides advantages of generating multiple, replicate surface structures which enable quantitative comparisons of the changes in dimension of nanostructures and films. The localization of OTS on wetted surfaces provides a fingerprint of the arrangement of water deposits. The dark spots of bare substrate in the center areas of the circular patterns on silicon and mica furnish a baseline for measuring the thickness of OTS assemblies and films. Average values for 100 cursor measurements of multiple, individual surface features are plotted in Figure 4.4 for silicon and mica, using the standard deviation as the error term. With the hydrophobic interface of silicon, as greater amounts of water were added, the heights increased to produce multilayered assemblies of OTS, with thickness values corresponding to as many as 8 molecular layers (Figure 4.4a). Within confined areas of the water meniscus of the latex beads, self-polymerization reactions with free silanols of trifunctional OTS was shown to produce multilayered surface structures. On the other hand, for mica the changes in thickness reflect how water spread out to fully cover the hydrophilic interface, as shown in Figure 4.4b. Multilayers were not detected until saturation coverage was reached, for the final sample of the series. Further quantitative analysis of AFM data is summarized using histograms of the height measurements, provided as supporting information in Figures D.1 and D.2.

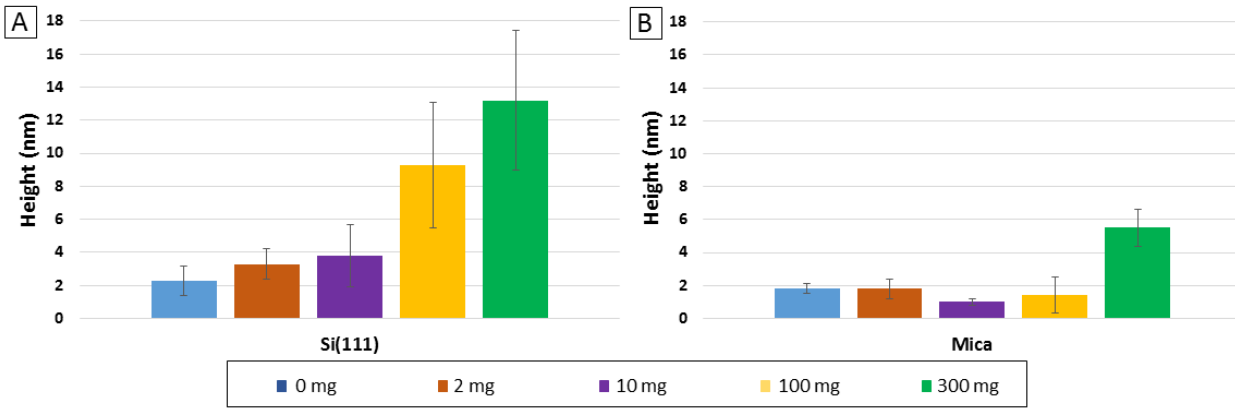

Figure 4.4. Comparison of the thickness of OTS surface structures formed on surfaces wetted by water vapor at selected concentrations, for (a) Si(111) and (b) mica(0001). Measurements were acquired with 100 cursor line profiles of replicate surface features.

For hydrophilic surfaces such as mica, it is generally understood that an ultrathin film of water spreads out to cover the surface in ambient conditions. In contrast, a hydrophobic surface such as silicon would have discontinuous water coverage, forming small droplets in places where water self-associates and is repelled by the surface. For the most part, the physical experiments with AFM which disclose the self-assembly of OTS on surface sites containing water provide indirect evidence to corroborate the expected effect of surface wettability for silicon and mica. Interestingly, the first two images of the series do not follow the expected wettability trends, which can be rationalized by the effects of spatial confinement as well as the proximity of the polystyrene interface near the base of latex particles.

4.3.5. Specificity of OTS for Binding at Sites of Water Tracked with AFM Phase Images.

With tapping-mode AFM, the phase frames which are concurrently acquired with topography images provide additional information of surface chemistry at the solid interface. In particular, for silicon samples, phase images help to address the question of whether OTS deposited in areas between the circular areas of OTS nanopatterns. Successive zoom-in views were captured for silicon samples prepared with 100 mg of water added to the reaction vessel, presented

in Figure 4.5. The heights of OTS nanopatterns are revealed in the sequence of topography frames in the top row (Figures 4.5a,b,c).

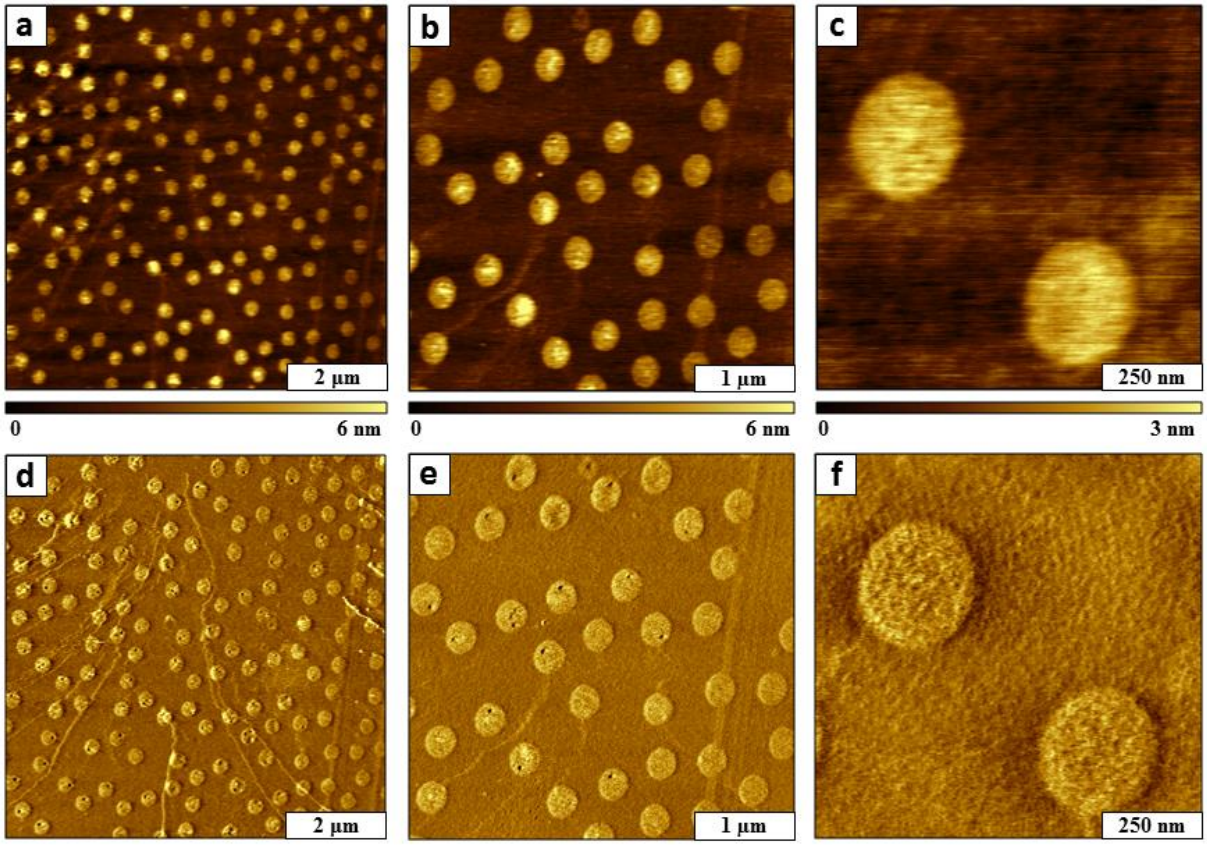

Figure 4.5. The distribution of OTS assemblies on Si(111) indirectly maps the localization of water condensed from vapor at the solid interface, after addition of 100 mg of water to the reaction vessel. (a) Topography view (8× 8 μm^2); (b) Zoom in topography view (4 × 4 μm^2); (c) magnified view of two circular OTS nanostructures (1 × 1 μm^2); (d) simultaneously acquired phase image for *a*; (e) corresponding phase image of *b*; (f) phase image of topograph *c*.

The areas in between which surround the circles of OTS are uniformly bright in color contrast, without evidence of OTS assembly, which indicates indirectly that sufficient water was not present in regions between meniscus sites to enable hydrosilation of OTS. The areas of OTS are also sensitively mapped in the concurrently acquired phase images in the bottom panels (Figures 4.5d,e,f). Compared to the topography frames, the color contrast is reversed in the phase images, the brighter colored areas indicate the regions of bare Si substrate without OTS. For the

hydrophobic interface of Si(111), OTS binding was localized to the confined regions formed by the water meniscus surrounding the latex spheres of the surface mask. Such results suggest that either the geometric confinement as well as the proximity of the upper curved surface of polystyrene form a hot spot for attracting water, which guides the subsequent surface placement for OTS self-assembly. With a hydrophobic substrate, taller water deposits surrounding the base of latex spheres served to promote vertical growth of trifunctional OTS to form multilayered assemblies through self-polymerization of silanol groups. In this example the growth of OTS permeated underneath the latex spheres, so that there is no central hole of uncovered silicon, following the path of water deposits on the surface.

With the same parameter of 100 mg of water added to the reaction vessel applied for the hydrophilic interface of mica, AFM images reveal the opposite trend for surface wetting in Figure 6. A continuous film of OTS was formed throughout areas of the mica surface except at the circular regions of the meniscus, revealed in topography frames of Figures 4.6a,b,c. Multilayers are not evident at the meniscus sites, and the film exhibits uniform thickness throughout the sample. Small holes are evident in areas protected by latex spheres for mica samples which measure 225 ± 25 nm in diameter. Instead of islands or ring nanopatterns at the meniscus sites that were observed with Si, a hexagonal arrangement of unfilled circles is apparent where the spheres of the latex mask were removed (Figures 4.6d,e,f). A close-up view reveals that there are a few gaps in the film which did not fill with OTS, and there is an island of OTS in many of the holes (Figure 4.6c,f). The shape of latex particles are not necessarily perfectly symmetric, a dimpled depression on the sphere surface can provide a small vacant area for water to deposit which subsequently provides sites for OTS assembly.

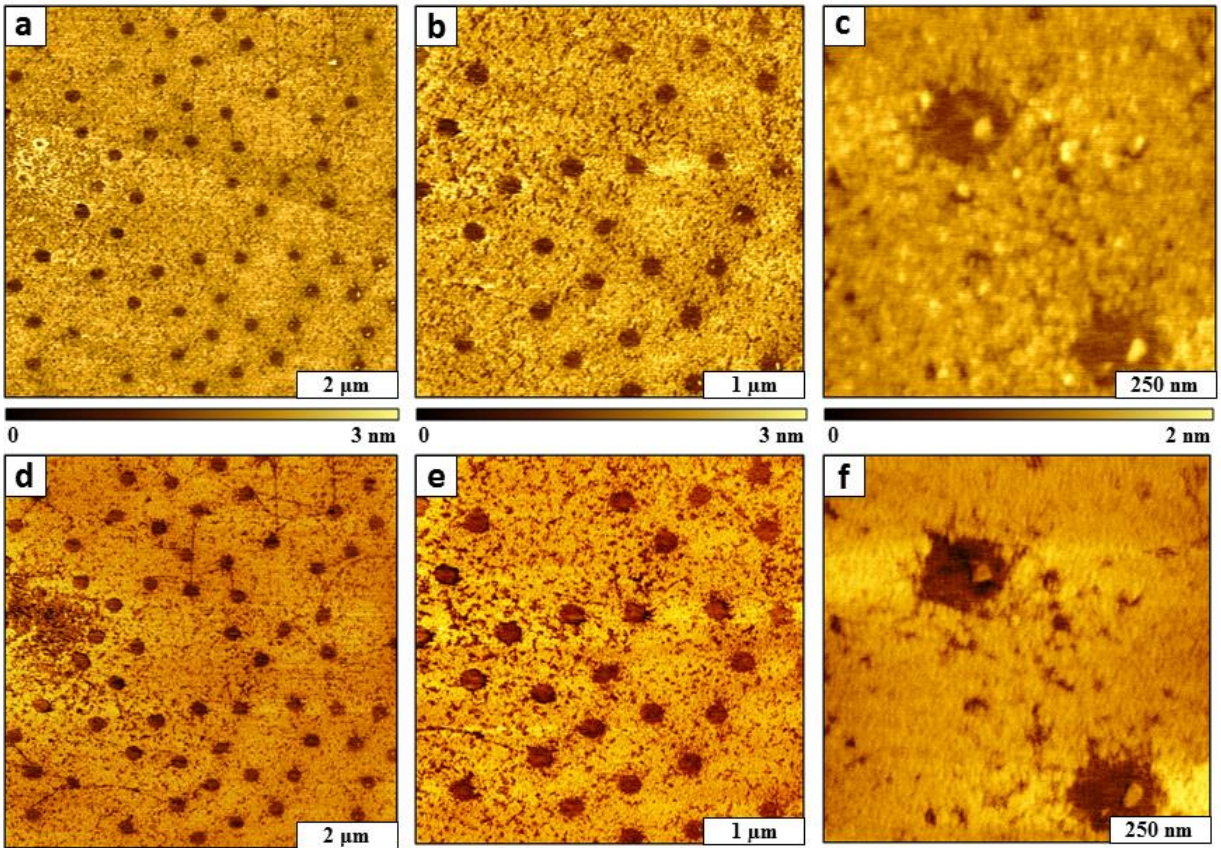

Figure 4.6. A monolayer of OTS formed on a mica which was wetted by adding 100 mg water to the reaction vessel, followed by heating. After reaction with OTS vapor, and removal of the latex mask, dark holes are evident where the spheres were displaced. (a) Topography view (8 × 8 μm^2); (b) zoom-in view (4 × 4 μm^2); (c) magnified view (1 × 1 μm^2); (d) phase image acquired for *a*; (e) phase image for *b*; (f) corresponding phase image of *c*.

When quantitatively comparing the areas of the surface covered with OTS with water added to the reaction vessels, each experiment showed greater surface coverage on mica compared to silicon (Figure 4.7). However, when no water was added the opposite trend was evident: there was greater OTS coverage on hydrophobic silicon for the control samples. For the control samples, the OTS deposition was localized to meniscus sites indicating areas with residual water that persisted after drying the substrates in an oven with desiccant. The estimates of surface coverage were made with 10 separate topographs for different locations of the sample, using 2 × 2 μm^2 frames.

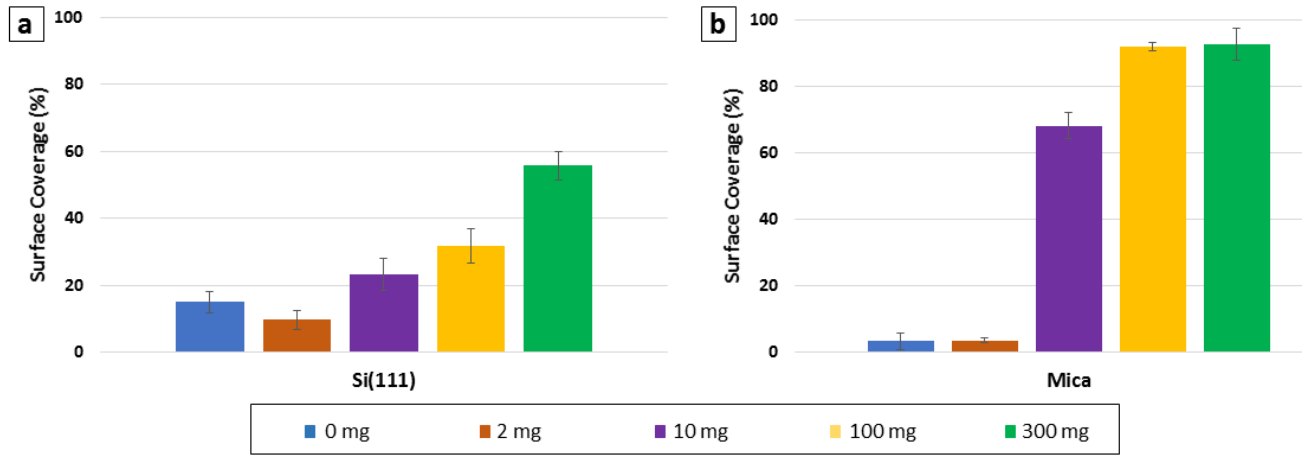

Figure 4.7. Measurements of the overall surface coverage of OTS formed on wetted surfaces of (a) Si(111) and (b) mica(0001).

4.3.6. Comparison of OTS Assembly on Hydrophobic and Hydrophilic Interfaces

The spreading of water on hydrophilic mica was corroborated by AFM views of the distribution of OTS assembled as a thin film covering areas throughout the sample that were not masked (Figures 4.2c,d,e). The hydrophobic interface of silicon produced taller deposits of water droplets in the areas close to the latex spheres to form multilayered nanorings (Figure 4.1c,d,e). However the distribution of OTS in the confined areas of the meniscus with trace amounts of water reveal anomalies. Comparing the control sample on mica (Figure 4.2a) to the control sample prepared on silicon (Figure 4.1a) there are distinct differences observed for OTS distribution when no water was added to the reaction vessel. Within the meniscus regions the water spread into a flat circle on Si(111), however on mica we observed that OTS formed dense rings surrounding the base of latex spheres. This is counterintuitive, since we would predict that water would spread out on mica rather than form a tight ring following the latex meniscus. The discrepancy can be attributed to the proximity of the solid curved surface of polystyrene. The outermost layer of polystyrene beads has been described as a sponge, for soaking up and retaining water. It is a “hairy”

particle, with spaghetti-like strands of PS polymer protruding at the interface when suspended in aqueous environments.[189 190] In solution, latex has been described as a having a hydrophobic core surrounded by a hydrophilic layer.[191] When considering the 3D shape of the water meniscus, the hydrophilicity of the outer surfaces of the latex beads influences the distribution of water within the confined areas of the meniscus sites. For the condition of very low humidity with the control sample, the interplay of the wettability factor for both the flat substrates and the curved surface of latex determines the experimental outcome. As more water was added, the predominant factor was the wettability of the substrate.

4.4. Conclusions

Experiments with binding trifunctional OTS were developed to visualize wetting phenomena at vapor/solid interfaces. The thickness and localization of OTS to form films and multilayered assemblies provided a map of the sites where water deposited from vapor phase on the surfaces of Si(111) and mica(0001), as examples of hydrophobic and hydrophilic interfaces respectively. Colloidal lithography was applied to prepare surface masks of latex spheres, which protected discrete circular areas of the substrate. The localization of water deposits formed from vapor phase processes is not homogeneous on silicon surfaces, instead molecules collect together around the meniscus of latex spheres to form droplets cooperatively rather than forming a continuous film. With low humidity, water was found to be localized near the bottom of the particles of the mask, forming a circular meniscus surrounding the base of the spheres. The effects of spatial confinement within the meniscus sites, as well as the hydrophilic nature of the polystyrene interface of the spheres influenced the distribution of OTS near the latex spheres. Further directions will be to pursue a molecular-level understanding of chemical and physical processes at liquid/solid interfaces that are attributable to water and surface wetting phenomena.

CHAPTER 5. ATOMIC FORCE MICROSCOPY INVESTIGATIONS WITH NANOPATTERNED ORGANIC THIN FILMS*

5.1. Introduction – Fundamental Studies of Organic thin films

Pioneering studies of organic films were first reported by Irving Langmuir with the introduction of Langmuir-Blodgett (L-B) films.[192] The collaborative work of Langmuir and Katharine Blodgett focused on depositing calcium stearate films on glass surfaces to form films thicker than a monolayer by immersing solid substrates into polar liquids.[193] Preparation of L-B films with a thickness of one quarter of the wavelength of light would produce antireflection coatings that can be used for eye glasses, lenses and other optical devices including microscopes and cameras to reduce reflection.[194] Organic thin films have been applied such as biosensors,[195-197] organic thin film transistors,[198-201] corrosion-resistant surfaces,[202-204] biomedical,[205-206] and electronic devices.[207-209]

Due to the ease of preparation, self-assembled monolayers (SAMs) of alkanethiols on Au(111) have been well studied.[56, 122, 210-211] Alkanethiol SAMs are prepared by submerging the substrate in dilute solutions of alkanethiols to form highly reproducible, dense monolayers. Applications of organosulfur-based SAMs are limited because chemisorbed S-Au bonds can be readily oxidized.[212] Studies have shown that *n*-alkanethiol SAMs break down at high temperatures,[213] or exposure to ultraviolet light,[214-216] ozone[106, 217-219] and oxidation.[220-221] Therefore, new directions with SAMs have focused on synthesis and preparation of more stable organic thin films which are not based on S-Au chemisorption. Electrografting and photografting of organic molecules from precursors such as amines, diazonium salts and Grignard reagents are alternative approaches used to form stronger bonds between organic layers and metals.[222-224] These

*The data in Chapter 5 are a part of a collaborative project with Dr. Ragains research group, Department of Chemistry, Louisiana State University.

methods produce films derived from carbon-centered radicals which are tightly bound by covalent C-Au bonds. Experimental and theoretical studies show that the C-Au bond provides improved stability for grafted organic thin films compared to analogous films formed with S-Au chemisorbed linkages.[225-226] The grafted films are thermally stable, do not degrade with chemicals or oxidation over time and are not removed or degraded by sonication and boiling solvents.[222]

5.2. Visible Light Induced Photografting of Aryl Thin Films on Au(111)

This chapter describes experiments using high-resolution AFM and nanolithography protocols for studies of the structure and properties of photografted aryl thin films. Aryl thin films were formed from aryl iodide precursors that are readily reduced to aryl radicals through visible light photocatalysis.[227-229]

Grafting organic radicals onto surfaces with UV irradiation or electrografting approaches requires more advanced and expensive technology. Also, approaches with UV photografting and electrografting often are plagued with forming multilayers.[230-232] Either Hg or Xe lamps that operate at high temperatures are required for UV photografting.[233] Radiation from UV lamps can damage the retina posing a health hazard. To overcome such challenges, a versatile method of visible-light promoted catalytic steps was developed to synthesize radical-derived thin films.[234] In this approach, carbon-centered radicals were grafted on Au(111) by visible light irradiation of a solution containing photocatalyst, radical precursors and reducing agents. The radicals were generated from diazonium salts. The LED sources of visible light that were used in this method are nonhazardous, operate at low temperatures and do not require complicated power sources, just one standard electrical outlet is sufficient. The visible light photocatalysis method was combined with particle lithography to prepare periodic arrangements of nanoholes within photografted polynitrophenylene films [93] and phthalimide esters on Au(111).[235]

In the mechanism proposed by Lee and co-workers, an aryl radical was formed through a series of reactions during photoreduction. An aryl radical abstracts a hydrogen atom in the termination step of the mechanism.[229] In the photografting experiments, the aryl radical grafts on Au(111) forming a gold-carbon bond instead of undergoing hydrogen abstraction (Scheme 5.1). The photografting reaction is governed by an iridium-based photocatalyst, trisphenyliridium [$Ir(ppy)_2(dtbbpy)^+$]. When the photocatalyst is irradiated with blue LEDs, a photon is adsorbed and is promoted to an oxidizing excited state. The excited state accepts an electron from the *N, N*-diisipropylethylamine (DIPEA) by single-electron transfer (SET) to form Ir(II) species. The resulting Ir(II) species acts as a strong reducing agent which transfers an electron to aryl halide to generate an aryl radical and iodide. The aryl radicals attach to a gold surface directly to form a covalent bond.[234]

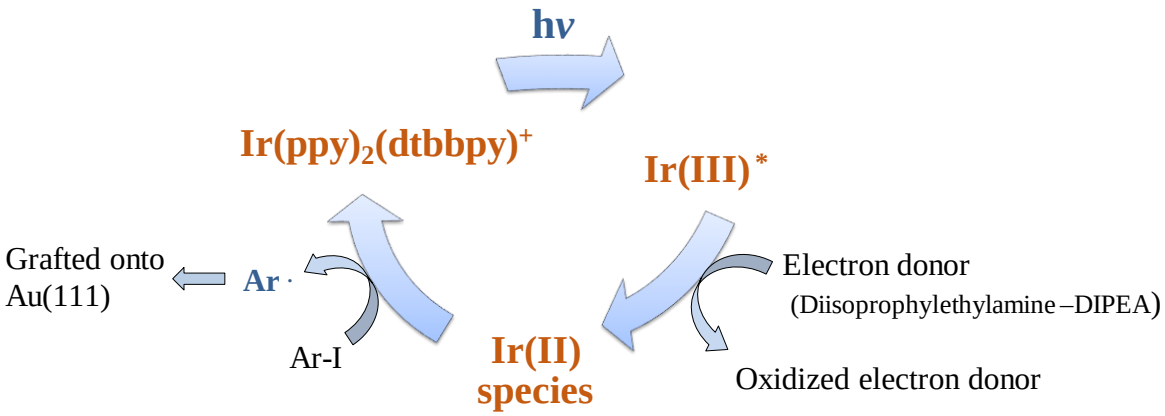

Scheme 5.1. General reaction mechanism for visible-light induced photografting of aryl radicals onto Au(111).

Modes of atomic force microscopy (AFM) were used for fundamental studies of the structure, properties and stability of photografted aryl thin films prepared on Au(111) in collaborative efforts with Dr. Ragain's group. Protocols of AFM-based nanoshaving and colloidal lithography were used to prepare surface structures to obtain information about the local thickness and the robustness of photografted films.

Thin films of aryl iodides were prepared on Au(111) by visible light photocatalytic reaction combined with immersion particle lithography (Figure 5.1). For the particle lithography approach for nanopatterning, gold substrates were coated with a surface mask of silica spheres and then immersed in a dilute solution of aryl halide, a photocatalyst and a reducing agent. Visible light

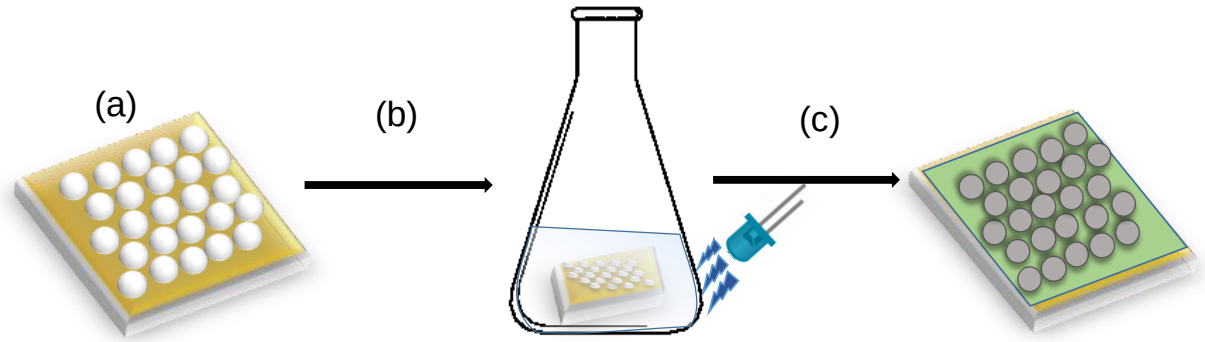

Figure 5.1. Steps for preparing aryl thin films using visible-light photografting combined with particle lithography. (a) A film of 500 nm silica spheres was prepared as a surface mask on Au(111), and annealed for 48 h at 150°C. (b) The masked substrate was immersed in a dilute mixture of aryl halide, photocatalyst and a reducing agent, and then irradiated with blue LED light. (c) The particle mask was removed by sonication in ethanol to generate nanopatterns within the photografted aryl film.

irradiation of the reaction mixture produced aryl radicals that graft onto uncovered areas of the gold substrate. When the surface mask is rinsed away, a periodic arrangement of nanoholes is formed within films of photografted aryl thin films. Measurements of film thickness and characterization of the morphology of photografted films were acquired with contact mode AFM in liquid media. The robustness of the photografted aryl films was evaluated with nanoshaving experiments conducted in a liquid cell filled with ethanol. The amount of force required to shave away small areas of the films provides an indication of the adhesion strength of molecular assemblies.

5.3. Experimental Methods

5.3.1. Materials and Reagents

Aryl iodide, Ir photocatalyst, [4,4′-Bis(1,1-dimethylethyl)-2,2′-bipyridine-N1,N1′]bis[2-(2-pyridinyl-N)phenyl-C]iridium(III)hexafluorophosphate, $Ir(dtbbpy)(ppy)_2][PF_6]$ and acetonitrile were purchased from Sigma-Aldrich (St. Louis, MO). *N*,*N*-Diisopropylethylamine (DIPEA) was purchased from Alfa Aesar (Tewksbury, MA). The irradiation source for photografting reactions was two 4W sapphire blue LED flex strips from Creative Lighting Solutions (Cleveland, OH, USA). Epoxy A and B (EPO-TEK, Billerica, MA) were mixed in 1:1 ratio to form the epoxy glue. Micro cover glass (VWR, Radnor, PA) and Ruby muscovite mica (S & J and Trading Co., NY) were used to prepare atomically flat gold substrates. Size sorted silica spheres (500 nm) were obtained from Thermo Scientific (Fremont, CA). Ethanol, 200 proof was obtained from Deacon Labs (Prussia, PA) and Milli-Q type 1 water, (18 megohms, Millipore, Bedford, MA) was used for rinsing and sonication steps. Gold pellets (99.99% purity) were purchased from Ted Pella (Redding, CA).

5.3.2. Protocol for Preparing a Surface Mask of Silica Particles on Gold Substrates

A thin layer (150 nm) of gold was deposited onto mica at 10^{-7} torr using a high-vacuum thermal evaporator (Angstrom Engineering Inc., Kitchener, OR) following a previously developed protocol.[236] Freshly cleaved Ruby muscovite mica was preheated to 350°C prior to gold deposition using quartz lamps at the back of the sample holder. The gold pellets were thermally evaporated at 10^{-7} Torr. The evaporated gold was deposited onto mica at a deposition rate of 3 Å/s. After deposition, the gold films were annealed at 365°C in vacuum for 30 min and then cooled to room temperature before taking out of the vacuum chamber. Template-stripped gold (TSG) substrates were prepared by a previously reported procedure.[237-238] Circular shaped cover glass and the mica

pieces with the gold film were placed into a UV-ozone generator for 30 min to clean the surfaces. Then glass slides were carefully glued onto the gold film using a small amount of epoxy (EPO-TEK, Billerica, MA). Epoxy glue was annealed by heating the sandwich of glass-gold-mica at 150 °C for 2 h. The glass discs were then mechanically stripped from mica to expose clean, atomically flat Au(111).

Silica spheres (400 µL) were suspended in 600 µL of deionized water and centrifuged for 10 min at 20,000 rpm. The resulting supernatant was decanted and the pellet was resuspended in 1 mL of deionized water. The mixture was re-centrifuged for three cleaning cycles to clean away any residual contaminants or surfactants that may present in the original solution. The pellet of the last centrifugation step was resuspended in 400 µL of deionized water. A drop of the silica sphere suspension (10 µL) was placed onto the template-stripped gold substrates and dried in air for 2 h. The sphere mask was then annealed by oven-drying for at 150°C for 96 h.

5.3.3. Photografting Procedure

A protocol with visible light photocatalysis introduced by Kim et al.[229] and Quarels et al.[235] was used to generate aryl radicals from selected aryl iodide precursors to form aryl thin films on Au(111). Stoichiometric amounts of selected aryl halides, trisphenyliridium photocatalyst [$Ir(ppy)_2(dtbbpy)^+$], diisopropylethylamine (DIPEA) as a reducing agent, and acetonitrile (MeCN) as the solvent were added to a 50 mL Erlenmeyer flask containing a stir bar. The gold substrate with sphere mask was added to the reaction mixture, then the flask was sealed with a rubber septum. A dry N_2 line was introduced through the rubber septum. The reaction mixture was carefully stirred after adding MeCN. The gold substrate should be held away from the stir bar to prevent possible damage due to mechanical contact when stirring. Visible light irradiation of the reaction mixture using a blue light emitting diode (LED) was conducted at room temperature or

45 °C for desired time. When the irradiation was completed, the Au(111) substrate was taken out and rinsed twice with deionized water and ethanol. The substrate was then sonicated for 2 min in ethanol and then for 2 minutes in deionized water to remove the sphere mask.

5.3.4. Surface Characterization using Atomic Force Microscopy (AFM)

Model 5500 and 5420 scanning probe microscopes (Keysight Technologies, Santa Rosa, CA) were used for AFM studies. Images were acquired with Pico View v 1.12 software in model 5420 and v1.18 in model 500. Tapping-mode AFM images were acquired using silicon AFM probes (Budget Sensors, PN Tap300Al-G) with an aluminum reflex coating. Tips with average spring constant of 40 N/m were used to acquire topography and corresponding phase images. Nanoshaving experiments were conducted using a liquid cell containing ethanol. Contact mode Si_3N_4 tips with an average spring constant of 0.6 N/m (Bruker Instruments, Camarillo, CA, USA) were used for nanoshaving and contact mode AFM imaging. Digital AFM images were processed using Gwyddion (v 2.30) software which is freely available.[181]

5.4. Results and Discussion

5.4.1. Photografting of Aryl Iodides by Visible Light Combined with Particle Lithography

In the first experiment, a surface mask of 500 nm silica spheres on Au(111) was immersed in a solution containing 4- iodoanisole, trisphenyliridium photocatalyst and DIPEA in MeCN. After the reaction was complete, the sphere mask was removed by sonication in ethanol for 4 min and the sample was imaged using contact mode AFM in liquid media (Figure 5.2). The arrangement of nanoholes shown in Figure 5.2a was generated according to the packing arrangement of silica spheres of the surface mask. The periodicity of the nanoholes measured 510 ± 97 nm (n = 20), which matches the diameter of the 500 nm silica spheres used as a surface mask. A close-up view of a single nanohole is shown in Figure 5.2b, showing irregularly shaped edges for the circular area. The vertical and horizontal diameters of the nanohole measured 196 nm and

143 nm. The surrounding region represents the film formed by covalently bound anisole radicals. The average thickness of the photografted film measured 2.0 ± 1.0 nm (n=50) and an example cursor profile is shown in Figure 5.2c.

The photografted radical contains a benzene ring with a methoxy group attached. The estimated theoretical length of the radical is 0.56 nm. The thickness of the monolayer of the thin film should be 0.77 nm when considering an Au-C bond length of 2.08 Å.[225] From the thickness measurements it appears that under the conditions used in this experiment, multilayers of anisole films that are ~3-4 times thicker than the monolayer have formed. Two distinct areas are apparent

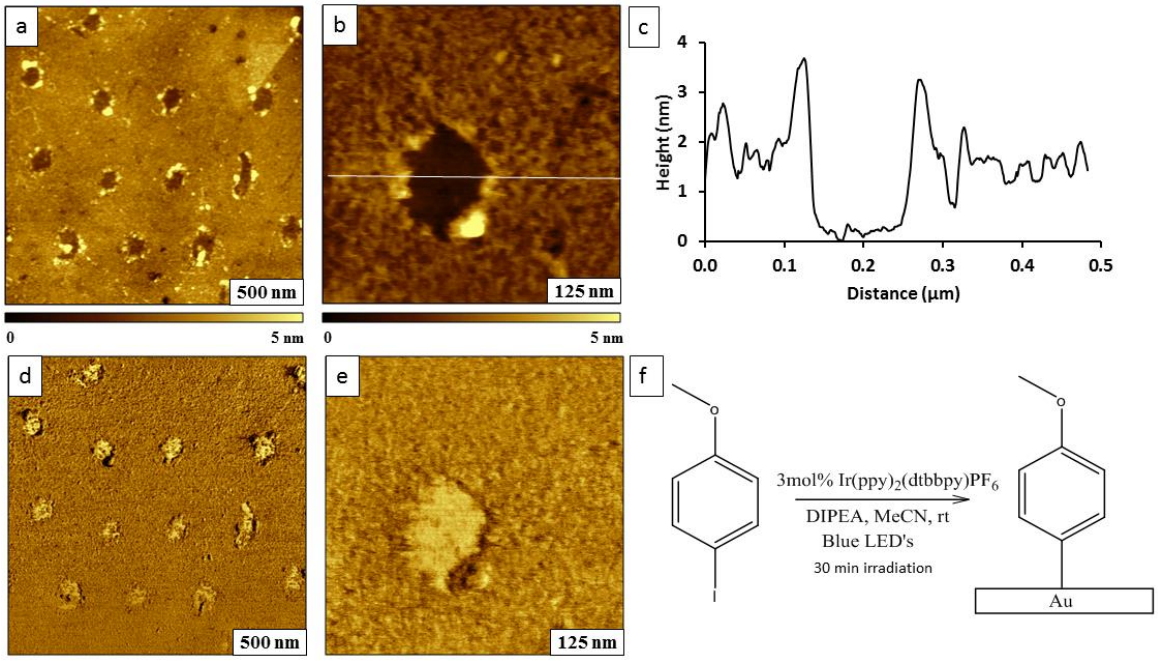

Figure 5.2. Photografted film of 4-iodoanisole on Au(111) with hexagonally packed arrangement of nanoholes, produced using particle lithography. (a) Topography image acquired in liquid (2 × 2 µm^2); (b) magnified view of a single nanohole (500 ×500 nm^2); (c) cursor profile for the line drawn in *b*; (d) corresponding lateral force image of *a*; (e) lateral force image for *b*; (f) photografting reaction scheme with 4-iodoanisole assembled on Au(111).

within the lateral force frames (Figures 5.2d and 5.2e) representing bare gold inside nanoholes as circular bright areas and the surrounding aryl thin film with a darker color. The areas are free of contaminants, which would appear as bright or dark spots on the lateral force frames. Visible light

irradiation of the reaction mixture containing 4-iodoanisole and stoichiometric amounts of $Ir(ppy)_2(dtbbpy)^+$ and DIPEA for 30 min using a blue light emitting diode (LED) at room temperature produced 4-iodoanisole radicals. The mechanism involves excitation of photocatalyst followed by single electron transfer (SET) to the aryl iodide. Aryl iodide loses iodide anion producing anisole radicals that eventually graft onto uncovered areas on Au(111) forming a gold-carbon covalent bond (Figure 5.2f).

The next series of experiments were designed as control experiments to evaluate if there is any possibility of forming thin films due to the grafting other components such as $Ir(ppy)_2(dtbbpy)^+$, DIPEA or MeCN present in the reaction mixture. Also, nanoshaving can provide information of the robustness of grafted thin films upon changing reaction conditions. Example AFM images of selected control experiments are shown in Figures 5.3 and Figure 5.4. A control experiment conducted to examine the result of thin film deposition without adding photocatalyst is shown in Figure 5.3. The sample shows a few surface deposits around the meniscus area of spheres forming ring-shaped nanostructures, however the film has an irregular, clustered morphology when compared to the continuous smooth film of the previous example (Figure 5.3a). The thickness of the film measured 2.1 ± 0.5 nm (n = 50) with a periodicity of 510 ± 60 nm. The bright spots throughout the topography view indicate nonspecific binding of components after the reaction was completed. The outer diameter of the single nanoring in Figure 5.3c has an irregular width ranging from 138 nm to 156 nm. The inner diameter measured ~50 nm, indicating the area where a silica sphere was displaced. Nonspecific attachment of adsorbates on Au(111) after photografting in the absence of photocatalyst has been observed in previous studies.[93, 235] However, further experiments need to be conducted to provide a complete explanation of the actual phenomena that occurs under reaction conditions of the control sample.

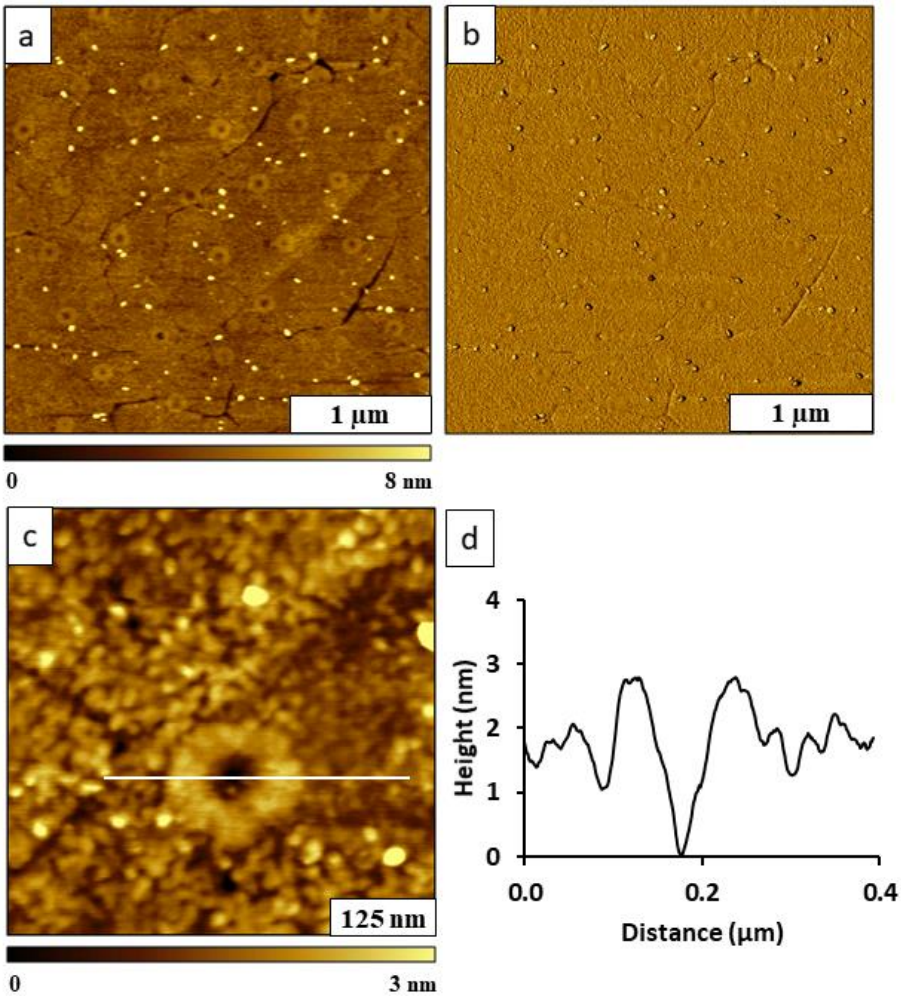

Figure 5.3. Control sample of photografting 4- iodoanisole without the presence of photocatalyst. (a) Topograph of nanostructures formed on Au(111) (3×3 μm^2); (b) corresponding phase image of *b*; (c) Zoom-in view of single nanohole (500 × 500 nm^2); (d) Cursor profile for the white line in *c*. The images were acquired with tapping-mode AFM in ambient air.

A further control experiment was completed without visible light irradiation during sample preparation (Figure 5.4). The AFM images reveal no evidence of a film or nanostructures formed on Au(111), showing that aryl radicals did not attach to the surface when visible light is not applied to the reaction mixture. The images show the typical features of a gold surface, with a few defects

and irregularly shaped gold plateaus. A few random particles of contaminants are evident in the topography (Figure 5.4a) and phase frames (Figure 5.4b).

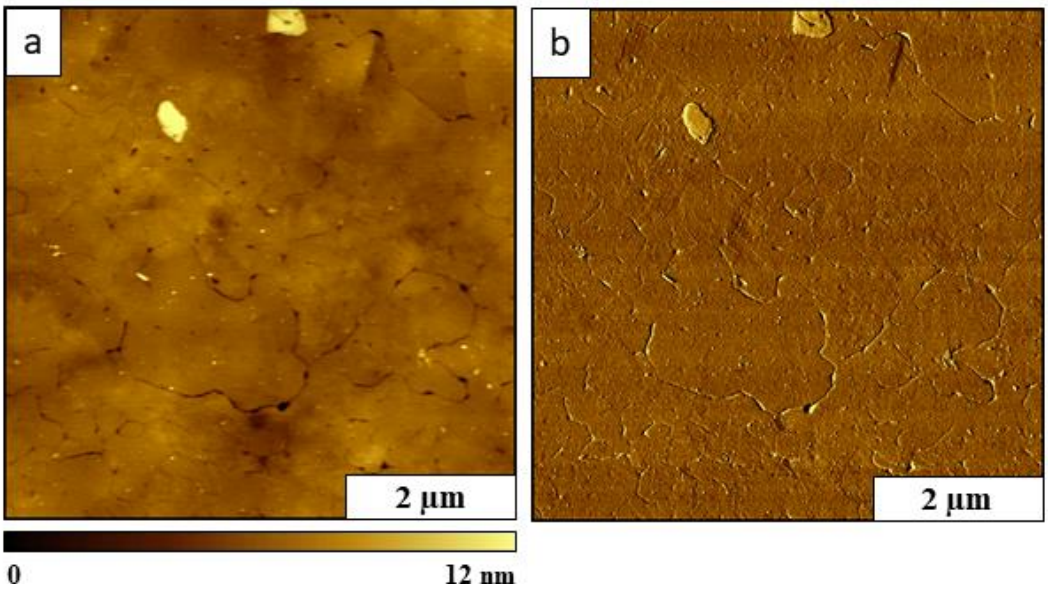

Figure 5.4. View of the sample surface acquired for a 4- iodoanisole sample prepared without applying visible light irradiation. (a) Tapping mode topography image (6 × 6 μm^2); (b) corresponding phase image for *a*.

5.4.2. AFM-Based Nanoshaving of Photografted Films

Nanoshaving is accomplished by applying a mechanical force to the AFM tip during scanning and "shaving away" molecules in a small area to uncover underlying regions of the substrate. Information of the robustness of the thin films can be obtained using nanoshaving experiments by evaluating whether the molecules can be shaved away when high force is applied to the AFM probe. When the films are stable and robust, greater force must be applied to the AFM tip to shave away molecules.

The results with nanoshaving are shown with topography images in Figure 5.5 for a photografted film of 4-iodoanisole. First, the sample was imaged with contact mode in ethanol to locate a flat area for nanoshaving (Figure 5.5a,b). Next, a square pattern was nanoshaved within an aryl thin film by applying 11 nN force to the AFM tip for 10 sweeps. Smaller forces were not successful for shaving. Silicon nitride tips have been used in previous studies with 2-9 nN force

applied to remove ω-functionalized alkanethiols Au(111).[239] A force of 11 nN was applied for nanoshaving photografted films of phthalimide esters.[235] The dark square pattern in Figure 5.5c reveals an area of uncovered substrate produced by nanoshaving. The relatively homogeneous color inside the nanoshaved square evidences clean removal of molecules of the film. The local thickness of the photografted film measured ~ 1.8 nm (Figure 5.5d). This value is in close agreement with the average thickness obtained for thin film in Figure 5.2. The nanoshaving experiment indicates that the robustness of the photografted anisole thin film is comparable to that of ω-functionalized alkanethiols.

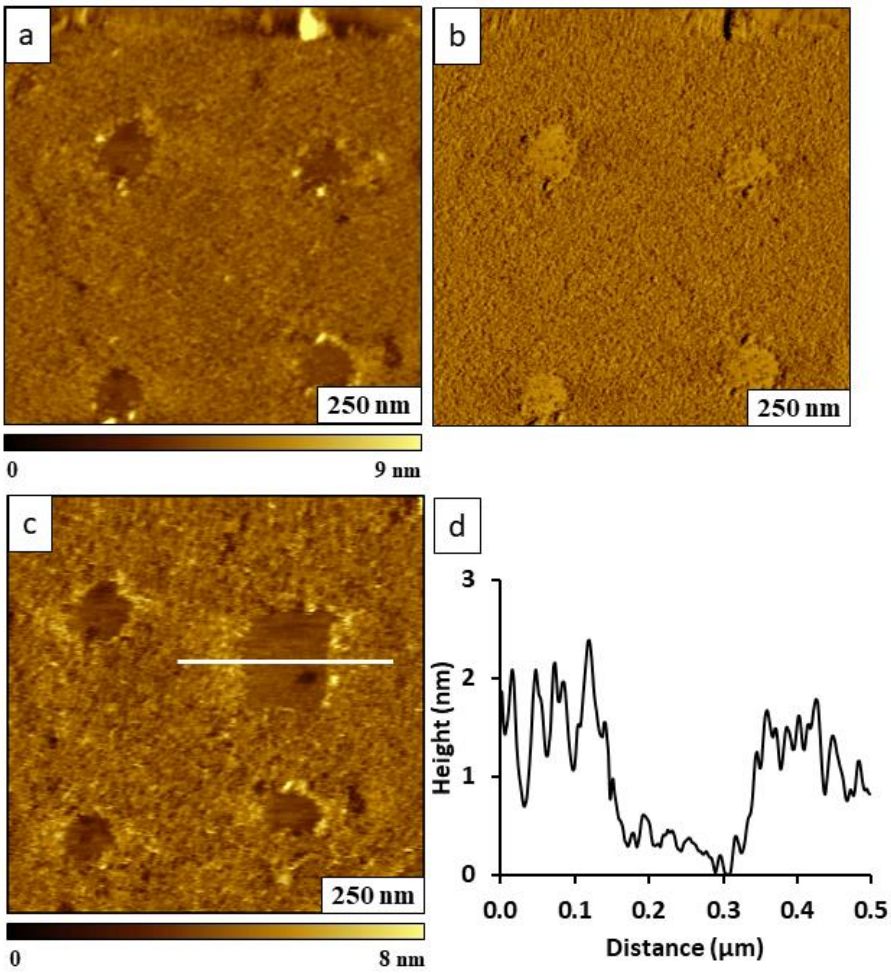

Figure 5.5. Nanoshaving of photografted film prepared with 4-iodoanisole precursor. (a) Topography image acquired before nanoshaving; (b) lateral force image for *a*; (c) after nanoshaving; (d) cursor profile for the nanoshaved area in *c*.

5.4.3. Photografting Experiments with Methyl 4-Iodobenzoate

An experiment conducted with a second type of aryl iodide, methyl 4-iodobenzoate, evidences the spontaneous grafting of aryl radicals on Au(111) (Figure 5.6). Nanoholes within the aryl thin film cannot be distinguished in the AFM topography image for a sample prepared with a particle mask (Figure 5.6a). Imaging in liquid improves the resolution of AFM topographic imaging since smaller force can be applied between the tip and the sample in a liquid environment, with minimal stick-slip adhesion of the scanning probe.[42] A spiral arrangement of overlapping gold steps is revealed in the zoom-in topography frame (Figure 5.6b) and lateral force image (Figure 5.6e). The height of a gold step is ~ 0.25 nm whereas the depth of an etch pit is about 0.2 nm. These values correspond to the thickness of one atomic layer of gold. Previous studies have documented measurements of gold steps and etch pits observed upon forming *n*-alkanethiol SAMs on Au(111).[240,] Our study reveals details of the morphology of the underlying gold substrate for samples formed by visible light photografting of aryl thin films.

The thickness of aryl thin films prepared by methyl 4-iodobenzoate was found to be 1.9 ± 0.4 nm (n=20) and a representative cursor profile of a single nanohole is given in Figure 5.6c. The estimated thickness of a monolayer formed with methyl benzoate radicals is 0.9 nm. The measured thickness value scales up to a bilayer under the given reaction conditions. A few randomly distributed nanoholes can be distinguished in the figure by comparing the topography frame (Figure 5.6a) with the simultaneously acquired lateral force image (Figure 5.6d). This provides evidence that photografting of methyl 4-iodobenzoate was successful for producing thin films of methyl benzoate attached to Au(111) via Au-C bonds (Figure 5.6f).

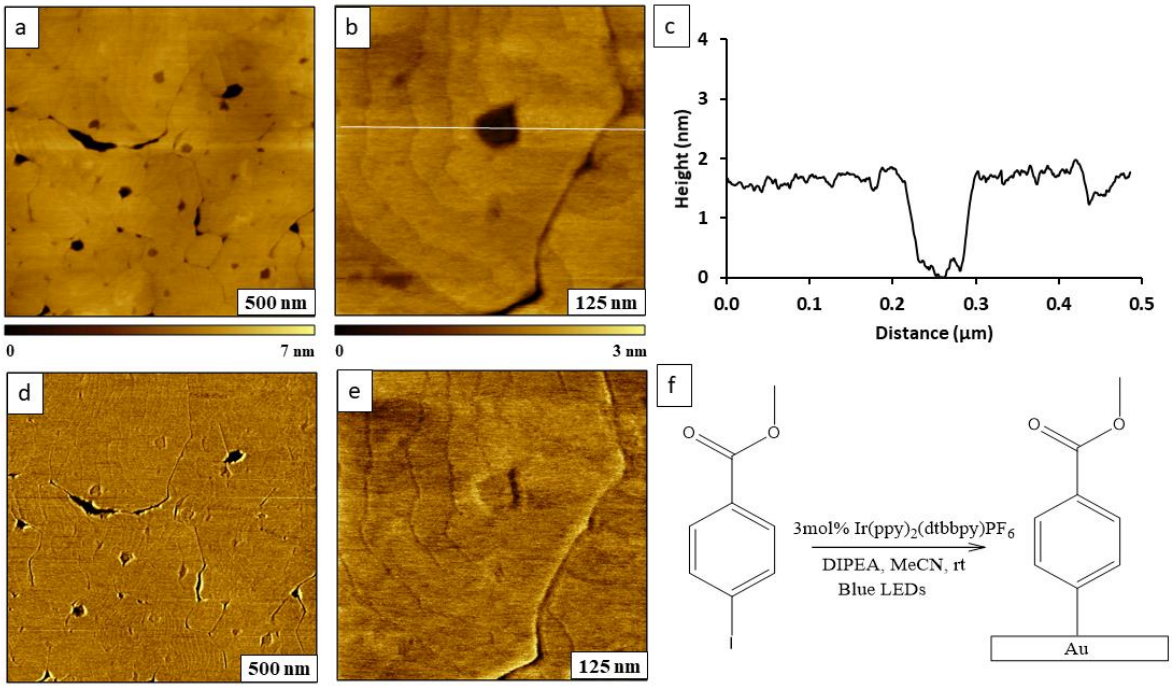

Figure 5.6. Thin film of methyl 4-iodobenzoate on Au(111) formed by particle lithography combined with photocatalysis. (a) Topography image acquired with contact mode in liquid (2 × 2 μm^2); (b) zoom-in image of a single nanohole (500 × 500 nm^2); (c) cursor profile across the nanohole in *b*; (d) corresponding lateral force image of *a*; (e) lateral force image of *b*; (f) reaction scheme for photografting methyl 4-iodobenzoate on Au(111).

5.4.3. Photografted Films of Hexafluorobenzene

The potential of forming photografted aryl thin films using different types of aryl halides as precursors was also examined. An aryl fluoride, hexafluorobenzene, was evaluated for surface grafting using visible-light photocatalysis using a protocols with immersion particle lithography (Figure 5.7). Samples prepared with hexafluorobenzene were imaged with contact mode AFM in ethanolic media. An arrangement of ring-shaped nanostructures is vaguely apparent in the topography image of Figure 5.7a, evidencing the feasibility for forming aryl thin films using aryl fluorides. The shape of three nanorings can also be resolved in the zoom-in topography frame of Figure 5.7b, which indicates that a thicker layer formed near the meniscus sites at the base of the silica particles of the surface mask.

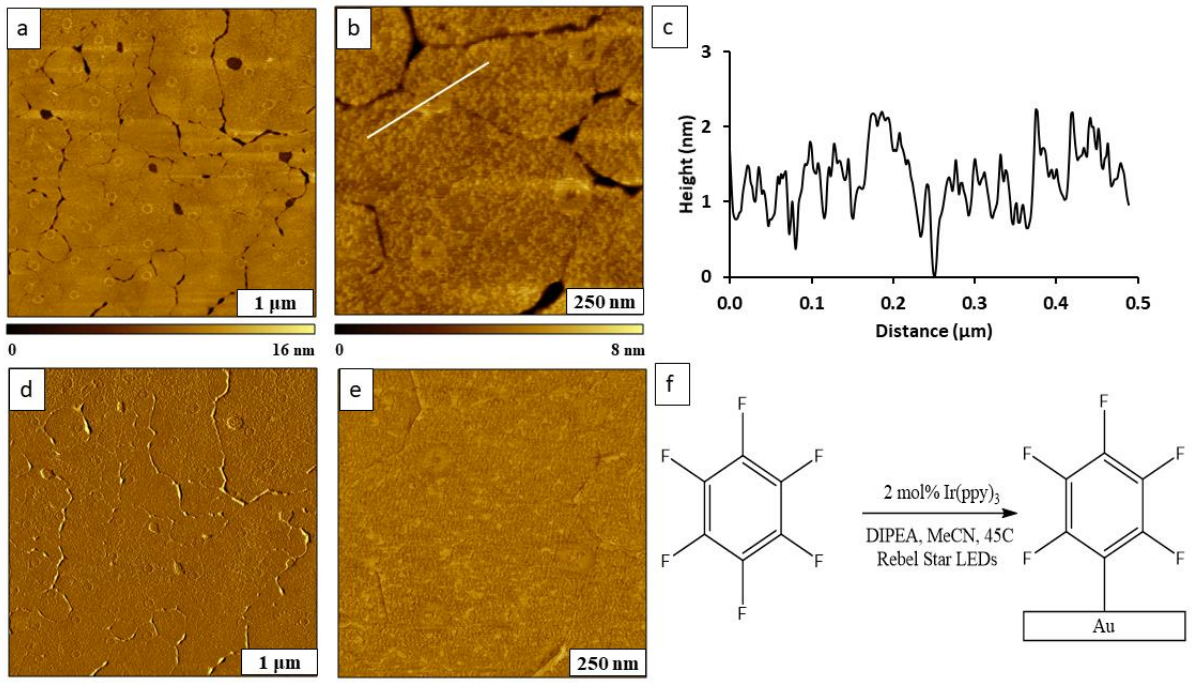

Figure 5.7. Nanorings prepared by photografting of hexafluorobenzene on Au(111). (a) Topography image (4 × 4 µm^2); (b) zoom-in view of a (1 × 1 µm^2); (c) line profile over one nanohole in *b*. (d) Corresponding lateral force image of *b*; (d) lateral force images of *a*; (e) lateral force image for *b*; (e) simplified reaction scheme for photografting hexafluorobenzene.

The height of a nanoring measured 1.8 ± 0.6 nm (n=50) with a periodicity of 480 ± 40 nm (n=20). The thickness indicates that multilayers formed, that can be attributed to the availability of six positions occupied by fluorine in each hexafluorobenzene molecule. The multiple fluorine groups enhance the possibility of forming aryl radicals during the photografting reaction. With greater availability of fluorine, the radicals tend to react with each other to form either dimers or monomers. As a consequence, multilayers were formed rather than the expected 0.63 nm film thickness for a monolayer. The average height is fairly close to the thickness shown in the example cursor profile in Figure 5.7c.

The robustness of photografted films of fluorobenzene was evaluated with nanoshaving experiments (Figure 5.8). The undisturbed area is shown in Figure 5.8a before nanofabrication. After a square pattern was nanoshaved with an applied force of 11 nN the area is slightly modified,

however molecules were not cleanly removed. Areas of the film indicated by the white square in Figure 5.8b shows that the film was not successfully shaved away with 10 sweeps using an applied force of 11 nN force. A vague square is barely visible and clean removal was not observed. A second attempt with a greater applied force of 22 nN is shown in Figure 5.8c. Molecules within the square were partially removed with higher force.

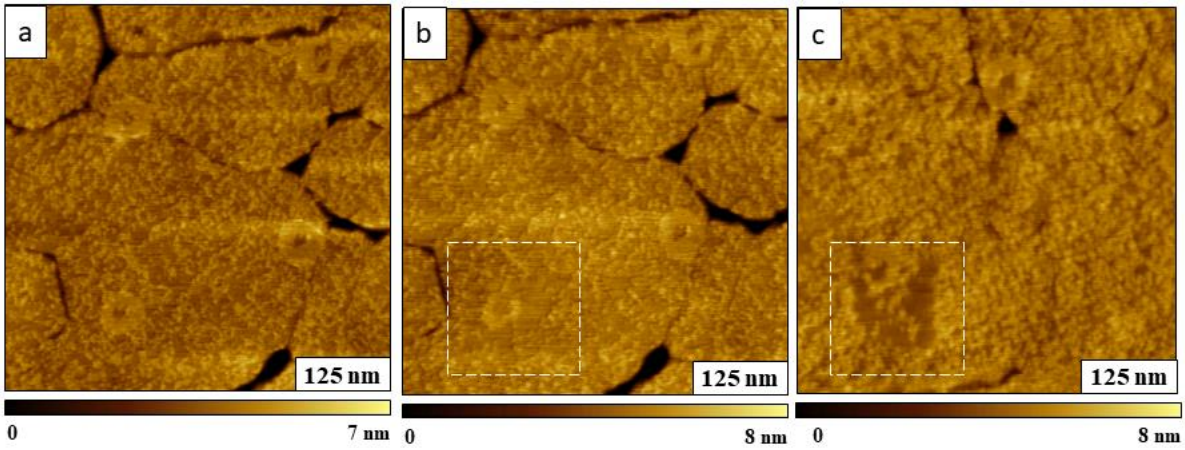

Figure 5.8. Nanoshaving experiments conducted with photografted aryl fluoride films prepared on Au(111). (a) Topograph of 500 × 500 nm^2 area taken with contact mode imaging in liquid; (a) topograph acquired after the first attempt of nanoshaving with 11 nN applied force; (b) topography frame showing a second attempt of nanoshaving with an applied force of 22 nN.

Control experiments were also conducted with the hexafluorobenzene photografting to see if surface films were formed in the absence of the photocatalyst (Figure 5.9) or without reducing agent (Figure 5.10). Contact mode AFM images of a control sample prepared without adding the Ir-based photocatalyst to the reaction mixture are shown in Figures 5.9a,b after immersion particle lithography. The nanostructured film contains nanoholes of bare gold substrate where silica spheres were rinsed away, furnishing a baseline for measuring film thickness. Irradiation of a hexafluorobenzene solution without adding the photocatalyst produced a thin film measuring 4.5 ± 0.8 nm (n=50) in thickness. An example cursor measurement is shown in Figure 5.9c. A square hole was nanoshaved in the experiment of Figures 5.9d,e to examine adhesion of the film. Local areas of the film prepared without the photocatalyst could be cleanly removed by applying a force

of 11 nN to the tip and sweeping 10 times in ethanolic media. The clean removal indicates that in the absence of photocatalyst the film formed by aryl fluoride radicals is less stable compared to the film prepared with a photocatalyst.

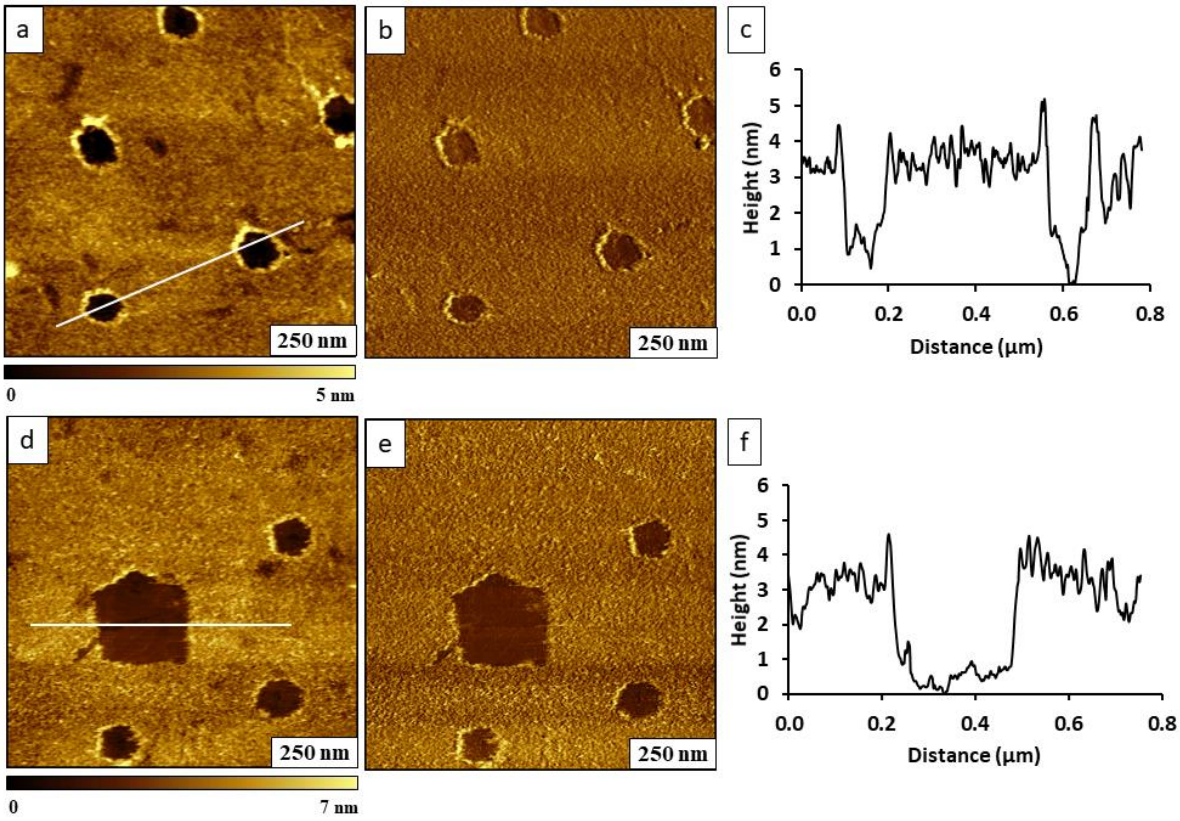

Figure 5.9. Control sample prepared with hexafluorobenzene photografting without adding photocatalyst. (a) Nanoholes viewed with a topography frame (1×1 μm^2) acquired with contact mode in liquid; (b) corresponding lateral force image; (c) An example cursor profile for the line across a single nanohole in *a*; (d) nanoshaved area (1×1 μm^2) within the aryl thin film; (e) lateral force image for *d*; (f) line profile across the nanoshaved area in *d*.

Nanostructures were not detected on a sample that was prepared with particle lithography without adding the reducing agent (Figure 5.10). The morphology that is typical of bare Au(111) are apparent, however there is no evidence of a film within the image. Surface features such as defects, scars and triangular terraces on Au(111) are revealed in topography frame of Figure 5.10a. There is no evidence of a film or molecular adsorbates, without reducing agent no surface assembly took place for the control sample without the presence of a reducing agent. The control experiments

indicate that the reducing agent is crucial for producing surface films with the photocatalyzed reaction.

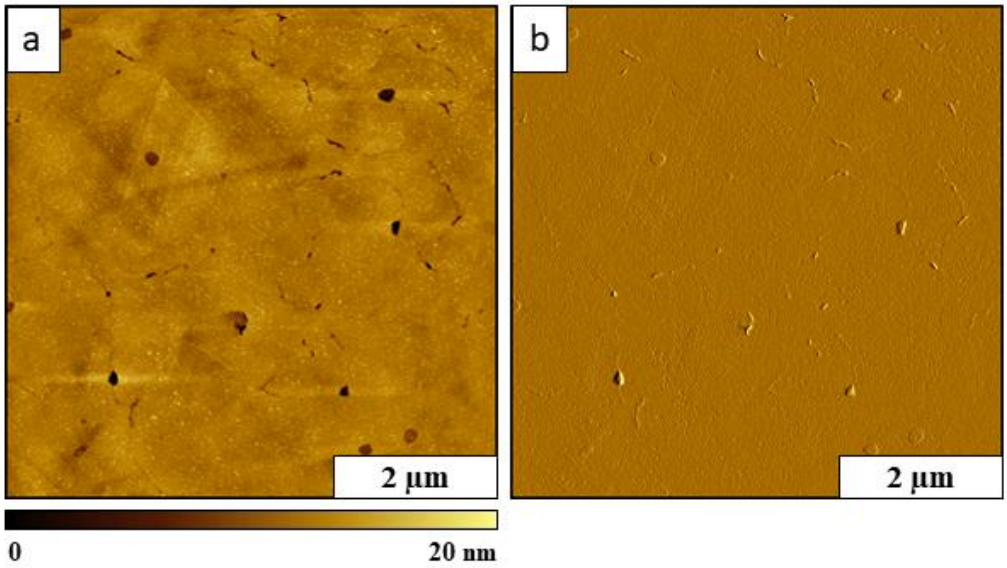

Figure 5.10. Control sample prepared with hexafluorobenzene photografted without adding reducing agent, DIPEA. (a)Tapping mode topography image acquired in air; (b) phase image of *a*.

5.4.4. Photografted Films Prepared with Aryl Halides

Photografting experiments were conducted using aryl halide precursors of iodopentafluorobenzene, 2,3,4,5,6-pentafluorobenzonitrile and methyl pentafluorobenzoate. Surface characterizations with AFM and nanoshaving results are shown in Figure 5.11 for studies with iodopentafluorobenzene. A thin film with nanorings was produced using visible light photocatalysis of iodopentafluorobenzene with immersion particle lithography. A periodic arrangement of circular nanostructures is visible in the topography frame of Figure 5.11a. At higher magnification (Figure 5.11b) the clustered morphology of the film reveals an irregular, somewhat rough morphology which is not smooth and continuous. This suggests that the surface packing is not saturated, a few areas of scars are not fully covered with molecules. The average thickness of the nanoring structures measured 3.1 ± 0.9 nm (n=50) which is ~6 times taller than the theoretical height of a fluorobenzyl monolayer film on Au(111). An example cursor profile is

shown in Figure 5.11c across an individual nanoring pattern. The shapes of the nanorings can also be resolved in the concurrently acquired lateral force images in Figures 5.11d,e. The reaction conditions are outlined in Figure 5.11f.

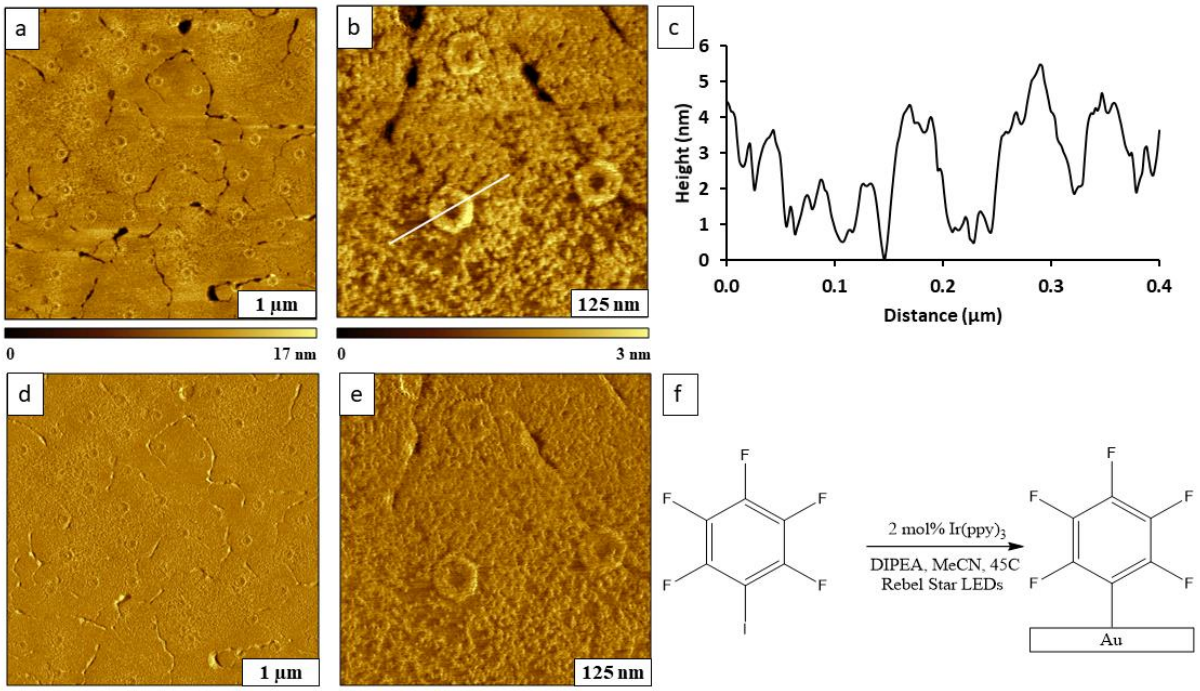

Figure 5.11. Nanopatterned thin film prepared by exposing iodopentafluorobenzene to visible light with the photocatalyst reaction combined with immersion particle lithography. (a) Contact mode topography image acquired in liquid (4 × 4 µm^2); (b) magnified view of a three nanoholes (500 × 500 nm^2); (c) cursor profile for the line on *b*; (d) corresponding lateral force image of *a*; (e) lateral force image simultaneously taken with *b*; (f) simplified reaction scheme of photografting iodopentafluorobenzene on to Au(111).

Nanoshaving was effective for removing photografted molecules was observed with an applied force of 11 nN (Figure 5.12) for a film prepared with photografting iodopentafluorobenzene. A view of the ring-shaped nanostructures produced with immersion particle lithography combined with photografting of iodopentafluorobenzene is shown in the topography frame of Figure 5.12a. After nanoshaving, a square hole was formed with molecules piled at the edges of the nanoshaved area (Figure 5.12b). With 10 sweeps, the removal of molecules in the square hole was incomplete for this sample.

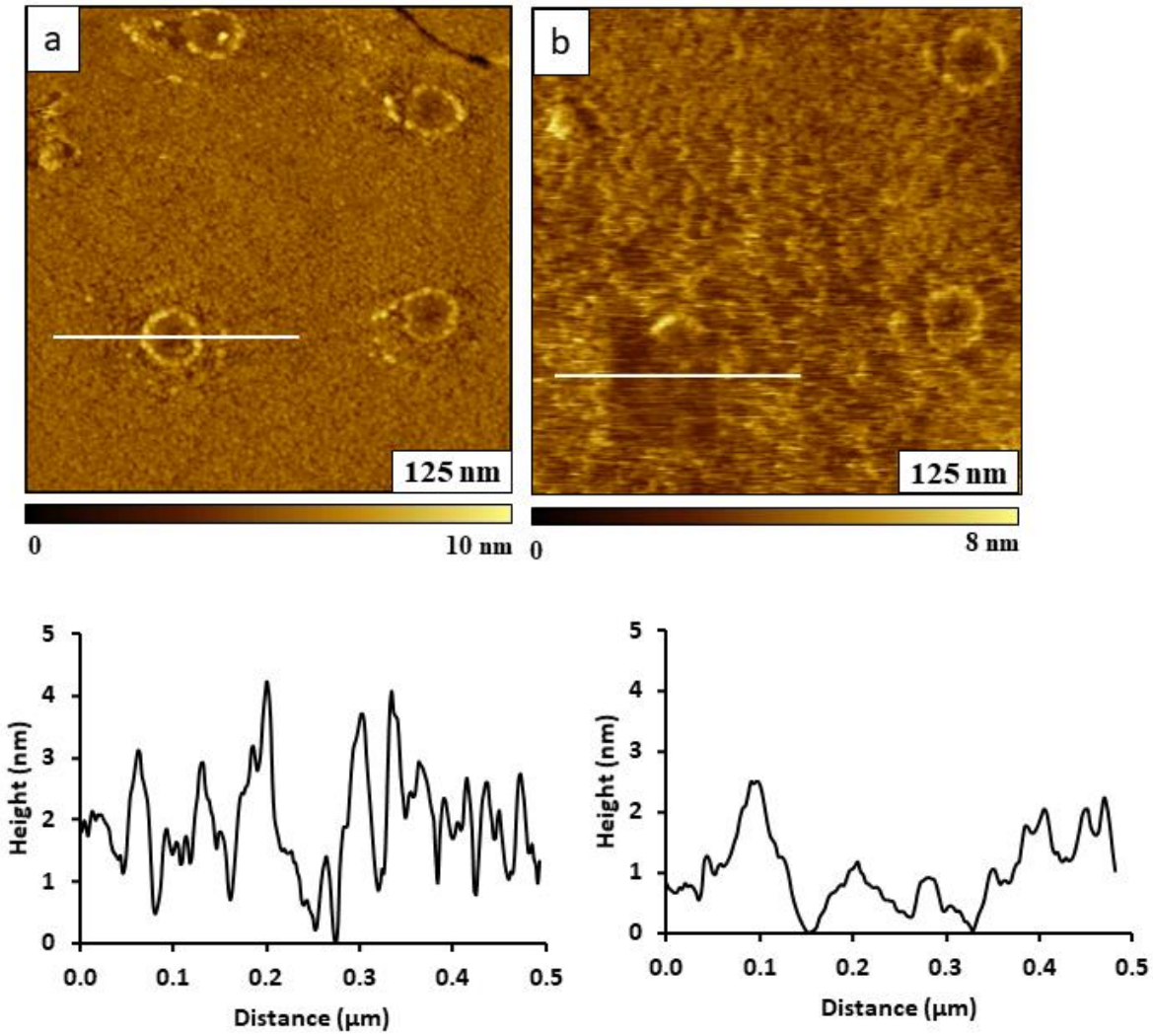

Figure 5.12. Nanoshaving experiments conducted on aryl thin films prepared with iodopenta-fluorobenzene precursors. (a) Topography image (500 × 500 nm^2) taken before nanoshaving; (b) topography image after a region was nanoshaved. Cursor profiles are displayed below each topography image for the white lines drawn across nanostructures. The nanoshaving experiment was conducted with 10 sweeps using contact mode.

Photoredox catalysis of ,3,4,5,6-pentafluorobenzonitrile was successful for producing aryl radicals that graft onto uncovered areas of Au(111) as shown in Figure 5.13. After the surface mask was removed, patterns of nanoholes were revealed at the areas that were initially covered with silica spheres. The edges of the nanoholes are slightly taller than the surrounding film, in areas surrounding the base of the silica spheres (Figures 5.13a, b). An example cursor profile across

one of the nanoholes is shown in Figure 5.13c. The average depth of nanoholes measured 1.6 ± 0.5 nm (*n*=50). The concurrently acquired lateral force frames reveal differences in chemical contrast for the areas of uncovered gold substrate within the center of the nanoholes compared to the surrounding matrix film. The general photografting reaction scheme is outlined in Figure 5.13f.

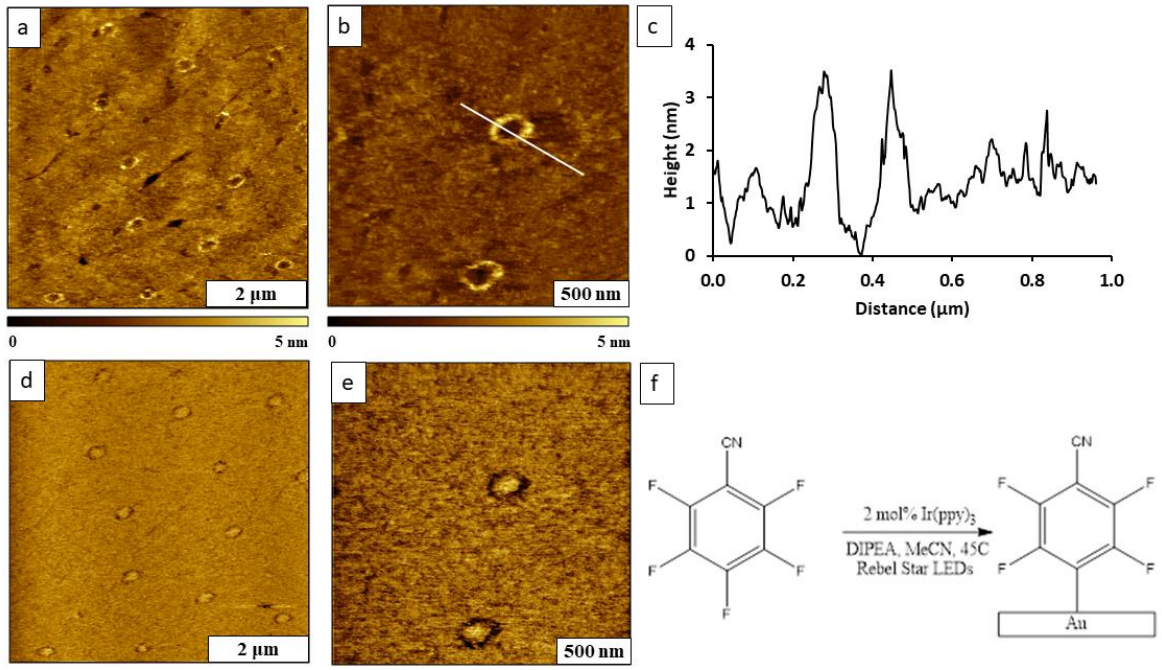

Figure 5.13. Nanoholes formed within an aryl film prepared using 2,3,4,5,6-pentafluorobenzonitrile as the precursor for visible light photocatalysis. (a) Topography image acquired in liquid (6 × 6 µm^2); (b) two nanoholes shown in a zoom-in image (2 × 2 µm^2); (c) cursor profile for the line on *b*; (d) lateral force frame for *a*; (e) lateral force images for *b*; (f) general reaction scheme for photografting pentafluorobenzonitrile on Au(111).

A multilayered film was formed with photografting of methyl pentafluorobenzoate. A dense, smooth morphology is revealed in the topography frames of Figures 5.14a,b. The arrangement of circular holes follows the periodic packing of the silica sphere mask used for immersion particle lithography. An example cursor line drawn across two of the nanoholes is shown in Figure 5.13c. The average thickness of the multilayered film measured 6.5 ± 1.0 nm

(*n*=50) which corresponds to ~9 molecular layers. Phase images which are concurrently acquired with tapping-mode topography frames provide sensitive maps of the elasticity of the sample

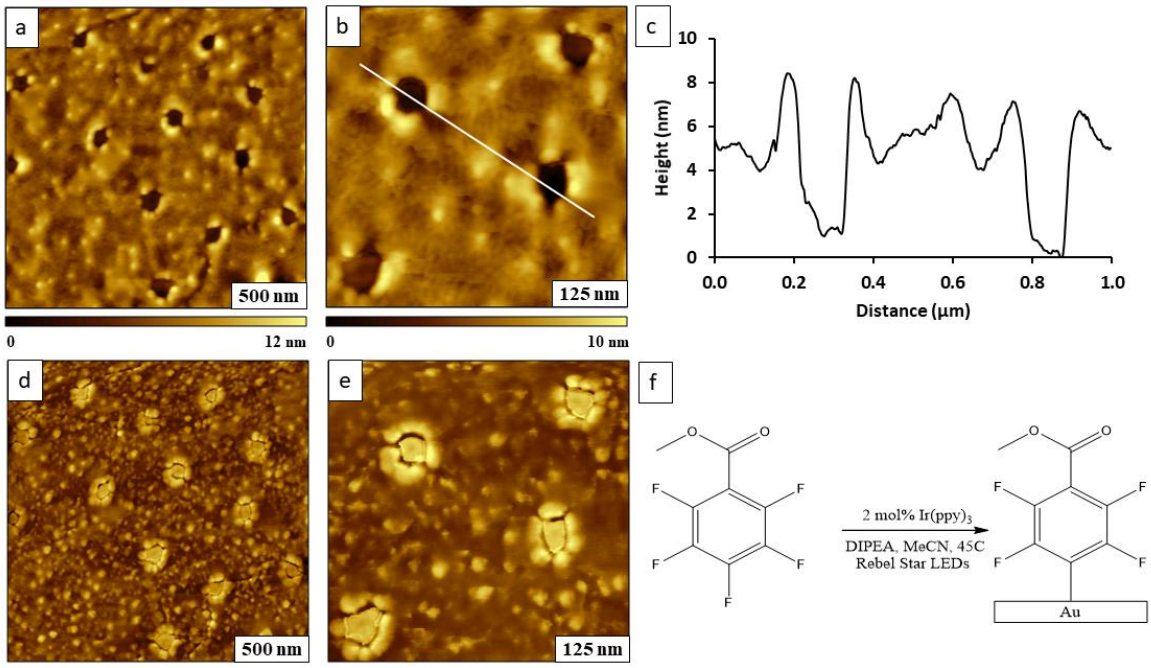

Figure 5.14. Nanoholes within an aryl film prepared by immersion particle lithography and photografting using a precursor of methyl pentafluorobenzoate. (a) Topography image acquired with tapping mode (2×2 μm^2); (b) zoom-in image (500×500 nm^2); (c) cursor profile for the line on *b*; (d) corresponding phase images of *a*; (e) phase image for *b*; (f) reaction scheme for photografting methyl pentafluorobenzoate on Au(111).

(Figure 5.13d,e). In this example the bright areas of the circular gold patches of the nanoholes are harder than the surrounding film. The bright clusters in areas between the nanoholes reveal an irregular film thickness. The thickness of the photografted film is not uniform throughout all areas of the sample. The island protrusions are also apparent in the topography images.

5.5. Conclusions

Nanostructured aryl thin films were produced on Au(111) by covalent attachment of aryl radicals formed via visible light irradiation (with blue LEDs) of Ir catalyst in the presence of DIPEA reducing agent. Multiple replicate patterns of nanoholes and ring-shaped nanostructures within aryl thin films were formed by combining visible light photocatalysis reaction with particle

lithography. The bare gold substrate exposed inside the nanoholes provides a reference point to measure the thickness of photografted films. Film thickness was measured by selecting AFM cursor profiles across surface features containing uncovered substrate. The overall morphology of photografted aryl thin films was visualized with high-resolution AFM studies. Multilayered films were generated as a consequence of the aryl radicals producing dimeric or monomeric radical units which undergo subsequent radical reactions in the solution mixture or even after the initial attachment to the gold substrate. Nanoshaving experiments were successfully applied to examine adhesion of photografted films prepared on gold substrates. Photografting generated strongly attached organic thin films by Au-C covalent attachment of aryl radicals to Au(111). The photografting method was combined with particle lithography to produce ordered arrays of nanostructures within photografted films.

CHAPTER 6. SURFACE COUPLING OF OCTAETHYL PORPHYRIN WITH SILICON TETRACHLORIDE *

6.1. Introduction

Porphyrins are excellent materials for molecular electronics, due to their diverse structural motifs and associated electrical, optical and chemical properties, and thermal stability.[241-246] The rigid planar structures and π- conjugated macrocycles of porphyrins inherently convey stability and robust electrical characteristics. Porphyrins have a macrocyclic tetrapyrrole structure, which may be functionalized with various substituents.[247] Modifications of the macrocycle, peripheral groups or bound metal ions can generate a range of electrical and photoelectrical properties.[248] At a basic level, electronic properties of porphyrins are controlled by the degree of π delocalization of the conjugated rings.[249] Porphyrins can be organized into supramolecular arrays, aggregates and crystals with diverse functions. The diverse architectures of porphyrins have been used for applications such as gas sensors,[250-251] phototherapeutics,[252-253] photovoltaic cells,[254-257] photocatalysis,[258-259] organic light-emitting diodes,[260-263] molecular wires,[264-265] and as components for molecular-based electronic devices.[266-270]

The orientation of porphyrins on surfaces is determined by factors such as the nature of the peripheral substituents and their position on the macrocycle.[271-272] When preparing surface films, the planar macrocycles of porphyrins spontaneously self-associate to form stacked structures. This natural capability of self-stacking has been a hurdle for developing processes for molecular patterning, since porphyrins do not form chemisorbed or covalent bonds to surfaces unless a peripheral group is added to the macrocycle to facilitate bonding. Due to the structural nature of tetrapyrrole molecules of porphyrins, the supramolecular organization of nanomaterials and films

* This chapter was previously published in ACS Omega in the article[3] linked here. https://pubs.acs.org/doi/10.1021/acsomega.8b03204 (See Appendix F). Further permissions related to the material excerpted should be directed to the ACS.

is driven by forces such as metal-ligand bonds, non-covalent ionic bonds, hydrogen bonding, π-π interactions, electrostatic and other intermolecular forces including van der Waals forces.[273-275] There is a tendency for the flat molecules to orient in a coplanar arrangement that is mediated by physisorption to the substrate as well as by electrostatic interactions between macrocycles to form layers of packed molecules in a cofacial arrangement, analogous to a stack of coins.

There is considerable precedent for studies of the synthesis, structures and properties of porphyrins and our studies build on such information. Several synthetic approaches have been reported for binding porphyrins to surfaces by designing peripheral groups to facilitate surface self-assembly, as a strategy to enable stronger bonding between the molecules and substrate. By incorporating thiols in peripheral groups of the molecular design, porphyrins can be linked to metal surfaces by chemisorption.[276-281] A silicon substrate was functionalized with 3-aminopropyltrimethoxysilane (APTMS) to link 5,10,15,20-tetrakis-(4-aminophenyl) porphyrin to surface amines using a urea coupling reaction with 1,4-phenylene diisocyanate.[282] Zinc and iron porphyrins were attached to silicon substrates functionalized with APTMS by forming an amide bond between the conjugated macrocycle and surface amino groups that were activated by carboxydiimidazole.[283] The nitrogen of pyridyl moieties was linked to chloro- groups of chloromethylphenylsilane to attach tetrapyridyl porphyrin (TPyP) to functionalized Si(100) substrates.[284] Cobalt tetraphenyl porphyrins were functionalized with peripheral groups of amines for binding to gold substrates, as reported by Lokesh et al.[285] As a strategy to covalently bind porphyrin to surfaces of Si(100) and quartz substrates, multilayer thin films were prepared with TPyP by coating the surface with [p-(chloromethyl)phenyl] trichlorosilane as a coupling layer and then assembling sequential layers with linkers connected to pyridyl groups of the porphyrin

ring.[286-287] Copper(I)-catalyzed azide-alkyne cycloaddition (CuAAC) reactivity, commonly referred to as "click" chemistry has also been used for binding porphyrins to surfaces.[288-289]

In previous reports, nanostructures of silicon complexes of porphyrins and phthalocyanines were successfully prepared using silane coupling to form covalently bound structures on surfaces of silicon, glass, and ITO.[290-292] The silicon atom is bound tightly to the centers of the porphyrin rings by four nitrogens of the conjugated rings. Porphyrins with a nonmetal element such as silicon have two chlorides connected at opposite faces of the macrocycles that facilitate reactions for binding to a surface as well as to form covalent bonds to additional molecules. The synthesis and characterization of several hexacoordinate silicon porphyrins have been reported, including octaethylporphyrin,[275] tetraphenylporphyrin,[293-295] tetra-p-tolylporphyrin and tetrakis(p-(trifluoromethyl)phenyl)porphyrin.[296] One-dimensional polymer wires of Si-porphyrin were prepared on glass and ITO substrates using a silane coupling strategy by Kanaizuka et al. in which a central Si atom was bound to the center of the porphyrin macrocycle.[290]

We are developing protocols using colloidal lithography to prepare surface films and nanostructures with porphryins that are covalently bound to silicon substrates. The approach is based on reactions with silicon tetrachloride ($SiCl_4$) to form skewered molecules that are centrally interconnected by covalent Si-O bonds. Using a "one pot" reaction with $SiCl_4$, porphyrins are linked to surfaces by Si-O bridges directly to a central Si atom inserted within the macrocycle. Likewise, the macrocycles of porphyrins can be linked together by hydrolysis and condensation steps to form chains with Si-O-Si bridges between the macrocycles. This strategy provides capabilities for controlling the configuration of the macrocycles in a cofacial orientation with covalent bonds. The surface assemblies have been referred to as a "shish kebob" arrangement in which molecules are skewered together by Si-O-Si bridges.[297] Bonds of Si-O are suitable for

forming connections to substrates such as silicon wafers, glass, mica, and metal oxides. One may predict that the covalent nature of Si-O-substrate linkages will impart stable, robust and novel electronic and photonic properties depending on the design of the macrocycles. The chemical nature of surface linkages is a critical variable for designing heterojunctions in configurations for molecular electronics.

Herein, we present results for linking porphyrins with Si-O-Si skewers to Si(111) using 2,3,7,8,12,13,17,18-octaethylporphyrin (OEP), which is a free base porphyrin that has eight ethyl groups at pyrrole positions of the macrocycle. Nanopatterning protocols were implemented to facilitate the preparation of well-defined interfaces with nanometer-level control of the spacing and composition of patterned elements. Colloidal lithography with silica spheres provides a practical approach to pattern molecules by masking discrete areas of the surface from molecular deposition. When the mask is removed, bare areas of the substrate are exposed that had been protected by the mask of spheres. The nanostructured films contain nanoholes, which provide an *in situ* reference for measuring film thickness, and also adventitiously furnish landmarks to enable side-by-side comparisons of surface morphology using studies with atomic force microscopy (AFM) (e.g. substrate *vs*. film).

6.2. Experimental Section

6.2.1. Materials and Reagents

Precut polished silicon wafers Si(111) were purchased from Ted Pella, Inc. (Redding, CA). Octadecyltrichlorosilane (OTS) was obtained from Acros Organics, Thermo Fisher Scientific (New Jersey). Silicon tetrachloride and 2,3,7,8,12,13,17,18-octaethylporphyrin (OEP) were obtained from TCI America (Portland, OR). Size sorted silica spheres (500 nm) were obtained from Thermo Scientific (Fremont, CA). Chloroform (HPLC grade) was acquired from Fisher

Scientific (Lenexa, KS). Concentrated sulfuric acid (98.0%) (J. T. Baker, Fisher Scientific) and hydrogen peroxide (30%) (British Drug Houses, VWR) were used to prepare piranha solution. Ethanol was purchased from Deacon Labs (Prussia, PA) and used as received. Anhydrous toluene was purchased from Merck Millipore (Billerica, MA).

6.2.2. UV/Vis Spectroscopy

Absorbance spectra were acquired with a Cary model 50 UV/vis spectrophotometer from Varian Instruments (Santa Clara, CA).

6.2.3. Atomic Force Microscopy

Samples were characterized using a model 5500 atomic force microscope (Keysight Technologies, Santa Rosa, Ca). Results were acquired using tapping- mode AFM. Nonconductive silicon nitride tips were used for AFM studies. Tapping-mode images were acquired using tips with an average spring constant between 10 and 130 N/m and resonance frequencies ranging from 272 to 464 kHz (Nanosensors, Neuchatel, Switzerland). Digital images were processed using Gwyddion software, which is supported by the Czech Metrology Institute.[298]

6.2.4. Preparation of Nanostructured Films of Si-OEP

An immersion procedure was used to generate a thin film of Si-OEP on Si(111). Pre-cut polished silicon wafers (Virginia Semiconductor, Frederickburg, VA) were rinsed with ultrapure water and then immersed in piranha solution for 1.5 h to remove surface contaminants. Piranha solution is a mixture of hydrogen peroxide and sulfuric acid with a (v/v) ratio of 1:3. Caution: piranha solution is highly corrosive and should be handled with great care. Next, the substrates were removed and rinsed with water. Thin films were made by adding 2.9 μL of neat $SiCl_4$ to 5 ml of a solution of OEP (0.5 mM) in chloroform. Silicon substrates were placed in the OEP solution to react for 5 h. The samples were then removed from solution, rinsed with ethanol and ultrapure

water and sonicated in chloroform. Next, the samples were dried under nitrogen and subsequently characterized with AFM.

6.2.5. Preparation of Nanopatterns

An aqueous suspension of silica spheres was prepared by successive cycles of centrifugation to remove contaminants. After centrifuging an aqueous solution of 500 nm silica spheres (0.2 mL), the supernatant was decanted and replaced with deionized water (0.2 mL). The spheres of the pellet were resuspended using vortex mixing. The process was repeated three times to ensure complete removal of contaminants. Next, an aliquot (10 μL) of the suspension was deposited onto a clean piece of silicon and dried in air. The samples were then placed into an oven at 150 ˚C for time intervals ranging from 3 h to 20 h.

To prepare patterns of nanoholes within a film of OTS, the substrate with a mask of silica spheres was immersed in a solution of OTS (0.1% in anhydrous toluene) for 5 h. The sample was then removed from solution and further rinsed with ethanol and deionized water. Next the surface mask of spheres was removed by sonication in ethanol and water. Nanopatterns of OEP were prepared by immersing the sample with nanoholes within an OTS matrix into a solution containing OEP and $SiCl_4$ in chloroform for 5 h or 24 h. The samples were removed and rinsed in ethanol and water followed by sonication in chloroform, then characterized with AFM.

6.3. Results and Discussion

Three types of surface platforms were prepared using protocols of colloidal lithography to evaluate the morphology and thickness of Si-OEP nanostructures grown on Si(111) surfaces. First, a film of Si-OEP was prepared that contained nanoholes of uncovered substrate that had been protected by a surface mask of silica spheres. After the mask was removed, the local areas of Si(111) within nanoholes furnished a baseline for measuring the thickness of the film which

surrounded the nanoholes. In the second nanopatterning strategy, the drying conditions of the masked substrate was altered to generate ring-shaped nanostructures. The third strategy for preparing samples was to make patterns of Si-OEP nanodots within a matrix film of octadecyltrichlorosilane (OTS). In the third example, the initial height of the OTS film provided a reference scale for measuring the growth of Si-OEP nanostructures within the nanoholes. Molecular-level characterizations with AFM were used to obtain direct views of Si-OEP nanostructures produced by surface self-assembly.

6.3.1. Samples of Nanoholes within a Film of Si-OEP

The steps for fabricating nanoholes within a film of Si-OEP are illustrated in Figure 6.1. An aqueous solution of monodisperse silica spheres was deposited onto a clean Si(111) substrate and then dried in air. The spheres spontaneously formed close-packed layers on an atomically flat substrate when dried in ambient conditions to furnish a surface mask for patterning (Figure 6.1a). The substrate with a mask of spheres was dried in ambient conditions then placed into an oven to temporarily anneal the silica beads to the surface, to prevent the spheres from being washed away during the immersion step. After the drying and annealing step, the masked substrate was then

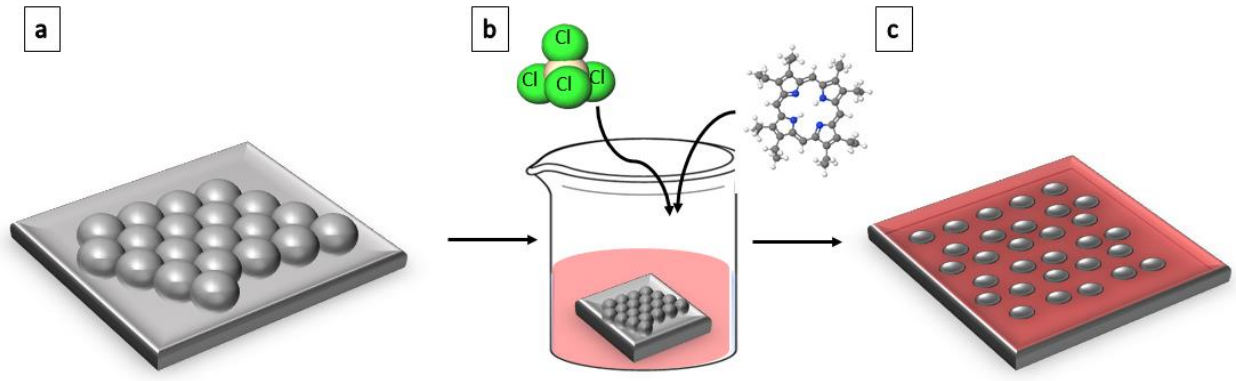

Figure 6.1. Basic steps for generating nanoholes within a film of Si-OEP using colloidal lithography. (a) An aqueous solution of silica spheres was deposited on a clean Si(111) substrate and dried. (b) The surface with the particle mask was immersed in a solution of OEP and $SiCl_4$ in chloroform for a one-pot reaction. (c) The sample was rinsed with sonication to remove the particle mask to generate nanoholes of uncovered substrate within an OEP film.

placed into a solution of OEP (0.5 mM in chloroform containing an excess of $SiCl_4$) to initiate coupling of porphyrin and silane (Figure 6.1b). In the final step, the mask of silica spheres was removed by sonication and rinsing to generate nanoholes of uncovered substrate within a matrix film of Si-OEP (Figure 6.1c). The thickness of the film grew taller with longer immersion intervals. Control samples were prepared without using $SiCl_4$, and also for a continuous film prepared without a surface mask; AFM images of the control experiments are provided in *Supporting Information*, Figures D.1 and D.2.

An example of the interesting morphology of a nanostructured film of skewered molecules of OEP bound to Si(111) through Si-O bridges is shown in Figure 6.2, after the mask of colloidal Si spheres was rinsed away from the surface. Areas of the film have a distinctive morphology of individual strands of skewered porphyrins which grow vertically from the surface which are not interconnected. The sample has a hexagonal arrangement of circular dark holes surrounded by a film of Si-OEP. In this example, the nanoholes were generated using a surface mask of monodisperse 500 nm silica spheres prepared by drying an aqueous suspension of colloidal silica in ambient conditions, followed by a brief annealing step (3 h). After drying, water persists throughout the sample in areas surrounding and between silica spheres of the surface mask. The masked substrate was then cooled and immersed in a solution of OEP and $SiCl_4$ for 24 h. The bright areas are regions of Si-OEP and the darker areas are the holes where the particle mask was removed (Figure 6.2a). The successive zoom-in views (Figure 6.2b and 6.2c) disclose an interesting topology, the areas of Si-OEP film are punctuated with small disks of the macrocycles. The regular sizes and shapes of the discs suggest a mostly co-planar orientation of columns of flat Si-OEP molecules that do not interconnect in lateral directions. The location, size and arrangement of the nanoholes are also resolved in the simultaneously acquired phase images (Figures 6.2e, 6.2f,

6.2g). There are 37 nanoholes within the 4 × 4 μm^2 frame, which have fairly regular sizes and shapes indicating the sites where silica spheres were removed. The spacing between the nanoholes is ~ 500 nm, which is derived from the geometry and arrangement of the particles of the surface mask. Within the nanoholes are exposed sites of uncovered substrate that were uncovered when the silica spheres were rinsed away. Example line profiles traced across the nanoholes are shown in Figures 6.2d and 6.2h. The average depth of the nanoholes measured 17 ± 4 nm referencing the uncovered holes as a baseline for cursor measurements. The error term is an estimate of the

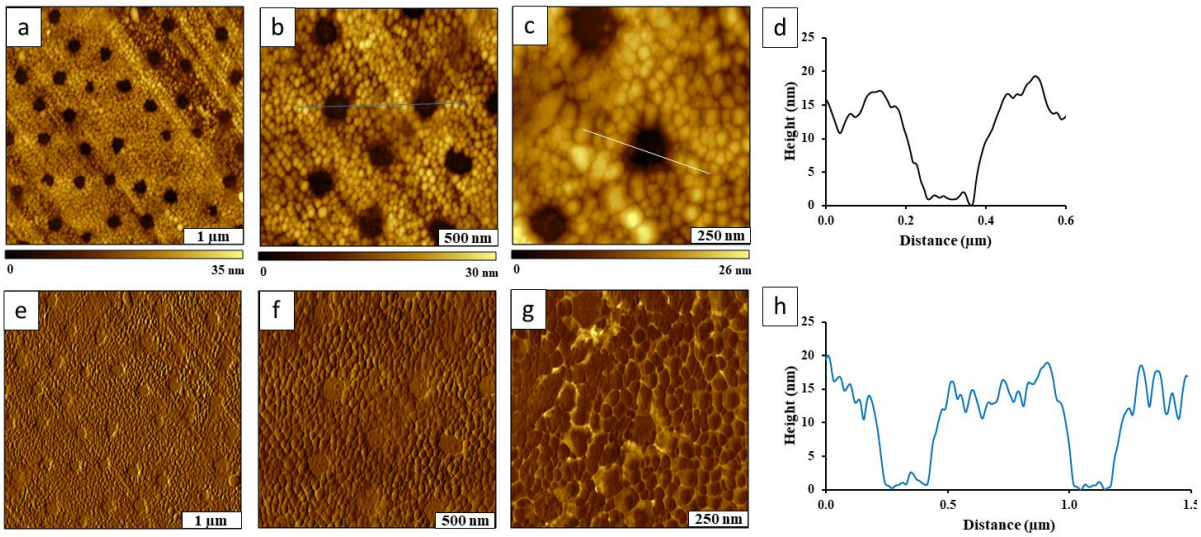

Figure 6.2. Nanoholes within a film of OEP-silane prepared on Si(111) after 24 h immersion, using a surface mask of monodisperse 500 nm SiO_2 particles. (a) Topography view of OEP nanoholes (4 × 4 μm^2); (b) Zoom-in topograph (2 × 2 μm^2); (c) magnified view of three nanoholes (1 × 1 μm^2); (d) Cursor profile for the white line in c; (e) simultaneously acquired phase image for *a*; (f) phase image of *b*; (g) phase image of *c*; (h) Cursor profile for the blue line traced in *b*.

background roughness of the line profiles. The surface coverage measured ~94 % for the film of Si-OEP film shown in Figure 6.2, the remaining areas are circles of exposed substrate. The widths of the Si-OEP disks are larger than would be expected for an individual macrocycle, because the AFM probe is much larger than the surface features. An ultra-sharp probe could likely reveal the true lateral dimensions, in future planned experiments. The molecules do not interconnect in lateral xy directions, which is evident by the way the AFM probe outlines multiple, discrete circular

features of highly regular sizes. The molecular assembly seems to occur only in the vertical direction with planar porphyrins assembling on the top of the macrocycles in a concatenated arrangement. The thickness of the film is not uniform. The values measured from individual cursor profiles across 50 nanoholes ranged from 5 to 24 nm in depth. (The size distribution is included as *supporting information* in Appendix Figure E.6 and the color change of solutions in Appendix Figure E.7). The thickness measurements indicate that a multilayered film was formed of 16-75 Si-OEP units which are interconnected by Si-O-Si linkers, using an estimate of 0.32 nm for each porphyrin unit of the skewered assemblies. The 0.32 nm value is based on the theoretical length of a Si-O bond.

The results in Figure 6.2 were acquired at a time point of 24 h of substrate immersion. Future planned experiments will address the kinetic details of surface assembly by evaluating changes in sample morphology after shorter reaction intervals.

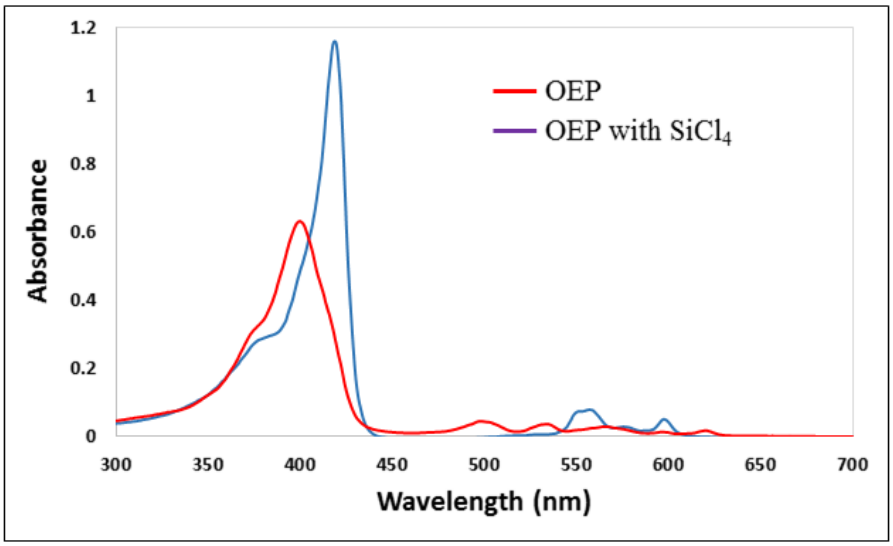

Figure 6.3. Absorption changes for the UV/vis spectra showing a characteristic red shift of the intense Soret band of OEP after reaction with $SiCl_4$.

Evidence that Si was successfully coordinated to the macrocycles of OEP can be readily detected by observing shifts in Soret and Q bands using UV/Vis spectroscopy. Structural changes

of the central atom or pendant substituents on the ring will also affect the transition energies profiled in absorbance spectra. The absorption bands in systems of chromophoric porphyrins arise from electronic transitions between the two HOMOs and two LUMOs of the aromatic rings of the macrocycle, indicating pi-pi transitions.[299] When $SiCl_4$ was added to a solution of OEP there is a characteristic red shift for the broad Soret band centered around 400 nm, which can be attributed to changes in molecular geometry when a Si atom is incorporated within the macrocycle (Figure 3). Differences in spectra for the Q bands were also detected, see *Supporting Information*, Appendix Figure E.3.

6.3.2. Ring-shaped Nanostructures of Si-OEP

Ring-shaped nanostructures of Si-OEP stacks were produced by altering the conditions for drying the surface mask of silica spheres. A sample was prepared with oven drying by heating a masked Si(111) substrate at 150 ˚C for 20 h and then immediately placing the dried sample into a solution of OEP and $SiCl_4$ in chloroform for 5 h. By heating the substrate for longer intervals (up to 20 h), most of the water throughout the surface was driven to evaporate, and only nanoscopic residues of moisture persisted in the water meniscus sites at the base of the particles. The shapes and arrangement of the nanorings are shown in Figure 6.4 where a few trace adsorbates of Si-OEP can be detected in areas in between the rings. Molecules of Si-OEP deposited at meniscus sites to form a ring-shaped arrangement surrounding the base of the silica spheres of the surface mask. The beads were completely removed by the steps of rinsing with sonication. The covalent attachment of Si-OEP ensured that the porphyrin film was not removed during solvent rinses, however the physisorbed silica beads were readily rinsed away to generate a nanostructured organic film, despite the annealing step.

There are about 30 nanorings within the topography image of Figure 6.4a, which scales to a surface density ~ 10^8 nanostructures/cm^2. The simultaneously acquired phase image discloses that the surrounding areas of substrate present a different surface chemistry than the areas of the nanorings (Figure 6.4b). Molecules of Si-OEP did not bind in areas without residual water, the step of heated drying removed water from regions of the substrate in between silica particles to prevent the growth of a continuous film. A close-up view of a single nanoring is shown in Figure

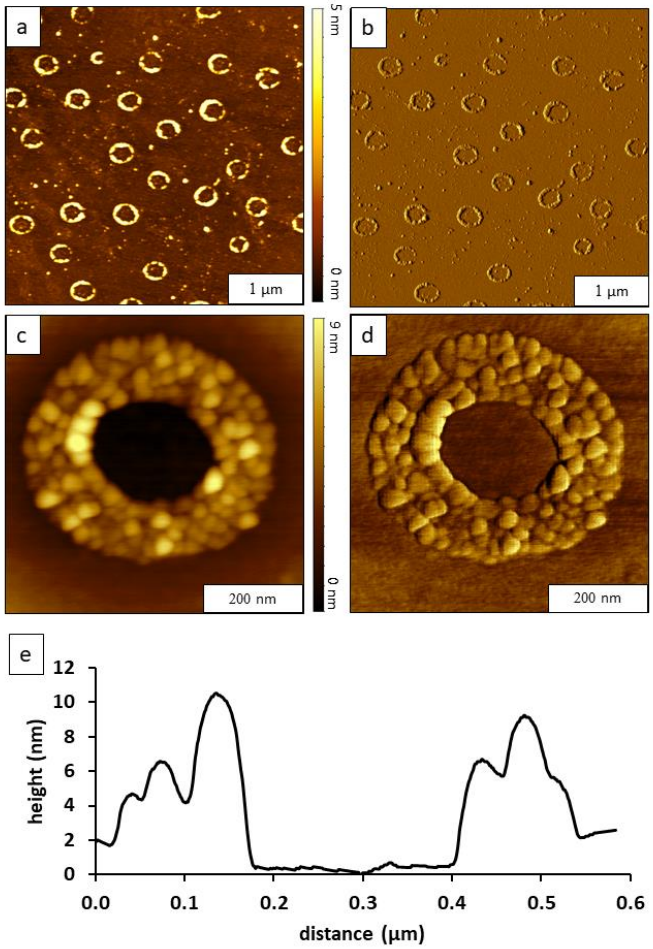

Figure 6.4. Ring-shaped nanostructures of OEP-silane formed on Si(111) by changing the drying conditions of the surface mask. The masked substrate was dried in an oven at 150°C before immersion in the reaction vessel. (a) Topography view of nanorings, 4 × 4 µm^2; (b) simultaneously acquired phase image. (c) Zoom-in view of a single Si-OEP nanoring, 600 × 600 nm^2; (d) corresponding phase image. (e) Cursor profile of the line traced in *c*. Images were acquired with tapping-mode AFM in air.

6.4c. An arrangement of round discs of Si-OEP assembled to form regular circular shapes surrounding a hole containing uncovered substrate. Insight of the fine details of the edges and shapes as well as the surface chemistry of the nanorings are mapped in the corresponding phase image (Figure 6.4d).

Attachment of Si-OEP takes place at surface sites that follow the shape of the ring-shaped deposits of the water meniscus which forms at the base of colloidal spheres of a surface mask. The size and shapes of the water meniscus areas are remarkably uniform at the nanoscale. An example cursor measurement across a single ring reveals the multilayer geometry (Figure 6.4e). The average height of the nanorings measured 6.8 ± 1.5 nm (n=50). Since there is variability in the heights of the nanorings, both a vertical and horizontal profile of 50 individual rings was acquired to generate a representative measurement. The average value of four measurement points at the top, bottom and left, right sides of the nanorings was used to gauge the height. A With colloidal lithography, the process scales up to tens of millions of surface features of similar geometry, thickness and composition. Essentially, colloidal lithography provides a means to pattern water on substrates, and molecules of Si-porphyrin bind selectively to the locations of the wetted substrate.

6.3.3. Nanodots of Si-OEP within an OTS Matrix

Nanostructures of Si-OEP were fabricated within a methyl-terminated resist layer by localizing the reaction to confined sites of nanoholes within a film of octadecyltrichlorosilane (OTS) that was prepared using an immersion step with colloidal lithography. Nanoholes within a film of methyl-terminated OTS was used to furnish nanoscopic containers for depositing Si-porphyrin. In previous studies we have successfully used OTS as a generic matrix to pattern 4-(chloromethyl)phenyl trichlorosilane,[300] polymers,[301] proteins,[302-303] rare-earth oxide nanoparticles,[304] as well as free-base and metallated porphyrins.[128]

The steps for spatially selective deposition of Si-OEP into uncovered nanoholes within an OTS film are depicted in Figure 6.5. Nanoholes of unprotected Si(111) were prepared by removing the particle mask. The sites of nanoholes were used to direct and confine the deposition and subsequent vertical layer by layer assembly of Si-OEP. In the first step, (Figure 6.5a) colloidal lithography was used to generate a template of nanoholes of uncovered substrate within a thin film

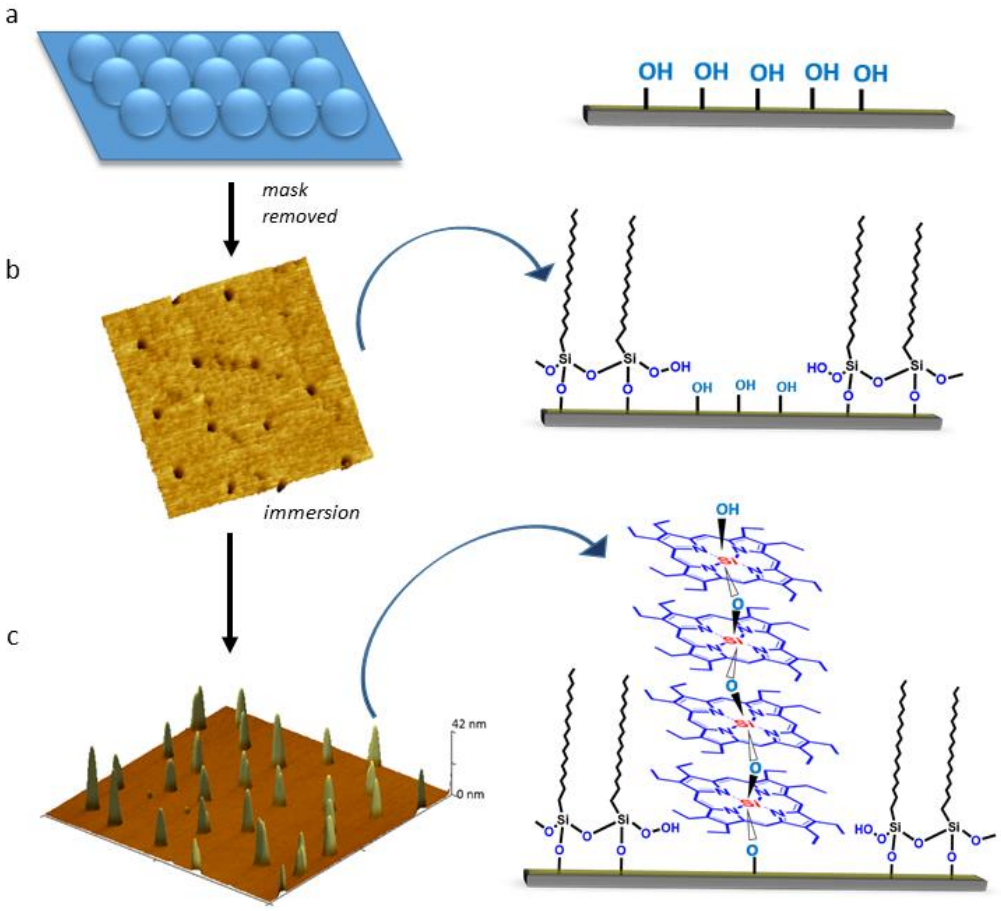

Figure 6.5. Procedure for preparing OEP nanodots within a resist film of OTS. (a) A particle mask was prepared on Si(111). The colloidal mask protected discrete circular areas from reaction when the sample was immersed in a solution containing OTS. (b) After removing the mask, substrates of nanoholes within an OTS matrix were formed. (c) After a second immersion step in the OEP single pot reaction, the substrates were removed and dried for AFM characterization to reveal (c) nanodots of OEP grown within the nanoholes.

of OTS using a surface mask of colloidal spheres. After removing the mask, (Figure 6.5b) the areas that had been protected by the spheres furnish circular sites of uncovered Si substrate which present hydroxyl groups, surrounded by a passivating layer of methyl-terminated OTS. In the final step

the substrate with nanoholes was placed into the porphyrin and $SiCl_4$ solution for a one-pot coupling reaction. After reaction, the sample was then removed and rinsed successively with chloroform and water for characterization with AFM (Figure 6.5c).

An example of nanoholes produced by immersing a colloidal mask in a solution of OTS is presented in Figure 6.6. Most of the areas of the surface are covered with a monolayer film of OTS on Si(111), however discrete holes of regular sizes are arranged throughout the sample according to the hexagonal packing of the surface mask (Figure 6.6a). A magnified view of 12 nanoholes is shown in Figure 6.6B, disclosing the highly regular shapes of the circular features. The theoretical length of OTS is 2.5 nm for an upright, fully extended orientation of the hydrocarbon backbone. The depth of the nanoholes for the OTS sample measured 2.3 ± 0.3 nm (n = 50) as shown with an example cursor profile in Figure 6.6c, which suggests that the film was fairly densely packed. The nanostructured film of OTS was used as a surface template for directing the deposition of Si-OEP for the experiment shown in Figure 6.7.

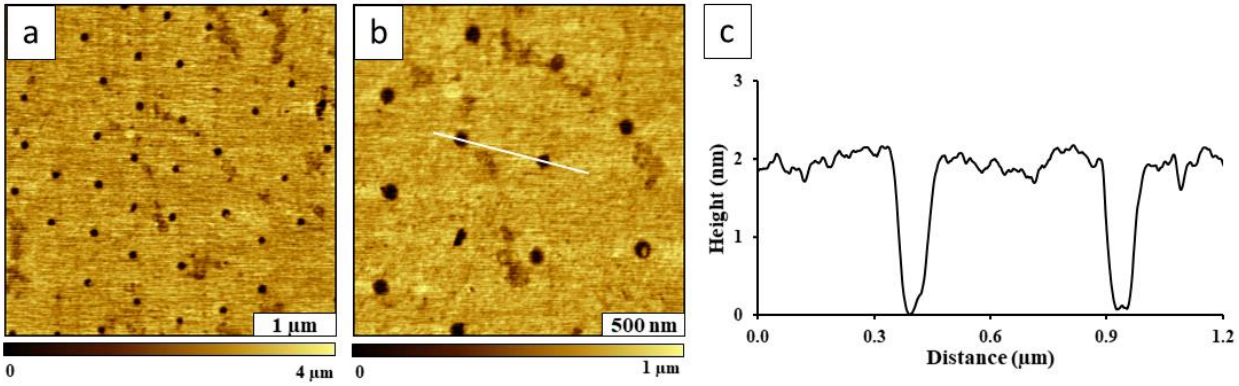

Figure 6.6. Nanoholes within a film of OTS viewed with topography frames acquired in air using tapping-mode AFM. (a) Topography view (4 × 4 µm^2); (b) Zoom in view (2 × 2 µm^2) of nanoholes; (c) cursor profile for the line drawn in *b*.

When a sample of nanoholes was submerged in a solution of Si-OEP, the porphyrins did not attach to areas of the sample protected by OTS which present methyl groups. Molecules of Si-OEP assembled on uncovered, bare areas inside the nanoholes to form nanostructures of regular shapes

and thickness, shown with representative AFM images in Figure 6.7. The time point for immersion of this example was 5 h, revealing heights that measure 6 ± 1 nm (n = 50) above the OTS matrix. In data not shown, immersion for 24 h formed taller structures measuring 6-13 nm in height. These experiments provide mechanistic clues of a layer-by-layer mode of surface assembly with Si-OEP that produces taller structures as molecules are added over time. Intermolecular Si-O-Si linkages form cofacially on the exposed face of the surface-linked porphyrins, to interconnect with the central Si atoms of the macrocycles in a skewered arrangement.

There are about 68 nanodots of Si-OEP in the topograph of Figure 6.7a, within a 6 × 6 μm^2 frame. The number of nanopatterns that can be generated is controlled by the diameter of the

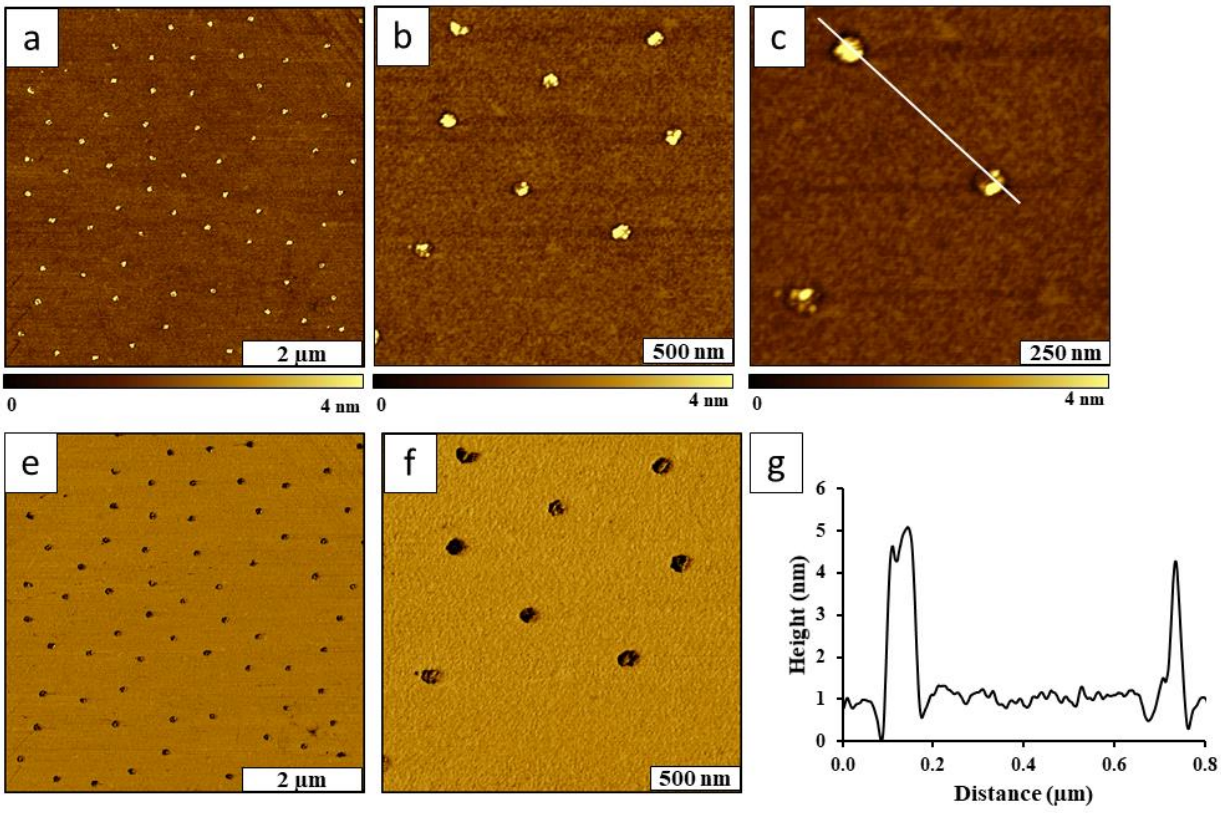

Figure 6.7. Nanodot patterns of OEP grown within nanoholes within an OTS matrix film. (a) Topography view of OEP nanodots (6 × 6 μm^2); (b) zoom-in view (2 × 2 μm^2); (c) magnified view (1 × 1 μm^2); (d) phase image acquired for *a*; (e) phase image for *b*; (f) cursor profile for the line in *c*.

particles chosen for the colloidal mask, correspondingly more structures are generated when smaller diameter spheres are used for lithography.[147, 305] The nanodots are have a hexagonal arrangement, with a periodicity that matches the diameter of the silica spheres (500 nm) used as a surface mask. Close-up views of the Si-OEP nanodots are presented in Figures 6.7b and 6.7c, revealing a morphology of multiple island aggregates packed within the nanocontainers. The clustered protrusions can also be vaguely resolved in the simultaneously acquired phase images of Figures 6.7d and 6.7e as small bumps inside the dark holes. The phase images enable sensitive detection of adsorbates in areas between the nanodots, in this example no contaminants are observed on areas of the OTS matrix film. An example cursor profile across two nanostructures is shown in Figure 6.7f, with heights measuring 5.1 and 4.3 nm, respectively.

At the nanoscale, there is some variability for the heights of the nanodots, shown in the histograms of Figure 6.8. With an immersion time of 5 h the heights above the OTS matrix ranged from 3-9 nm, with an average value of 5.8 ± 1.3 nm. With a longer immersion time of 24 h, the heights ranged from 6 to 13 nm, with an average value of 8.7 ± 1.8 nm. Example images for nanodots prepared after 24 h immersion is provided in *Supporting Information*, Appendix Figure E.4. The variability of the heights of nanodots can be attributed to slight changes in the diameters

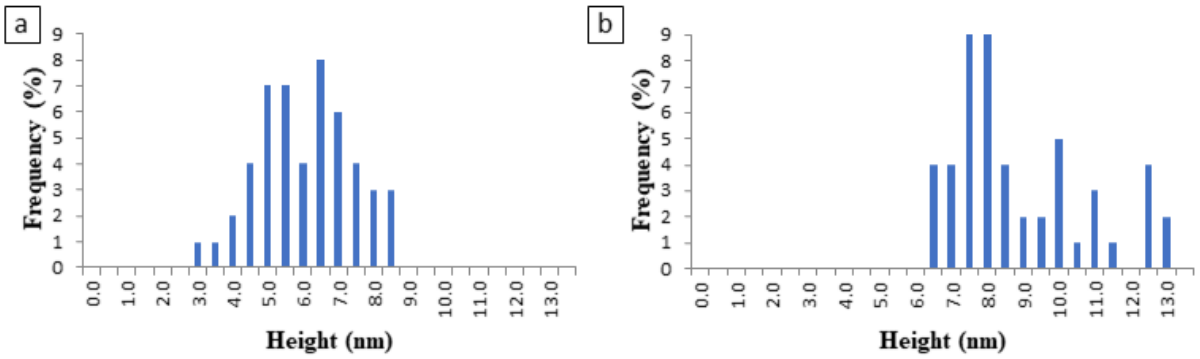

Figure 6.8. Comparison of height measurements for OEP nanodots derived from cursor profiles (A) after 5 h immersion; (B) after 24 h immersion of substrates with nanoholes of OTS/Si(111).

of the nanoholes which occur naturally from variations of particle sizes of the surface mask as well as slight surface imperfections.

6.3.4. The Role of Water in Surface Binding

The particle masks were found to effectively block molecules from depositing underneath spheres at the points of direct contact with the substrate, molecules of Si-OEP were directed to assemble at interstitial sites in between the silica beads or at meniscus sites at the wetted areas of the substrate. Organosilane nanostructures of selected morphologies can be fabricated with colloidal lithography by controlling certain experimental parameters such as concentration, immersion intervals and the drying conditions for the surface mask. In ambient conditions, a layer of water forms on surfaces; trace amounts of water initiate self-assembly of organosilanes to form a molecularly thin organic film. Through trial and error, we have learned that the nature of the substrate can influence silanization reactions. For example, with the relatively hydrophilic surface of mica, water will spread out to form a continuous layer which will correspondingly generate organic films of uniform thickness throughout areas of the sample. However, with hydrophobic substrates such as Si(111), the nature of the surface directs organosilane assembly according to the arrangement of water deposits.[306] For colloidal lithography protocols, the amount of water present on the surface can be controlled by altering the drying conditions of the masked substrate before the immersion step.[118, 307]

The key differences when comparing the surface morphology of samples of Figure 6.2 and Figure 6.4 were the drying conditions of the surface mask used for preparing samples with colloidal lithography and the intervals for immersion in Si-OEP. The process for attaching silanes to substrates requires nanoscopic residues of water on the surface; areas with thicker layers of water will furnish sites for self-polymerization to produce multilayered films. With colloidal lithography,

the locations of water on the surface define the reaction sites for attaching $SiCl_4$ and OEP. In essence, the drying step of colloidal lithography is a way to control the shapes and thickness of Si-OEP nanostructures. In ambient conditions we know that macroscopic residues of moisture form on mirrors and glass surfaces to form water films or fog. Intuitively with colloidal lithography, by drying a sample in air under ambient conditions, the entire surface would have a film of water throughout the sample, except at sites protected by the particle mask. Therefore, an ambient drying step produces a film of molecules with nanoholes in areas where the particles of the mask were removed as revealed in the example of Figure 6.2. However, when using a heated drying step for the particle mask, nanorings were produced in areas where water persisted selectively at the meniscus sites surrounding the base of the silica spheres as shown in Figure 6.4. When using silica spheres of smaller diameter, the size of the meniscus is smaller and the corresponding ring nanopatterns are smaller in size. Thus, colloidal lithography provides a tool for controlling the sites of reactions at the nanoscale, as well as providing a way to choose the geometry and spacing between patterns of nanoholes or nanorings.

6.4. Conclusions

Nanostructured films, nanorings, and nanodots of Si-OEP were patterned through covalent Si-O-Si bonds using a silane coupling reaction combined with colloidal lithography. Molecules were added over time to form multilayers, as demonstrated by measuring changes in height after increasing the time intervals for immersing silicon substrates from 5 to 24 h. With colloidal lithography, the geometry of nanostructures was affected by the drying step of preparing surface masks, which defines the placement of water residues on the surface. The nanostructures consisted of multiple strands of porphyrin stacks that assembled from the surface through a siloxane backbone attached covalently to the central Si atom of the macrocycles in a skewered arrangement.

The experimental results with Si-OEP provide a basis for developing protocols with other porphyrins and can likely be extended to phthalocyanines which have a macrocycle comprised of four isoindole groups linked by nitrogen atoms. Further directions will be to study the role of substitutions with peripheral groups, (phenyl, methyl, pyridyl, polar, nonpolar, etc.) as well as the effects of symmetry for modification of the macrocycle. Our goals are to correlate nanoscale properties (conductance, photocurrent generation) with designed surface structures of porphyrins in which the coupling between the surface and porphyrins is mediated by stable covalent interactions.

CHAPTER 7. TWO-POT SYNTHESIS OCTAETHYLPORPHYRIN ENCAPSULATED NANOPARTICLES FORMED BY Si-O-Au LINKAGES

7.1. Introduction

In recent years, nanoscience has become a popular field of research and it has been found that Au nanoparticles have many applications in photodynamic therapy,[308-310] sensors,[311-312] medical diagnostics,[313-314] electronic devices[315] and as a catalyst.[316] Au nanoparticles are particularly under the interest of such applications due to their unusual dependence of the optical and electronic properties on the particle size.[317-318] There are a number of studies for preparing three-dimensional architectures of Au nanoparticles by modifying the surface with functional molecules such as alkanethiols,[319-320] phosphines,[321] fullerenes,[322] cyclodextrins,[323] dendrimers[324] and nucleic acids.[325] Chemical binding of Au nanoparticles with molecules bearing functional moieties enhances the nanoparticle stability in aqueous media by neutralizing surface charge and preventing particle aggregations. Furthermore, it alters the electron density on the Au nanoparticles enhancing optical, electrical and photochemical properties of nanoparticles.

Several innovative strategies for preparing nanoparticles with porphyrins and phthalocyanines have been reported. Commonly, Au nanoparticles with a porphyrin or phthalocyanine-alkanethiolate coating were prepared by attaching an alkanethiolate derivative to the macrocycle.[326-332] Alkanethiolate produce ordered monolayer assembly around Au nanoparticles[333] and these attachments can be modified with other thiols through exchange reactions or by couplings.[334-335] Three dimensional conjugates of porphyrin and Au nanoparticles suppress the energy transfer quenching of porphyrin singlet excited state caused by flat Au surfaces or Au clusters.[330-331] Another advantage is that they exhibit high light-harvesting capability compared to their single molecular counterparts due to larger porphyrin coverage ratio to Au

surface and enhanced light absorptivity.[332] Therefore, porphyrin-Au conjugates are suitable in the production of efficient and low-cost organic solar cells.[326, 336]

Typically, a monodentate alkanethiol, with 3 to 11 [331, 337] or 5 to 15[326] carbon chain, is used as the spacer group to drive self-assembly of porphyrin where macrocycles vertically align on to the Au nanoparticles via a single Au-S bond per molecule. Recent advancements in this field have synthesized macrocyclic porphyrin ligands with multiple thiol derivatives that attach parallel to the Au nanoparticle surface.[338-340] Although these approaches have demonstrated successful stabilization of Au nanoparticles and enhanced photochemical properties, only a monolayer of porphyrin was formed on Au nanoparticles. Multilayers of porphyrins assembled horizontally on Au nanoparticles, with potentially increased photocurrent activity, has not been reported so far. We propose to develop protocols to encapsulate metal nanoparticles with porphyrins multilayers using strategies based on silicon coupling. The orientation of porphyrins on surfaces is determined by factors such as the nature of the peripheral substituents and their position on the macrocycle. The strategy of preparing a coplanar arrangement of octaethylporphyrin (OEP) multilayers that are mediated by covalent Si-O bonds is described in Chapter 6 of this dissertation. The same OEP-silane coupling mechanism was applied to prepare core-shell nanoparticles encapsulated with porphyrins as a route for studying the influence of molecular orientation on Au nanoparticles for photochemical properties. Verkleij et al. [341] and Lusker et al.[342] have prepared Au nanoparticles functionalized with a silane containing a thiol terminal group where binding onto Au nanoparticles is favored through thiol terminal. That happens due to the high affinity of thiol group toward Au surface compared to silane moiety. When suspended in aqueous media, bare Au nanoparticles are partially oxidized or hydroxylated by the oxygen present in solution.[343-344] These surface hydroxyl groups are ideal contact points for the silane terminals of the OEP network to bind on to the

Ausurface forming siloxane bonds in our study. As a consequence of the O-Si-O bonding motif, we predict that the linkages between molecules and substrates will be robust and will resist the effects of oxidation and heat. The silane backbone sits upright in reference to the Au nanoparticle; hence the porphyrins orient parallelly in co-facial arrangement. This novel architecture provides a model of efficient and amplified photocurrent generation from multiple macrocycles within one system. In this study, silicon coupling strategies were applied to encapsulate metal nanoparticles with porphyrins. Essentially, Au nanoparticles that are comprised of octaethylporphyrin macrocycles linked with Si-O bridges were synthesized and characterized with atomic force microscopy. The synthesis of Au nanoparticles was completed using the citrate reduction method.[345] The Au nanoparticles were encapsulated within a skewered porphyrin molecules that are centrally interconnected by covalent Si-O bonds completed using a "two-pot" reaction method.[290, 346] The cofacial arrangement of porphyrins for the coated nanoparticles is anticipated to enhance electronic and photonic properties of the nanomaterials. Particle lithography protocols were used to pattern porphyrin coated Au nanoparticles on glass substrates. Previously, Au nanoparticles have been patterned into nanodots by particle lithography.[342] In addition, Au nanorings have been formed with colloidal lithography,[135] electron beam lithography[347-348] and using a block copolymer templates.[349] Au nanoparticles encapsulated within OEP-Si network produced ring-shaped nanostructures. The prepared nanomaterials will provide a measurement platform for studies with advanced modes of AFM to enable direct comparisons of the properties of hetero-material junctions (metal-molecule-metal) implementing Si-O bonds as the "alligator" clamp.

7.2. Experimental Section

7.2.1. Materials and Reagents

VWR micro cover glass (VWR, Radnor, PA) were used as substrates. Gold (III) chloride trihydrate and trisodium citrate were both obtained from Sigma-Aldrich (St. Louis, MO). Silicon tetrachloride and 2,3,7,8,12,13,17,18-octaethylporphyrin were obtained from TCI America (Portland, OR). Size sorted silica spheres (500 nm) were obtained from Thermo Scientific (Fremont, CA). Chloroform (HPLC grade) was acquired from Fisher Scientific (Lenexa, KS). Piranha solution was prepared with concentrated sulfuric acid (98.0%) (J. T. Baker, Fisher Scientific) and hydrogen peroxide (30%) (British Drug Houses, VWR). Ethanol, 200 proof was obtained from Deacon Labs (Prussia, PA). Milli-Q type 1 water, (18 megohms, Millipore, Bedford, MA) was used to form water for rinsing steps.

7.2.2. Synthesis of Au Nanoparticles

The citrate-reduction protocol for synthesizing Au nanoparticles was followed as published previously.[350] An aliquot of 125 mL solution of 0.25 mM gold chloride was boiled under reflux for approximately thirty minutes at 300° C in a round bottom flask. An aliquot of 6.25 mL solution of 40 mM trisodium citrate was then added to the Au solution. Within ten minutes, the solution transformed from clear to a rose-pink color. The solution was removed from heat and stirred at room temperature for about thirty minutes.

7.2.3. Synthesis of Au Nanoparticles Encapsulated with Silane-Coupled OEP

The protocol was adopted from the previously reported method.[3, 351] A solution of 0.5 mM OEP (5 mL) was mixed with 5 μL of silicon tetrachloride in chloroform. The mixture was stirred for five minutes, followed by the addition of a 1 mL aliquot of Au nanoparticles. Stirring was continued for 24 h.

7.2.4. Particle lithography of Au nanoparticles encapsulated with silane coupled OEP

A procedure for preparing arrays of Au nanoparticles was developed with particle lithography on glass substrates. This helps to avoid obtaining clusters of nanoparticles on surfaces due to self-aggregation. A suspension of 400 μL of silica spheres and 600 μL ultrapure water was centrifuged at 20 000 rpm for 10 min. The supernatant was removed and the pellet was resuspended in 1 mL water. These steps were repeated three times. The pellet of the final centrifugation step was resuspended in 200 μL of ultrapure water. An aliquot of this suspension (20 μL) was deposited on glass substrates creating a surface mask of silica spheres. Glass substrates were cleaned with piranha solution: a mixture of hydrogen peroxide and sulfuric acid with a (v/v) ratio of 1:3, by immersing for 1.5 h. (Caution this solution is highly corrosive and should be handled with care). The sphere mask was dried for 3 h. The substrates were then kept in the oven at 150° C for 24 h to anneal silica spheres. The substrates were removed from the oven and cooled down to room temperature. A solution of Au nanoparticles coupled with OEP (10 μL) was deposited carefully on top of the masked glass substrate and then samples were dried in air for approximately 120 h. The glass samples were cleaned by sonicating in ethanol for 10 min. Lastly, the samples were dried with a stream of nitrogen gas for evaluation of samples with atomic force microscopy (AFM).

7.2.5. Atomic Force Microscopy (AFM)

An Agilent Technologies AFM 5420 (Santa Clara, CA) in tapping-mode was used to characterize samples. Tapping-mode AFM images were acquired with silicon AFM probes (Budget Sensors, PN Tap300Al-G) with an aluminum reflex coating. The average resonance frequency and the force constant of the probes were 300 kHz and of 40 N/m respectively. Gwyddion software (Version 2.52) was used for analysis and digital processing AFM images.[181]

7.2.6. UV Visible Spectrophotometer

A Cary 50 Bio UV Visible Spectrophotometer was used for acquiring UV/Vis spectra.

7.3. Results and Discussion

7.3.1. Synthesis of Au Nanoparticles Encapsulated within OEP Coupled via Silane

We have conducted experiments for linking porphyrins with Si- O-Si skewers to Si(111) using a free base porphyrin that contained eight ethyl groups at pyrrole positions of the macrocycle in Chapter 6. A representation of silane coupling into the center of OEP macrocycle followed by attaching Si-OEP on to Au nanoparticle is shown in Scheme 7.1. To prepare core-shell nanoparticles, a solution of Si-OEP was prepared by mixing OEP and $SiCl_4$ in chloroform. A portion of nanoparticles was added with mixing to this mixture. When $SiCl_4$ is mixed with OEP, a shish "kebob' configuration of cofacially aligned OEP is formed through Si-O bridges directly coordinated to the center of macrocycles. Each of these networks contain free hydroxyl groups at

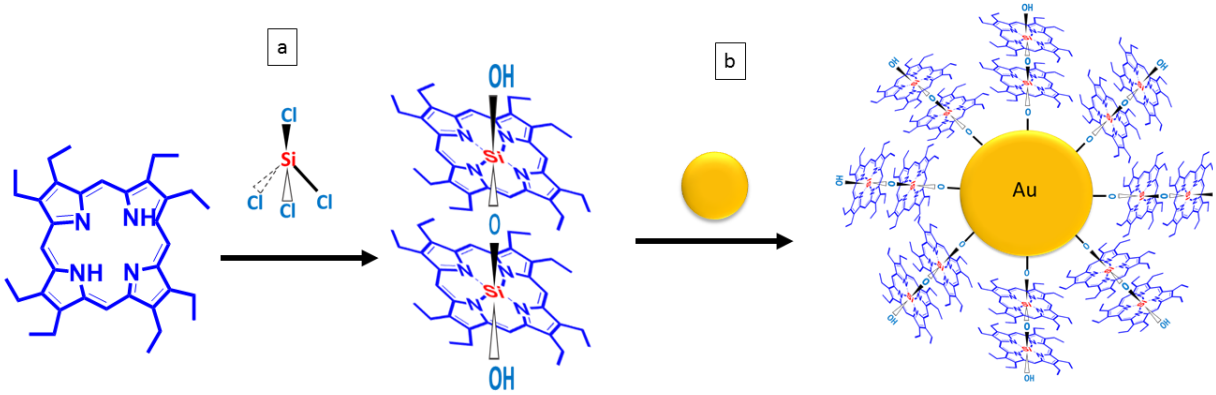

Scheme 7.1. (a) The coordination of silicon tetrachloride to the macrocycles of the porphyrin, (b) encapsulation of Au nanoparticles within Si-OEP network.

the two terminals. These hydroxyl groups facilitate Si-OEP networks to form surface linkages with hydroxyl groups on Au nanoparticle surface through hydrolysis reaction forming Au nanoparticles encapsulated within porphyrin layers. The significance of the new material is that

the molecules form a shell surrounding the metal nanoparticles in which the macrocycles are oriented in a coplanar fashion following the curved geometry of the central core, analogous to an antenna.

A visible color changes are apparent in each reaction mixture during the preparation of Au nanoparticles encapsulated within Si-OEP (Figure 7.1). A solution of OEP in chloroform is red in color and it changes to a pink color after $SiCl_4$ coordination. Solution color turns to deep red when OEP is bound to Au nanoparticles. UV/Vis spectra of each solution were obtained as shown in Figure 7.1, dilutions were conducted as necessary to optimize absorbance values in a similar range.

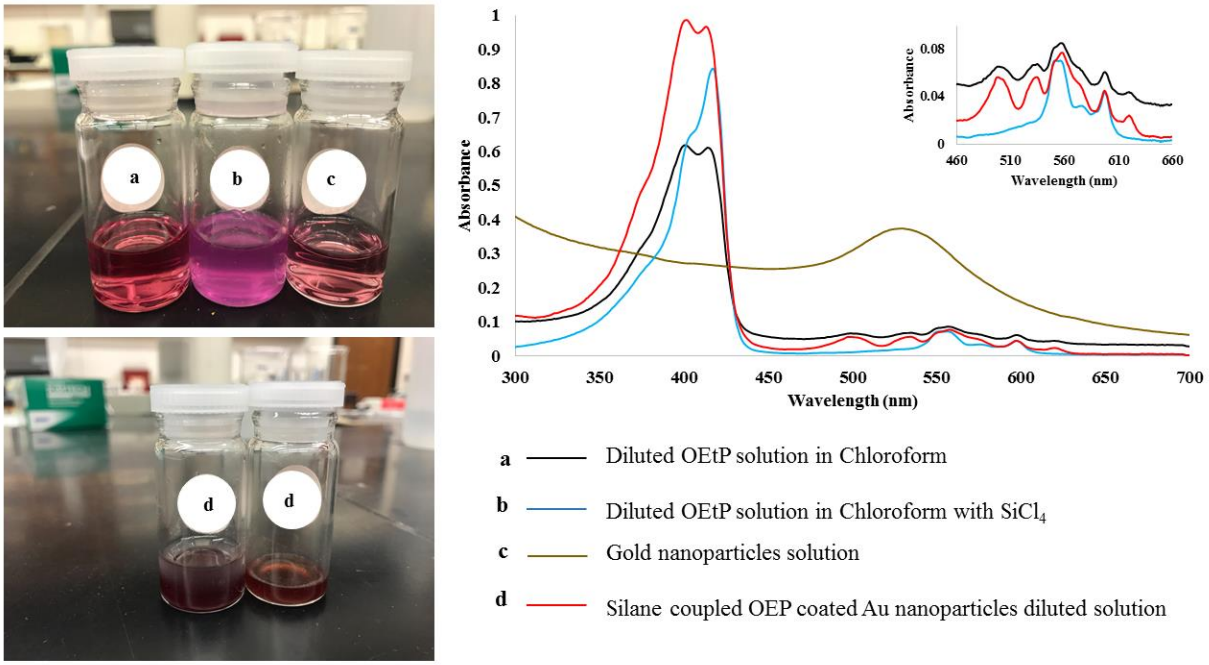

Figure 7.1. Left side: Photographs showing color changes of each reaction mixture (a) OEP solution; (b) OEP solution after adding silicon tetrachloride; (c) Au nanoparticle solution; (d) solution of Au nanoparticles encapsulated within OEP. Right: UV/Vis spectra of each reaction mixture.

A peak shift was detected between for the broad Soret band around 400 nm, as well as for the four characteristic Q bands between 500 and 600 nm in UV/Vis spectra of OEP solution after addition of the silane.[290, 330] This is because the geometry of OEP is changed when Si is inserted

into the macrocycle, and further structural changes occur as the molecules are bound to Au nanoparticles. Analysis with UV/Vis spectroscopy shows that the peak for the Au nanoparticles was consistent with previously published spectra which normally lies in the range of 520 and 580 nm.[352] However, the UV/Vis spectra of Si-OEP coated Au nanoparticles hardly show the corresponding Au peak around 540 nm and rather an identical spectra, with increased absorbance, to blue line which was given by the solution of absorbance of Si-OEP moiety is observed with the red line in Figure 7.1. The reason for this is unknown at the moment. Further experiments need to be conducted by tuning concentration ratio of Au nanoparticles to Si-OEP to study this phenomenon as to why this occurs and how to achieve the correct stoichiometry between coating molecules to nanoparticles.

7.3.2. Tapping-Mode AFM Characterization uncoated Au Nanoparticles

A range of sizes was observed for the nanoparticles when a drop of the nanoparticles was placed on a glass slide and dried for AFM studies. The brighter spots in the tapping mode topography frames (Figure 7.2a and 7.2b) reveal the dispersity individual nanoparticles on the glass substrate. A size range of 1 nm to 2 nm for synthesized Au nanoparticles was measured with the cursor profile (Figure 7.2c). This height information was used as the reference to study the overall size change of nanoparticles after encapsulating within Si-OEP network. Corresponding phase images (Figure 7.2d and 7.2e) acquired with tapping mode locate positioning of Au nanoparticles immobilized on a glass substrate.

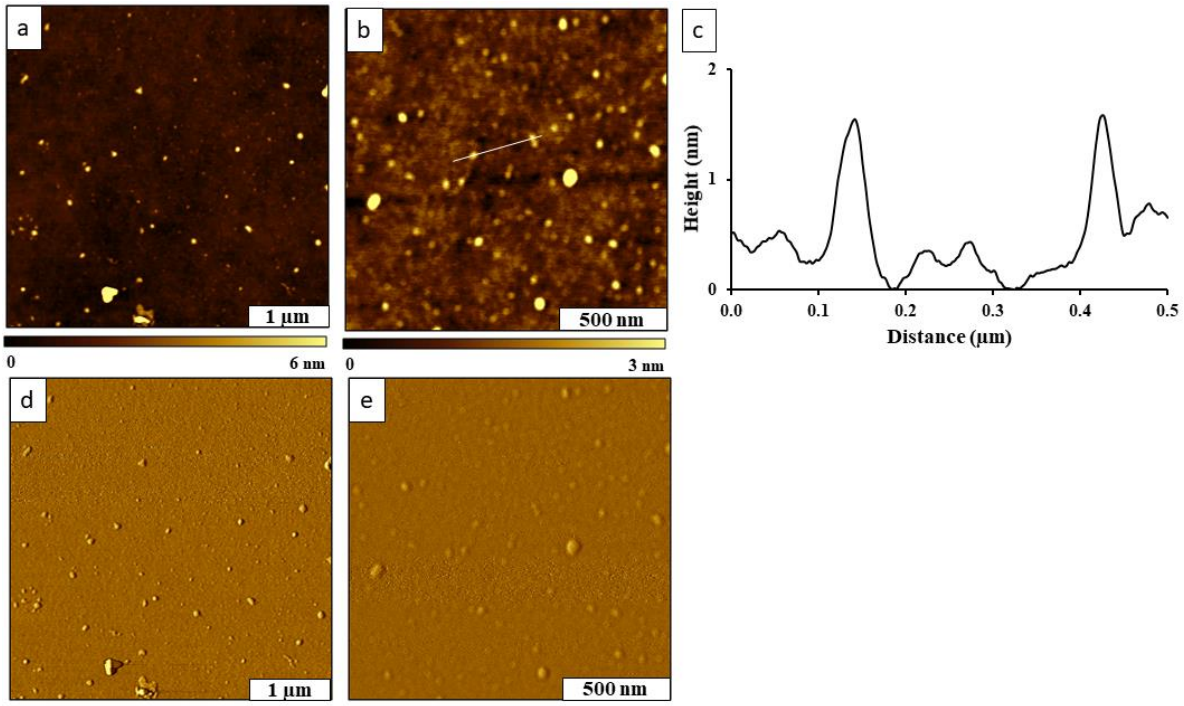

Figure 7.2. Au Nanoparticles deposited on glass. Images were acquired using tapping-mode AFM. (a) Topography image (4 × 4 µm^2); (b) corresponding phase image of *a*; (c) higher magnification topography image (2 × 2 µm^2); (d) corresponding phase image for *c*;(e) cursor profile for the white line drawn in *c*.

7.3.3. Particle Lithography with Au Nanoparticles

The basic idea for particle lithography was to prepare a surface mask of 500 nm silica spheres as a surface mask, and then add a drop of a sample containing Au nanoparticles to organize surrounding the beads of the template (Scheme 7.2). Typically, samples of dilute

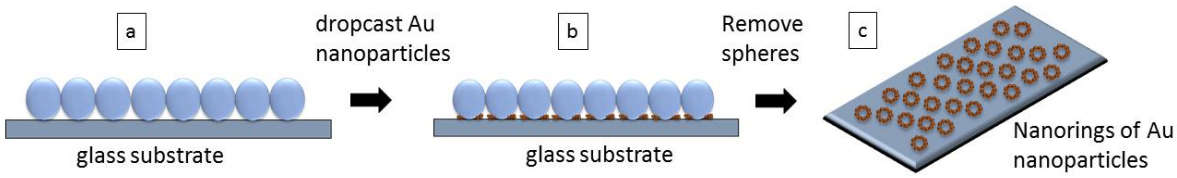

Scheme 7.2. The process of forming rings of nanoparticles around silica spheres using particle lithography. (a) Silica sphere mask was prepared on a glass substrate; (b) after Deposition of Au nanoparticle suspension; (c)once the spheres are rinsed away from the substrate, rings of nanoparticles persist in an organized pattern.

solutions of nanoparticles are dried on a substrate for AFM characterizations. However, with naturally dried samples, self-aggregation to form dense, close-packed clusters. This approach can be problematic for resolving individual nanoparticles. Colloidal patterning can be applied to generate uniform ring arrangements of nanoparticles. As the solution evaporates after a drop of nanoparticle solution is deposited onto the hexagonally ordered silica sphere mask, the capillary action drags smaller nanoparticles into the regions with less solution level. Since the diameter of the nanoparticles is very smaller (50 to 100-fold), individual particles get packed in the regions around the meniscus of the silica spheres forming a ring shape.

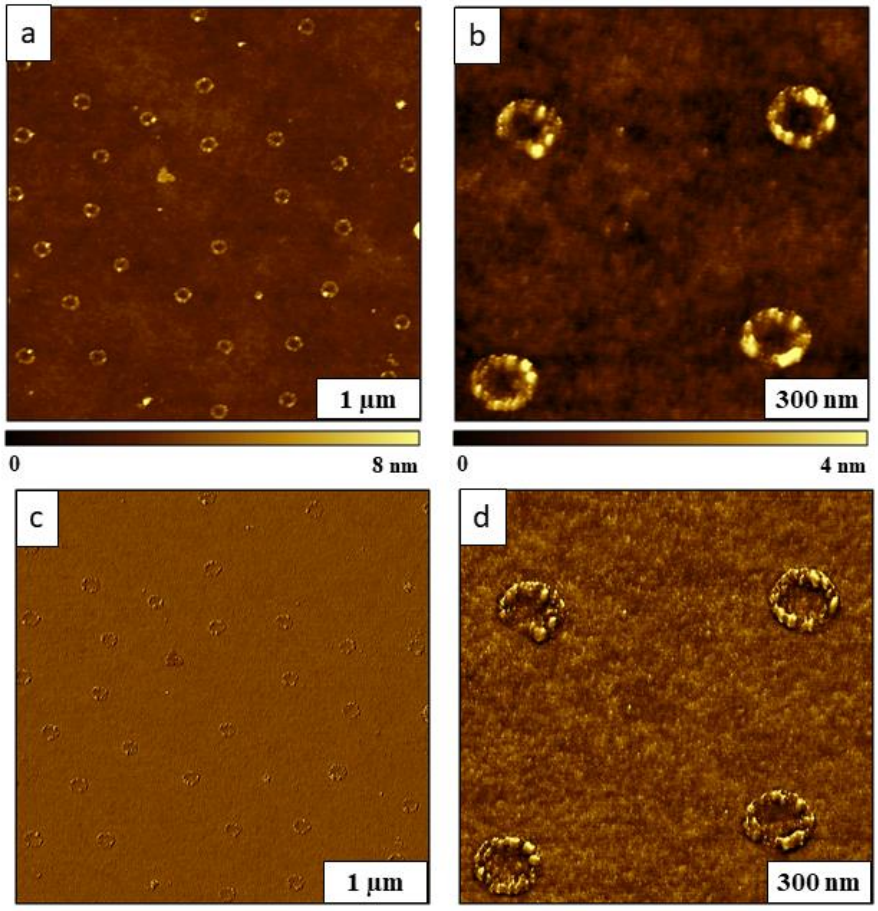

Figure 7.3. Ring arrangements of Au nanoparticles prepared with particle lithography. Images were acquired using tapping mode AFM in ambient air. (a) Topography image (4 × 4 μm^2); (b) zoom-in topography image (1.2 × 1.2 μm^2); (c) phase image for *a*; (d) phase image for *b*.

Example results for samples of bare nanoparticles patterned using particle lithography are shown in Figure 7.3. The smaller nanoparticles of Au attach to the surface surrounding the larger spheres. The result is an arrangement of rings of Au nanoparticles that surround the circumference of the silica particles as shown in Figures 7.3a and 7.3b. Since the silica particles have a diameter of 500 nm, this is the distance in between each ring. The ring shapes are more clearly distinguishable in the phase images of Figures 7.3c and 7.3d.

The morphology of a single ring formed by bare Au nanoparticles as viewed with tapping mode AFM in topography and phase channels is shown in Figure 7.4. As the liquid evaporated during drying, Au nanoparticles have localized in the meniscus area of colloidal spheres forming a ring structure with 200 nm diameter. An average height of 2.4 ± 0.7 nm (n =50) was measured for uncoated Au nanoparticles with height data gathered from cursor profiles. One example cursor profile is shown in Figure 4c. (Figure 7.4c)

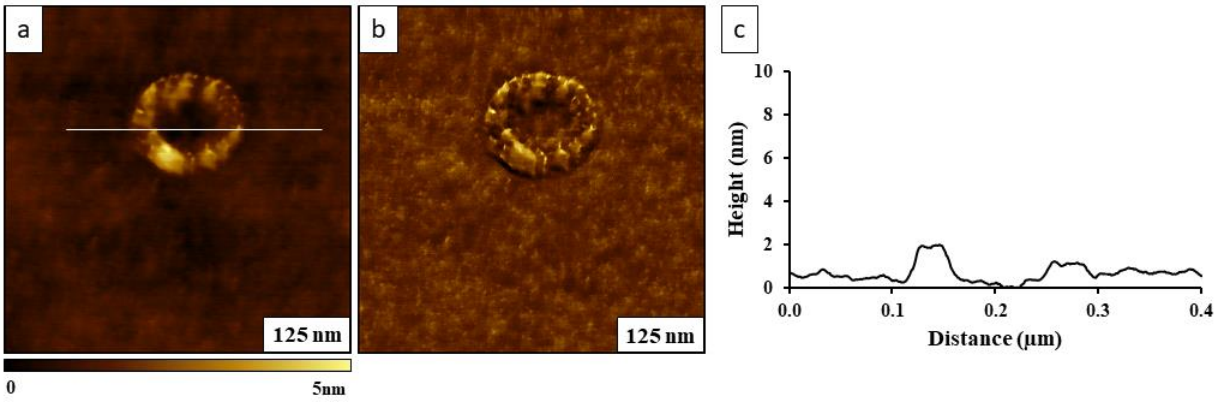

Figure 7.4. A single nanoring formed with Au nanoparticles (a) topography view (500 × 500 nm^2) of; (b) corresponding phase image; (c) height profile for the line on *a*.

7.3.4. Tapping-Mode AFM Characterization of Si-OEP encapsulated Au Nanoparticles

After attaching OEP by reaction with silicon tetrachloride, a sample of the Si-OEP nanoparticles was characterized with tapping-mode AFM. In Figures 7.5a and 7.5b, AFM images show surface views of a random arrangement of Au nanoparticles encapsulated with Si-OEP that

were deposited on glass substrates. The cursor profile (Figure 7.5c) shows a height of 2-3 nm, which is taller than the measurement for bare Au nanoparticles (1-2 nm). The height increase is evidence that the encapsulation was successful. The true gauge of whether OEP was linked to metal cores is revealed in the concurrently acquired tapping-mode phase images (Figures 7.5d and 7.5e). Phase images can sensitively detect areas with differences in elastic response between the core of the Au nanoparticles and the surrounding soft porphyrin coating. In this example, the molecular shell is much softer than the central Au core, and therefore we see a bright halo surrounding every particle in the frame. This suggests that a multilayer coating has formed which has sufficient thickness to be detectable with a tapping AFM probe.

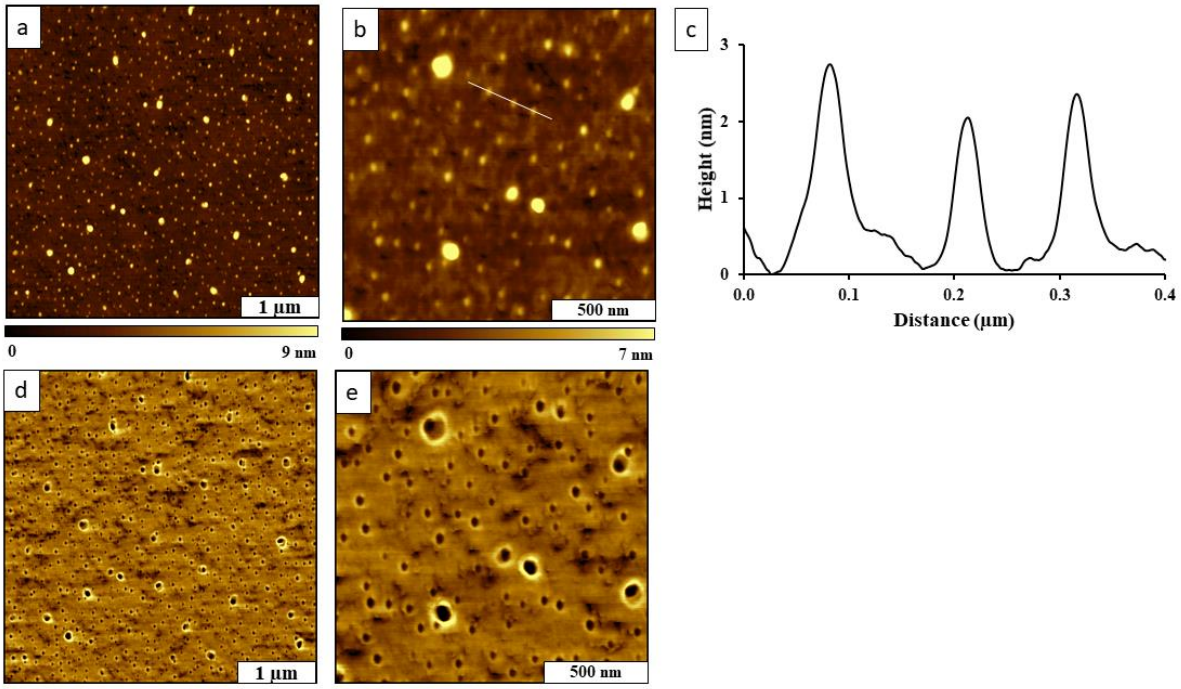

Figure 7.5. Au nanoparticles encapsulated with Si-OEP prepared on a glass substrate by drop-deposition. (a) Topography image (4 × 4 μm^2); (b) magnified topography image (1.5 × 1.5 μm^2); (c) cursor profile for the line in *c*; (d) Phase image corresponding to *a*; (e) Simultaneously-acquired phase image for *b*. Images acquired using tapping-mode AFM in air.

7.3.5. Particle Lithography with Si-OEP Encapsulated Au Nanoparticles

In Figure 7.6, the set of AFM images show the results for preparing nanorings of Si-OEP encapsulated Au nanoparticles using particle lithography. The topography frames show a

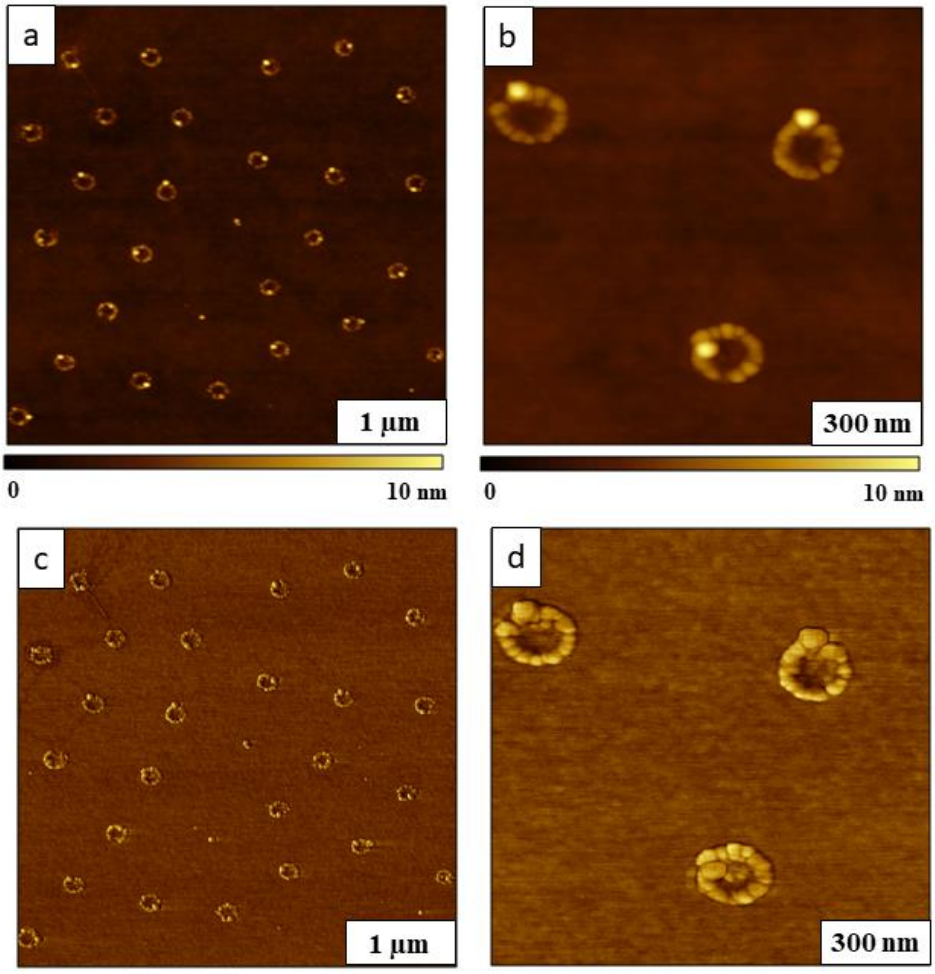

Figure 7.6. Nanorings of Au nanoparticles encapsulated with Si-OEP prepared on a glass substrate by drop-deposition prepared with particle lithography. Images acquired using tapping-mode AFM. (a) Topography image (4 × 4 μm^2); (b) Topography image (1.2 × 1.2 μm^2); (c) phase image of *a*; (d) corresponding phase image to *b*.

hexagonal arrangement of rings that follow the periodic arrangement of silica spheres of the surface mask. The spacing between the rings is precisely 500 nm, which is the diameter of the silica spheres used for patterning. We assume that the localization of Si-OEP/Au nanoparticles at the meniscus sites is facilitated by two factors as compared to bare Au nanoparticles. One is the

capillary forces arise with the evaporation of the solvent. The second factor is the free hydroxyl groups present at the Si-OEP shish "kebob" at the opposite end to the OEP-Au attachment. These free hydroxyl groups are attached to a silicon atom, essentially a silane backbone. The silane can self-assemble onto glass substrate via forming siloxane bonds. Therefore, the covalent Si-O-Si bond with the substrate facilitates the nanoring forming in the case of Au nanoparticles encapsulated within Si-OEP.

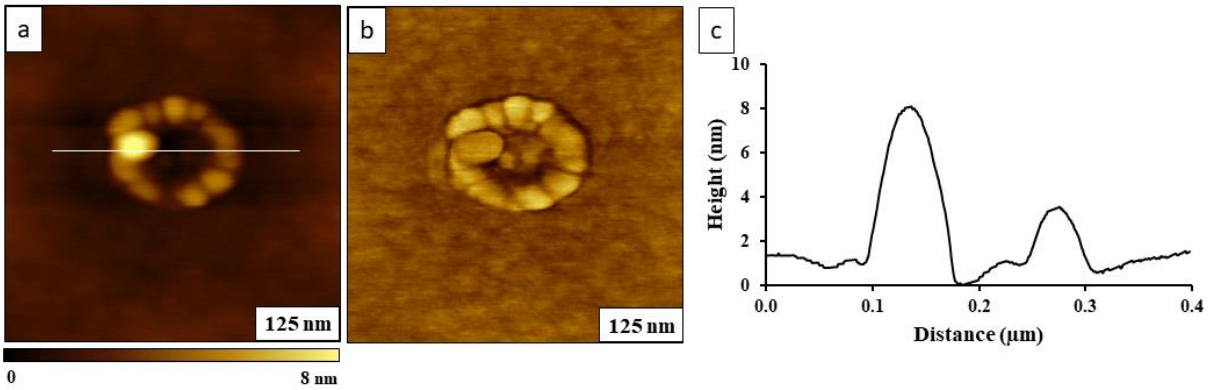

Figure 7.7. A view of a single ring formed with Si-OEP coated Au nanoparticles (a) topography view (500 × 500 μm^2); (b) corresponding phase image; (c) height profile for the line on *a*.

An individual nanoring formed with Si-OEP coated Au nanoparticles is in Figure 7.7. The topography and phase images in figures 7a and 7b show domains of isolated nanoparticles. The lateral dimension of an individual domain is much larger compared to the surrounding Si-OEP molecules. The occurs as a tip convolution effect when the aspect ratio of the AFM tip is not sharp enough to provide molecular resolution. In this example, the AFM images reveal that the overall size of the nanoparticles has increased to 7.7 ± 1.6 nm (n =50) evidencing nanoparticles have been successfully encapsulated with Si-OEP.

7.4. Conclusion

Au nanoparticles were successfully synthesized and encapsulated with octaethylporphyrin using a silane coupling reaction. A range of sizes was observed for the nanoparticles in the

topography frame, however the true gauge of whether OEP was linked to metal cores is revealed in the concurrently acquired tapping-mode phase image. Particle lithography was applied to prepare nanostructures of Au nanoparticles encapsulated in octaethylporphyrin. After imaging, a height increase was observed after encapsulation of the Au nanoparticles. Further evidence that encapsulation of nanoparticles with Si-OEP was successful can be readily detected by observing shifts in Soret and Q bands using UV/Vis spectroscopy. The absorption bands in systems of porphyrins arise from electronic transitions between the HOMOs and LUMOs for pi-pi transitions of the macrocycles. Structural changes of the central atom caused by attaching Au nanoparticles affect the transition energies profiled in absorbance spectra providing a band shift. Future experiments are planned to test this approach with nickel, iron or silver nanoparticles, as well as using other porphyrin and phthalocyanines for the coatings. Advanced AFM modes such as current-sensing AFM and conductive probe microscopy will be applied to study the changes of photocurrent happen after attaching Au nanoparticles to Si-OEP architectures. The coated nanoparticles will be patterned with particle lithography on conductive substrates for these studies. Another aspect of developing these new materials is to investigate the possible application of Si-OEP/Au nanoparticles to design heterojunction thin-film solar cells on semiconductor substrates.

CHAPTER 8. CONCLUSIONS AND FUTURE WORKS

8.1 Conclusions

Investigations of the dissertation focused on the design, synthesis and characterization of nanostructures, organic thin films and nanoparticles using measurement and imaging modes of scanning probe microscopy (SPM). A key strategy was to prepare well-defined nanostructures for controlling the arrangement of nanomaterials on surfaces using scanning probe lithography (SPL) and chemical approaches with particle lithography. Local information of the detailed morphology and physical characteristics of nanostructures were characterized in real space using advanced modes of atomic force microscopy (AFM) with exquisite resolution. Test platforms of organothiols, organosilanes, porphyrins, aryl thin films, Ni and Au nanoparticles were prepared with high throughput using particle lithography, which enabled multiple, replicate measurements of surface features with reproducible dimensions.

Periodic arrangements of nickel nanorings were fabricated by electroless deposition of nickel onto organosilane nanorings that had been prepared with immersion particle lithography. Control of the dimensions of surface features, such as the thickness, spacing, and shape of composite nickel/palladium nanorings was accomplished with protocols of immersion particle lithography. Sensitive mapping of magnetic areas of nickel nanopatterns prepared on Si(111) was conducted with magnetic sample modulation (MSM) combined with contact mode AFM. The MSM-AFM mode provided detailed maps of the location and vibrational response of Pd and Ni nanorings specifically with respect to differences in the amplitude and phase of sample vibration-actuated by an external electromagnetic field. For the MSM-AFM set-up, a non-magnetic AFM probe is used to detect sample vibration. Dynamic measurements were obtained for samples by incrementally ramping either the magnetic field strength and driving frequency parameters.

Molecular-level studies of chemical and physical processes at vapor/solid interfaces that are attributable to water and surface wetting phenomena were completed. Experiments were designed to capture molecular-level events that occur after the self-assembly of organosilanes on wetted surfaces. The research focus targeted understanding the detailed molecular mechanisms which govern the hydrolysis and condensation reactions of trifunctional organosilanes with model surfaces of mica and Si(111). The role of water is known to initiate reactions of organosilanes to form crosslinked films, however, our understanding of the overall complex molecular mechanism of surface self-assembly is incomplete. Nanolithography approaches with particle lithography furnished a practical surface platform for studying events after the deposition and reaction of vapor-phase water and heated organosilane vapor which assembled on model hydrophobic and hydrophilic surfaces.

Surface characterizations of molecularly thin films synthesized with aryl halides grafted onto Au(111) surfaces via photoredox catalysis were accomplished using measurements with AFM and nanofabrication protocols. The thickness of thin films of photografted radicals was measured using particle lithography to form nanoholes in the film. The film thickness was derived by referencing uncovered areas of the substrate as a baseline. Likewise, nanoshaving experiments in ethanolic media provided information about how strongly the molecules adhered to the gold substrate. Information about the role of photocatalyst and the reducing agent in a photografting experiment was obtained by *ex situ* AFM characterization of samples after photografting reactions were completed.

New films and nanomaterials with porphyrin and phthalocyanine chromophores were synthesized, which are covalently bound by Si-O-surface linkages coordinated to the centers of the macrocycles. Incorporating a central Si atom within the chromophores will impart interesting

and tunable electronic and photonic properties to nanomaterials because of the capability for skewering chromophores together in a "kebob" arrangement. Bonds of Si-O are suitable for forming robust, covalent bridges to substrates such as silicon wafers, glass, mica, and metal oxides. Likewise, the macrocycles of porphyrins and phthalocyanines can be linked together by hydrolysis and condensation steps to form chains. Crystals of porphyrins and phthalocyanines have been broadly used for electronic LCD displays and are integrated in the designs of photovoltaic cells such as dye-sensitized and bulk heterojunction organic solar cells. The organic films within such devices are formed with crystal aggregates of planar molecules which are held together mainly by electrostatic interactions and pi-pi stacking. Our design for new thin film materials and core-shell nanoparticles placed Si-O spacers between macrocycles to generate a discrete geometric configuration such that the macrocycles is precisely arranged in a coplanar orientation relative to the surface. Results were presented for making films and coated nanoparticles with octaethyl porphyrin.

The AFM studies of this dissertation provide insight into the complexity of surface-assembly reactions as well as routes for preparing metal and organic nanostructures. Experiments with particle lithography were used to evaluate reaction outcomes at the solid interface. Protocols with particle lithography and SPL can be applied for studies with both solution and vapor phase reactions to gain information of size-dependent scaling of chemical and physical properties of nanomaterials and thin films.

8.2 Future Directions

In future directions, composite nanopatterns containing two or three different metals will be studied using MSM-AFM. Can the MSM approach be used to differentiate between different metals of a mixture? Thus far, nickel nanorings were evaluated with MSM, however magnetic

nanostructures with of a mixture of metals will be constructed and characterized to evaluate the sensitivity of MSM. Since the atomic nature of the element determines magnetic character, therefore differences in magnetic susceptibility in ambient conditions should be sensitively resolved with MSM-AFM. Nanostructures can be constructed with Fe, Au and Ni for studies, extending the ELD nanofabrication protocols combining particle lithography to other magnetic elements. A common trend for studies of the synthesis and characterization of metal nanostructures is to evaluate morphology and size dependent plasmonic properties.[353-354] The plasmonic resonance characteristics of metal nanorings will be further studied in our future experiments.

Experimental studies with *ex situ* AFM were used for tracking water distribution at the vapor/solid interface using organosilanes as marker molecules which localize in areas with water deposits. Further studies will be designed to investigate the effects of molecular endgroups (methyl, mercapto, amino, hydroxyl, etc.) for sequestration of water. We hypothesize that the architectures selected as the functional head groups of organosilanes for experiments will considerably influence the outcome of experiments. Water can be attracted by the free endgroups of organosilanes over fairly long distances. The hydrophilicity of the headgroups likely may serve to sequester water for localizing reactions to confined regions of a model surface. Current experimental data provide the groundwork for designing predictive models with molecular dynamics simulations. Water structure and dynamics at the solid-vapor interface will be studied with a series of atomistic molecular dynamics simulations as a function of changing hydrophilicity of the substrate. Another set of simulations will be carried out to examine the interfacial structure of aqueous solution of water near the spherical particle substrates. The third set of simulations will examine the solvation of organosilanes attached to different substrates as a function of headgroup composition. For each system, studies will be designed to quantify the effects of changing water

concentration on interfacial properties including wetting and surface ordering. Further physical experiments will also be conducted at the liquid/solid interface, by immersing wetted substrates into solutions containing selected organosilanes.

Several future experiments will be conducted to evaluate reaction outcomes at the interface resulting from coaxially oriented porphyrin macrocycles in a skewered arrangement. Specifically, measurements of molecular orientation and material properties will be accomplished with collaborative studies with LSU physics department to use synchrotron facilities at CAMD for photoemission spectroscopy (PES), X-ray photoelectron spectroscopy (XPS) and NEXAFS characterizations. At the molecular level, the electronic and photonic properties of materials are derived from surface orientation and molecular arrangement. To broaden the scope of analysis and to obtain a molecular level understanding of chemical structures and processes, the "kebob" strategy will be tested with other porphyrins such as tetraphenyl porphyrin (TPP) and tetrapyridyl porphyrin as well as with macrocycles of phthalocyanines. Physical measurements of electronic conductance and photocurrents with advanced modes of scanning probe microscopy for synthesized films and nanoparticles. The effect of systematic changes in molecular associations with selected macrocycles (i.e. functional substituents, type of molecule) will be tested and correlated with the associated electronic and photonic properties. Studies will be accomplished with nanoparticles and films using conductive probe atomic force microscopy (CP-AFM) and photocurrent AFM according to the nature of the substrate. The main target will be to find the structures and configurations which generate photocurrents, building on the wealth of information already published for porphyrins and phthalocyanines.

The future research plans for photografting of aryl halides will be to test protocols for filling nanoholes within aryl thin films with *n*-alkanethiol molecules. Exposed areas of gold are

available for self-assembly reactions with a second molecule, such as *n*-alkanethiols. Nanostructures of *n*-alkanethiols that form in the exposed sites of nanoholes provide capabilities to compare morphology and thickness side-by-side with photografted aryl films. The thiol nanostructures can be further characterized using advanced AFM modes such as force modulation microscopy. The FMM mode is used to sensitively characterized the mechanical properties of samples, such as elastic response and viscoadhesion. Changes in elastic response can be used to distinguish materials with differing composition.[71] The mechanical properties of photografted aryl thin films and nanopatterns will be examined with FMM.

A further research direction will be to use chemical force microscopy (CFM) to study organic thin films prepared by photografting. For CFM, a functionalized AFM tip is used to evaluate the chemical nature at the interface of a sample. Maps of chemical interactions between an AFM tip and the sample can be sensitively visualized. The AFM tip can be coated with organic molecules with selected functional groups to provide chemical sensitivity.[355] In previous reports, CFM has been applied for studying interactions between SAMs with selected terminal functional groups coated on the probe and the surface.[356] In future research direction, functionalized AFM tips can be used to investigate chemical changes at the interface of different types of photografted aryl thin films. Protocols could also be developed to functionalize AFM tips by photografting aryl thin films onto AFM probes using visible-light photografting.

8.3 Synopsis

Surface investigations with SPM can provide molecular-level details of the associated size-dependent electronic, magnetic and photochemical properties of nanomaterials. Such studies help to further our fundamental understanding of the molecular designs which govern the electronic and photophysical behavior of molecules and nanomaterials, which are already used for

commercial applications. Our studies provide insight of how the surface arrangements of inorganic and molecular assemblies that are coordinated to a surface influence the overall properties of the materials. Innovative strategies which apply physical experiments will be needed to fully understand the complexity of the surface-assembly reactions as well as the structures of the materials that are generated. At a fundamental level, the electronic and photonic properties of materials are derived from surface orientation and molecular arrangement. Measurements of molecular orientation and material properties are planned with collaborative studies in the chemistry and physics departments at LSU using scanning probe microscopy (SPM) and radiation-based spectroscopies.

REFERENCES

1. Kuruppu Arachchige, N. M. K.; Chambers, P. C.; Taylor, A. M.; Highland, Z. L.; Garno, J. C., Nickel Nanofilms Electrolessly Deposited on Organosilane Nanorings and Characterized by Contact Mode AFM Combined with Magnetic Sample Modulation. *ACS Appl. Nano Mater* **2019**.

2. Kuruppu Arachchige, N. M. K.; Revati, K.; Garno, J., Heterogeneous Assembly of Water from the Vapor Phase – Physical Experiments with Binding Trifunctional Organosilanes at the Vapor/Solid Interface. *Langmuir* **2019,** *Submitted*.

3. Chambers, P. C.; Kuruppu Arachchige, N. M. K.; Taylor, A. M.; Garno, J. C., Surface Coupling of Octaethylporphyrin with Silicon Tetrachloride. *ACS Omega* **2019,** *4* (2), 2565-2576.

4. Binnig, G.; Rohrer, H., Scanning tunneling microscopy. *IBM J. Res. Dev.* **2000,** *44* (1.2), 279-293.

5. Binnig, G.; Quate, C. F.; Gerber, C., Atomic Force Microscope. *Phys. Rev. Lett.* **1986,** *56* (9), 930-933.

6. Lu, W.; Zeng, K., Characterization of local electric properties of oxide materials using scanning probe microscopy techniques: A review. *Funct. Mater. Lett.* **2018,** *11* (05), 1830002.

7. Serri, M.; Mannini, M.; Poggini, L.; Vélez-Fort, E.; Cortigiani, B.; Sainctavit, P.; Rovai, D.; Caneschi, A.; Sessoli, R., Low-Temperature Magnetic Force Microscopy on Single Molecule Magnet-Based Microarrays. *Nano Lett.* **2017,** *17* (3), 1899-1905.

8. Majumdar, A.; Lai, J.; Chandrachood, M.; Nakabeppu, O.; Wu, Y.; Shi, Z., Thermal imaging by atomic force microscopy using thermocouple cantilever probes. *Rev. Sci. Instrum.* **1995,** *66* (6), 3584-3592.

9. Drew, M. E.; Konicek, A. R.; Jaroenapibal, P.; Carpick, R. W.; Yamakoshi, Y., Nanocrystalline diamond AFM tips for chemical force spectroscopy: fabrication and photochemical functionalization. *J. Mater. Chem.* **2012,** *22* (25), 12682-12688.

10. Martin, Y.; Williams, C. C.; Wickramasinghe, H. K., Atomic force microscope–force mapping and profiling on a sub 100- Å scale. *J. Appl. Phys.* **1987,** *61* (10), 4723-4729.

11. Martin, Y.; Wickramasinghe, H. K., Magnetic imaging by ‘‘force microscopy’’ with 1000 Å resolution. *Appl. Phys. Lett.* **1987,** *50* (20), 1455-1457.

12. Maivald, P.; Butt, H. J.; Gould, S. A. C.; Prater, C. B.; Drake, B.; Gurley, J. A.; Elings, V. B.; Hansma, P. K., Using force modulation to image surface elasticities with the atomic force microscope. *Nanotechnology* **1991,** *2* (2), 103.

13. Zhong, Q.; Inniss, D.; Kjoller, K.; Elings, V. B., Fractured polymer/silica fiber surface studied by tapping mode atomic force microscopy. *Surf. sci. lett.* **1993,** *290* (1), L688-L692.

14. Dougherty, W. M.; Bruland, K. J.; Garbini, J. L.; Sidles, J. A., Detection of AC magnetic signals by parametric mode coupling in a mechanical oscillator. *Meas. Sci.Technol.* **1996,** *7* (12), 1733-1739.

15. Kelley, T. W.; Granstrom, E.; Frisbie, C. D., Conducting Probe Atomic Force Microscopy: A Characterization Tool for Molecular Electronics. *Adv. Mater.* **1999,** *11* (3), 261-264.

16. Li, J.-R.; Lewandowski, B. R.; Xu, S.; Garno, J. C., Detecting the Magnetic Response of Iron Oxide Capped Organosilane Nanostructures Using Magnetic Sample Modulation and Atomic Force Microscopy. *Analytical Chemistry* **2009,** *81* (12), 4792-4802.

17. Jalili, N.; Laxminarayana, K., A review of atomic force microscopy imaging systems: application to molecular metrology and biological sciences. *Mechatronics* **2004,** *14* (8), 907-945.

18. Sokolov, I. Y.; Henderson, G. S.; Wicks, F. J., The contrast mechanism for true atomic resolution by AFM in non-contact mode: quasi-non-contact mode? *Surf. Sci.* **1997,** *381* (1), L558-L562.

19. Burnham, N. A.; Behrend, O. P.; Oulevey, F.; Gremaud, G.; Gallo, P. J.; Gourdon, D.; Dupas, E.; Kulik, A. J.; Pollock, H. M.; Briggs, G. A. D., How does a tip tap? *Nanotechnology* **1997,** *8* (2), 67.

20. Stark, M.; Möller, C.; Müller, D. J.; Guckenberger, R., From Images to Interactions: High-Resolution Phase Imaging in Tapping-Mode Atomic Force Microscopy. *Biophys. J.* **2001,** *80* (6), 3009-3018.

21. Binnig, G.; Ch, G.; Stoll, E.; Albrecht, T. R.; Quate, C. F., Atomic Resolution with Atomic Force Microscope. *Europhys. Lett.* **1987,** *3* (12), 1281.

22. Shi, X.; Xu, L.; Zhou, Y.; Zou, C.; Wang, R.; Pan, G., An in situ study of chemical-mechanical polishing behaviours on sapphire (0001) via simulating the chemical product-removal process by AFM-tapping mode in both liquid and air environments. *Nanoscale* **2018,** *10* (42), 19692-19700.

23. Jaafar, M.; Martínez-Martín, D.; Cuenca, M.; Melcher, J.; Raman, A.; Gómez-Herrero, J., Drive-amplitude-modulation atomic force microscopy: From vacuum to liquids. *Beilstein J Nanotechnol.* **2012,** *3*, 336-344.

24. Hansma, P.; Elings, V.; Marti, O.; Bracker, C., Scanning tunneling microscopy and atomic force microscopy: application to biology and technology. *Science* **1988,** *242* (4876), 209-216.

25. Albrecht, T. R.; Quate, C. F., Atomic resolution imaging of a nonconductor by atomic force microscopy. *J. Appl. Phys.* **1987,** *62* (7), 2599-2602.

26. Barth, C.; Henry, C. R., Atomic Resolution Imaging of the (001) Surface of UHV Cleaved MgO by Dynamic Scanning Force Microscopy. *Phys. Rev. Lett.* **2003,** *91* (19), 196102.

27. Gratz, A. J.; Manne, S.; Hansma, P. K., Atomic Force Microscopy of Atomic-Scale Ledges and Etch Pits Formed During Dissolution of Quartz. *Science* **1991,** *251* (4999), 1343-1346.

28. Lauritsen, J. V.; Reichling, M., Atomic resolution non-contact atomic force microscopy of clean metal oxide surfaces. *J. Phys.: Condens. Matter* **2010,** *22* (26), 263001.

29. Grow, R. J.; Minne, S. C.; Manalis, S. R.; Quate, C. F., Silicon nitride cantilevers with oxidation-sharpened silicon tips for atomic force microscopy. *J Microelectromech S* **2002,** *11* (4), 317-321.

30. Binnig, G.; Smith, D. P. E., Single- tube three- dimensional scanner for scanning tunneling microscopy. *Rev. Sci. Instrum.* **1986,** *57* (8), 1688-1689.

31. Meyer, G.; Amer, N. M., Simultaneous measurement of lateral and normal forces with an optical- beam- deflection atomic force microscope. *Appl. Phys. Lett.* **1990,** *57* (20), 2089-2091.

32. Mate, C. M.; McClelland, G. M.; Erlandsson, R.; Chiang, S., Atomic-scale friction of a tungsten tip on a graphite surface. *Phys. Rev. Lett.* **1987,** *59* (17), 1942-1945.

33. Albrecht, T. R.; Quate, C. F., Atomic resolution imaging of a nonconductor by atomic force microscopy. *Europhys. Lett.* **1987,** *62* (7), 2599-2602.

34. Ma, Z.; Kim, Y.; Park, S.; Hirai, Y.; Tsuchiya, T.; Kim, D.; Tabata, O., Direct measurement of transversely isotropic DNA nanotube by force–distance curve-based atomic force microscopy. *Micro Nano Lett* **2015,** *10* (10), 513-517.

35. Iwata, K.; Yamazaki, S.; Mutombo, P.; Hapala, P.; Ondráček, M.; Jelínek, P.; Sugimoto, Y., Chemical structure imaging of a single molecule by atomic force microscopy at room temperature. *Nat. Commun.* **2015,** *6*, 7766.

36. Kang, H.; Qian, X.; Guan, L.; Zhang, M.; Li, Q.; Wu, A.; Dong, M., Studying the Adhesion Force and Glass Transition of Thin Polystyrene Films by Atomic Force Microscopy. *Nanoscale Res. Lett.* **2018,** *13* (1), 5.

37. Dufrêne, Y. F.; Ando, T.; Garcia, R.; Alsteens, D.; Martinez-Martin, D.; Engel, A.; Gerber, C.; Müller, D. J., Imaging modes of atomic force microscopy for application in molecular and cell biology. *Nat. Nanotech.* **2017,** *12*, 295.

38. Cappella, B.; Dietler, G., Force-distance curves by atomic force microscopy. *Surf. Sci. Rep.* **1999,** *34* (1), 1-104.

39. Weisenhorn, A. L.; Hansma, P. K.; Albrecht, T. R.; Quate, C. F., Forces in atomic force microscopy in air and water. *Appl. Phys. Lett.* **1989,** *54* (26), 2651-2653.

40. Butt, H.-J.; Cappella, B.; Kappl, M., Force measurements with the atomic force microscope: Technique, interpretation and applications. *Surf. Sci. Rep.* **2005,** *59* (1), 1-152.

41. Zhai, X.; Lee, H.; Tian, T.; Lee, T.; Garno, J., Nanoscale Lithography Mediated by Surface Self-Assembly of 16-[3,5-Bis(Mercaptomethyl)phenoxy]hexadecanoic Acid on Au(111) Investigated by Scanning Probe Microscopy. *Molecules* **2014,** *19* (9), 13010.

42. Hansma, P.; Cleveland, J.; Radmacher, M.; Walters, D.; Hillner, P.; Bezanilla, M.; Fritz, M.; Vie, D.; Hansma, H.; Prater, C., Tapping mode atomic force microscopy in liquids. *Appl. Phys. Lett.* **1994,** *64* (13), 1738-1740.

43. Putman, C. A. J.; Werf, K. O. V. d.; Grooth, B. G. D.; Hulst, N. F. V.; Greve, J., Tapping mode atomic force microscopy in liquid. *appl. Phys. Lett.* **1994,** *64* (18), 2454-2456.

44. Adams, J. D.; Erickson, B. W.; Grossenbacher, J.; Brugger, J.; Nievergelt, A.; Fantner, G. E., Harnessing the damping properties of materials for high-speed atomic force microscopy. *Nat. Nanotech.* **2015,** *11*, 147.

45. Korayem, M. H.; Nahavandi, A., Analyzing the vibrational response of an AFM cantilever in liquid with the consideration of tip mass by comparing the hydrodynamic and contact repulsive force models in higher modes. *Appl. Phys. A* **2017,** *123* (4), 265.

46. Marti, O.; Drake, B.; Hansma, P. K., Atomic force microscopy of liquid- covered surfaces: Atomic resolution images. *Appl. Phys. Lett.* **1987,** *51* (7), 484-486.

47. Asakawa, H.; Holmström, E.; Foster, A. S.; Kamimura, S.; Ohno, T.; Fukuma, T., Direct Imaging of Atomic-Scale Surface Structures of Brookite TiO_2 Nanoparticles by Frequency Modulation Atomic Force Microscopy in Liquid. *J. Phys. Chem. C* **2018,** *122* (42), 24085-24093.

48. Fukuma, T.; Kobayashi, K.; Matsushige, K.; Yamada, H., True molecular resolution in liquid by frequency-modulation atomic force microscopy. *Appl. Phys. Lett.* **2005,** *86* (19), 193108.

49. Pillet, F.; Formosa-Dague, C.; Baaziz, H.; Dague, E.; Rols, M.-P., Cell wall as a target for bacteria inactivation by pulsed electric fields. *Sci. Rep.* **2016,** *6*, 19778.

50. Magonov, S. N.; Elings, V.; Whangbo, M. H., Phase imaging and stiffness in tapping-mode atomic force microscopy. *Surf. Sci.* **1997,** *375* (2), L385-L391.

51. Bar, G.; Thomann, Y.; Brandsch, R.; Cantow, H. J.; Whangbo, M. H., Factors Affecting the Height and Phase Images in Tapping Mode Atomic Force Microscopy. Study of Phase-Separated Polymer Blends of Poly(ethene-co-styrene) and Poly(2,6-dimethyl-1,4-phenylene oxide). *Langmuir* **1997,** *13* (14), 3807-3812.

52. Stark, R. W.; Schitter, G.; Stemmer, A., Tuning the interaction forces in tapping mode atomic force microscopy. *Phys. Rev. B* **2003,** *68* (8), 085401.

53. Proksch, R., Multifrequency, repulsive-mode amplitude-modulated atomic force microscopy. *appl. Phys. Lett.* **2006,** *89* (11), 113121.

54. Daniels, S. L.; Ngunjiri, J. N.; Garno, J. C., Investigation of the magnetic properties of ferritin by AFM imaging with magnetic sample modulation. *Anal. Bioanal. Chem.* **2009,** *394* (1), 215.

55. Kulkarni, S. A.; Kolhatkar, A. G.; Lee, T. R.; Garno, J. C., Vibrational response of clusters of Fe3O4 nanoparticles patterned on glass surfaces investigated with magnetic sample modulation AFM. *Nanoscale* **2018,** *10* (43), 20426-20434.

56. Kelley, A. T.; Serem, W. K.; Daniels, S. L.; Englade-Franklin, L. E.; Morrison, G.; Flurry, N.; Chan, J. Y.; Garno, J. C., Vibrational Response of $FeNi_3$ Nanoparticles to the Flux of a Modulated Electromagnetic Field Detected by Contact-Mode Atomic Force Microscopy. *J. Phys. Chem. C*, **2013,** *117* (36), 18768-18776.

57. Straka, L.; Fekete, L.; Heczko, O., Antiphase boundaries in bulk Ni-Mn-Ga Heusler alloy observed by magnetic force microscopy. *Appl. Phys. Lett.* **2018,** *113* (17), 172901.

58. Cao, Y.; Kumar, P.; Zhao, Y.; Suzuki, Y.; Yoshimura, S.; Saito, H., High magnetization Co-GdOx superparamagnetic granular films as magnetic coating materials for high-sensitivity alternating magnetic force microscopy tip. *J. Magn. Magn. Mater.* **2018,** *462*, 119-126.

59. Florin, E. L.; Radmacher, M.; Fleck, B.; Gaub, H. E., Atomic force microscope with magnetic force modulation. *Rev. Sci. Instrum.* **1994,** *65* (3), 639-643.

60. Rebêlo, L. M.; de Sousa, J. S.; Filho, J. M.; Schäpe, J.; Doschke, H.; Radmacher, M., Microrheology of cells with magnetic force modulation atomic force microscopy. **2014,** *10* (13), 2141-2149.

61. Chen, M.; Balhara, V.; Jaimes Castillo, A. M.; Balsevich, J.; Johnston, L. J., Interaction of saponin 1688 with phase separated lipid bilayers. *Biochim. Biophys. Acta, Biomembr.* **2017,** *1859* (7), 1263-1272.

62. Schindler, H.; Badt, D.; Hinterdorfer, F. K. P.; Raab, A.; Wielert-Badt, S.; Pastushenko, V. P., Optimal sensitivity for molecular recognition MAC-mode AFM. *Ultramicroscopy* **2000,** *82* (1), 227-235.

63. Ge, G.; Han, D.; Lin, D.; Chu, W.; Sun, Y.; Jiang, L.; Ma, W.; Wang, C., MAC mode atomic force microscopy studies of living samples, ranging from cells to fresh tissue. *Ultramicroscopy* **2007,** *107* (4), 299-307.

64. Li, F.-B.; Thompson, G. E.; Newman, R. C., Force modulation atomic force microscopy: background, development and application to electrodeposited cerium oxide films. *Appl. Surf. Sci.* **1998,** *126* (1), 21-33.

65. DeVecchio, D.; Bhushan, B., Localized surface elasticity measurements using an atomic force microscope. *Rev. Sci. Instrum.* **1997,** *68* (12), 4498-4505.

66. Volodin, A.; Ahlskog, M.; Seynaeve, E.; Van Haesendonck, C.; Fonseca, A.; Nagy, J. B., Imaging the Elastic Properties of Coiled Carbon Nanotubes with Atomic Force Microscopy. *Phys. Rev. Lett.* **2000,** *84* (15), 3342-3345.

67. Piétrement, O.; Troyon, M., Quantitative elastic modulus measurement by magnetic force modulation microscopy. *Tribol Lett.* **2000,** *9* (1), 77-87.

68. Radmacher, M.; Tillmann, R. W.; Gaub, H. E., Imaging viscoelasticity by force modulation with the atomic force microscope. *Biophys. J.* **1993,** *64* (3), 735-742.

69. Yamamoto, S.-i.; Yamada, H., Interpretation of Direct and Indirect Force Modulation Methods Using Polymer Films. *Langmuir* **1997,** *13* (18), 4861-4864.

70. Kimura, K.; Kobayashi, K.; Yamada, H.; Matsushige, K., High resolution molecular chain imaging of a poly(vinylidenefluoride–trifluoroethylene) crystal using force modulation microscopy. *Nanotechnology* **2007,** *18* (30), 305504.

71. Overney, R.; Meyer, E.; Frommer, J.; Güntherodt, H.-J.; Fujihira, M.; Takano, H.; Gotoh, Y., Force microscopy study of friction and elastic compliance of phase-separated organic thin films. *Langmuir* **1994,** *10* (4), 1281-1286.

72. Zhang, J.; Parlak, Z.; Bowers, C. M.; Oas, T.; Zauscher, S., Mapping mechanical properties of organic thin films by force-modulation microscopy in aqueous media. *Beilstein J Nanotechnol.* **2012,** *3*, 464-474.

73. Yamada, H.; Hirata, Y.; Miyake, J., Force modulation imaging of protein membranes. *J. Vac. Sci. Technol. A* **1995,** *13* (3), 1742-1745.

74. Hisashi Haga; Shigeo Sasaki; Mayumi Morimoto; Kazushige Kawabata; Etsuro Ito; Kazuhiro Abe; Takashi Sambongi, Imaging Elastic Properties of Soft Materials Immersed in Water Using Force Modulation Mode in Atomic Force Microscopy. *J. Am. Chem. Soc* **1998,** *37* (6S), 3860.

75. Zlotnikov, I.; Zolotoyabko, E.; Fratzl, P., Nano-scale modulus mapping of biological composite materials: Theory and practice. *Prog. Mater Sci.* **2017,** *87*, 292-320.

76. Radmacher, M., Measuring the elastic properties of biological samples with the AFM. *IEEE J Transl Eng Health Med* **1997,** *16* (2), 47-57.

77. Troyon, M.; Wang, Z.; Pastre, D.; Lei, H. N.; Hazotte, A., Force modulation microscopy for the study of stiff materials. *Nanotechnology* **1997,** *8* (4), 163.

78. Corletto, A.; Yu, L.; Shearer, C. J.; Gibson, C. T.; Shapter, J. G., Dip Pen Nanolithography: Direct-Patterning SWCNTs Using Dip Pen Nanolithography for SWCNT/Silicon Solar Cells (Small 16/2018). *Small* **2018,** *14* (16), 1870071.

79. Park, S. J.; Ok, J. G.; Park, H. J.; Lee, K.-T.; Lee, J. H.; Kim, J. D.; Cho, E.; Baac, H. W.; Kang, S.; Guo, L. J.; Hart, A. J., Modulation of the effective density and refractive index of carbon nanotube forests via nanoimprint lithography. *Carbon* **2018,** *129*, 8-14.

80. Luis, G. R.; Jian, L., Atomic force microscope nanolithography: dip-pen, nanoshaving, nanografting, tapping mode, electrochemical and thermal nanolithography. *J. Phys.: Condens. Matter* **2009,** *21* (48), 483001.

81. Bu, D.; Riechers, S.; Liang, J.; Liu, G.-y., Impact of nanografting on the local structure of ternary self-assembled monolayers. *Nano Research* **2015,** *8* (6), 2102-2114.

82. Tian, T.; LeJeune, Z. M.; Serem, W. K.; Yu, J.-J.; Garno, J. C., Nanografting: A Method for Bottom-up Fabrication of Designed Nanostructures. In *Tip-Based Nanofabrication: Fundamentals and Applications*, Tseng, A. A., Ed. Springer New York: New York, NY, 2011; pp 167-205.

83. Liu, M.; Amro, N. A.; Chow, C. S.; Liu, G.-y., Production of Nanostructures of DNA on Surfaces. *Nano Lett.* **2002,** *2* (8), 863-867.

84. Bano, F.; Fruk, L.; Sanavio, B.; Glettenberg, M.; Casalis, L.; Niemeyer, C. M.; Scoles, G., Toward Multiprotein Nanoarrays Using Nanografting and DNA Directed Immobilization of Proteins. *Nano Lett.* **2009,** *9* (7), 2614-2618.

85. Liu, G.-Y.; Amro, N. A., Positioning protein molecules on surfaces: A nanoengineering approach to supramolecular chemistry. *Proc. Natl. Acad. Sci. USA* **2002,** *99* (8), 5165-5170.

86. Garno, J. C.; Yang, Y.; Amro, N. A.; Cruchon-Dupeyrat, S.; Chen, S.; Liu, G.-Y., Precise Positioning of Nanoparticles on Surfaces Using Scanning Probe Lithography. *Nano Lett.* **2003,** *3* (3), 389-395.

87. Liu, G.-y.; Salmeron, M. B., Reversible Displacement of Chemisorbed n-Alkanethiol Molecules on Au(111) Surface: An Atomic Force Microscopy Study. *Langmuir* **1994,** *10* (2), 367-370.

88. Xu, S.; Liu, G.-y., Nanometer-Scale Fabrication by Simultaneous Nanoshaving and Molecular Self-Assembly. *Langmuir* **1997,** *13* (2), 127-129.

89. Rosa, L. G.; Jiang, J.; Lima, O. V.; Xiao, J.; Utreras, E.; Dowben, P. A.; Tan, L., Selective nanoshaving of self-assembled monolayers of 2-(4-pyridylethyl)triethoxysilane. *Mat. Lett.* **2009,** *63* (12), 961-964.

90. Headrick, J. E.; Armstrong, M.; Cratty, J.; Hammond, S.; Sheriff, B. A.; Berrie, C. L., Nanoscale Patterning of Alkyl Monolayers on Silicon Using the Atomic Force Microscope. *Langmuir* **2005,** *21* (9), 4117-4122.

91. Shi, J.; Chen, J.; Cremer, P. S., Sub-100 nm Patterning of Supported Bilayers by Nanoshaving Lithography. *J. Am. Chem. Soc.* **2008,** *130* (9), 2718-2719.

92. Hwang, E.; Lusker, K. L.; Garno, J. C.; Losovyj, Y.; Nesterov, E. E., Semiconducting polymer thin films by surface-confined stepwise click polymerization. *Chem. Commun.* **2011,** *47* (43), 11990-11992.

93. Verberne-Sutton, S. D.; Quarels, R. D.; Zhai, X.; Garno, J. C.; Ragains, J. R., Application of visible light photocatalysis with particle lithography to generate polynitrophenylene nanostructures. *J. Am. Chem. Soc* **2014,** *136* (41), 14438-14444.

94. Cruchon-Dupeyrat, S.; Porthun, S.; Liu, G. Y., Nanofabrication using computer-assisted design and automated vector-scanning probe lithography. *Appl. Surf. Sci.* **2001,** *175-176*, 636-642.

95. Drexler, C. I.; Causey, C. P.; Mullen, T. J., 1-Adamantanethiol as a versatile nanografting tool. *Scanning* **2015,** *37* (1), 6-16.

96. Liu, G.-Y.; Xu, S.; Qian, Y., Nanofabrication of Self-Assembled Monolayers Using Scanning Probe Lithography. *Acc. Chem. Res.* **2000,** *33* (7), 457-466.

97. Liu, J.-F.; Cruchon-Dupeyrat, S.; Garno, J. C.; Frommer, J.; Liu, G.-Y., Three-Dimensional Nanostructure Construction via Nanografting: Positive and Negative Pattern Transfer. *Nano Lett.* **2002,** *2* (9), 937-940.

98. Case, M. A.; McLendon, G. L.; Hu, Y.; Vanderlick, T. K.; Scoles, G., Using Nanografting to Achieve Directed Assembly of de novo Designed Metalloproteins on Gold. *Nano Lett.* **2003,** *3* (4), 425-429.

99. Hu, Y.; Das, A.; Hecht, M. H.; Scoles, G., Nanografting De Novo Proteins onto Gold Surfaces. *Langmuir* **2005,** *21* (20), 9103-9109.

100. Ulman, A., Formation and Structure of Self-Assembled Monolayers. *Chem. Rev.* **1996,** *96* (4), 1533-1554.

101. Schmaltz, T.; Sforazzini, G.; Reichert, T.; Frauenrath, H., Self-Assembled Monolayers as Patterning Tool for Organic Electronic Devices. *Adv. Mater.* **2017,** *29* (18), 1605286.

102. Liu, D.; Luo, Q.; Deng, F.; Li, Z.; Li, B.; Shen, Z., Ultrasensitive electrochemical biosensor based on the oligonucleotide self-assembled monolayer-mediated immunosensing interface. *Anal. Chim. Acta* **2017,** *971*, 26-32.

103. Bagherzadeh, M.; Jaberinia, F., Electrochemical study of Monel alloy corrosion in hydrochloric acid solution and pyrrolidine dithiocarboxylate self-assembled monolayers as its corrosion protector. *J Alloys Compd.* **2018,** *750*, 677-686.

104. James, L. W.; Amit, K.; Hans, A. B.; Enoch, K.; George, M. W., Microcontact printing of self-assembled monolayers: applications in microfabrication. *Nanotechnology* **1996,** *7* (4), 452.

105. Ulman, A., Self-assembled monolayers of alkyltrichiorosilanes: Building blocks for future organic materials. *Adv. Mater.* **1990,** *2* (12), 573-582.

106. Schoenfisch, M. H.; Pemberton, J. E., Air Stability of Alkanethiol Self-Assembled Monolayers on Silver and Gold Surfaces. *J. Am. Chem. Soc.* **1998,** *120* (18), 4502-4513.

107. Lavrich, D. J.; Wetterer, S. M.; Bernasek, S. L.; Scoles, G., Physisorption and Chemisorption of Alkanethiols and Alkyl Sulfides on Au(111). *J. Phys. Chem. B* **1998,** *102* (18), 3456-3465.

108. Niwa, M.; Date, M.; Higashi, N., In Situ Photopolymerization of Methacrylic Acid at a Self-Assembled Xanthate Monolayer Surface on Gold. Formation of Poly(methacrylic acid) Brushes and Their Interaction with Cytochrome c. *Macromolecules* **1996,** *29* (11), 3681-3685.

109. Palacios-Rivera, R.; Barrena, E.; Faraudo, J.; Gargiani, P.; Niño, M. A.; Arvanitis, D.; Kowalik, I.; de Miguel, J. J.; Ocal, C., Enantiopure Supramolecular Motifs of Self-Assembled Diamine-Based Chiral Molecules on Cu(100). *J. Phys. Chem. C* **2018,** *122* (42), 24129-24136.

110. Bashir, A.; Iqbal, D.; Jain, S. M.; Barbe, K.; Abu-Husein, T.; Rohwerder, M.; Terfort, A.; Zharnikov, M., Promoting Effect of Protecting Group on the Structure and Morphology of Self-Assembled Monolayers: Terphenylylethanethioactate on Au(111). *J. Phys. Chem. C* **2015,** *119* (45), 25352-25363.

111. Gazit, E., Self-assembled peptide nanostructures: the design of molecular building blocks and their technological utilization. *Chem. Soc. Rev.* **2007,** *36* (8), 1263-1269.

112. Sagiv, J., Organized monolayers by adsorption. 1. Formation and structure of oleophobic mixed monolayers on solid surfaces. *J. Am. Chem. Soc.* **1980,** *102* (1), 92-98.

113. Zhu, M.; Lerum, M. Z.; Chen, W., How To Prepare Reproducible, Homogeneous, and Hydrolytically Stable Aminosilane-Derived Layers on Silica. *Langmuir* **2012,** *28* (1), 416-423.

114. Bush, B. G.; DelRio, F. W.; Opatkiewicz, J.; Maboudian, R.; Carraro, C., Effect of Formation Temperature and Roughness on Surface Potential of Octadecyltrichlorosilane Self-Assembled Monolayer on Silicon Surfaces. *J. Phys. Chem. A* **2007,** *111* (49), 12339-12343.

115. Hancer, M., The effect of humidity on the stability of octadecyltrichlorosilane for the self-assembled monolayer coating applications. *Prog. Org. Coat.* **2008,** *63* (4), 395-398.

116. Brownfield, A. L.; Causey, C. P.; Mullen, T. J., Influence of Solvent on Octadecyltrichlorosilane Nanostructures Fabricated Using Particle Lithography. *J. Phys. Chem. C* **2015,** *119* (22), 12455-12463.

117. McGovern, M. E.; Kallury, K. M. R.; Thompson, M., Role of Solvent on the Silanization of Glass with Octadecyltrichlorosilane. *Langmuir* **1994,** *10* (10), 3607-3614.

118. Brownfield, A. L.; Causey, C. P.; Mullen, T. J., Effects of surface water on organosilane nanostructure fabrication using particle lithography. *Thin Solid Films* **2015,** *594*, 184-191.

119. Li, J.-R.; Garno, J. C., Elucidating the Role of Surface Hydrolysis in Preparing Organosilane Nanostructures via Particle Lithography. *Nano Letters* **2008,** *8* (7), 1916-1922.

120. Nuzzo, R. G.; Allara, D. L., Adsorption of bifunctional organic disulfides on gold surfaces. *J. Am. Chem. Soc* **1983,** *105* (13), 4481-4483.

121. Xu, S.; Cruchon-Dupeyrat, S. J.; Garno, J. C.; Liu, G.-Y.; Jennings, G. K.; Yong, T.-H.; Laibinis, P. E., In situ studies of thiol self-assembly on gold from solution using atomic force microscopy. *J. Chem. Phys.* **1998,** *108* (12).

122. Vericat, C.; Vela, M. E.; Salvarezza, R. C., Self-assembled monolayers of alkanethiols on Au(111): surface structures, defects and dynamics. *Phys. Chem. Chem. Phys.* **2005,** *7* (18), 3258-3268.

123. Wen, R.; Lahiri, A.; Azhagurajan, M.; Kobayashi, S.-i.; Itaya, K., A New in Situ Optical Microscope with Single Atomic Layer Resolution for Observation of Electrochemical Dissolution of Au(111). *J. Am. Chem. Soc.* **2010,** *132* (39), 13657-13659.

124. Ishida, N.; Nishihara, R.; Imanaka, H.; Imamura, K., Nanostructures of 3-aminopropyltriethoxysilane created on flat substrate by combining colloid lithography and vapor deposition. *Colloids Surf. A* **2016,** *495*, 39-45.

125. Taylor, A. M.; Okoth, E. A.; Arachchige, N. M. K. K.; Vicente, M. G. H.; Garno, J. C., Nanostructures of Functionalized Zinc Phthalocyanines Prepared with Colloidal Lithography: Evaluation of Surface Orientation and Dimensions using Scanning Probe Microscopy. *Colloids and Surfaces A: Physicochemical and Engineering Aspects* **2018**.

126. Kosiorek, A.; Kandulski, W.; Glaczynska, H.; Giersig, M., Fabrication of Nanoscale Rings, Dots, and Rods by Combining Shadow Nanosphere Lithography and Annealed Polystyrene Nanosphere Masks. *Small* **2005,** *1* (4), 439-444.

127. Xu, X.; Yang, Q.; Wattanatorn, N.; Zhao, C.; Chiang, N.; Jonas, S. J.; Weiss, P. S., Multiple-Patterning Nanosphere Lithography for Fabricating Periodic Three-Dimensional Hierarchical Nanostructures. *ACS Nano* **2017,** *11* (10), 10384-10391.

128. Zhai, X.; Arachchige, N. M. K. K.; Derosa, P.; Garno, J. C., Conductive-probe measurements with nanodots of free-base and metallated porphyrins. *J. Colloid Interface Sci.* **2017,** *486*, 38-45.

129. Asoh, H.; Sakamoto, S.; Ono, S., Metal Patterning on Silicon Surface By Site-Selective Electroless Deposition Through Colloidal Crystal Templating. *J. Colloid Interface Sci.* **2007,** *316* (2), 547-552.

130. Deckman, H. W.; Dunsmuir, J. H., Natural lithography. *Appl. Phys. Lett.* **1982,** *41* (4), 377-379.

131. Chou, S. Y., Patterned Magnetic Nanostructures and Quantized Magnetic Disks. *Proc. IEEE.* **1997,** *85* (4), 652-671.

132. Wang, C.; Han, X.; Xu, P.; Wang, J.; Du, Y.; Wang, X.; Qin, W.; Zhang, T., Controlled Synthesis of Hierarchical Nickel and Morphology-Dependent Electromagnetic Properties. *J. Phys. Chem. C*, **2010,** *114* (7), 3196-3203.

133. Rothman, J.; Kläui, M.; Lopez-Diaz, L.; Vaz, C. A. F.; Bleloch, A.; Bland, J. A. C.; Cui, Z.; Speaks, R., Observation of a Bi-Domain State and Nucleation Free Switching in Mesoscopic Ring Magnets. *Phys. Rev. Lett.* **2001,** *86* (6), 1098-1101.

134. Ozel, T.; Ashley, M. J.; Bourret, G. R.; Ross, M. B.; Schatz, G. C.; Mirkin, C. A., Solution-Dispersible Metal Nanorings with Deliberately Controllable Compositions and Architectural Parameters for Tunable Plasmonic Response. *Nano Lett.* **2015,** *15* (8), 5273-5278.

135. Aizpurua, J.; Hanarp, P.; Sutherland, D. S.; Käll, M.; Bryant, G. W.; García de Abajo, F. J., Optical Properties of Gold Nanorings. *Phys. Rev. Lett.* **2003,** *90* (5), 057401.

136. Halpern, A. R.; Corn, R. M., Lithographically Patterned Electrodeposition of Gold, Silver, and Nickel Nanoring Arrays with Widely Tunable Near-Infrared Plasmonic Resonances. *ACS Nano* **2013,** *7* (2), 1755-1762.

137. Shimon, G.; Adeyeye, A. O.; Ross, C. A., Comparative Study of Magnetization Reversal Process Between Rectangular and Circular Thin Film Rings. *J. Appl. Phys.* **2012,** *111* (1), 013909.

138. Deng, T.; Prentiss, M.; Whitesides, G. M., Fabrication of magnetic microfiltration systems using soft lithography. *Appl. Phys. Lett.* **2002,** *80*, 461-463.

139. Lee, K.-B.; Park, S.; Mirkin, C. A., Multicomponent Magnetic Nanorods for Biomolecular Separations. *Angew. Chem. Int. Ed.* **2004,** *43*, 3048 –3050.

140. Heyderman, L. J.; David, C.; Kläui, M.; Vaz, C. A. F.; Bland, J. A. C., Nanoscale Ferromagnetic Rings Fabricated by Electron-Beam Lithography. *J. Appl. Phys.* **2003,** *93* (12), 10011-10013.

141. Jamieson, C.; Manchester, F. D., The Magnetic Susceptibility of Pd, PdH and PdD between 4 and 300 K. *J. Phys. F.* **1972,** *2*, 323-336.

142. Near, R.; Tabor, C.; Duan, J.; Pachter, R.; El-Sayed, M., Pronounced Effects of Anisotropy on Plasmonic Properties of Nanorings Fabricated by Electron Beam Lithography. *Nano Lett.*, **2012,** *12* (4), 2158-2164.

143. Libo, L.; An, M.; Wu, G., Model of Electroless Ni Deposition on SiCp/Al Composites and Study of the Interfacial Interaction of Coatings with Substrate Surface. *Appl. Surf. Sci.* **2005,** *252*, 959-965.

144. Farrell, R. A.; Kehagias, N.; Shaw, M. T.; Reboud, V.; Zelsmann, M.; Holmes, J. D.; Sotomayor Torres, C. M.; Morris, M. A., Surface-Directed Dewetting of a Block Copolymer for Fabricating Highly Uniform Nanostructured Microdroplets and Concentric Nanorings. *ACS Nano* **2011,** *5* (2), 1073-1085.

145. Ouchi, T.; Arikawa, Y.; Homma, T., Fabrication of Copt Magnetic Nanodot Arrays by Electrodeposition Process. *J. Magn. Magn. Mater.* **2008,** *320* (22), 3104-3107.

146. Cho, K.; Loget, G.; Corn, R. M., Lithographically Patterned Nanoscale Electrodeposition of Plasmonic, Bimetallic, Semiconductor, Magnetic, and Polymer Nanoring Arrays. *J. Phys. Chem. C.* **2014,** *118* (50), 28993-29000.

147. Li, J.-R.; Lusker, K. L.; Yu, J.-J.; Garno, J. C., Engineering the Spatial Selectivity of Surfaces at the Nanoscale Using Particle Lithography Combined with Vapor Deposition of Organosilanes. *ACS Nano* **2009,** *3* (7), 2023-2035.

148. Junhu, Z.; Yunfeng, L.; Xuemin, Z.; Bai, Y., Colloidal Self- Assembly Meets Nanofabrication: From Two- Dimensional Colloidal Crystals to Nanostructure Arrays. *Adv. Mater.,* **2010,** *22* (38), 4249-4269.

149. Li, J.-R.; Lewandowski, B. R.; Xu, S.; Garno, J. C., Detecting the Magnetic Response of Iron Oxide Capped Organosilane Nanostructures Using Magnetic Sample Modulation and Atomic Force Microscopy. *Anal. Chem.* **2009,** *81*, 4792-4802.

150. Liu, X.; Choi, B.; Gozubenli, N.; Jiang, P., Periodic Arrays of Metal Nanorings and Nanocrescents Fabricated by A Scalable Colloidal Templating Approach. *J. Colloid Interface Sci.* **2013,** *409*, 52-58.

151. Duan, G.; Cai, W.; Luo, Y.; Li, Z.; Lei, Y., Hierarchical Structured Ni Nanoring and Hollow Sphere Arrays by Morphology Inheritance Based on Ordered Through-Pore Template and Electrodeposition. *J. Phys. Chem. B.* **2006,** *110* (32), 15729-15733.

152. Krishnan, K. H.; John, S.; Srinivasan, K. N.; Praveen, J.; Ganesan, M.; Kavimani, P. M., An Overall Aspect of Electroless Ni-P Depositions—A Review Article. *Metall. Mater. Trans A* **2006,** *37* (6), 1917-1926.

153. Rebbecchi, T. A.; Chen, Y., Template-Based Fabrication Of Nanoporous Metals. *J. Mater. Res.* **2017,** *33*, 2-15.

154. Gerasopoulos, K.; Pomerantseva, E.; McCarthy, M.; Brown, A.; Wang, C.; Culver, J.; Ghodssi, R., Hierarchical Three-Dimensional Microbattery Electrodes Combining Bottom-Up Self-Assembly and Top-Down Micromachining. *ACS Nano* **2012,** *6*, 6422-6432.

155. Shacham-Diamand, Y.; Osaka, T.; Okinaka, Y.; Sugiyama, A.; Dubin, V., 30 Years of Electroless Plating for Semiconductor And Polymer Micro-Systems. *Microelectron. Eng.* **2015,** *132*, 35-45.

156. Lo, C.-C.; Huang, C.-C.; Liu, C.-M.; Chen, C.; Kuo, C.-Y.; Lin, H.-J.; Tseng, Y.-C., Magnetic Properties of Electroless-Deposited Ni And Ni–NiO Core–Shell Nano-Arrays. *J. Magn. Magn. Mater* **2011,** *323* (15), 1950-1953.

157. Kawaji, J.; Kitaizumi, F.; Oikawa, H.; Niwa, D.; Homma, T.; Osaka, T., Area Selective Formation of Magnetic Nanodot Arrays on Si Wafer by Electroless Deposition. *J. Magn. Magn. Mater.* **2005,** *287*, 245-249.

158. Huang, C.-C.; Lo, C.-C.; Tseng, Y.-C.; Liu, C.-M.; Chen, C., Magnetostructural Phase Transition in Electroless-Plated Ni Nanoarrays. *J. Appl. Phys.* **2011,** *109* (11), 113905.

159. Chien-Min, L.; Yuan-Chieh, T.; Chih, C.; Ming-Chieh, H.; Tzu-Yzan, C.; Yu-Ting, C., Superparamagnetic and Ferromagnetic Ni Nanorod Arrays Fabricated on Si Substrates Using Electroless Deposition. *Nanotechnology* **2009,** *20* (41), 415703.

160. Kind, H.; Bittner, A. M.; Cavalleri, O.; Kern, K.; Greber, T., Electroless Deposition of Metal Nanoislands on Aminothiolate-Functionalized Au(111) Electrodes. *J. Phys. Chem. B,* **1998,** *102* (39), 7582-7589.

161. Zhang, Q.; Wu, M.; Zhao, W., Electroless Nickel Plating on Hollow Glass Microspheres. *Surf. Coat. Technol.* **2005,** *192* (2), 213-219.

162. Osaka, T.; Yoshino, M., New Formation Process of Plating Thin Films on Several Substrates By Means of Self-Assembled Monolayer (SAM) Process. *Electrochim. Acta* **2007,** *53* (2), 271-277.

163. Brandow, S. L.; Chen, M. S.; Aggarwal, R.; Dulcey, C. S.; Calvert, J. M.; Dressick, W. J., Fabrication of Patterned Amine Reactivity Templates Using 4-Chloromethylphenylsiloxane Self-Assembled Monolayer Films. *Langmuir* **1999,** *15* (16), 5429-5432.

164. Chen, M. S.; Brandow, S. L.; Schull, T. L.; Chrisey, D. B.; Dressick, W. J., A Non-Covalent Approach for Depositing Spatially Selective Materials on Surfaces. *Adv. Funct. Mater.*, **2005,** *15* (8), 1364-1375.

165. Dressick, W. J.; Dulcey, C. S.; Georger, J. H.; Calabrese, G. S.; Calvert, J. M., Covalent Binding of Pd Catalysts to Ligating Self- Assembled Monolayer Films for Selective Electroless Metal Deposition. *J. Electrochem. Soc.* **1994,** *141* (1), 210-220.

166. Lee, I.; Hammond, P. T.; Rubner, M. F., Selective Electroless Nickel Plating of Particle Arrays on Polyelectrolyte Multilayers. *Chem. Mater.*, **2003,** *15* (24), 4583-4589.

167. Wang, T. C.; Chen, B.; Rubner, M. F.; Cohen, R. E., Selective Electroless Nickel Plating on Polyelectrolyte Multilayer Platforms. *Langmuir* **2001,** *17* (21), 6610-6615.

168. Alexandre, G.; Thomas, B.; Pascal, V.; Pascale, J.; Serge, P., 3D Amino- Induced Electroless Plating: A Powerful Toolset for Localized Metallization on Polymer Substrates. *ChemPhysChem* **2011,** *12* (16), 2973-2978.

169. Kimura, M.; Yamagiwa, H.; Asakawa, D.; Noguchi, M.; Kurashina, T.; Fukawa, T.; Shirai, H., Site-Selective Electroless Nickel Plating on Patterned Thin Films of Macromolecular Metal Complexes. *ACS Appl. Mater. Interfaces,* **2010,** *2* (12), 3714-3717.

170. Zhang, M. C.; Kang, E. T.; Neoh, K. G.; Tan, K. L., Electroless Plating of Copper and Nickel on Surface-Modified Poly(tetrafluoroethylene) Films. *J. Electrochem. Soc.* **2001,** *148* (2), C71-C80.

171. Liu, H.; Li, J.; Wang, L., Electroless Nickel Plating on APTHS Modified Wood Veneer for EMI Shielding. *Appl. Surf. Sci.* **2010,** *257* (4), 1325-1330.

172. Brandow, S. L.; Dressick, W. J.; Marrian, C. R. K.; Chow, G. M.; Calvert, J. M., The Morphology of Electroless Ni Deposition on a Colloidal Pd(II) Catalyst. *J. Electrochem. Soc.* **1995,** *142* (7), 2233-2243.

173. H., G. R.; X., J. S.; D., Z. Y.; W., L. J., Electroless Nickel Deposition of A Palladium-Activated Self- Assembled Monolayer on Polyester Fabric. *J. Appl. Polym. Sci.,* **2013,** *127* (5), 4186-4193.

174. Castaño, F. J.; Ross, C. A.; Frandsen, C.; Eilez, A.; Gil, D.; Smith, H. I.; Redjdal, M.; Humphrey, F. B., Metastable States in Magnetic Nanorings. *Phys. Rev. B* **2003,** *67* (18), 184425.

175. Saitoh, E.; Kawabata, M.; Harii, K.; Miyajima, H.; Yamaoka, T., Manipulation of Vortex Circulation in Decentered Ferromagnetic Nanorings. *J. Appl. Phys.* **2004,** *95* (4), 1986-1988.

176. Li, S. P.; Peyrade, D.; Natali, M.; Lebib, A.; Chen, Y.; Ebels, U.; Buda, L. D.; Ounadjela, K., Flux Closure Structures in Cobalt Rings. *Phys. Rev. Lett.* **2001,** *86* (6), 1102-1105.

177. Li, J.-R.; Garno, J. C., Elucidating the Role of Surface Hydrolysis in Preparing Organosilane Nanostructures via Particle Lithography. *Nano Lett.* **2008,** *8*, 1916-1922.

178. Saner, C. M. K.; Lusker, K. L.; LeJeune, Z. M.; Serem, W. K.; Garno, J. C., Self-Assembly of Octadecyltrichlorosilane: Surface Structures Formed Using Different Protocols of Particle Lithography. *Beilstein J. Nanotechnol.* **2012,** *3*, 114-22.

179. Wang, W.; Ji, S.; Lee, I., A Facile Method of Nickel Electroless Deposition on Various Neutral Hydrophobic Polymer Surfaces. *Appl. Surf. Sci.* **2013,** *283* (Supplement C), 309-320.

180. Yoshino, M.; Masuda, T.; Yokoshima, T.; Sasano, J.; Shacham-Diamand, Y.; Matsuda, I.; Osaka, T.; Hagiwara, Y.; Sato, I., Electroless Diffusion Barrier Process Using SAM on Low-K Dielectrics. *J. Electrochem. Soc.* **2007,** *154* (3), D122-D125.

181. Nečas, D.; Klapetek, P., Gwyddion: An Open-Source Software for SPM Data Analysis. *Cent. Eur. J. Phys.* **2012,** *10* (1), 181-188.

182. Brandow, S. L.; Chen, M. S.; Wang, T.; Dulcey, C. S.; Calvert, J. M.; Bohland, J. F.; Calabrese, G. S.; Dressick, W. J., Size- Controlled Colloidal Pd(II) Catalysts for Electroless Ni Deposition in Nanolithography Applications. *J. Electrochem. Soc.* **1997,** *144* (10), 3425-3434.

183. Tsai, T.-K.; Chao, C.-G., The Growth Morphology and Crystallinity of Electroless NiP Deposition on Silicon. *Appl. Surf. Sci.* **2004,** *233* (1), 180-190.

184. Daniels, S. L.; Ngunjiri, J. N.; Garno, J. C., Investigation of the magnetic properties of ferritin by AFM imaging with magnetic sample modulation. *Anal. Bioanal. Chem.* **2009,** *394*, 215-223.

185. Wadu-Mesthrige, K.; Amro, N.; Garno, J. C.; Cruchon-Dupeyrat, S.; Liu, G.-Y., Contact resonance imaging - A simple approach to improve the resolution of AFM for biological and polymeric materials. *Appl. Surf. Sci.* **2001,** *175-176*, 391-398.

186. Lusker, K. L.; Yu, J.-J.; Garno, J. C., Particle lithography with vapor deposition of organosilanes: A molecular toolkit for studying confined surface reactions in nanoscale liquid volumes. *Thin Solid Films* **2011,** *519* (15), 5223-5229.

187. Tillman, N.; Ulman, A.; Schildkraut, J. S.; Penner, T. L., Incorporation of phenoxy groups in self-assembled monolayers of trichlorosilane derivatives. Effects on film thickness, wettability, and molecular orientation. *J. Am. Chem. Soc.* **1988,** *110* (18), 6136-6144.

188. Vallant, T.; Brunner, H.; Mayer, U.; Hoffmann, H.; Leitner, T.; Resch, R.; Friedbacher, G., Formation of Self-Assembled Octadecylsiloxane Monolayers on Mica and Silicon Surfaces Studied by Atomic Force Microscopy and Infrared Spectroscopy. *J. Phys. Chem. B* **1998,** *102* (37), 7190-7197.

189. Wu, X.; van de Ven, T. G. M., Characterization of Hairy Latex Particles with Colloidal Particle Scattering. *Langmuir* **1996,** *12* (16), 3859-3865.

190. Seebergh, J. E.; Berg, J. C., Evidence of a hairy layer at the surface of polystyrene latex particles. *Colloids Surf. A* **1995,** *100*, 139-153.

191. Borget, P.; Lafuma, F.; Bonnet-Gonnet, C., Characterizations and properties of hairy latex particles. *J. Colloid Interface Sci.* **2005,** *285* (1), 136-145.

192. Langmuir, I., The constitution and fundamental properties of solids and liquids. Ii. Liquids.1. *J. Am. Chem. Soc* **1917,** *39* (9), 1848-1906.

193. Blodgett, K. B., Monomolecular films of fatty acids on glass. *J. Am. Chem. Soc* **1934,** *56* (2), 495-495.

194. Blodgett, K. B., Use of interference to extinguish reflection of light from glass. *Physical Review* **1939,** *55* (4), 391.

195. Ostroff, R. M.; Hopkins, D.; Haeberli, A. B.; Baouchi, W.; Polisky, B., Thin film biosensor for rapid visual detection of nucleic acid targets. *Clin. Chem.* **1999,** *45* (9), 1659-1664.

196. Xu, M.; Obodo, D.; Yadavalli, V. K., The design, fabrication, and applications of flexible biosensing devices. *Biosens. Bioelectron* **2019,** *124-125*, 96-114.

197. Pal, R. K.; Farghaly, A. A.; Wang, C.; Collinson, M. M.; Kundu, S. C.; Yadavalli, V. K., Conducting polymer-silk biocomposites for flexible and biodegradable electrochemical sensors. *Biosens. Bioelectron* **2016,** *81*, 294-302.

198. Popescu, D.; Popescu, B.; Brändlein, M.; Melzer, K.; Lugli, P., Modeling of Electrolyte-Gated Organic Thin-Film Transistors for Sensing Applications. *IEEE Trans. Electron Devices* **2015,** *62* (12), 4206-4212.

199. Lin, P.; Yan, F., Organic Thin-Film Transistors for Chemical and Biological Sensing. *Adv. Mater.* **2012,** *24* (1), 34-51.

200. Dimitrakopoulos, C. D.; Malenfant, P. R., Organic thin film transistors for large area electronics. *Adv. Mater.* **2002,** *14* (2), 99-117.

201. Algarni, S. A.; Althagafi, T. M.; Al Naim, A.; Grell, M., A water-gated organic thin film transistor as a sensor for water-borne amines. *Talanta* **2016,** *153*, 107-110.

202. Laguzzi, G.; Luvidi, L., Evaluation of the anticorrosive properties of benzotriazole alkyl derivatives on 6% Sn bronze alloy. *Surf. Coat. Technol.* **2010,** *204* (15), 2442-2446.

203. Brunoro, G.; Frignani, A.; Colledan, A.; Chiavari, C., Organic films for protection of copper and bronze against acid rain corrosion. *Corros sci* **2003,** *45* (10), 2219-2231.

204. Balbo, A.; Chiavari, C.; Martini, C.; Monticelli, C., Effectiveness of corrosion inhibitor films for the conservation of bronzes and gilded bronzes. *Corros sci* **2012,** *59*, 204-212.

205. Zhang, Z.; Zhang, M.; Chen, S.; Horbett, T. A.; Ratner, B. D.; Jiang, S., Blood compatibility of surfaces with superlow protein adsorption. *Biomaterials* **2008,** *29* (32), 4285-4291.

206. Kuribara, K.; Wang, H.; Uchiyama, N.; Fukuda, K.; Yokota, T.; Zschieschang, U.; Jaye, C.; Fischer, D.; Klauk, H.; Yamamoto, T.; Takimiya, K.; Ikeda, M.; Kuwabara, H.; Sekitani, T.; Loo, Y.-L.; Someya, T., Organic transistors with high thermal stability for medical applications. *Nat. Commun.* **2012,** *3*, 723.

207. Yu, D.; Yang, Y.-Q.; Chen, Z.; Tao, Y.; Liu, Y.-F., Recent progress on thin-film encapsulation technologies for organic electronic devices. *Opt. Commun.* **2016,** *362*, 43-49.

208. Pettersson, L. A. A.; Roman, L. S.; Inganäs, O., Modeling photocurrent action spectra of photovoltaic devices based on organic thin films. *J. Appl. Phys.* **1999,** *86* (1), 487-496.

209. Eslamian, M., Inorganic and Organic Solution-Processed Thin Film Devices. *Nano-Micro Lett* **2016,** *9* (1), 3.

210. Hacker, C. A.; Batteas, J. D.; Garno, J. C.; Marquez, M.; Richter, C. A.; Richter, L. J.; van Zee, R. D.; Zangmeister, C. D., Structural and Chemical Characterization of Monofluoro-Substituted Oligo(phenylene−ethynylene) Thiolate Self-Assembled Monolayers on Gold. *Langmuir* **2004,** *20* (15), 6195-6205.

211. Tamada, K.; Nagasawa, J.; Nakanishi, F.; Abe, K.; Hara, M.; Knoll, W.; Ishida, T.; Fukushima, H.; Miyashita, S.; Usui, T.; Koini, T.; R. Lee, T., Structure of SAMs generated from functionalized thiols on gold. *Thin Solid Films* **1998,** *327-329*, 150-155.

212. Schlenoff, J. B.; Li, M.; Ly, H., Stability and self-exchange in alkanethiol monolayers. *J. Am. Chem. Soc* **1995,** *117* (50), 12528-12536.

213. Chandekar, A.; Sengupta, S. K.; Whitten, J. E., Thermal stability of thiol and silane monolayers: A comparative study. *Appl. Surf. Sci.* **2010,** *256* (9), 2742-2749.

214. Zhang, Y.; Terrill, R. H.; Bohn, P. W., Ultraviolet Photochemistry and ex Situ Ozonolysis of Alkanethiol Self-Assembled Monolayers on Gold. *Chem. Mater.* **1999,** *11* (8), 2191-2198.

215. Brewer, N. J.; Rawsterne, R. E.; Kothari, S.; Leggett, G. J., Oxidation of Self-Assembled Monolayers by UV Light with a Wavelength of 254 nm. *J. Am. Chem. Soc.* **2001,** *123* (17), 4089-4090.

216. Huang, J.; Dahlgren, D. A.; Hemminger, J. C., Photopatterning of Self-Assembled Alkanethiolate Monolayers on Gold: A Simple Monolayer Photoresist Utilizing Aqueous Chemistry. *Langmuir* **1994,** *10* (3), 626-628.

217. Zhang, Y.; Terrill, R. H.; Tanzer, T. A.; Bohn, P. W., Ozonolysis Is the Primary Cause of UV Photooxidation of Alkanethiolate Monolayers at Low Irradiance. *J. Am. Chem. Soc* **1998,** *120* (11), 2654-2655.

218. Norrod, K. L.; Rowlen, K. L., Ozone-Induced Oxidation of Self-Assembled Decanethiol: Contributing Mechanism for "Photooxidation"? *:J. Am. Chem. Soc.* **1998,** *120* (11), 2656-2657.

219. Lee, M.-T.; Hsueh, C.-C.; Freund, M. S.; Ferguson, G. S., Air Oxidation of Self-Assembled Monolayers on Polycrystalline Gold: The Role of the Gold Substrate. *Langmuir* **1998,** *14* (22), 6419-6423.

220. Vericat, C.; Vela, M.; Benitez, G.; Carro, P.; Salvarezza, R., Self-assembled monolayers of thiols and dithiols on gold: new challenges for a well-known system. *Chem. Soc. Rev.* **2010,** *39* (5), 1805-1834.

221. Jans, K.; Bonroy, K.; De Palma, R.; Reekmans, G.; Jans, H.; Laureyn, W.; Smet, M.; Borghs, G.; Maes, G., Stability of Mixed PEO−Thiol SAMs for Biosensing Applications. *Langmuir* **2008,** *24* (8), 3949-3954.

222. Belanger, D.; Pinson, J., Electrografting: a powerful method for surface modification. *Chem. Soc. Rev.* **2011,** *40* (7), 3995-4048.

223. Chehimi, M. M.; Hallais, G.; Matrab, T.; Pinson, J.; Podvorica, F. I., Electro- and Photografting of Carbon or Metal Surfaces by Alkyl Groups. *J. Phys. Chem. C* **2008,** *112* (47), 18559-18565.

224. Berisha, A.; Combellas, C.; Hallais, G.; Kanoufi, F.; Pinson, J.; Podvorica, F. I., Photochemical Grafting and Patterning of Metallic Surfaces by Organic Layers Derived from Acetonitrile. *Chem. Mater.* **2011,** *23* (15), 3449-3459.

225. de la Llave, E.; Ricci, A.; Calvo, E. J.; Scherlis, D. A., Binding between Carbon and the Au(111) Surface and What Makes It Different from the S−Au(111) Bond. *J. Phys. Chem. C* **2008,** *112* (45), 17611-17617.

226. Shewchuk, D. M.; McDermott, M. T., Comparison of Diazonium Salt Derived and Thiol Derived Nitrobenzene Layers on Gold. *Langmuir* **2009,** *25* (8), 4556-4563.

227. Ghosh, I.; Marzo, L.; Das, A.; Shaikh, R.; König, B., Visible Light Mediated Photoredox Catalytic Arylation Reactions. *Acc. Chem. Res.* **2016,** *49* (8), 1566-1577.

228. Senaweera, S. M.; Singh, A.; Weaver, J. D., Photocatalytic Hydrodefluorination: Facile Access to Partially Fluorinated Aromatics. *J. Am. Chem. Soc.* **2014,** *136* (8), 3002-3005.

229. Kim, H.; Lee, C., Visible- Light- Induced Photocatalytic Reductive Transformations of Organohalides. *Angew. Chem.* **2012,** *124* (49), 12469-12472.

230. Kariuki, J. K.; McDermott, M. T., Formation of Multilayers on Glassy Carbon Electrodes via the Reduction of Diazonium Salts. *Langmuir* **2001,** *17* (19), 5947-5951.

231. Adenier, A.; Combellas, C.; Kanoufi, F.; Pinson, J.; Podvorica, F. I., Formation of Polyphenylene Films on Metal Electrodes by Electrochemical Reduction of Benzenediazonium Salts. *Chem. Mater.* **2006,** *18* (8), 2021-2029.

232. Brooksby, P. A.; Downard, A. J., Electrochemical and Atomic Force Microscopy Study of Carbon Surface Modification via Diazonium Reduction in Aqueous and Acetonitrile Solutions. *Langmuir* **2004,** *20* (12), 5038-5045.

233. Tanaka, M.; Sawaguchi, T.; Sato, Y.; Yoshioka, K.; Niwa, O., Surface Modification of GC and HOPG with Diazonium, Amine, Azide, and Olefin Derivatives. *Langmuir* **2011,** *27* (1), 170-178.

234. Bouriga, M.; Chehimi, M. M.; Combellas, C.; Decorse, P.; Kanoufi, F. d. r.; Deronzier, A.; Pinson, J., Sensitized Photografting of Diazonium Salts by Visible Light. *Chem. Mater.* **2012,** *25* (1), 90-97.

235. Quarels, R. D.; Zhai, X.; Kuruppu, N.; Hedlund, J. K.; Ellsworth, A. A.; Walker, A. V.; Garno, J. C.; Ragains, J. R., Application of visible-light photosensitization to form alkyl-radical-derived thin films on gold. *Beilstein J. Nanotechnol.* **2017,** *8*, 1863-1877.

236. Zhai, X.; Alexander, D.; Derosa, P.; Garno, J. C., Distance-Dependent Measurements of the Conductance of Porphyrin Nanorods Studied with Conductive Probe Atomic Force Microscopy. *Langmuir* **2017,** *33* (5), 1132-1138.

237. Samorí, P.; Diebel, J.; Löwe, H.; Rabe, J. P., Template-Stripped Gold Supported on Ni as a Substrate for SAMs. *Langmuir* **1999,** *15* (7), 2592-2594.

238. Hegner, M.; Wagner, P.; Semenza, G., Ultralarge atomically flat template-stripped Au surfaces for scanning probe microscopy. *Surf. Sci.* **1993,** *291* (1), 39-46.

239. Kelley, A. T.; Ngunjiri, J. N.; Serem, W. K.; Lawrence, S. O.; Yu, J.-J.; Crowe, W. E.; Garno, J. C., Applying AFM-Based Nanofabrication for Measuring the Thickness of Nanopatterns: The Role of Head Groups in the Vertical Self-Assembly of ω-Functionalized n-Alkanethiols. *Langmuir* **2010,** *26* (5), 3040-3049.

240. Azzam, W., A novel method for elimination of the gold-islands formed in the self-assembled monolayers of benzeneselenol on Au (111) surface. *Appl. Surf. Sci.* **2010,** *256* (7), 2299-2303.

241. Liu, C.-Y.; Pan, H.-L.; Fox, M. A.; Bard, A. J., High-Density Nanosecond Charge Trapping in Thin-Films of the Photoconductor ZnODEP. *Science* **1993,** *261*, 897-899.

242. Fox, M. A., Fundamentals in the Design of Molecular Electronic Devices: Long-Range Charge Carrier Transport and Electronic Coupling. *Acc. Chem. Res.* **1999,** *32*, 201-207.

243. Adams, D. M.; Kerimo, J.; Liu, C.-Y.; Bard, A. J.; Barbara, P. F., Electric field modulated near-field photo-luminescence of organic thin films *J. Phys. Chem. B* **2000,** *104*, 6728-6736.

244. Kimura, M.; Saito, Y.; Ohta, K.; Hanabusa, K.; Shirai, H.; Kobayashi, N., Self-Organization of Supramolecular Complex Composed of Rigid Dendritic Porphyrin and Fullerene *J. Am. Chem. Soc.* **2002,** *124*, 5274-5275.

245. Burrows, H. D.; Gonsalves, A. M. R.; Leitao, M. L. P.; Miguel, M. D. G.; Pereira, M. M., Phase transitions and self-assembly in meso-tetrakis(undecyl)porphyrin. *Supramolec. Sci.* **1997,** *4*, 241-246.

246. Tsuda, A.; Osuka, A., Fully Conjugated Porphyrin Tapes with Electronic Absorption Bands That Reach into Infrared. *Science* **2001,** *293*, 79-82.

247. Suslick, K. S.; Rakow, N. A.; Kosal, M. E.; Chou, J.-H., The materials chemistry of porphyrins and metalloporphyrins. *J. Porphyrins Phthalocyanines* **2000,** *4*, 407-413.

248. Guo, X. L.; Dong, Z. C.; Trifonov, A. S.; Miki, K.; Kimura, K.; Mashiko, S., STM-induced molecular fluorescence. *Appl. Phys. A* **2005,** *81*.

249. Reimers, J. R.; Hall, L. E.; Crossley, M. J.; Hush, N. S., Rigid fused oligoporphyrins as potential versatile molecular wires. 2. B3LYP and SCF calculated geometric and electronic properties of 98 oligoporphyrin and related molecules. *J. Phys. Chem. A* **1999,** *103*, 4385-4397.

250. Filippini, D.; Alimelli, A.; Natale, C. D.; Paolesse, R.; D'Amico, A.; Lundstrom, I., Chemical Sensing with Familiar Devices. *Angew. Chem. Int. Ed.* **1999,** *45*, 3800-3803.

251. Malinski, T.; Taha, Z., Nitric-Oxide Release from a Single Cell Measured In Situ by a Porphyrinic-Based Microsensor. *Nature* **1992,** *358*, 676-678.

252. Lo, P.-C.; Huang, J.-D.; Cheng, D. Y. Y.; Chan, E. Y. M.; Fong, W.-P.; Ko, W.-H.; Ng, D. K. P., New amphiphilic silicon(IV) phthalocyanines as efficient photosensitizers for photodynamic

therapy: Synthesis, photophysical properties, and in vitro photodynamic activities. *Chem. Eur. J.* **2004,** *10* (19), 4831-4838.

253. Galstyan, A.; Kauscher, U.; Block, D.; Ravoo, B. J.; Strassert, C. A., Silicon(IV) phthalocyanine-decorated cyclodextrin vesicles as a self-assembled phototherapeutic agent against MRSA. *ACS Appl. Mater. Interfaces* **2016,** *8* (20), 12631-12637.

254. Zysman-Colman, E.; Ghosh, S. S.; Xie, G.; Varghese, S.; Chowdhury, M.; Sharma, N.; Cordes, D. B.; Slawin, A. M. Z.; Samuel, I. D. W., Solution-processable silicon phthalocyanines in electroluminescent and photovoltaic devices. *ACS Appl. Mater. Interfaces* **2016,** *8* (14), 9247-9253.

255. Maree, C. H. M.; Roosendaal, S. J.; Savenije, T. J.; Schropp, R. E. I.; Schaafsma, T. J.; Habraken, F. H. P. M., Photovoltaic effects in porphyrin polymer films and heterojunctions. *J. Appl. Phys.* **1996,** *80*, 3381-3389.

256. Murata, K.; Ito, S.; Takahashi, K.; Hoffman, B. M., Photocurrent from photocorrosion of aluminum electrode in porphyrin/Al Schottky-barrier cells. *Appl. Phys. Lett.* **1997,** *71*, 674-676.

257. Cai, J.; Chen, H.; Huang, J.; Wang, J.; Tian, D.; Dong, H.; Jiang, L., Controlled self-assembly and photovoltaic characteristics of porphyrin derivatives on a silicon surface at solid-liquid interfaces. *Soft matter* **2014,** *10* (15), 2612-2618.

258. Chen, Y.; Li, A.; Huang, Z.-H.; Wang, L.-N.; Kang, F., Porphyrin-based nanostructures for photocatalytic applications. *Nanomater.* **2016,** *6* (3), 51.

259. Ussia, M.; Bruno, E.; Spina, E.; Vitalini, D.; Pellegrino, G.; Ruffino, F.; Privitera, V.; Carroccio, S. C., Freestanding photocatalytic materials based on 3D graphene and polyporphyrins. *Sci. Rep.* **2018,** *8*.

260. Harima, Y.; Okazaki, H.; Kunugi, Y.; Yamashita, K.; Ishii, H.; Seki, K., Formation of Schottky barriers at interfaces between metals and molecular semiconductors of p- and n- type conductances. *Appl. Phys. Lett.* **1996,** *69*, 1059-1061.

261. Chowdhury, A.; Chowdhury, J.; Pal, P.; Pal, A. J., Light-emitting diodes from molecularly thin porphyrin derivative: Effect of molecular packing. *Solid State Communications* **1998,** *107*, 725-729.

262. Baldo, M. A.; O'Brien, D. F.; You, Y.; Shoustikov, A.; Sibley, S.; Thompson, M. E.; Forrest, S. R., Highly efficient phosphorescent emission from organic electroluminescent devices. *Nature* **1998,** *395*, 151-154.

263. Kwong, R. C.; Sibley, S.; Dubovoy, T.; Baldo, M.; Forrest, S. R.; Thompson, M. E., Efficient, saturated red organic light emitting devices based on phosphorescent platinum(II) porphyrins. *Chem. Mater.* **1999,** *11*, 3709-3713.

264. Sendt, K.; Johnston, L. A.; Hough, W. A.; Crossley, M. J.; Hush, N. S.; Reimers, J. R., Switchable Electronic Coupling in Model Oligoporphyrin Molecular Wires Examined through the

Measurement and Assignment of Electronic Absorption Spectra. *J. Am. Chem. Soc.* **2002,** *124*, 9299-9309.

265. Robertson, N.; McGowan, C. A., A comparison of potential molecular wires as components for molecular electronics. *Chem. Soc. Rev.* **2003,** *32*, 96-103.

266. Jurow, M.; Schuckman, A. E.; Batteas, J. D.; Drain, C. M., Porphyrins as molecular electronic components of functional devices. *Coord. Chem. Rev.* **2010,** *254* (19), 2297-2310.

267. Roth, K. M.; Dontha, N.; Dabke, R. B.; Gryko, D. T.; Clausen, C.; Lindsey, J. S.; Bocian, D. F.; Kuhr, W. G., Molecular approach toward information storage based on the redox properties of porphyrins in self-assembled monolayers. . *J. Vac. Sci. Technol.* **2000,** *18*, 2359.

268. Jiao, J.; Anariba, F.; Tiznado, H.; Schmidt, I.; Lindsey, J. S.; Zaera, F.; Bocian, D. F., Stepwise Formation and Characterization of Covalently Linked Multiporphyrin-Imide Architectures on Si(100). *J. Am. Chem. Soc.* **2006,** *128*, 6965-6974.

269. Roth, K. M.; Liu, Z.; Gryko, D. T.; Clausen, C.; Lindsey, J. S.; Bocian, D. F.; Kuhr, W. G., Chapter 5. Charge-retention characteristics of self-assembled monolayers of molecular-wire-linked porphyrins on gold. In *Molecules as Components of Electronic Devices,*, Lieberman, M., Ed. Oxford University Press: Washington DC, 2003.

270. Liu, C.-Y.; Pan, H. L.; Fox, M. A.; Bard, A. J., Reversible charge trapping/detrapping in a photoconductive insulator of liquid crystal zinc porphyrin. *Chem. Mater.* **1997,** *9*, 1422-1429.

271. Milic, T.; Garno, J. C.; Smeureanu, G.; Batteas, J. D.; Drain, C. M., Organization of Self-Assembled Tetrameric Porphyrin Arrays on Surfaces. *Langmuir* **2004,** *20*, 3974-3983.

272. Garno, J. C.; Xu, C.; Batteas, J. D.; Drain, C. M., Chapter 13. Designing Supramolecular Porphyrin Arrays for Surface Assembly and Patterning of Optoelectronic Materials. In *Metal-Containing and Metallosupramolecular Polymers and Materials,* ,, S., U.; Schubert, G. R. N.; Manners, I., Eds. American Chemical Society: Washington, DC, 2005; Vol. 928.

273. Gao, Y.; Zhang, X.; Ma, C.; Li, X.; Jiang, J., Morphology-Controlled Self-Assembled Nanostructures of 5,15-Di[4-(5-acetylsulfanylpentyloxy)phenyl]porphyrin Derivatives. Effect of Metal−Ligand Coordination Bonding on Tuning the Intermolecular Interaction. *J. Am. Chem. Soc.* **2008,** *130* (50), 17044-17052.

274. Ariga, K.; Hill, J. P.; Ji, Q., Layer-by-layer assembly as a versatile bottom-up nanofabrication technique for exploratory research and realistic application. *Phys. Chem. Chem. Phys.* **2007,** *9* (19), 2319-2340.

275. Kadish, K. M.; Xu, Q. Y.; Barbe, J. M.; Guilard, R., Synthesis and reactivity of sigma.-bonded silicon metalloporphyrins. Spectroscopic characterization and electrochemistry of (P)Si(R)2, (P)Si(R)X, and (P)SiX2, where R = C6H5 or CH3 and X = OH- or ClO4. *Inorg. Chem.* **1988,** *27* (7), 1191-1198.

276. Gong, M.; Cao, Z.; Liu, W.; Nichols, E. M.; Smith, P. T.; Derrick, J. S.; Liu, Y.-S.; Liu, J.; Wen, X.; Chang, C. J., Supramolecular Porphyrin Cages Assembled at Molecular−Materials Interfaces for Electrocatalytic CO Reduction. *ACS Cent. Sci.* **2017,** *3*, 1032-1040.

277. Pawlicki, A. A.; Vilan, A.; Jurow, M.; Drain, C. M.; Batteas, J. D., The Influence of Nearest-Neighbour Interactions and Assembly Dynamics on the Transport Properties of Porphyrin Supramolecular Assemblies on Au(111). *Faraday Dicuss.* **2017,** *204*, 349-366.

278. Lu, X.; Lv, B.; Xue, Z.; Li, M.; Zhang, L.; Kang, J., Self-Assembled Monolayers of a Thiol-Derivatized Porphyrin on Gold Electrode: Film formation and Electrocatalytic Dioxygen Reaction. *Thin Solid Films* **2005,** *488*, 230-235.

279. Eriksson, K. L. E.; Chow, W. W. Y.; Puglia, C.; Backvall, J.-E.; Gothelid, E.; Oscarsson, S., Performance of a Biomimetic Oxidation Catalyst Immobilized on Silicon Wafers: Comparison with Its Gold Congener. *Langmuir* **2010,** *26*, 16349-16354.

280. Vesper, B. J.; Salaita, K.; Zong, H.; Mirkin, C. A.; Barrett, A. G. M.; Hoffman, B. M., Surface-Bound Porphyrazines: Controlling Reduction Potentials of Self-Assembled Monolayers through Molecular Proximity/Orientation to a Metal Surface. *J. Am. Chem. Soc.* **2004,** *126*, 16653-16658.

281. Xi, W.; Zhang, W.; An, B.-K.; Burn, v.; Davis, J. J., Tunnelling Conductance of Vectorial Porphyrin Monolayers. *J. Mater. Chem.* **2008,** *18*, 3109-3120.

282. Uddin, S. M. N.; Nagao, Y., Multilayer Growth of Porphyrin-Based Polyurea Thin Film Using Solution-Based Molecular Layer Deposition Technique. *Langmuir* **2017,** *33*, 12777-12784.

283. Gadenne, V.; Portea, L.; Patrone, L., Structure and Growth Mechanism of Self-assembled Monolayers of Metal Protoporphyrins and Octacarboxylphthalocyanine on Silicon Dioxide. *RSC Adv.* **2014,** *4*, 64506-64513.

284. Contino, A.; Maccarrone, G.; Fragal, M. E.; Spitaleri, v.; Gulino, A., Conjugated Gold–Porphyrin Monolayers Assembled on Inorganic Surfaces. *Chem. Eur. J.* **2017,** *23*, 14937-14943.

285. Lokesh, K. S.; Keersmaecker, M. D.; Adriaens, A., Self Assembled Films of Porphyrins with Amine Groups at Different Positions: Influence of Their Orientation on the Corrosion Inhibition and the Electrocatalytic Activity. *Molecules* **2012,** *17*, 7824-7842.

286. Li, D.; Swanson, B. I.; Robinson, J. M.; Hoffbauer, M. A., Porphyrin based self-assembled monolayer thin films: Synthesis and characterization. *J. Am. Chem. Soc.* **1993,** *115* (15), 6975-6980.

287. Li, D.; Buscher, C. T.; Swanson, B. I., Synthesis, characterization, and properties of covalently bound, self-assembled porphyrin multilayer thin films. *Chem. Mater.* **1994,** *6* (6), 803-810.

288. Palomaki, P. K. B.; Krawicz, A.; Dinolfo, P. H., Thickness, Surface Morphology, and Optical Properties of Porphyrin Multilayer Thin Films Assembled on Si(100) Using Copper(I)-Catalyzed Azide-Alkyne Cycloaddition. *Langmuir* **2011,** *27*, 4613-4622.

289. Topka, M. R.; Dinolfo, P. H., Synthesis, Characterization, and Fluorescence Properties of Mixed Molecular Multilayer Films of BODIPY and Zn(II) Tetraphenylporphyrins. *ACS Appl. Mater. Inter.* **2015,** *7*, 8053-8060.

290. Kanaizuka, K.; Izumi, A.; Ishizaki, M.; Kon, H.; Togashi, T.; Miyake, R.; Ishida, T.; Tamura, R.; Haga, M.-a.; Moritani, Y.; Sakamoto, M.; Kurihara, M., Molecular Nanostamp Based on One-Dimensional Porphyrin Polymers. *ACS Appl. Mater. Interfaces* **2013,** *5* (15), 6879-6885.

291. Kawaguchi, T.; Okamura, S.; Togashi, T.; Harada, W.; Hirahara, M.; Miyake, R.; Haga, M.-a.; Ishida, T.; Kurihara, M.; Kanaizuka, K., Potential tuning of nanoarchitectures based on phthalocyanine nanopillars: Construction of effective photocurrent generation systems. *ACS Appl. Mater. Interfaces* **2015,** *7* (34), 19098-19103.

292. Togashi, T.; Izumi, A.; Hiroki, K.; Katsuhiko, K.; Manabu, I.; Ryosuke, M.; Chang, H.-C.; Haga, M.-a.; Sakamoto, M.; Kurihara, M., Spontaneous construction of nanoneedles using ruthenium complex-conjugated porphyrins on substrates. *Chem. Lett.* **2014,** *43* (8), 1201-1203.

293. Kane, K. M.; Lorenz, C. R.; Heilman, D. M.; Lemke, F. R., Substituent Effects on the Spectroscopic Properties and Reactivity of Hexacoordinate Silicon(IV) Porphyrin Complexes. *Inorg. Chem.* **1998,** *37*, 669-673.

294. Lee, D.-C.; Morales, G. M.; Lee, Y.; Yu, L., Cofacial porphyrin multilayers via layer-by-layer assembly. *Chem. Comm.* **2006,** (1), 100-102.

295. Zheng, J.-Y.; Konishi, K.; Aida, T., Crystallographic Studies of Organosilicon Porphyrins: Stereoelectronic Effects of Axial Groups on the Nonplanarity of the Porphyrin Ring. *Inorg. Chem.* **1998,** *37*, 2591-2594.

296. Kane, K. M.; Lemke, F. R.; Petersen, J. L., *trans*-Difluorosilicon(IV) Complexes of Tetra-p-tolylporphyrin and Tetrakis(p-(trifluoromethyl)phenyl)porphyrin: Crystal Structures and Unprecedented Reactivity in Hexacoordinate Difluorosilanes. *Inorg. Chem.* **1997,** *36*, 1354-1359.

297. Sakurai, T.; Yoneda, S.; Sakaguchi, S.; Kato, K.; Takata, M.; Seki, S., Donor/Acceptor Segregated π^{-} Stacking Arrays by Use of Shish- Kebab-Type Polymeric Backbones: Highly Conductive Discotic Blends of Phthalocyaninatopolysiloxanes and Perylenediimides. *Macromolecules* **2017,** *50*, 9265-9275.

298. Nečas, D.; Klapetek, P., Gwyddion: an open-source software for SPM data analysis. *Central Eur. J. Phys.* **2012,** *10* (1), 181-188.

299. Giovannetti, R., The Use of Spectrophotometry UV-Vis for the Study of Porphyrins. In *Macro To Nano Spectroscopy*, Uddin, J., Ed. Intech: Rijeka, Croatia, 2012; pp 87-108.

300. Chambers, P. C.; Garno, J. C., Heterostuctures of 4-(chloromethyl)phenyltrichlorosilane and 5,10,15,20-tetra(4-pyridyl)-21H,23H-porphine prepared on Si(111) using particle lithography: Nanoscale characterization of the main steps of nanopatterning. *Beilstein J. Nanotechnol.* **2018,** *9*, 1211-1219.

301. Lu, L.; Lahasky, S. H.; Zhang, D.; Garno, J. C., Directed Growth of Polymer Nanorods Using Surface-Initiated Ring-Opening Polymerization of N‑ Allyl N‑ Carboxyanhydride. *ACS Appl. Mater. Interfaces* **2016,** *8*, 4014-4022.

302. Ngunjiri, J. N.; Stark, D. J.; Tian, T.; Briggman, K. A.; Garno, J. C., Immobilization of proteins on carboxylic acid functionalized nanopatterns. *Anal. Bioanal. Chem.* **2013,** *405* (6), 1985-1993.

303. Highland, Z. L.; Garno, J. C., Spatially selective binding of green fluorescent protein on designed organosilane nanopatterns prepared with particle lithography. *Biointerphases* **2017,** *12*, 02C402.

304. Englade-Franklin, L. E.; Morrison, G.; Verberne-Sutton, S. D.; Francis, A. L.; Chan, J. Y.; Garno, J. C., Surface-directed synthesis of Erbium-doped Yttrium oxide nanoparticles within organosilane zeptoliter containers. *ACS Appl. Mater. Inter.* **2014,** *6*, 15942-15949.

305. Saner, C. K.; Lusker, K. L.; LeJeune, Z. M.; Serem, W. K.; Garno, J. C., Self-assembly of octadecyltrichlorosilane: Surface structures formed using different protocols of particle lithography. *Beilstein J. Nanotechnol.* **2012,** *3*, 114-122.

306. Li, J. R.; Garno, J. C., Elucidating the role of surface hydrolysis in preparing organosilane nanostructures via particle lithography. *Nano Lett.* **2008,** *8* (7), 1916-1922.

307. Li, J. R.; Lusker, K. L.; Yu, J. J.; Garno, J. C., Engineering the Spatial Selectivity of Surfaces at the Nanoscale Using Particle Lithography Combined with Vapor Deposition of Organosilanes. *ACS Nano* **2009,** *3* (7), 2023-2035.

308. Yang, Y.; Gao, N.; Hu, Y.; Jia, C.; Chou, T.; Du, H.; Wang, H., Gold nanoparticle-enhanced photodynamic therapy: effects of surface charge and mitochondrial targeting. *Ther. Deliv.* **2015,** *6* (3), 307-321.

309. Rengan, A. K.; Bukhari, A. B.; Pradhan, A.; Malhotra, R.; Banerjee, R.; Srivastava, R.; De, A., In Vivo Analysis of Biodegradable Liposome Gold Nanoparticles as Efficient Agents for Photothermal Therapy of Cancer. *Nano Lett.* **2015,** *15* (2), 842-848.

310. Aioub, M.; Austin, L. A.; El-Sayed, M. A., Chapter 2 - Gold nanoparticles for cancer diagnostics, spectroscopic imaging, drug delivery, and plasmonic photothermal therapy. In *Inorganic Frameworks as Smart Nanomedicines*, Grumezescu, A. M., Ed. William Andrew Publishing: 2018; pp 41-91.

311. Bindhu, M. R.; Umadevi, M., Silver and gold nanoparticles for sensor and antibacterial applications. *SAA* **2014,** *128*, 37-45.

312. Ahmad, R.; Griffete, N.; Lamouri, A.; Felidj, N.; Chehimi, M. M.; Mangeney, C., Nanocomposites of Gold Nanoparticles@Molecularly Imprinted Polymers: Chemistry, Processing, and Applications in Sensors. *Chem. Mater.* **2015,** *27* (16), 5464-5478.

313. Cordeiro, M.; Ferreira Carlos, F.; Pedrosa, P.; Lopez, A.; Baptista, P. V., Gold Nanoparticles for Diagnostics: Advances towards Points of Care. *Diagnostics (Basel)* **2016,** *6* (4), 43.

314. Viswambari Devi, R.; Doble, M.; Verma, R. S., Nanomaterials for early detection of cancer biomarker with special emphasis on gold nanoparticles in immunoassays/sensors. *Biosens. Bioelectron.* **2015,** *68*, 688-698.

315. Sousa, L. M.; Vilarinho, L. M.; Ribeiro, G. H.; Bogado, A. L.; Dinelli, L. R., An electronic device based on gold nanoparticles and tetraruthenated porphyrin as an electrochemical sensor for catechol. *R. Soc. Open Sci.* **2017,** *4* (12), 170675-170675.

316. Lopez, N.; Janssens, T. V. W.; Clausen, B. S.; Xu, Y.; Mavrikakis, M.; Bligaard, T.; Nørskov, J. K., On the origin of the catalytic activity of gold nanoparticles for low-temperature CO oxidation. *J. Catal.* **2004,** *223* (1), 232-235.

317. Henglein, A.; Meisel, D., Radiolytic Control of the Size of Colloidal Gold Nanoparticles. *Langmuir* **1998,** *14* (26), 7392-7396.

318. Piella, J.; Bastús, N. G.; Puntes, V., Size-Controlled Synthesis of Sub-10-nanometer Citrate-Stabilized Gold Nanoparticles and Related Optical Properties. *Chem. Mater.* **2016,** *28* (4), 1066-1075.

319. Hu, J.; Zhang, J.; Liu, F.; Kittredge, K.; Whitesell, J. K.; Fox, M. A., Competitive Photochemical Reactivity in a Self-Assembled Monolayer on a Colloidal Gold Cluster. *J. Am. Chem. Soc.* **2001,** *123* (7), 1464-1470.

320. Takao, O.; Katsuhiro, I.; Satoko, N.; Kazushi, M., Enhancement of self-assembly of large (>10 nm) gold nanoparticles on an ITO substrate. *Appl. Phys. Express* **2014,** *7* (6), 065001.

321. Cano, I.; Huertos, M. A.; Chapman, A. M.; Buntkowsky, G.; Gutmann, T.; Groszewicz, P. B.; van Leeuwen, P. W. N. M., Air-Stable Gold Nanoparticles Ligated by Secondary Phosphine Oxides as Catalyst for the Chemoselective Hydrogenation of Substituted Aldehydes: a Remarkable Ligand Effect. *J. Am. Chem. Soc.* **2015,** *137* (24), 7718-7727.

322. Islam, M. T.; Molugu, S. K.; Cooke, P. H.; Noveron, J. C., Fullerene stabilized gold nanoparticles. *New J. Chem.* **2015,** *39* (8), 5923-5926.

323. Zhao, Y.; Huang, Y.; Zhu, H.; Zhu, Q.; Xia, Y., Three-in-One: Sensing, Self-Assembly, and Cascade Catalysis of Cyclodextrin Modified Gold Nanoparticles. *J. Am. Chem. Soc.* **2016,** *138* (51), 16645-16654.

324. Kong, L.; Alves, C. S.; Hou, W.; Qiu, J.; Möhwald, H.; Tomás, H.; Shi, X., RGD Peptide-Modified Dendrimer-Entrapped Gold Nanoparticles Enable Highly Efficient and Specific Gene Delivery to Stem Cells. *ACS Appl. Mater. Interfaces* **2015,** *7* (8), 4833-4843.

325. Yao, G.; Pei, H.; Li, J.; Zhao, Y.; Zhu, D.; Zhang, Y.; Lin, Y.; Huang, Q.; Fan, C., Clicking DNA to gold nanoparticles: poly-adenine-mediated formation of monovalent DNA-gold nanoparticle conjugates with nearly quantitative yield. *NPG Asia Mater.* **2015,** *7*, e159.

326. Hasobe, T.; Imahori, H.; Kamat, P. V.; Ahn, T. K.; Kim, S. K.; Kim, D.; Fujimoto, A.; Hirakawa, T.; Fukuzumi, S., Photovoltaic Cells Using Composite Nanoclusters of Porphyrins and Fullerenes with Gold Nanoparticles. *J. Am. Chem. Soc.* **2005,** *127* (4), 1216-1228.

327. Wieder, M. E.; Hone, D. C.; Cook, M. J.; Handsley, M. M.; Gavrilovic, J.; Russell, D. A., Intracellular photodynamic therapy with photosensitizer-nanoparticle conjugates: cancer therapy using a 'Trojan horse'. *Photochem. Photobiol. Sci.* **2006,** *5* (8), 727-734.

328. Kotiaho, A.; Lahtinen, R.; Efimov, A.; Metsberg, H.-K.; Sariola, E.; Lehtivuori, H.; Tkachenko, N. V.; Lemmetyinen, H., Photoinduced Charge and Energy Transfer in Phthalocyanine-Functionalized Gold Nanoparticles. *J. Phys. Chem. C* **2010,** *114* (1), 162-168.

329. Hone, D. C.; Walker, P. I.; Evans-Gowing, R.; FitzGerald, S.; Beeby, A.; Chambrier, I.; Cook, M. J.; Russell, D. A., Generation of Cytotoxic Singlet Oxygen via Phthalocyanine-Stabilized Gold Nanoparticles: A Potential Delivery Vehicle for Photodynamic Therapy. *Langmuir* **2002,** *18* (8), 2985-2987.

330. Imahori, H.; Kashiwagi, Y.; Hanada, T.; Endo, Y.; Nishimura, Y.; Yamazaki, I.; Fukuzumi, S., Metal and size effects on structures and photophysical properties of porphyrin-modified metal nanoclusters. *J. Mater. Chem.* **2003,** *13* (12), 2890-2898.

331. Imahori, H.; Arimura, M.; Hanada, T.; Nishimura, Y.; Yamazaki, I.; Sakata, Y.; Fukuzumi, S., Photoactive Three-Dimensional Monolayers: Porphyrin−Alkanethiolate-Stabilized Gold Clusters. *J. Am. Chem. Soc.* **2001,** *123* (2), 335-336.

332. Fukuzumi, S.; Endo, Y.; Kashiwagi, Y.; Araki, Y.; Ito, O.; Imahori, H., Novel Photocatalytic Function of Porphyrin-Modified Gold Nanoclusters in Comparison with the Reference Porphyrin Compound. *J. Phys. Chem. B* **2003,** *107* (43), 11979-11986.

333. Badia, A.; Cuccia, L.; Demers, L.; Morin, F.; Lennox, R. B., Structure and Dynamics in Alkanethiolate Monolayers Self-Assembled on Gold Nanoparticles: A DSC, FT-IR, and Deuterium NMR Study. *J. Am. Chem. Soc.* **1997,** *119* (11), 2682-2692.

334. Brust, M.; Walker, M.; Bethell, D.; Schiffrin, D. J.; Whyman, R., Synthesis of thiol-derivatised gold nanoparticles in a two-phase Liquid–Liquid system. *J. Chem. Soc., Chem. Commun.* **1994,** (7), 801-802.

335. Templeton, A. C.; Wuelfing, W. P.; Murray, R. W., Monolayer-Protected Cluster Molecules. *Acc. Chem. Res.* **2000,** *33* (1), 27-36.

336. Hasobe, T.; Fukuzumi, S.; Kamat, P. V., Hierarchical assembly of porphyrins and fullerenes for solar cells. *Interface-Pennington* **2006,** *15* (2), 47.

337. Imahori, H.; Kashiwagi, Y.; Endo, Y.; Hanada, T.; Nishimura, Y.; Yamazaki, I.; Araki, Y.; Ito, O.; Fukuzumi, S., Structure and Photophysical Properties of Porphyrin-Modified Metal Nanoclusters with Different Chain Lengths. *Langmuir* **2004,** *20* (1), 73-81.

338. Ohyama, J.; Hitomi, Y.; Higuchi, Y.; Shinagawa, M.; Mukai, H.; Kodera, M.; Teramura, K.; Shishido, T.; Tanaka, T., One-phase synthesis of small gold nanoparticles coated by a horizontal porphyrin monolayer. *Chem. Commun.* **2008,** (47), 6300-6302.

339. Kanehara, M.; Takahashi, H.; Teranishi, T., Gold(0) Porphyrins on Gold Nanoparticles. *Angew. Chem.* **2008,** *47* (2), 307-310.

340. Beer, P. D.; Cormode, D. P.; Davis, J. J., Zinc metalloporphyrin-functionalised nanoparticle anion sensors. *Chem. Commun.* **2004,** (4), 414-415.

341. Buining, P. A.; Humbel, B. M.; Philipse, A. P.; Verkleij, A. J., Preparation of Functional Silane-Stabilized Gold Colloids in the (Sub)nanometer Size Range. *Langmuir* **1997,** *13* (15), 3921-3926.

342. Lusker, K. L.; Li, J.-R.; Garno, J. C., Nanostructures of Functionalized Gold Nanoparticles Prepared by Particle Lithography with Organosilanes. *Langmuir* **2011,** *27* (21), 13269-13275.

343. Sylvestre, J.-P.; Poulin, S.; Kabashin, A. V.; Sacher, E.; Meunier, M.; Luong, J. H. T., Surface Chemistry of Gold Nanoparticles Produced by Laser Ablation in Aqueous Media. *J. Phys. Chem. B* **2004,** *108* (43), 16864-16869.

344. Pfeiffer, C.; Rehbock, C.; Hühn, D.; Carrillo-Carrion, C.; de Aberasturi, D. J.; Merk, V.; Barcikowski, S.; Parak, W. J., Interaction of colloidal nanoparticles with their local environment: the (ionic) nanoenvironment around nanoparticles is different from bulk and determines the physico-chemical properties of the nanoparticles. *J. Royal Soc. Interface 11* (96), 20130931-20130931.

345. Ji, X.; Song, X.; Li, J.; Bai, Y.; Yang, W.; Peng, X., Size Control of Gold Nanocrystals in Citrate Reduction: The Third Role of Citrate. *J. Am. Chem. Soc.* **2007,** *129* (45), 13939-13948.

346. Togashi, T.; Izumi, A.; Kon, H.; Kanaizuka, K.; Ishizaki, M.; Miyake, R.; Chang, H.-C.; Haga, M.-a.; Sakamoto, M.; Kurihara, M., Spontaneous Construction of Nanoneedles Using Ruthenium Complex-conjugated Porphyrins on Substrates. *Chem. Lett.* **2014,** *43* (8), 1201-1203.

347. Jiang, H.; Sabarinathan, J., Effects of Coherent Interactions on the Sensing Characteristics of Near-Infrared Gold Nanorings. *J. Phys. Chem. C* **2010,** *114* (36), 15243-15250.

348. Hao, J.; Tingjie, L.; Jun, Y.; Silvia, M.; Jayshri, S., Optimization of gold nanoring arrays for biosensing in the fiber-optic communication window. *Nanotechnology* **2013,** *24* (46), 465502.

349. Wang, L.; Montagne, F.; Hoffmann, P.; Pugin, R., Gold nanoring arrays from responsive block copolymer templates. *Chem. Commun.* **2009,** (25), 3798-3800.

350. Taylor, A. M., Nanopatterns of zinc phthalocyanines, gold nanoparticles, and porphyrins prepared using particle lithography: Characterization of patterning steps with scanning probe microscopy. *Louisiana State University, Baton Rouge, Louisiana* **2017,** *Dissertation*.

351. Chambers II, P. C., Self-assembly mechanisms of organosilanes and porphyrins investigated with scanning probe microscopy. *Louisiana State University, Baton Rouge, Louisiana* **2017,** *Dissertation*.

352. Amendola, V.; Meneghetti, M., Size Evaluation of Gold Nanoparticles by UV−vis Spectroscopy. *J. Phys. Chem. C* **2009,** *113* (11), 4277-4285.

353. Wang, H.; Brandl, D. W.; Nordlander, P.; Halas, N. J., Plasmonic Nanostructures: Artificial Molecules. *Acc. Chem. Res.* **2007,** *40* (1), 53-62.

354. Jones, M. R.; Osberg, K. D.; Macfarlane, R. J.; Langille, M. R.; Mirkin, C. A., Templated Techniques for the Synthesis and Assembly of Plasmonic Nanostructures. *Chem. Rev.* **2011,** *111* (6), 3736-3827.

355. Noy, A.; Vezenov, D. V.; Lieber, C. M., Chemical force microscopy. *Annu. Rev. Mater. Sci.* **1997,** *27* (1), 381-421.

356. Noy, A.; Frisbie, C. D.; Rozsnyai, L. F.; Wrighton, M. S.; Lieber, C. M., Chemical Force Microscopy: Exploiting Chemically-Modified Tips To Quantify Adhesion, Friction, and Functional Group Distributions in Molecular Assemblies. *J. Am. Chem. Soc* **1995,** *117* (30), 7943-7951.

357. Lu, L.; Xu, S.; Zhang, D.; Garno, J. C., Sample stage designed for force modulation microscopy using a tip-mounted AFM scanner. *Analyst* **2016,** *141* (5), 1753-1760.

APPENDIX A. SUPPORTING INFORMATION FOR CHAPTER 3

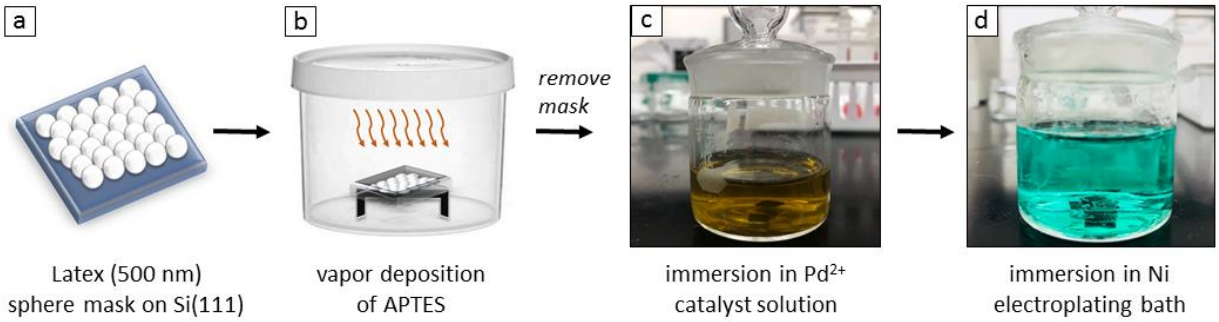

Figure A.1. Overview of the steps for chemical fabrication of metallized nanorings using immersion particle lithography. (a) A surface mask of monodisperse spheres was prepared on Si(111) by drying a drop of colloidal latex suspension. (b) A heated vapor of 3-aminopropyltriethoxysilane (APTES) was applied, then the mask was removed by rinsing and sonication. (c) The sample with APTES nanorings was immersed in catalyst solution (amber color). (d) In the final step, the sample was immersed in a Ni plating bath (blue color) to form nanostructures.

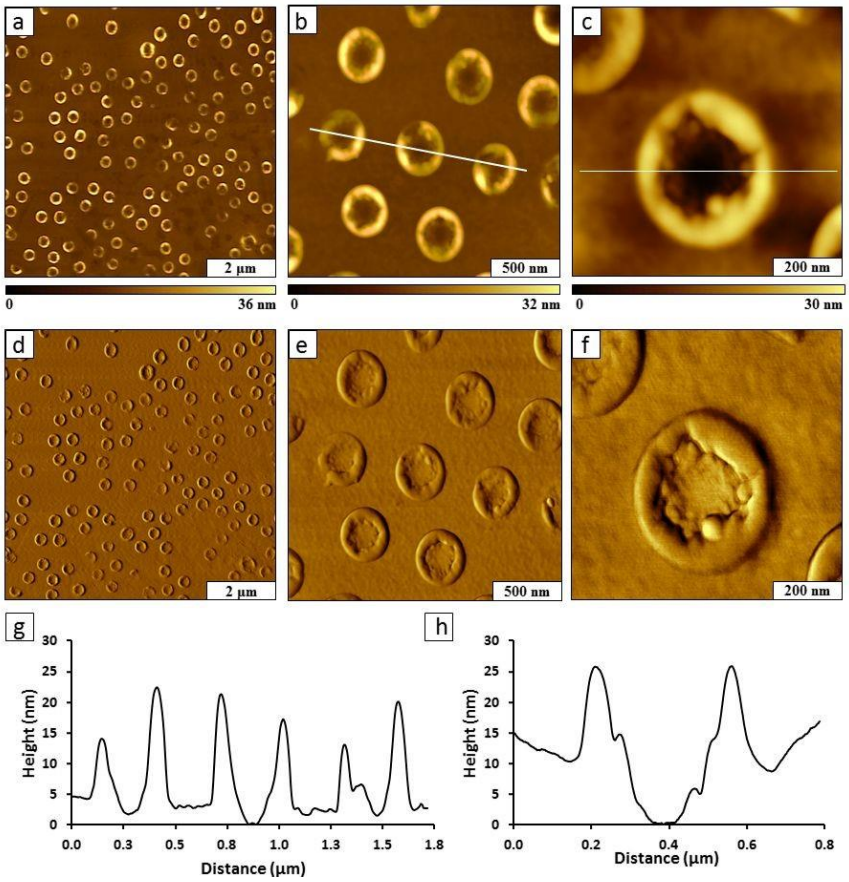

Figure A.2. The periodic arrangement of metal nanorings on nanopatterns of 3-aminopropyl triethoxysilane (APTES), shown with successive zoom-in atomic force microscopy (AFM) images. Samples were prepared by electroless deposition of Ni using a Pd catalyst. (a) Topography view of a wide area (8 × 8 µm^2) of nanorings, prepared with 500 nm silica spheres. (b) Zoom-in (2 × 2 µ m^2) topograph; (c) close-up topography view of an individual nanoring; (d) concurrently acquired phase image for *a*; (e) phase image for *b*; (f) phase image for *c*. (g) Height profile is drawn across three nanorings for the line in *b*; (h) cursor profile across a single nanoring in *c*. Images were acquired using tapping-mode AFM in ambient air. This is a replicate experiment for the example of Figure 3.1 which demonstrates the superb reproducibility of chemistry-based approaches with colloidal lithography.

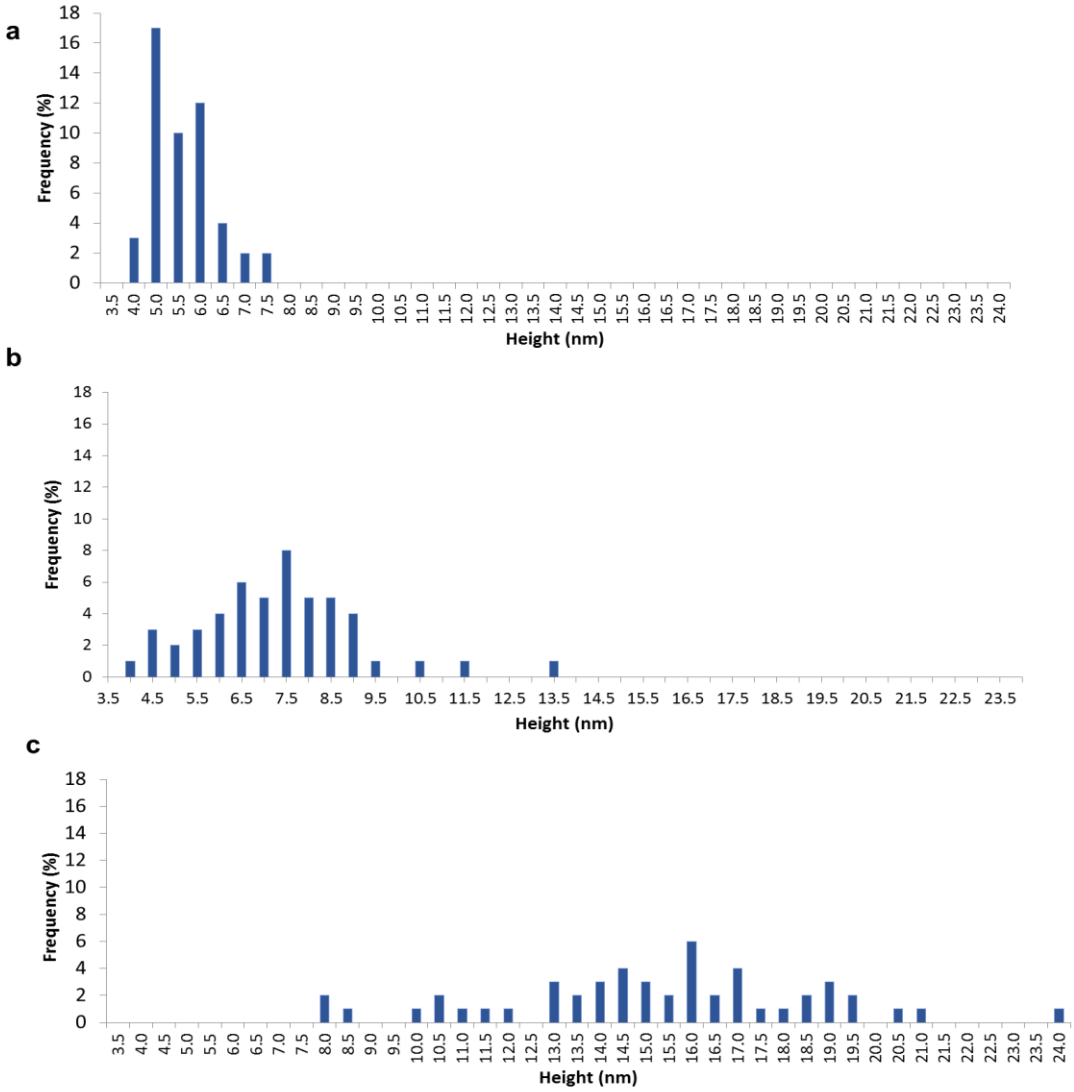

Figure A.3. Height analysis for surface structures after each key step of sample preparation. Histogram representing height distribution of (a) APTES nanorings, (b) after attaching Pd to APTES nanorings and (c) Ni nanorings. The sizes of the nanorings increased after each step as catalyst and Ni deposits were added. To collect the data, representative cursor profiles of nanostructures (n = 50) were selected from several areas of each sample.

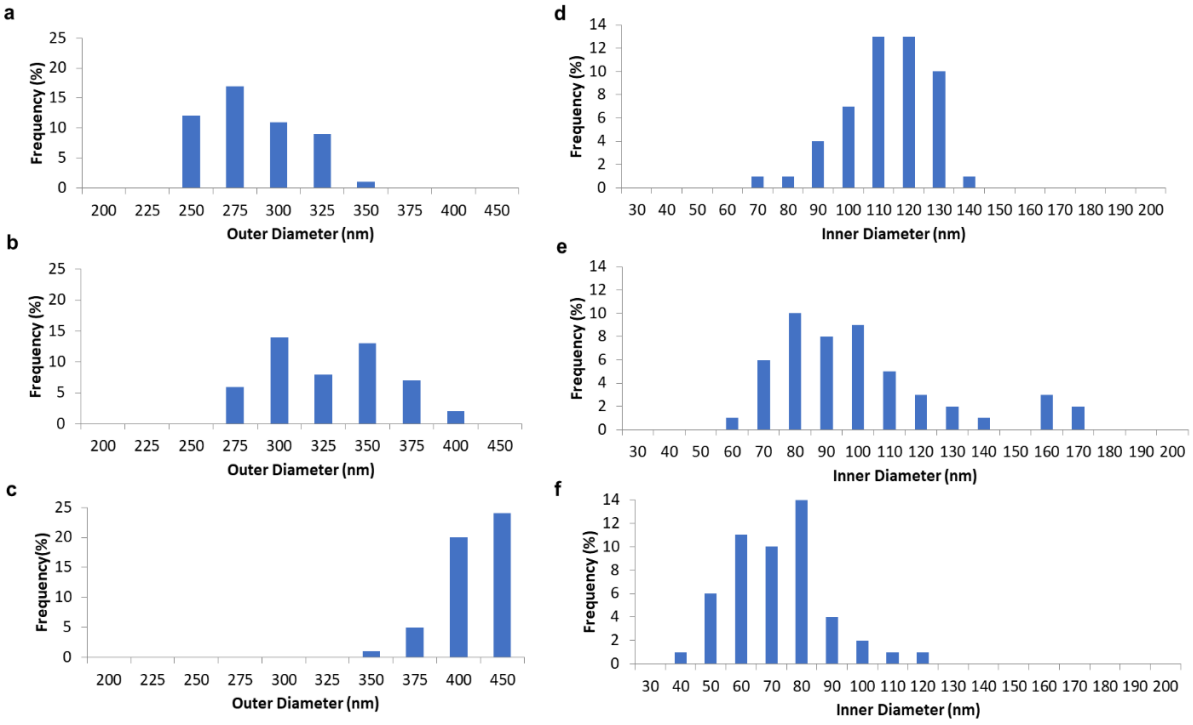

Figure A.4. Histogram analysis of the changes in width for the outer and inner diameter of the nanorings after each reaction step. Histogram representing outer diameter of (a) APTES nanorings; (b) after attaching Pd; (c) Ni nanorings. The nanorings grew in width at each step of the reaction, however the inside diameters of the center holes became smaller as the nanorings increased in lateral dimensions. Changes measured for the inner diameter of (d) APTES nanorings; (e) after attaching Pd, and (f) Ni nanorings. The charts represent measurements of cursor profiles of 50 individual nanorings selected from several areas of each sample.

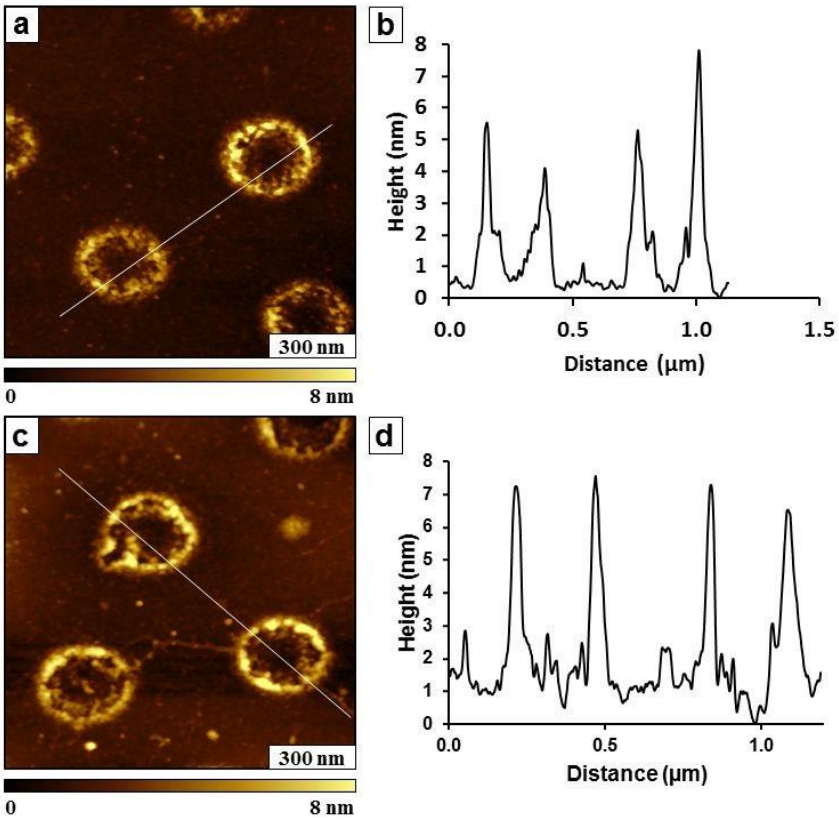

Figure A.5. A control experiment was designed to assess the role of the Pd catalyst in forming Ni coatings. Images are shown for APTES nanorings after conducting electroless nickel deposition without a catalyst; (a) nanorings of APTES, topography image; (b) cursor profile traced across two rings in *a*. (c) Topograph after immersion of the sample in a Ni plating bath; (d) cursor profile for the line in *c*. In this experiment, samples containing

APTES nanorings were directly immersed in Ni electroless plating bath, skipping the step of immersion in a Pd catalyst solution. After 3 h immersion in the Ni plating bath, the samples were rinsed with ultrapure water and dried with nitrogen. Samples were then imaged with tapping-mode AFM to evaluate changes in height and morphology. There were no significant differences in dimensions detected for APTES nanorings after Ni plating in the absence of a catalyst. In data not shown, MSM-AFM images likewise did not successfully resolve the presence of magnetic materials, further indicating the essential role of the catalyst for electroless plating of Ni.

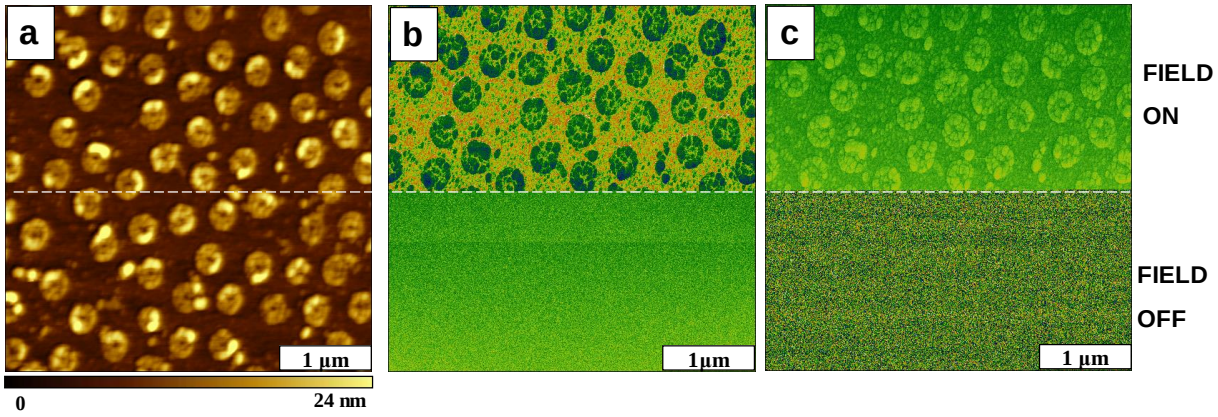

Figure A.6. Changes in MSM images with and without an AC electromagnetic field tested with a sample of Ni nanorings at a field strength of 0.2 T. (a) MSM topograph of Ni nanostructures (4 ×4 μm^2); (b) simultaneously acquired MSM amplitude frame; (c) corresponding MSM phase image. The field was turned off halfway through the data acquisition.

During the first half of the scan, the MSM amplitude and phase channels reveal distinct color contrast for the areas of Ni nanorings. Topography frames reveal sample topology by mapping signals of the difference between the top and bottom elements of a quadrant photodetector, which result from the up and down vertical motion of the AFM probe. The phase and amplitude channels are derived with lock-in detection, by referencing the input waveform used to drive sample modulation as a way to map dynamic changes in sample vibration during the scan. When the AC electromagnetic field was turned off during the second half of imaging, neither the amplitude or phase channels produce resolvable details, indicating when there was no sample vibration. The top and bottom half of the topography frame are indistinguishable in this example, which indicates that sample modulation occurs mainly in the z-direction, since lateral vibration would produce broadening of features in topography images.

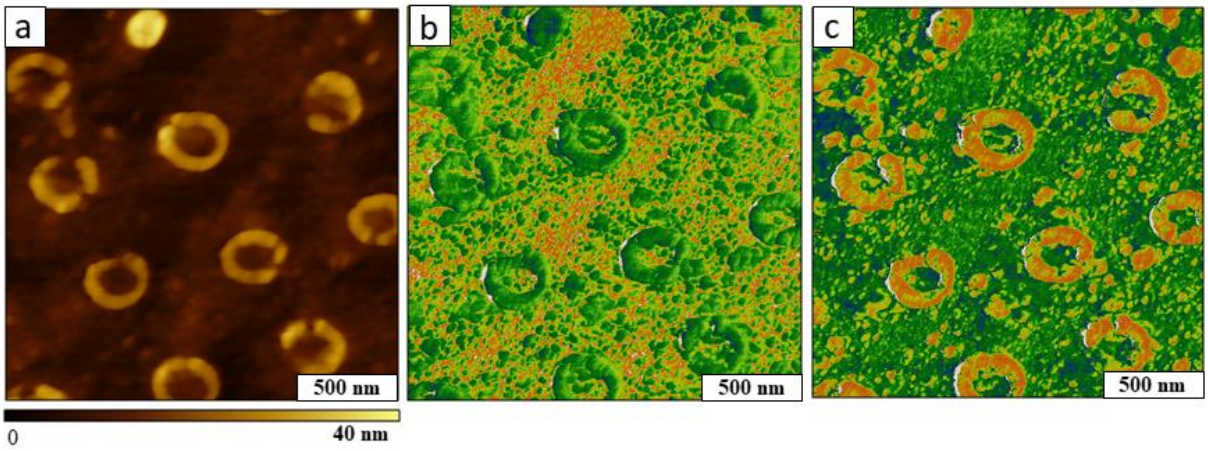

Figure A.7. Images acquired with MSM-AFM for Ni nanorings shown for the replicate sample of Figure A.1. Images were acquired in ambient air with 0.2 T field strength and a resonance frequency of 222 kHz. (a) MSM-topography frame; concurrently acquired (b) phase and (c) amplitude channels for a 2 × 2 μm^2 area. The fine details of the surface corrugation in areas between the Ni nanorings can be sensitively resolved in the phase image.

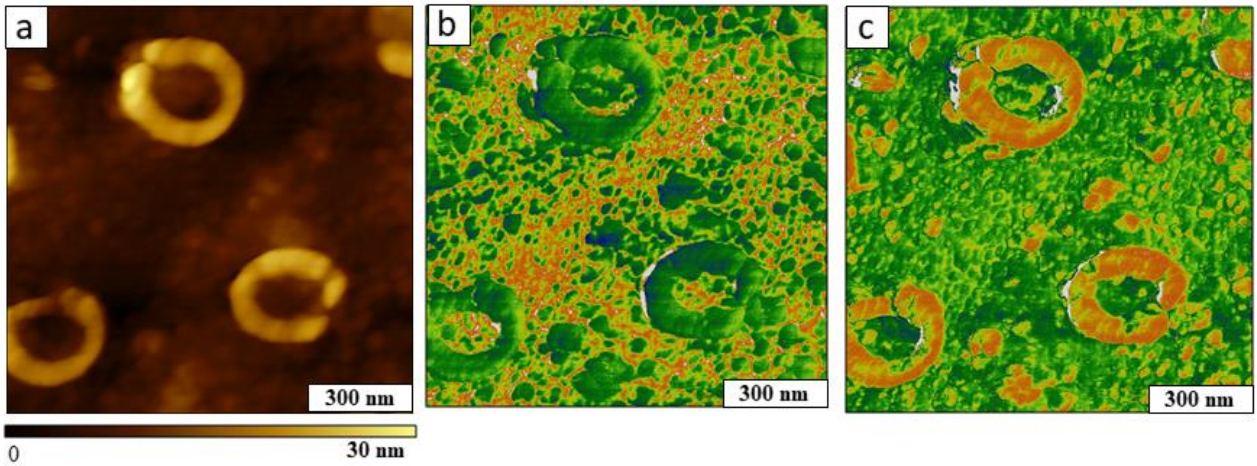

Figure A.8. Three nickel rings shown with MSM-AFM for the replicate sample of Figure A.2. Images were acquired in ambient air with 0.2 T field strength and a resonance frequency of 222 kHz. (a) MSM-topography frame; concurrently acquired (b) phase and (c) amplitude channels for a 2 × 2 μm^2 area.

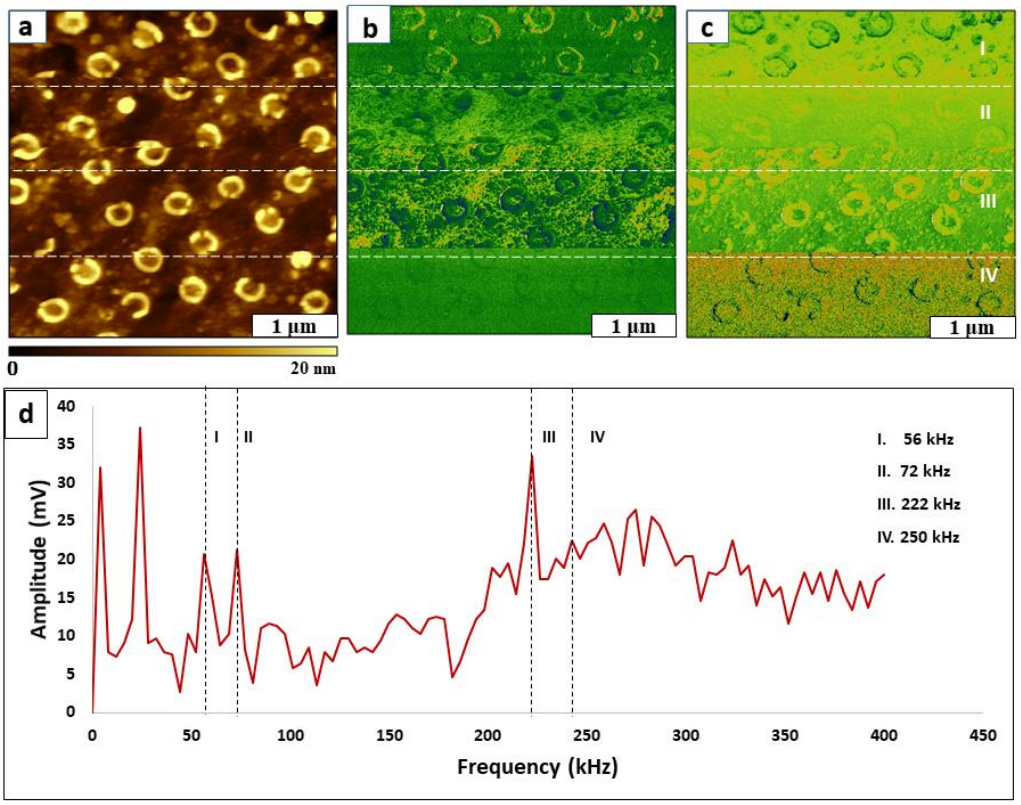

Figure A.9. Changes in contrast within a single frame were detected during MSM imaging of Ni nanopatterns shown in Figure A.1 using selected resonance frequencies to drive the sample oscillation. (a) MSM topography channel; (b) concurrently acquired MSM amplitude and (c) MSM phase image. (d) Frequency spectra obtained with a field strength of 0.2 T. Images were acquired in ambient air for an image area of $4 \times 4\ \mu m^2$.

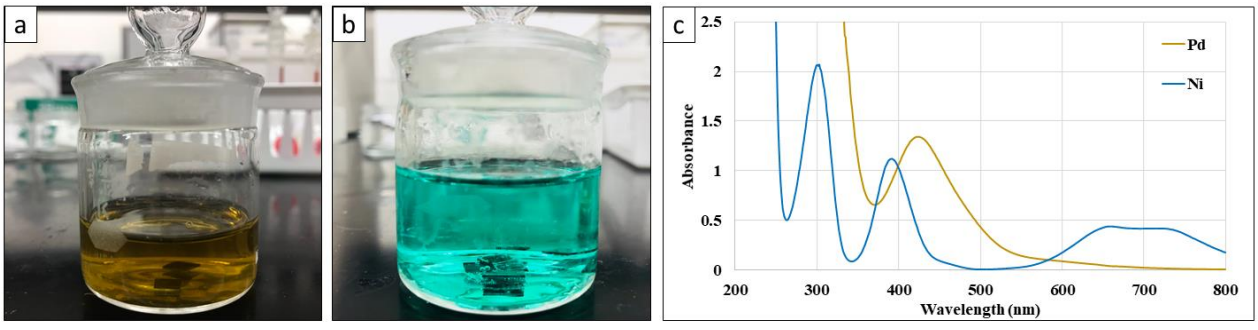

Figure A.10. Si(111) substrates with APTES nanorings immersed in each reaction solutions used for nickel electroless deposition. (a) Pd catalyst solution; (b) nickel electroless plating bath; (c) UV-visible spectra of Pd and Ni solutions. When the samples were immersed in a nickel solution, the formation of air bubbles around the liquid/substrate interface was observed. This occurred as a result of H_2 formation during the reaction between Pd and Ni^{2+} ions that undergo autocatalytic reaction.

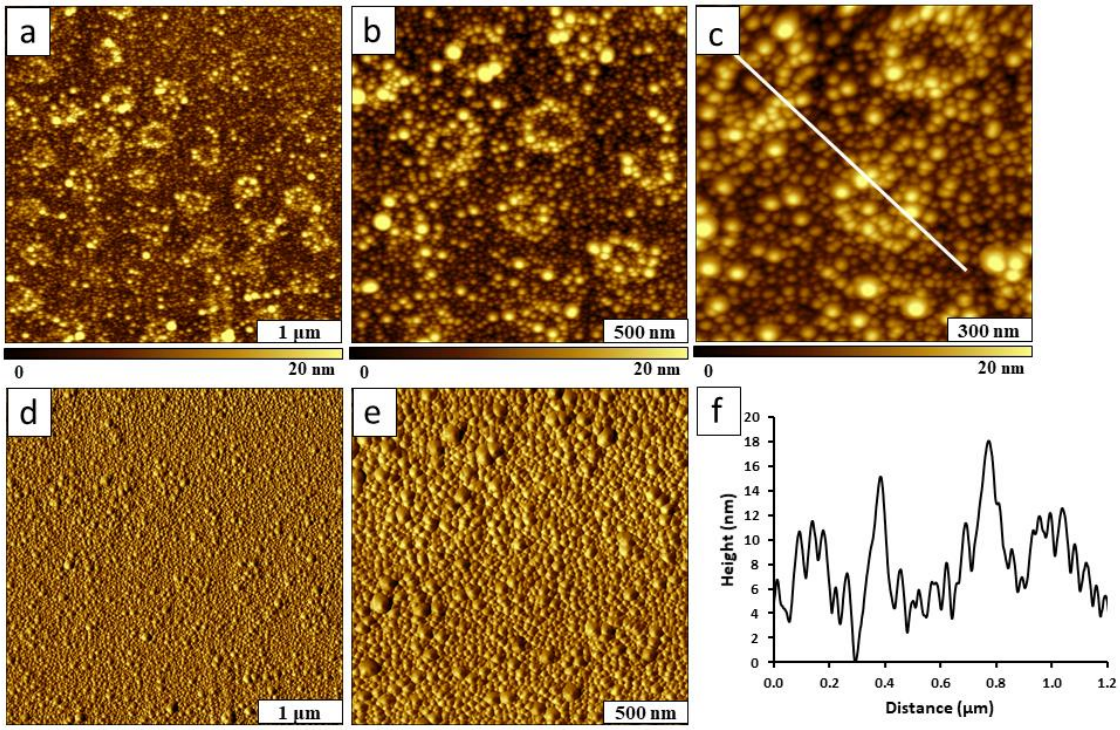

Figure A.11. Successive zoom-in images of Ni nanorings prepared with longer immersion (6 h) time. (a) Tapping-mode topography image (4× 4 μm^2); (b) zoom-in view of a 2 × 2 μm^2 area; (c) magnified view of three nanorings (1.2 × 1.2 μm^2); (d) phase channel for *a*; (e) corresponding phase channel for *b*; (f) the cursor profile for line drawn on *c*.

The electroless deposition of nickel was conducted for 6 h to examine how the morphology and the size change with longer immersion times. The height of resultant nanorings remained fairly similar to the nanostructures produced with 3 h reaction. However, longer deposition formed more Ni deposits in the surrounding areas of the actual nanorings.

APPENDIX B. OPERATING PROCEDURE OF MAGNETIC SAMPLE MODULATION (MSM)

1. Use the MAC mode sample stage and a contact mode nosecone that does not contain any magnetic parts for MSM, shown in Figure B.1.

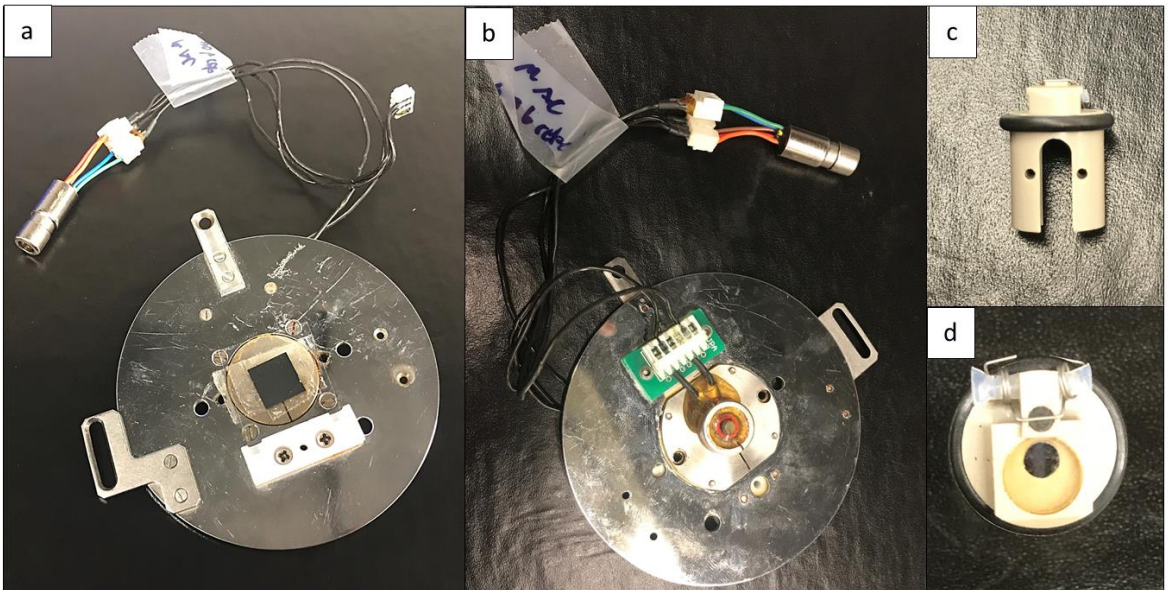

Figure B.1. Photographs of the equipment used for MSM imaging. (a) Front side of the MAC mode sample stage; (b) back side showing the wire coil solenoid; (c) side view of the contact mode nose cone; (d) top view of the nosecone assembly.

2. Connect BNC cables between the AFM controller (model N9605A), head electronic box (HEB) and MAX II controller as shown in Figure B.2.

- The AUX output of the HEB back panel should be connected to the phase output of the MAC III controller.
- A second cable should be connected to the amplitude output of the MAC III controller and to the AUX IN of the AFM controller.

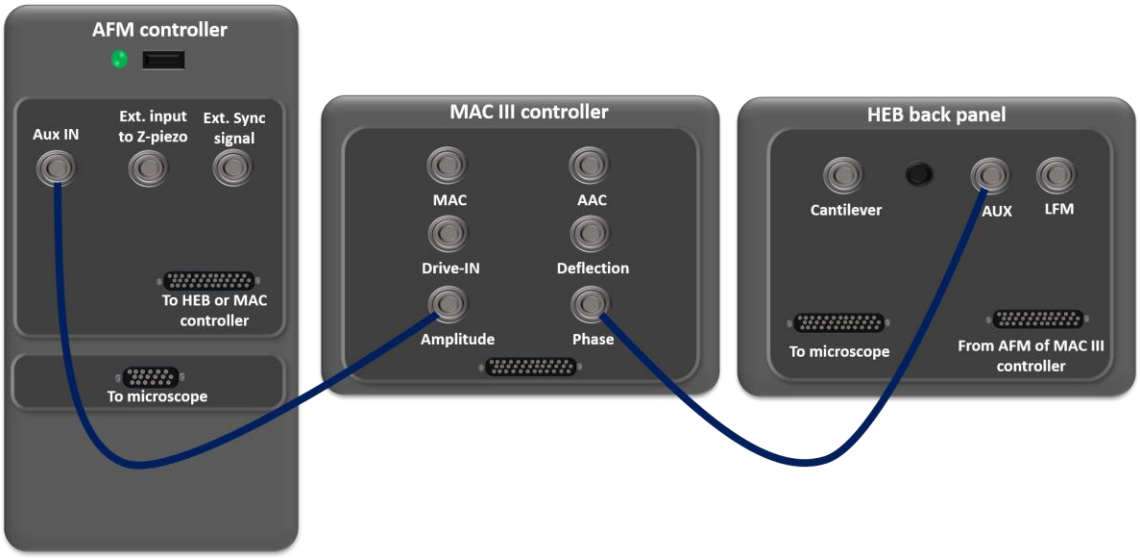

Figure B.2. Cable diagram for MSM operation and data collection.

3. Install the nosecone into the AFM multipurpose scanner and place the sample onto the MAC mode sample stage.
4. Once the sample is mounted, connect the wires of sample stage to the bottom of the microscope stand (Figure B.3).

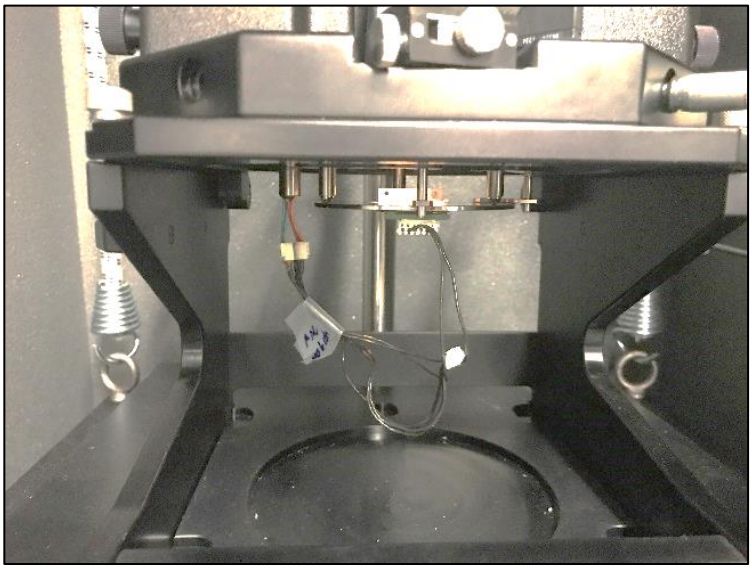

Figure B.3. Connect the lead wires of the sample stage to the scanner support stand.

5. Use a soft cantilever for contact mode operation for MSM-AFM. (Tips with magnetic coating or high spring constants should not be used.)
6. Install the AFM tip onto the scanner and connect the scanner into the microscope. Before installing the scanner to the microscope, the sample stage approach distance should be adjusted using the "open/close' switch of the head electronic box to leave a sufficient gap between the scanner and the sample.
7. In the PicoView (v 1.20.2) software, select contact mode (Figure B.4a) parameters under the main menu. Focus the laser spot on the tip and program the acquisition software with typical contact mode settings: deflection to -1 and friction to 0 (Figure B.4b).

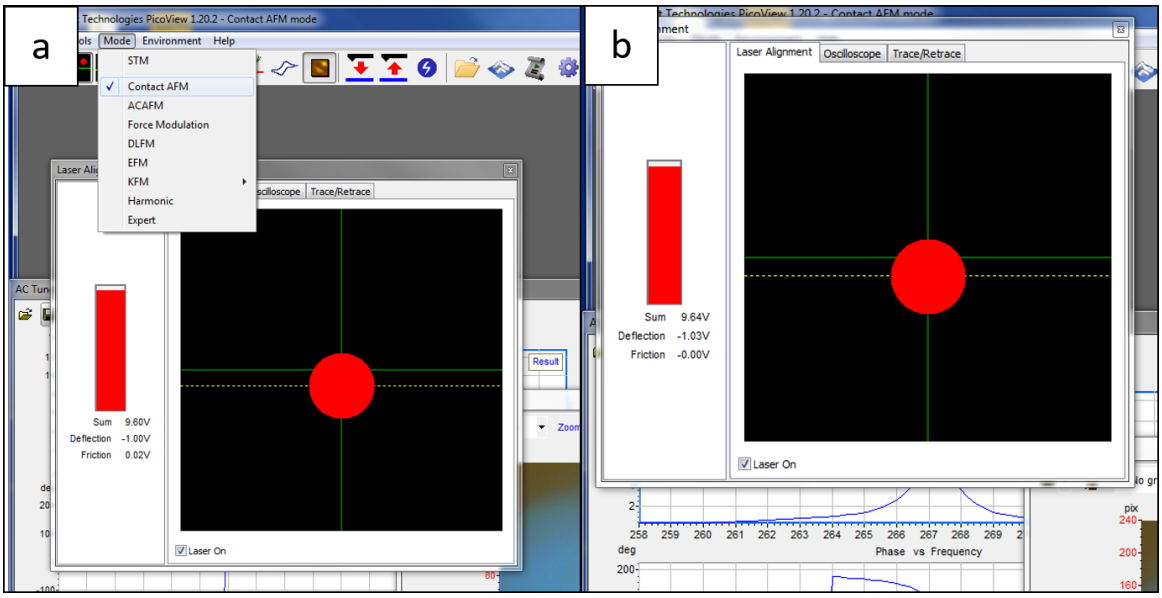

Figure B.4. Software settings for MSM (a) contact mode selection (b) laser alignment.

9. Open the AFM AC mode frequency plot window from AC tune under the main menu. and select MAC mode settings under drive mechanism (Figure B.5).

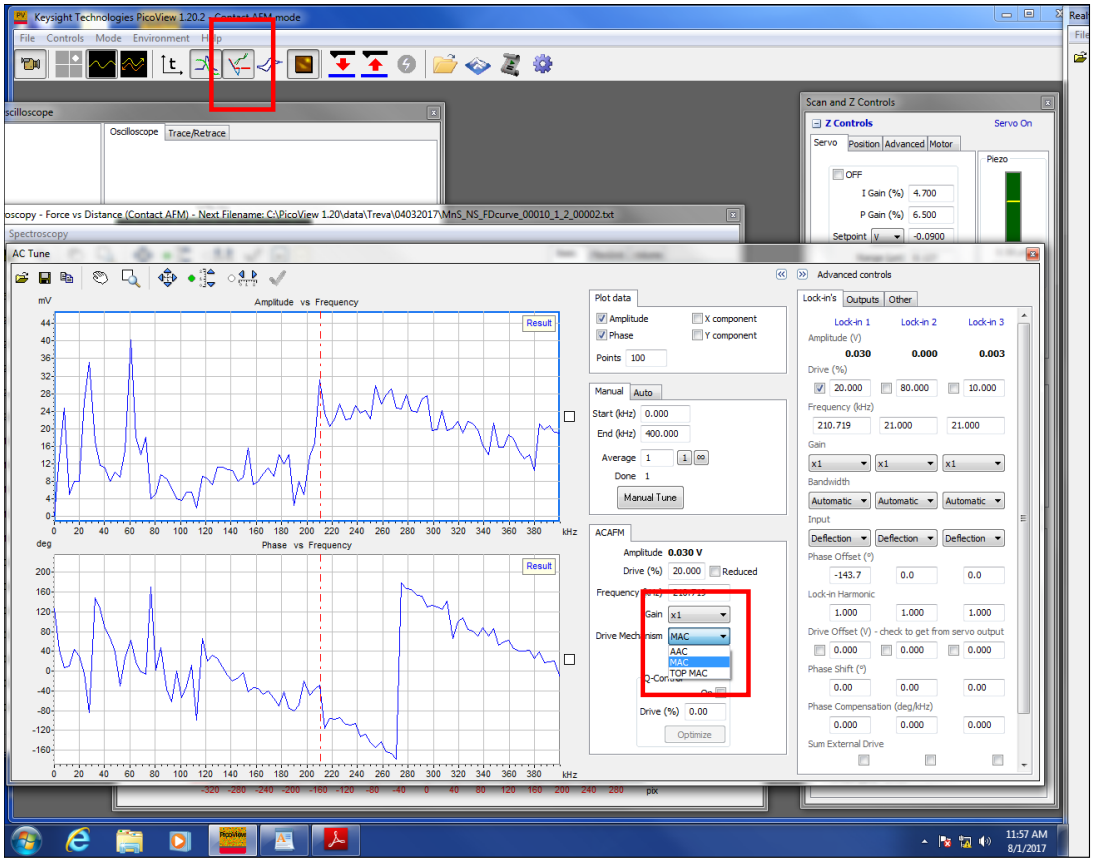

Figure B.5. AC tune and MAC mode settings selection.

11. On the output tab of advanced AC controls window, set Aux1 to Amplitude1 (corresponds to MSM amplitude), Aux 2 to Phase1 (corresponds to MSM amplitude). Uncheck the pass-through boxes for both Aux 1 and Aux 2 to pass the signal directly from the microscope to the AFM controller (Figure B.6).

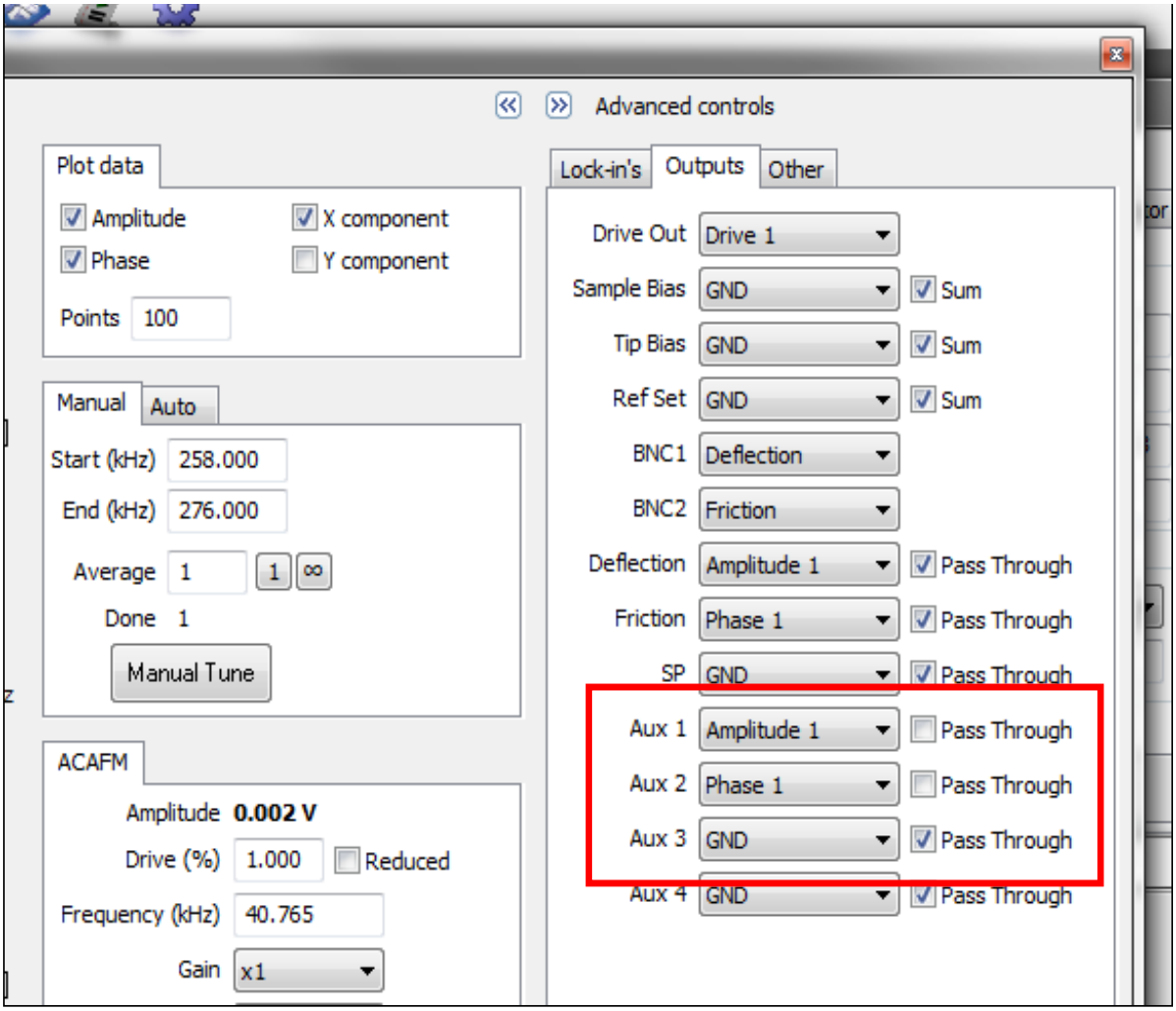

Figure B.6. Selection of output channels for MSM imaging.

10. In the real-time imaging window, choose eight channels of Topography (trace and retrace), Aux1(trace and retrace), Aux2 (trace and retrace), Deflection and Friction (Figure B.7)

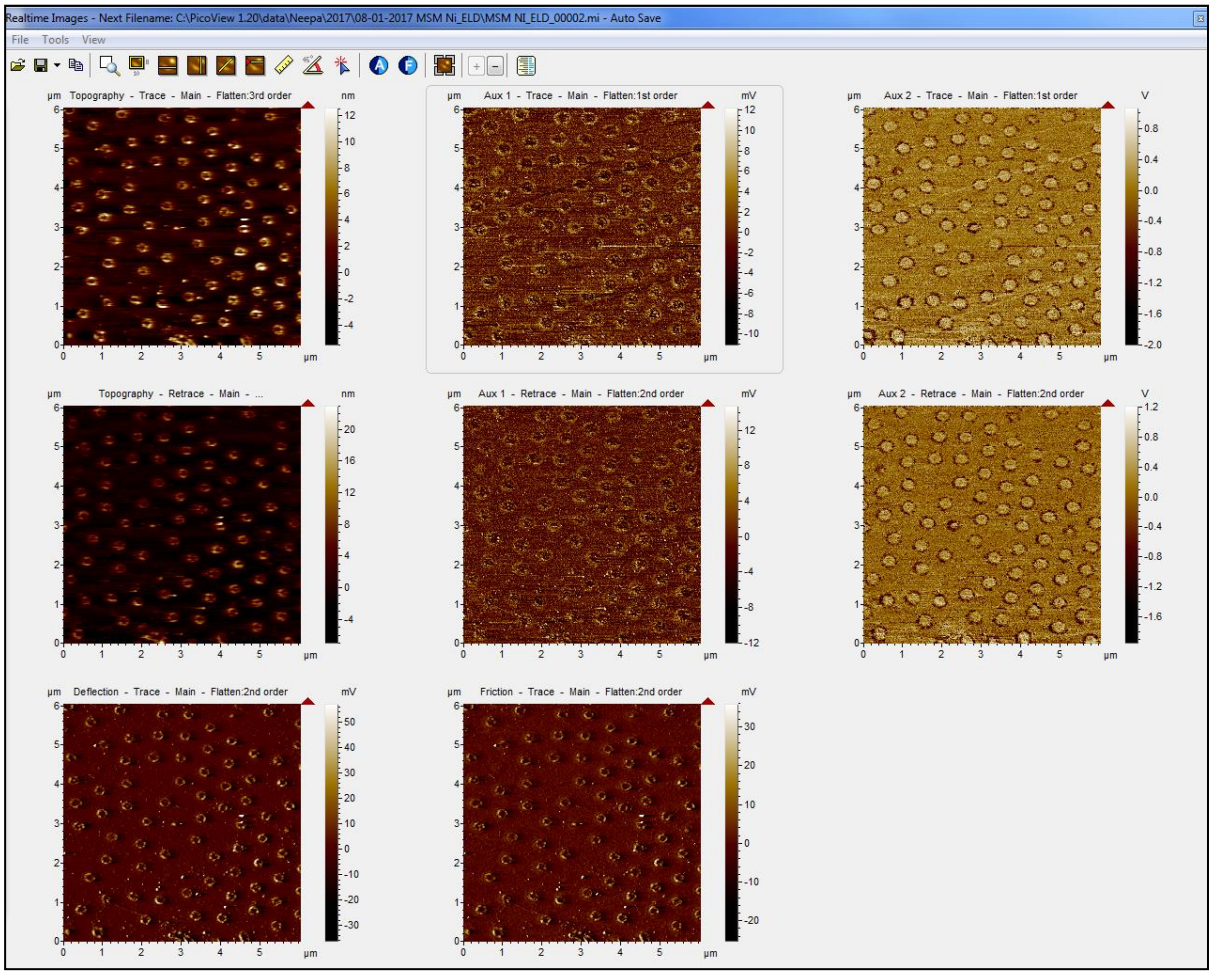

Figure B.7. Real time imaging windows selected for MSM imaging.

11. Acquire frequency spectra when the tip is disengaged. With the manual tune tab, enter 0 kHz as the starting frequency and 400 kHz as the end frequency. Make sure the drive mechanism is set to MAC. Then obtain a frequency sweep. Ideally, no peaks will be present when the tip is disengaged (Figure B.8).

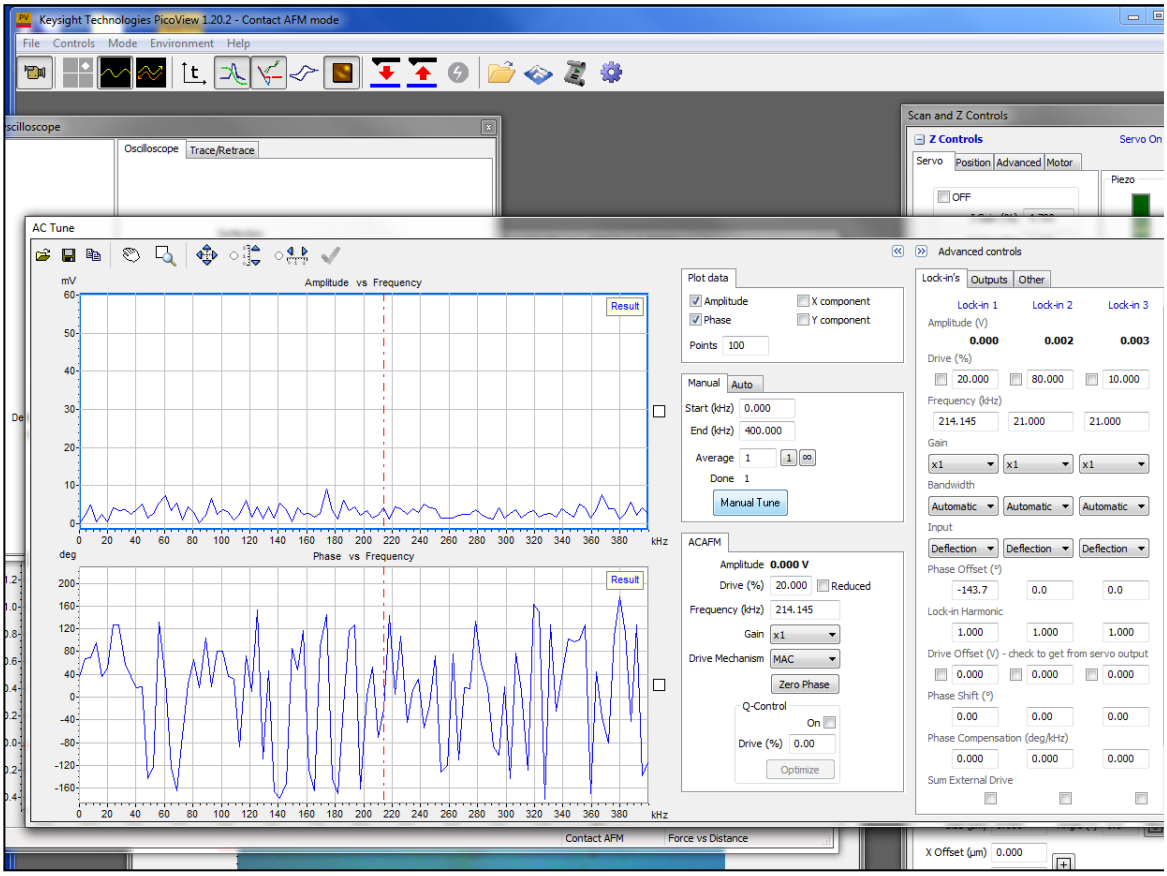

Figure B.8. Frequency spectra are obtained while the tip is disengaged.

12. In the scan and z controls window, select the Servo tab and enter force setpoint as 0 V. Then approach the tip to make contact with the sample (Figure B.9).

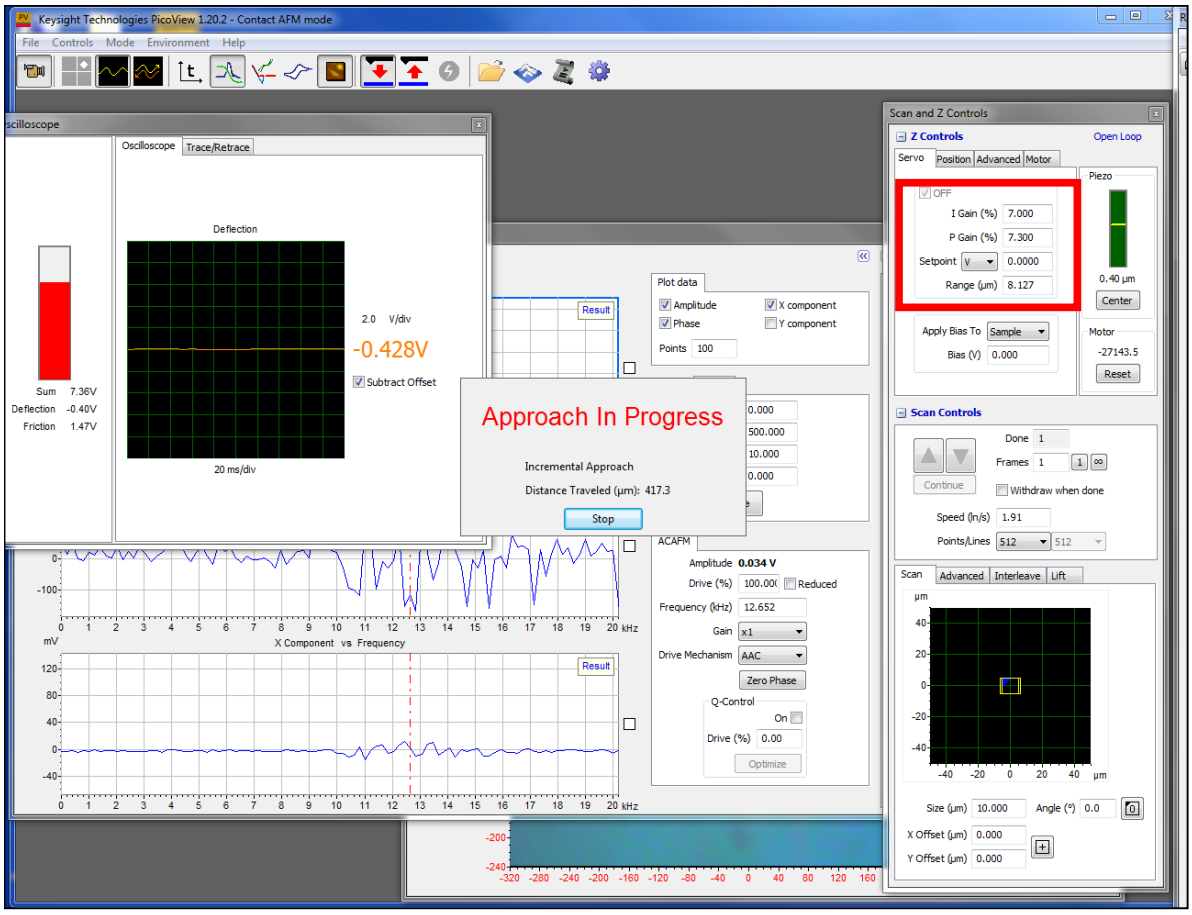

Figure B.9. PicoView software messages observed during the approach cycle for the AFM tip to make contact with sample.

13. Once tip has made contact with the sample, acquire images in contact mode to find an area that contains features of interest.
14. Next, obtain frequency sweeps while tip remains in contact with the sample (Figure B.10). Enter a value for Drive %, select the MAC drive mechanism in the manual tune tab. Check the box of drive % of the lock-in 1 channel in the lock-in tab to ensure that the AC drive is ON.

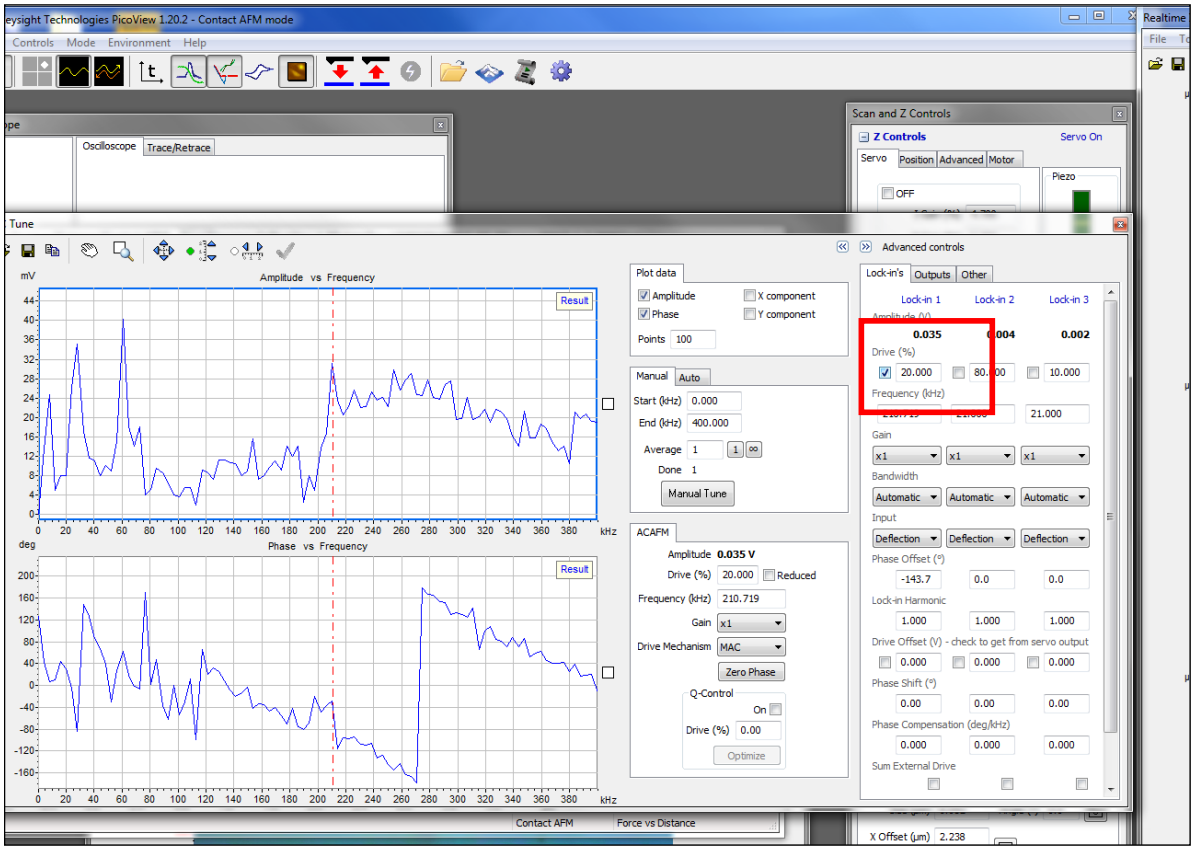

Figure B.10. Frequency spectra acquired when the tip is engaged with the sample.

15. Several sample resonance peaks are generated when the tip is engaged. Resonance peaks with higher amplitude can be selected for imaging. Contrast changes in the amplitude and phase channels can be evaluated to select the best resonance frequency for imaging. (Figure B.11)

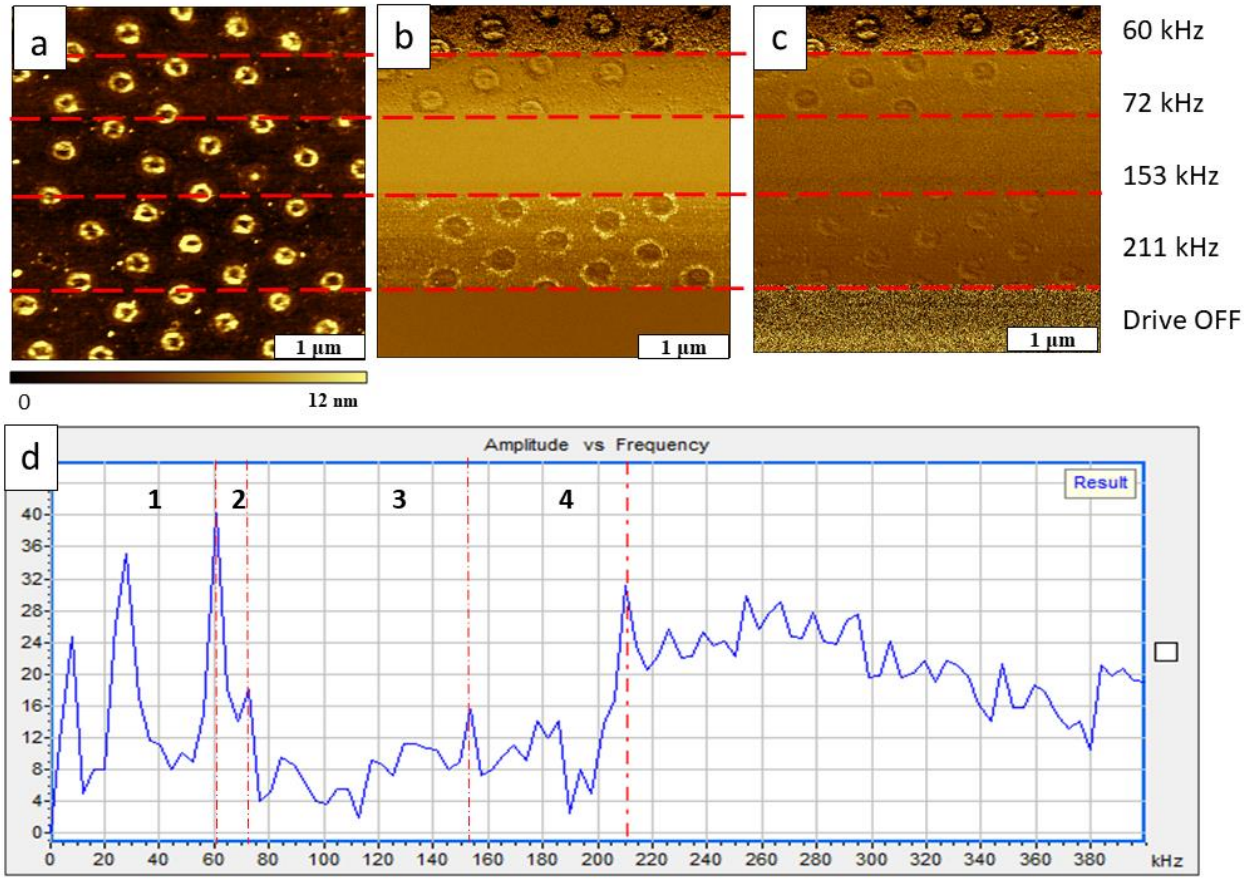

Figure B.11. View of Ni nanostructures acquired with selected resonance frequencies using dynamic MSM-AFM. (a) Topography; (b) MSM-amplitude; (c) MSM-phase; (d) spectrum showing the selected frequencies.

APPENDIX C. LETTER OF PERMISSION FOR CHAPTER 3

Home | Account Info | Help

Title: Nickel Nanofilms Electrolessly Deposited on Organosilane Nanorings and Characterized by Contact Mode AFM Combined with Magnetic Sample Modulation

Author: Neepa M. K. Kuruppu Arachchige, Phillip C. Chambers, Ashley M. Taylor, et al

Publication: ACS Applied Nano Materials

Publisher: American Chemical Society

Date: Mar 1, 2019

Logged in as:

Neepa Malsi Kumari Kuruppu Arachchige

Account #:

3001394177

LOGOUT

PERMISSION/LICENSE IS GRANTED FOR YOUR ORDER AT NO CHARGE

This type of permission/license, instead of the standard Terms & Conditions, is sent to you because no fee is being charged for your order. Please note the following:

- Permission is granted for your request in both print and electronic formats, and translations.
- If figures and/or tables were requested, they may be adapted or used in part.
- Please print this page for your records and send a copy of it to your publisher/graduate school.
- Appropriate credit for the requested material should be given as follows: "Reprinted (adapted) with permission from (COMPLETE REFERENCE CITATION). Copyright (YEAR) American Chemical Society." Insert appropriate information in place of the capitalized words.
- One-time permission is granted only for the use specified in your request. No additional uses are granted (such as derivative works or other editions). For any other uses, please submit a new request.

BACK CLOSE WINDOW

APPENDIX D. SUPPORTING INFORMATION FOR CHAPTER 4

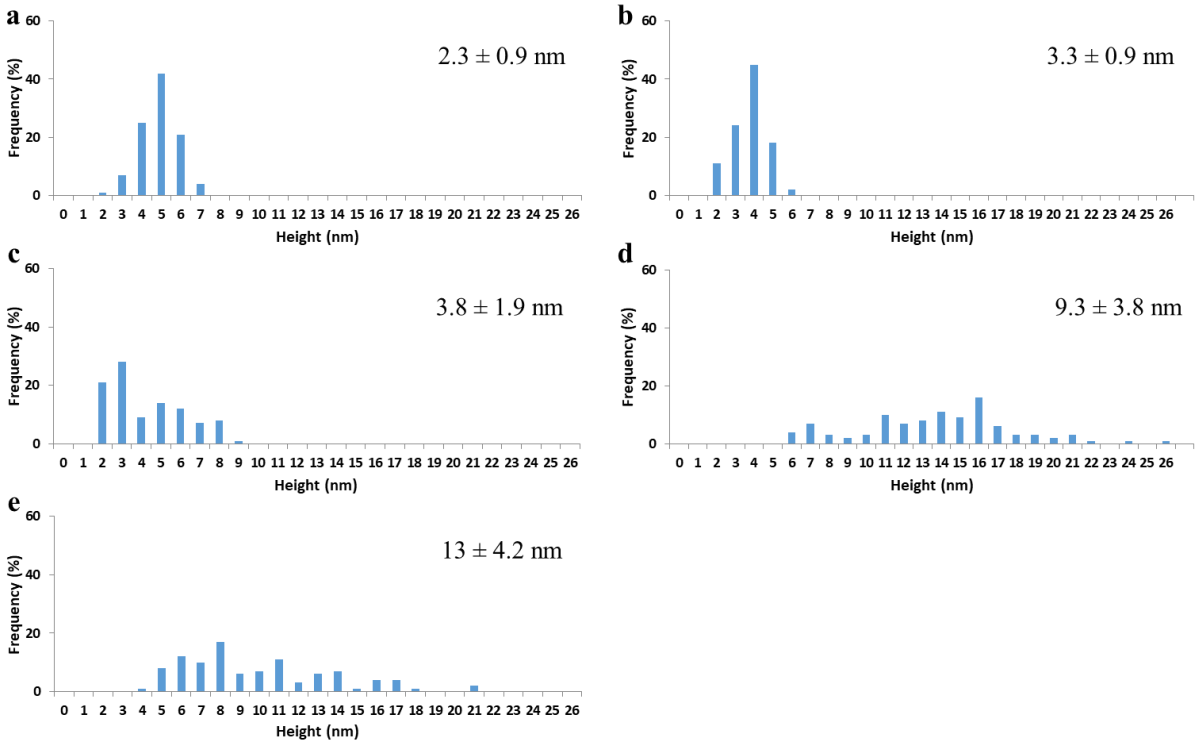

Figure D.1. Distribution of the heights of OTS assemblies on Si(111) when selected amounts of water were added to the reaction vessels. Histograms are shown for (a) 0 mg; (b) 2 mg; (c) 10 mg; (d) 100 mg; and (e) 300 mg added to the containers. Information of the heights were obtained from individual cursors drawn across 100 different nanostructures within atomic force microscopy (AFM) topography images. The average and standard deviation values are shown in the right corner of each graph.

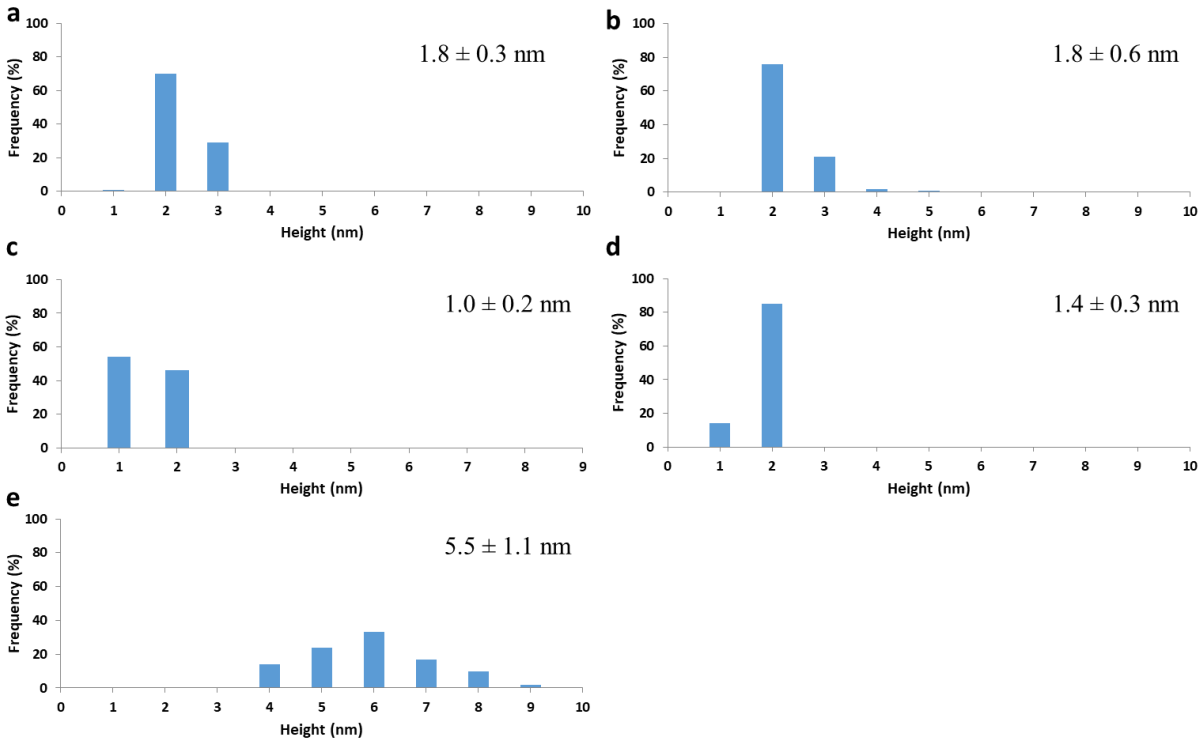

Figure D.2. Successive changes in the height of OTS assemblies formed on mica with selected amounts of water added to reaction vessels. Histograms are shown for samples prepared (a) 0 mg; (b) 2 mg; (c) 10 mg; (d) 100 mg; and (e) 300 mg of added water. Cursor profiles were taken across 100 individual nanostructures. The average value and standard deviation are shown in the right corner of each plot.

Table D.1. Surface coverage of OTS measured for silicon and mica wetted with increments of water added to the reaction vessel.

	Silicon	**Mica**
Water Added (mg)	Surface coverage (%)	Surface coverage (%)
0	15 ± 3.3	3.4 ± 2.5
2	9.7 ± 2.9	3.6 ± 0.8
10	23 ± 4.8	68 ± 4.0
100	32 ± 5.0	92 ± 1.3
300	56 ± 4.3	93 ± 4.9

The overall surface coverage of OTS ranged from 10% to 56% on silicon and from 3% to 93% on mica. The trend for surface coverage increased with water content for both substrates, however the hydrophilic interface mica showed higher values compared to silicon. The water condensed to form a continuous film and spread out on mica, and the subsequent binding of OTS followed the arrangement of water deposits to assemble as a film. The water repellency of silicon produced a discontinuous arrangement of droplets, preferentially localizing at the meniscus sites of silicon. The contained areas enclosed in the water meniscus sites of the latex particle mask generated multilayered assemblies of nanorings on the hydrophobic interface of silicon. The estimates of surface coverage of OTS films formed on Si(111) and mica(0001) were derived by pixel counting, using a manually derived color threshold. Values in the table are an average obtained from 10 topographs of different regions of the samples. ($2 \times 2\ \mu m^2$)

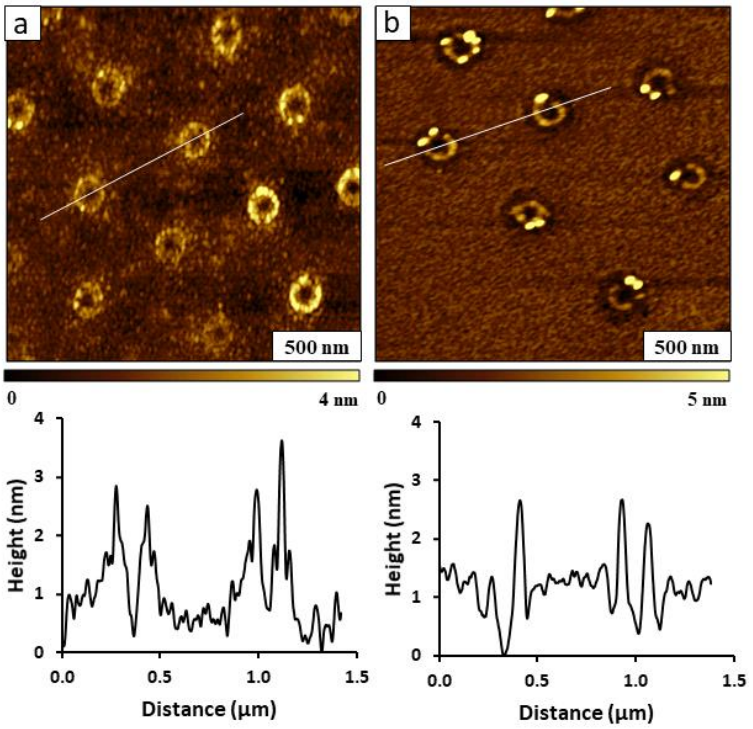

Figure D.3. Nanorings of OTS formed on (a) Si(111) and (b) mica substrates with vapor deposition with ambient drying of the masked substrates. Samples with latex films were dried under ambient conditions for 4 h on silica substrates and for 24 h on mica. The samples were immediately transferred to glass jars containing 300 µL of neat octadecyltrichlorosilane (OTS).

Additional water was not added to the jars. Vapor deposition was completed after 18 h exposure for Si(111) and 6 h for mica. The sphere mask was removed from Si(111) samples by sonication in ethanol. Mica samples were multiple rinses to remove the latex mask, without sonication. The OTS layers on Si(111) had an average height of 4.2 ±0.9 nm (*n*=50) with a surface coverage of 26 ± 5%. The average height for the samples prepared on mica measured 2.6 ± 0.6 nm with 66 ± 8 % surface coverage.

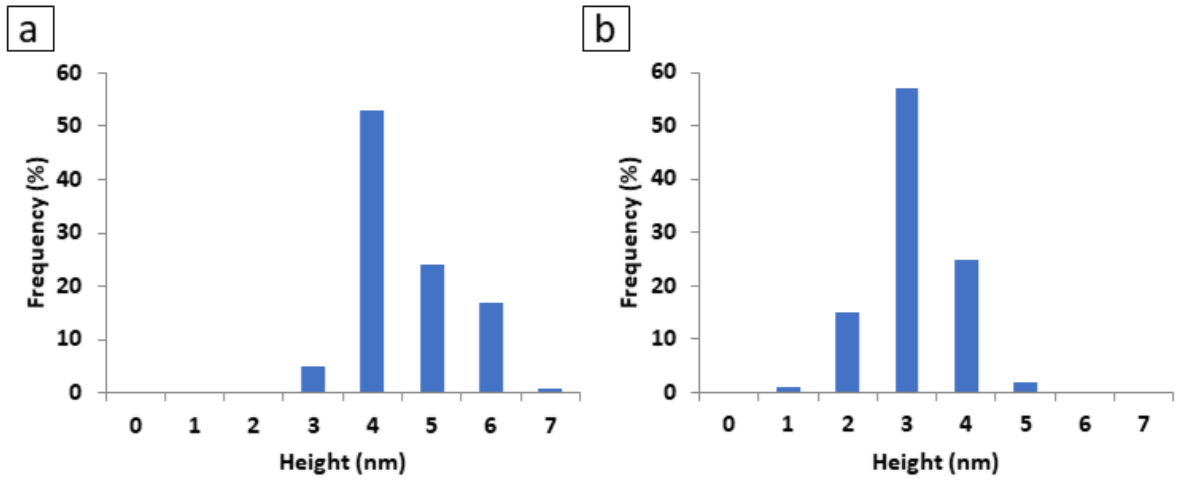

Figure D.4. Height distribution of OTS layers on (a) Si(111) and (b) mica(0001) prepared without adding water or heating the substrates, as described in Figure D.3.

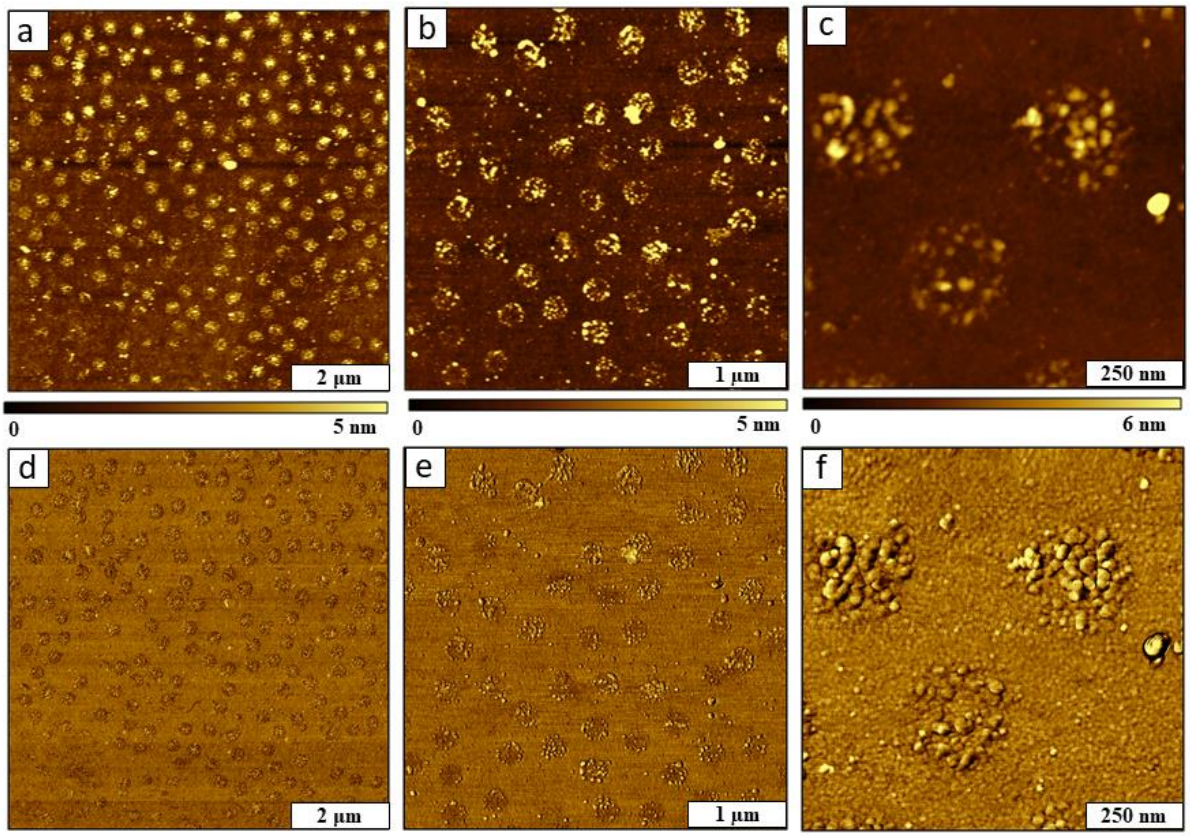

Figure D.5. Successive zoom-in views revealing the localization of water on Si(111) showing the distribution of OTS for a control sample prepared without water. a) Topography view (8× 8 μm^2); (b) Zoom in topography image (4 × 4 μm^2); (c) magnified view of two OTS nanostructures (1 × 1 μm^2); (d) simultaneously acquired phase image for *a*; (E) corresponding phase image for *b*; (f) phase image for *c*.

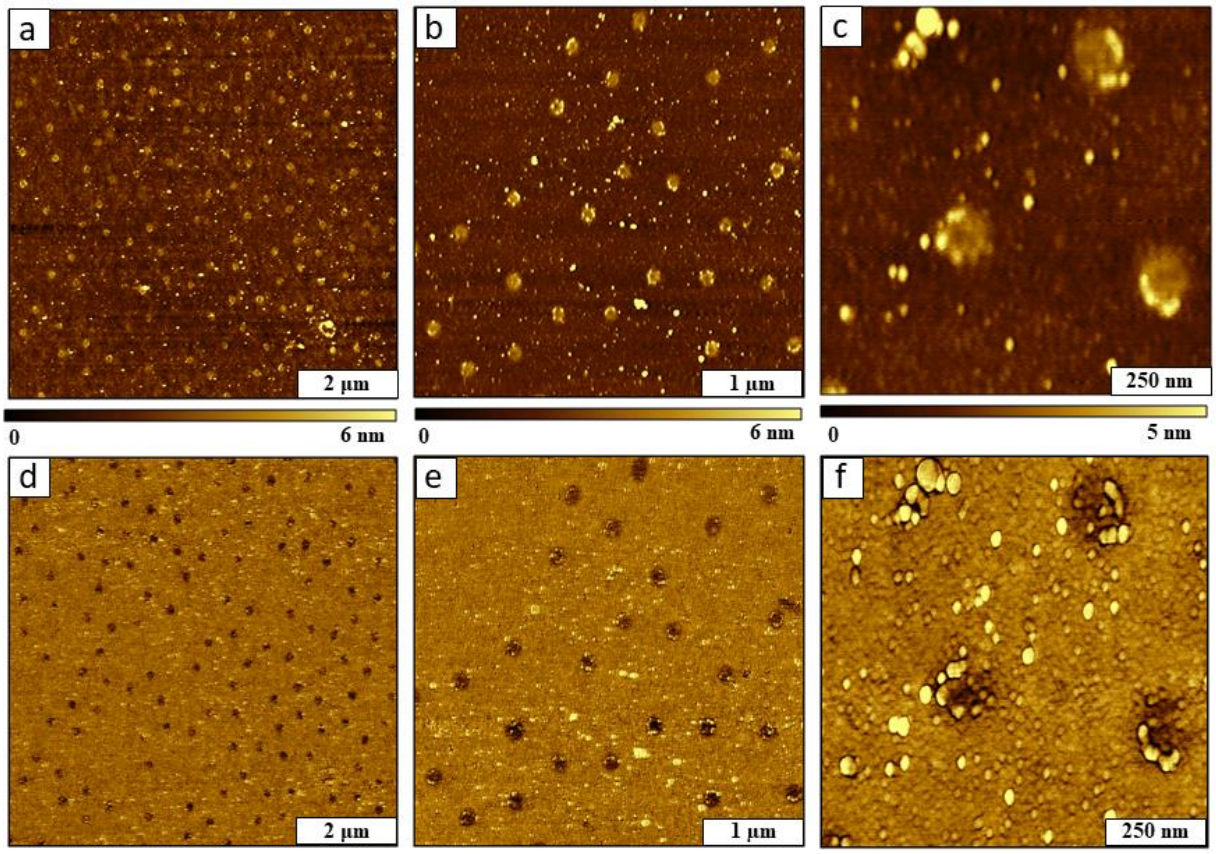

Figure D.6. The localization of water on Si(111) detected by the distribution of OTS at the water volume of 2 mg.(a) Topography view (8× 8 μm^2); (b) Zoom in topography image (4 × 4 μm^2); (c) magnified view of two OTS nanostructures (1 × 1 μm^2); (d) simultaneously acquired phase image for *a*; (e) phase image for *b*; (f) phase image for *c*.

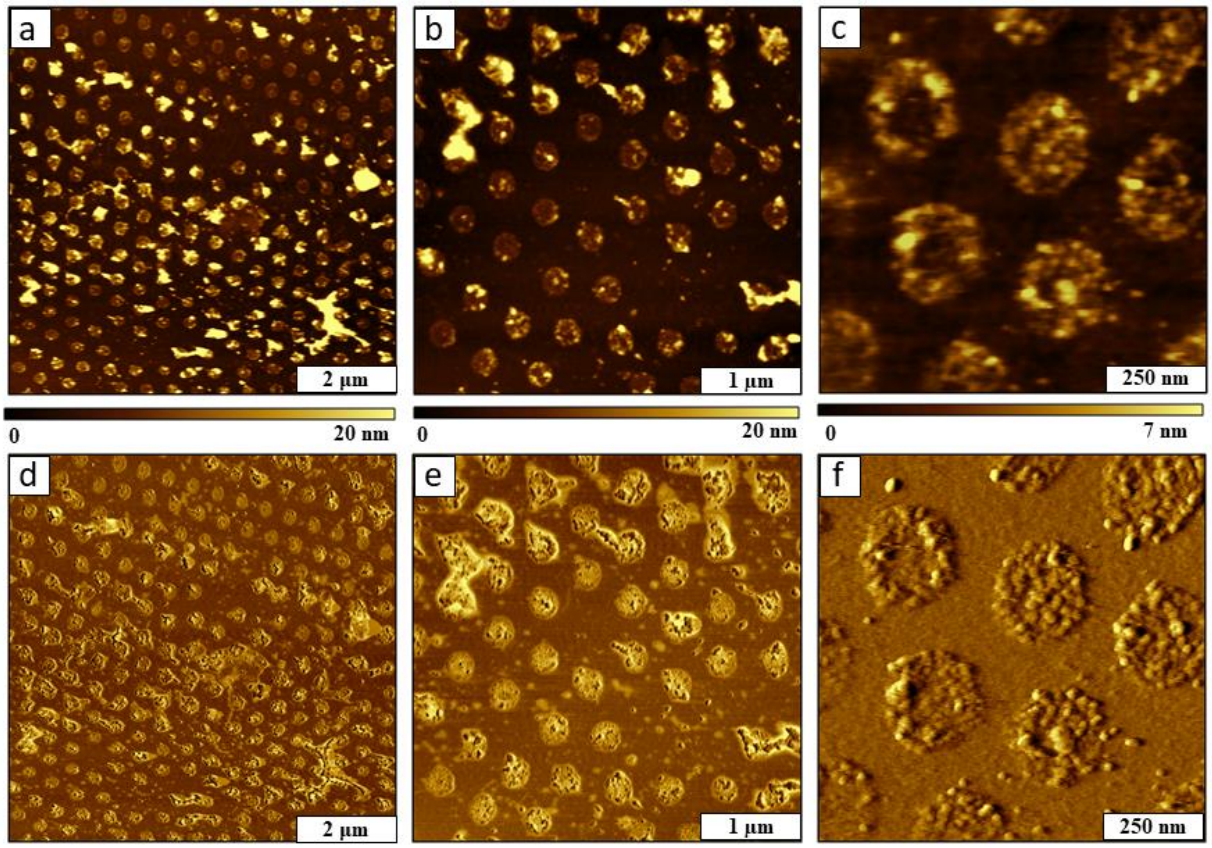

Figure D.7. Attachment of OTS to wetted areas of a silicon substrate when 100 mg of water was added to the reaction vessel. (a) Topography view (8× 8 μm^2); (b) Zoom in topography image (4 × 4 μm^2); (c) magnified view of two OTS nanostructures (1 × 1 μm^2); (d) concurrently acquired phase image for *a*; (e) phase image for *b*; (f) phase image for *c*.

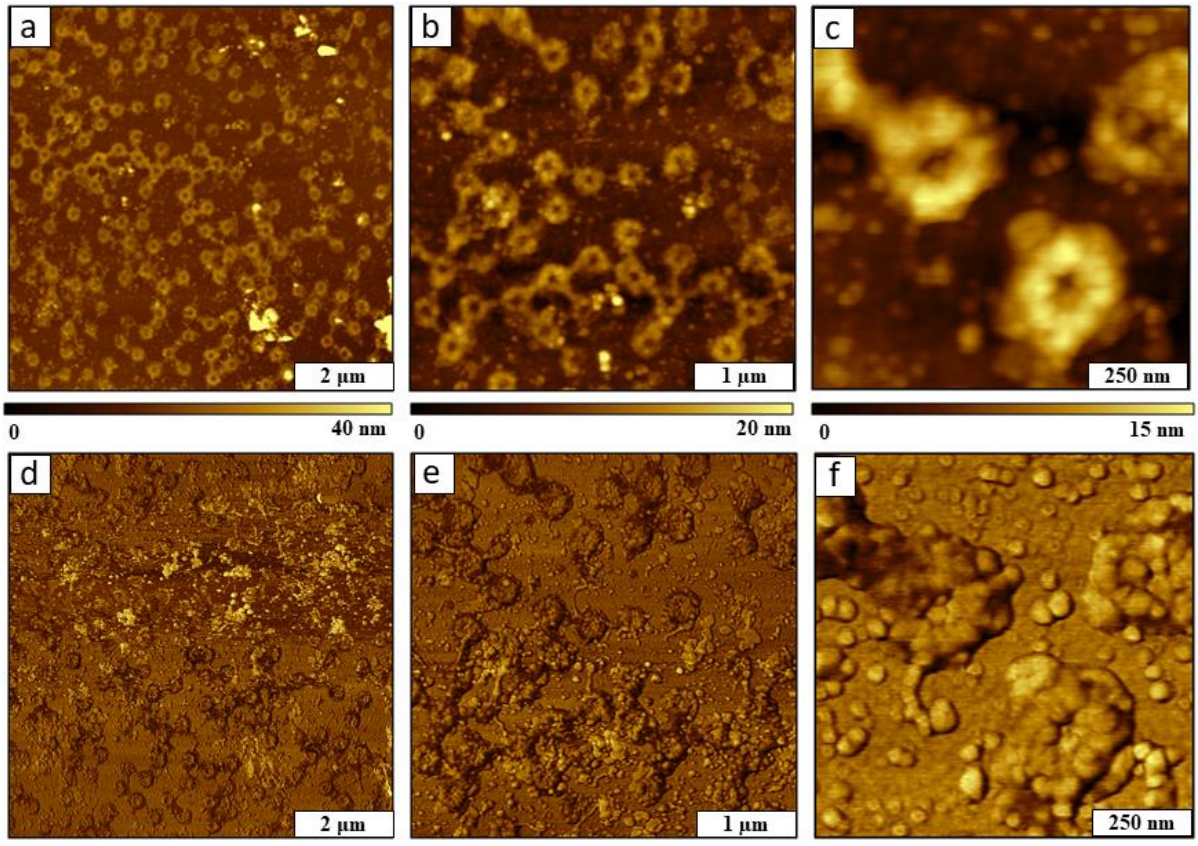

Figure D.8. The distribution of OTS assembled on Si(111) at the water volume of 300 mg. (a) Topography view (8× 8 μm^2); (b) Zoom in topograph (4 × 4 μm^2); (c) magnified view of two OTS nanostructures (1 × 1 μm^2); (d) phase image for *a*; (e) phase image for *b*; (f) phase image for *c*.

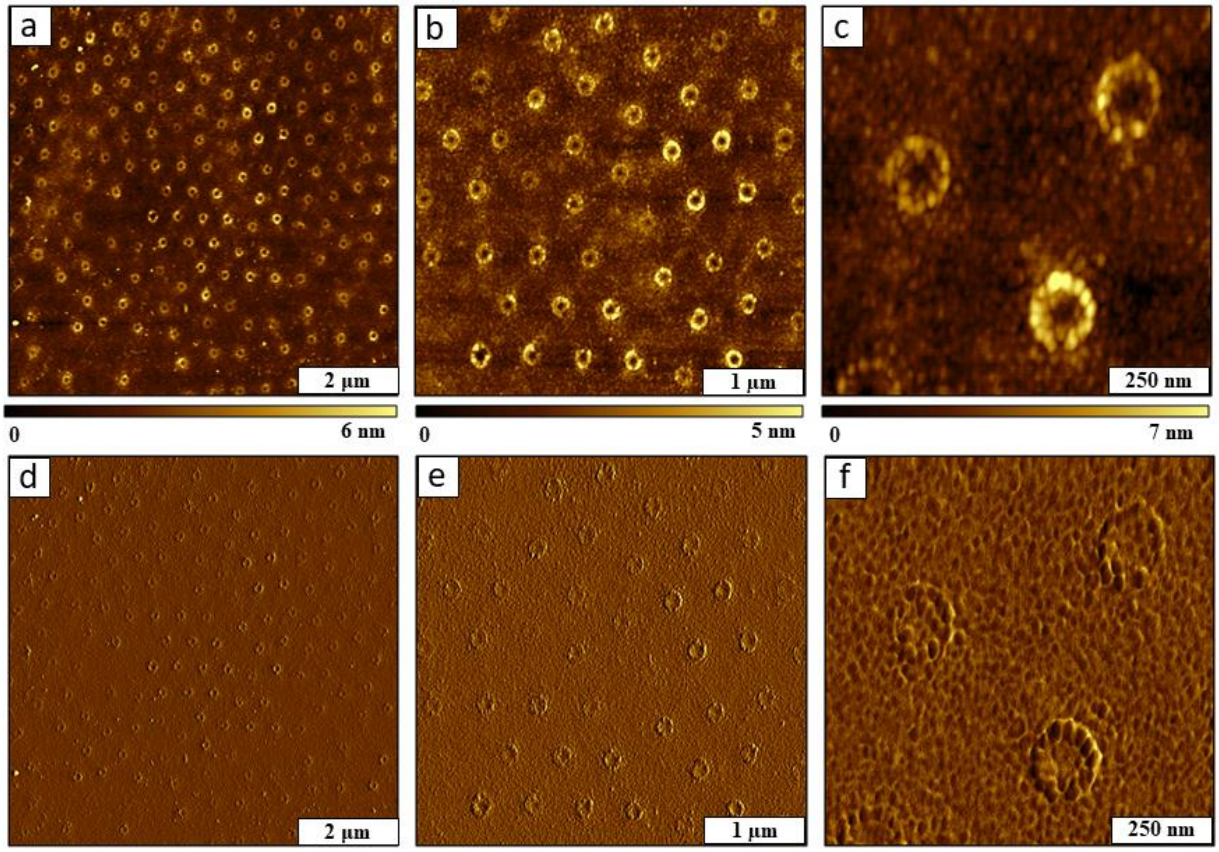

Figure D.9. Nanostructures of OTS formed on Si(111) surface vapor deposition with ambient drying of the masked substrates. (a) Topography view (8× 8 μm^2); (b) Zoom in topograph (4 × 4 μm^2); (c) magnified view of two OTS nanostructures (1 × 1 μm^2); (d) phase image for *a*; (e) corresponding phase image for *b*; (f) phase image for *c*.

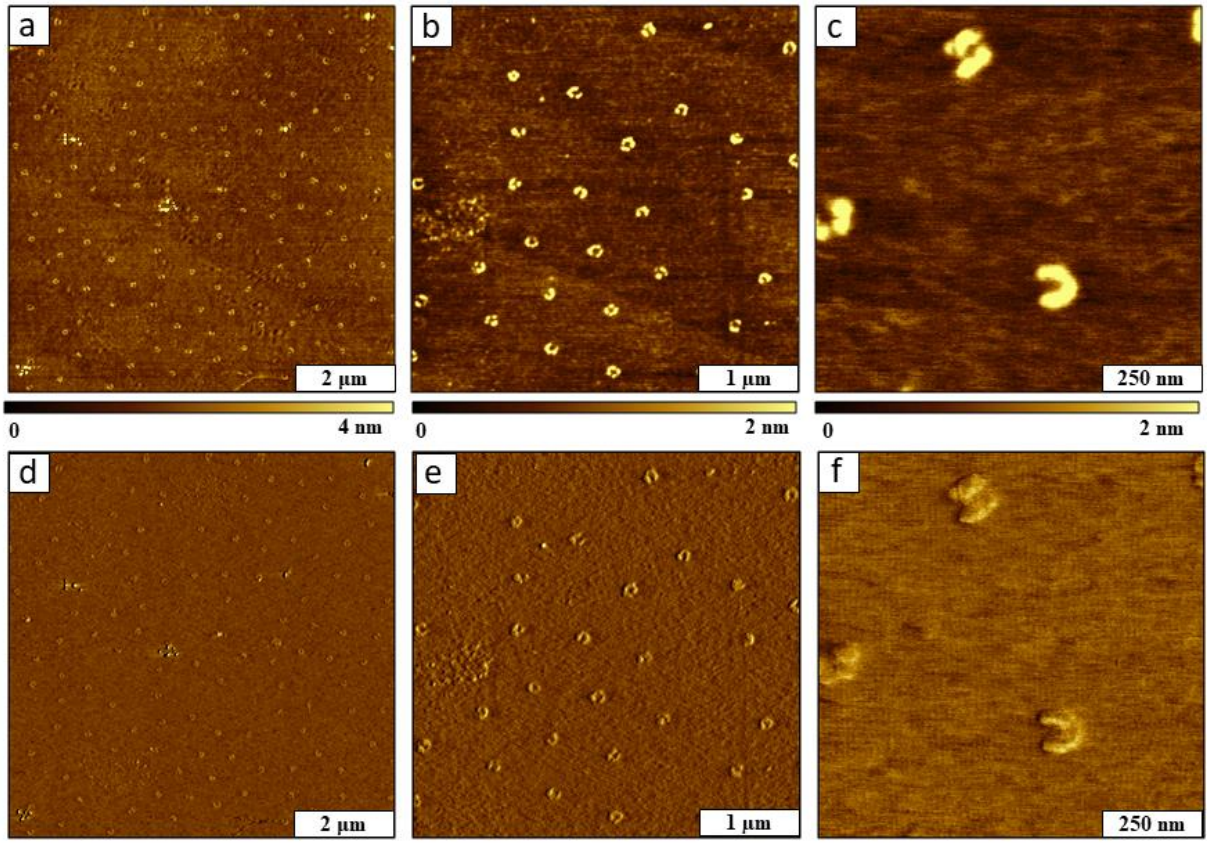

Figure D.10. The distribution of OTS assemblies formed on sites with water residues that formed on mica with no water added to the reaction vessel. (a) Topography view (8× 8 μm^2); (b) Zoom in topography view (4 × 4 μm^2); (c) magnified w of two OTS nanostructures (1 × 1 μm^2); (d) simultaneously acquired phase image for *a*; (e) phase image for *b*; (f) phase image for *c*.

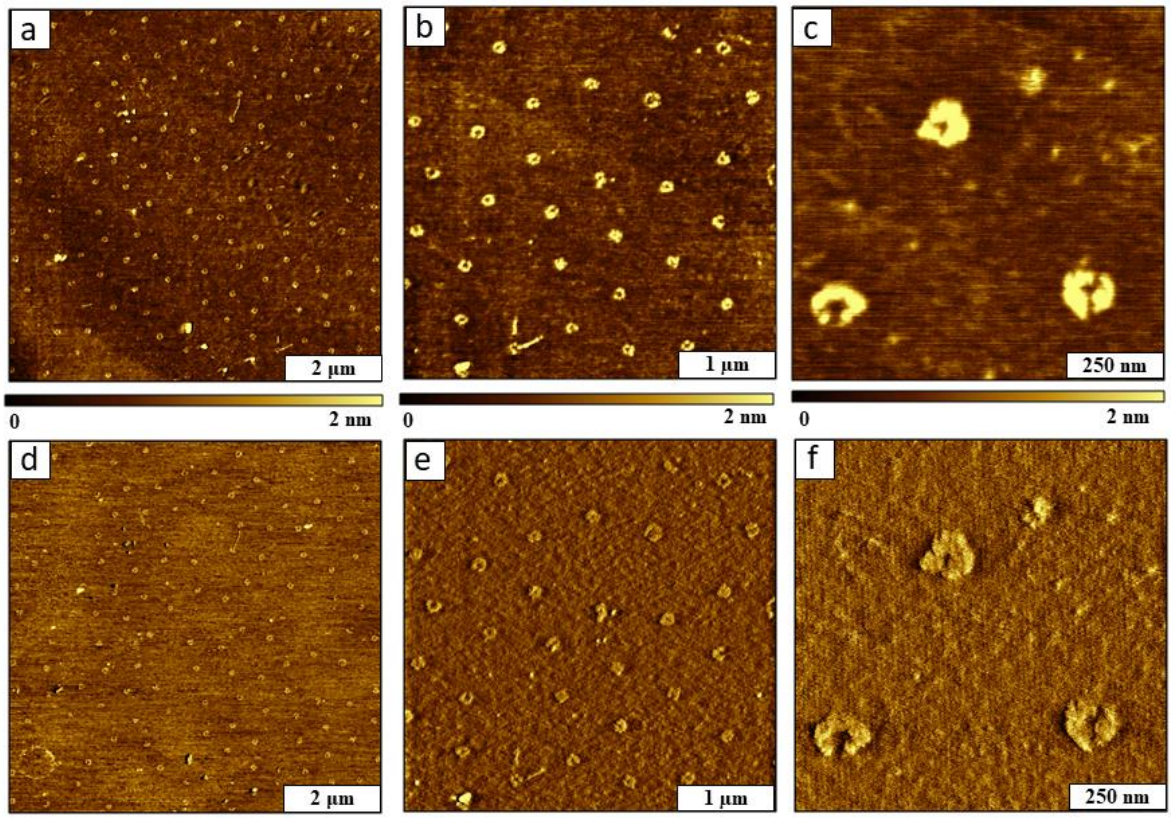

Figure D.11. Nanopatterns of OTS formed on mica with 2 mg of water added to the reaction vessel. (a) Topography view (8× 8 μm^2); (b) Zoom in topography view (4 × 4 μm^2); (c) magnified view of two OTS nanostructures (1 × 1 μm^2); (d) phase image for *a*; (e) phase image for *b*; (f) phase image for *c*.

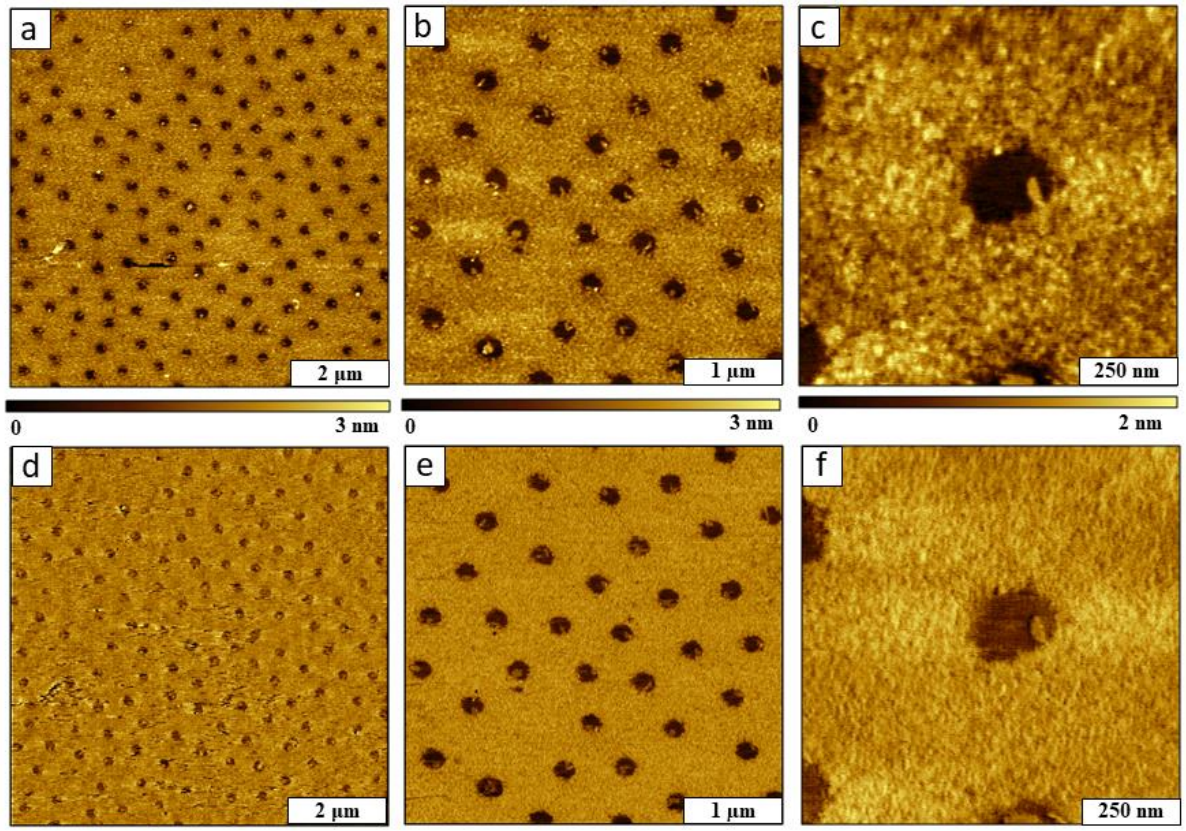

Figure D.12. Film of OTS with nanoholes of uncovered substrate formed on mica with 100 mg of water added to the reaction vessel. (a) Topography view (8× 8 μm^2); (b) Zoom in topography view (4 × 4 μm^2); (c) magnified view a nanohole within OTS (1 × 1 μm^2); (d) lateral force image for *a*; (e) lateral force image for *b*; (f) lateral force image for *c*.

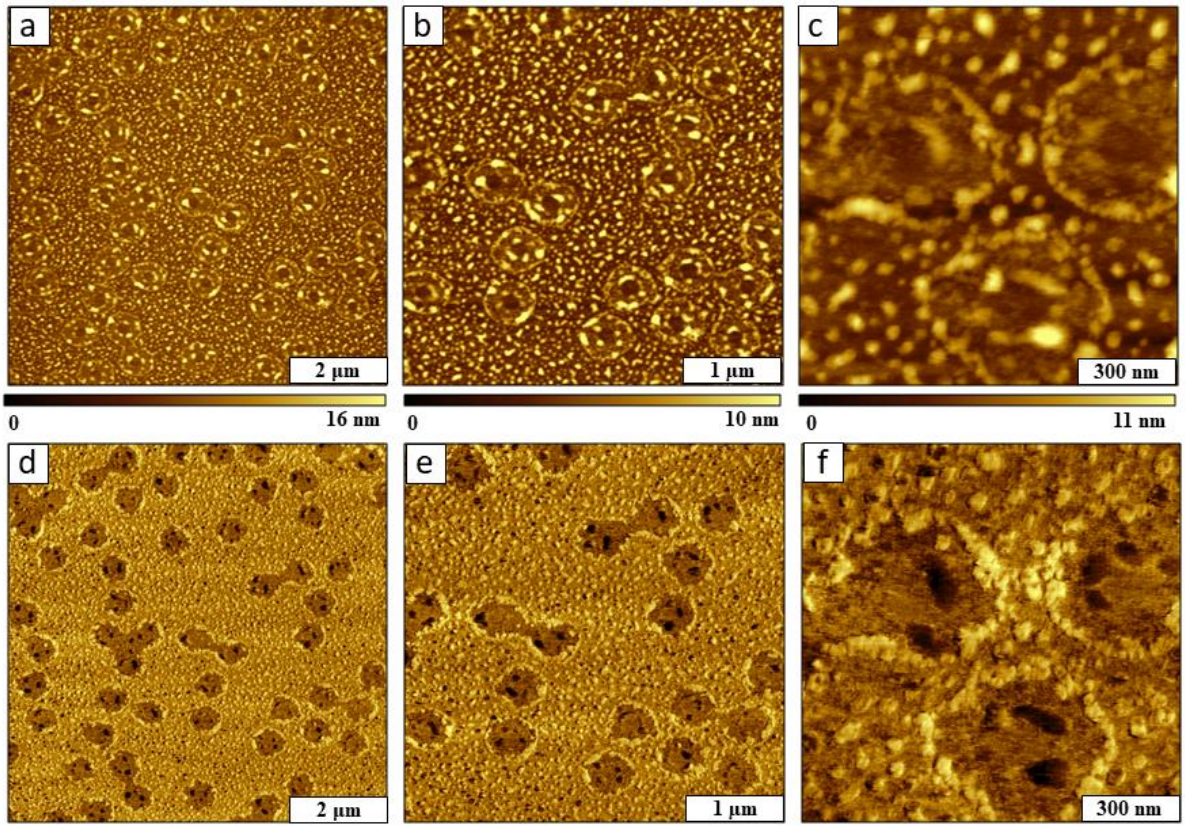

Figure D.13. Nanostructured film of OTS formed when 300 mg of water was added to the reaction vessel with a masked mica substrate. (a) Topography view (8× 8 μm^2); (b) Zoom in topograph (4 × 4 μm^2); (c) magnified view of two OTS nanostructures (1.2 × 1.2 μm^2); (d) lateral force image for *a*; (e) lateral force image for *b*; (f) lateral force image for *c*.

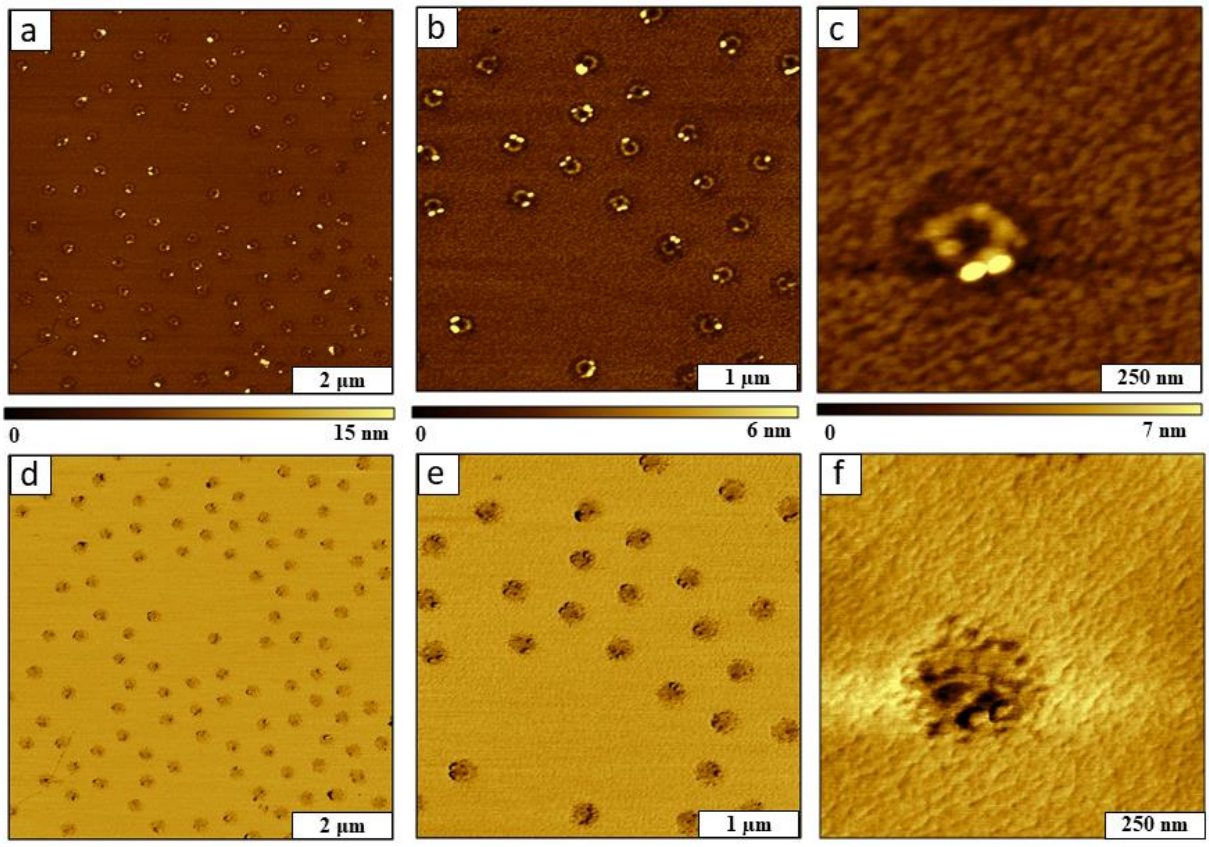

Figure D.14. Sample prepared with vapor deposition of OTS onto a silica mask that was dried for 4 h in ambient conditions on mica. The sample was immediately transferred to a vessel containing 300 µL of OTS. Water was not added to the reaction vessel. (a) Topography view (8× 8 μm^2); (b) Zoom in view (4 × 4 μm^2); (c) close-up view of a single OTS nanoring (1 × 1 μm^2); (d) simultaneously acquired phase image for *a*; (e) phase image for *b*; (f) phase image for *c*.

APPENDIX E. SUPPORTING INFORMATION FOR CHAPTER 6

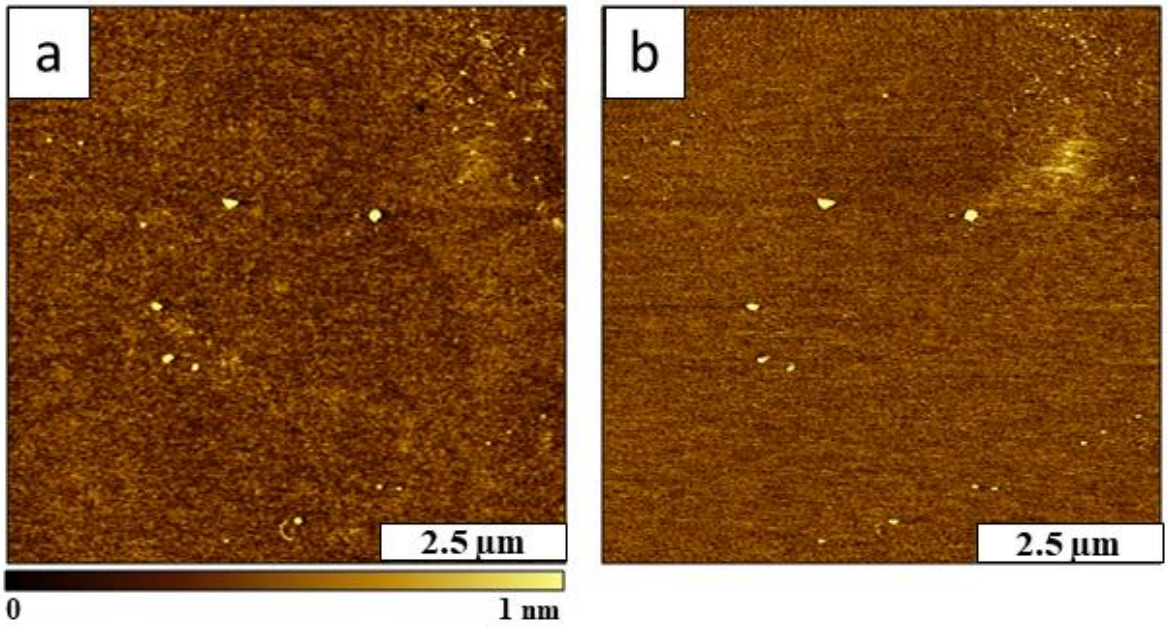

Figure E.1. Control experiment to investigate the surface adsorption of octaethyl porphyrin (OEP) without the addition of silicon tetrachloride, $SiCl_4$. Without $SiCl_4$, there are a few adsorbates of OEP on the Si(111) surface, no film was formed as shown in (A) the topography frame; and (B) corresponding phase image. Most of the OEP that was bound to the surface was removed by the rinsing step, however there are a few small adsorbates and aggregates of OEP molecules.

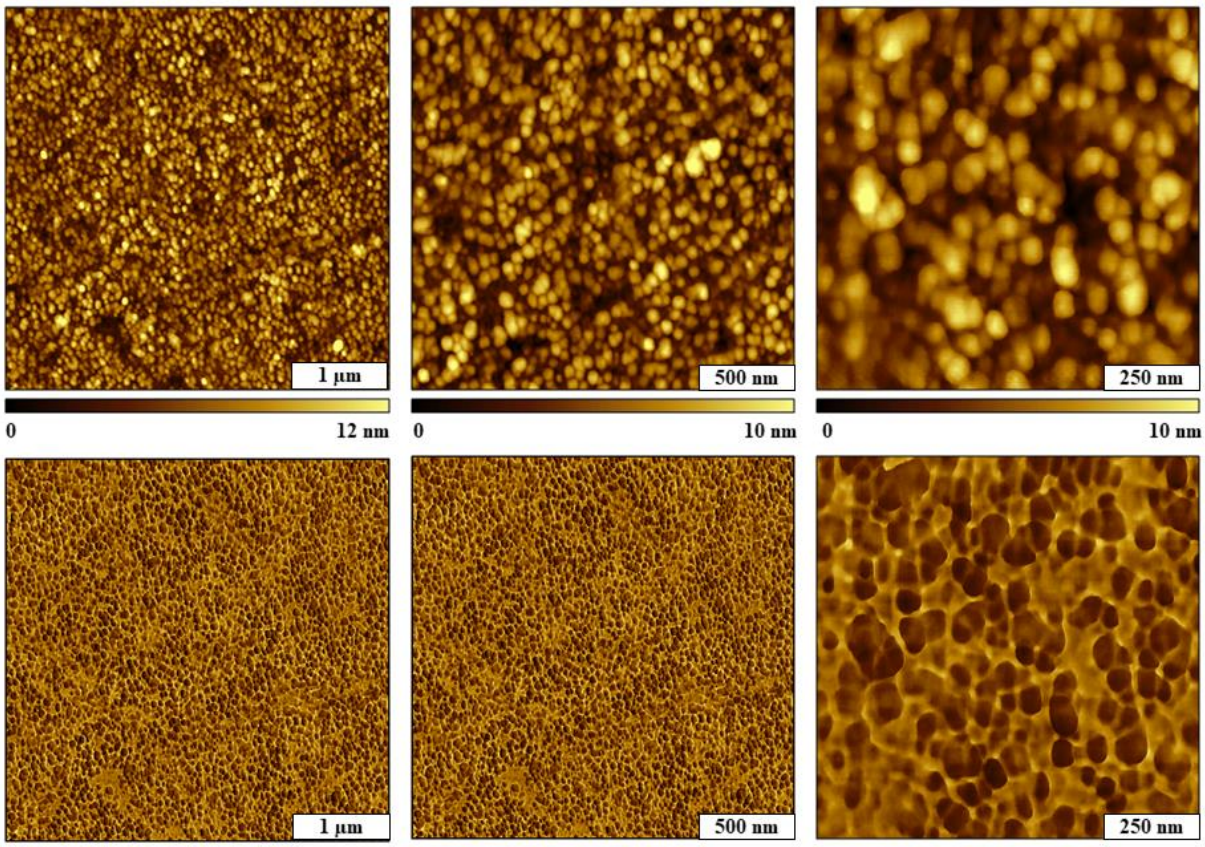

Figure E.2. Surface morphology of a film of Si-OEP formed after 5 h immersion of a silicon substrate in a solution of OEP and $SiCl_4$.With addition of $SiCl_4$, an irregular, dense film formed on the surface with multiple island protrusions. Tapping-mode topography frames are shown in the top row with the matching phase frames in the bottom panels. The true sizes of the surface features are exaggerated in lateral dimensions due to a convolution of the probe shape and the geometry of ultra-small nanostructures.

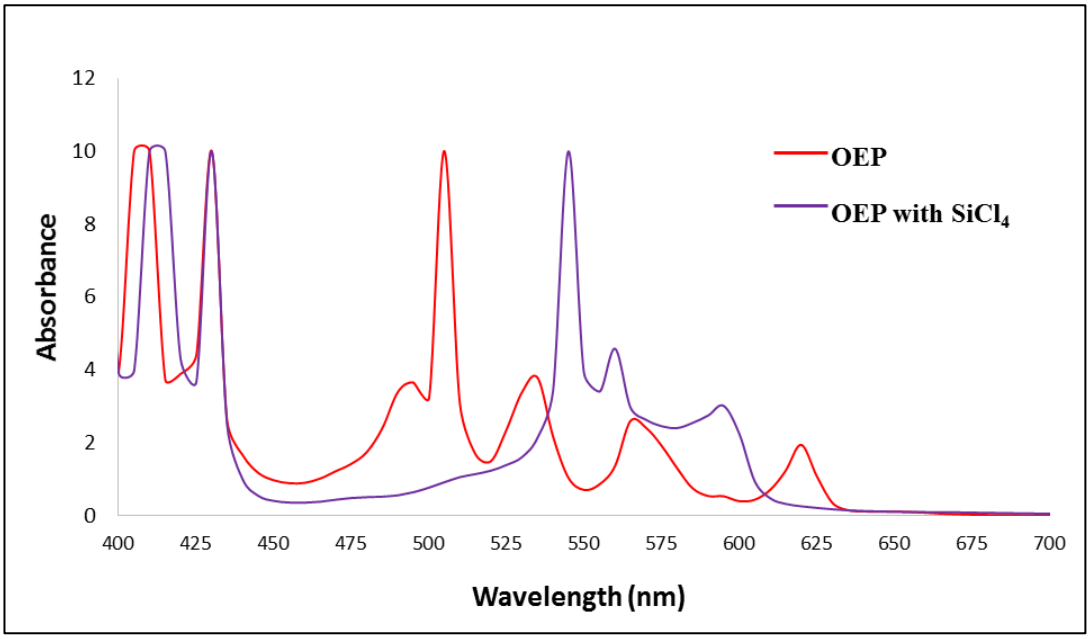

Figure E.3.Absorbance spectra for octaethyl porphyrin (OEP) before and after addition of $SiCl_4$ show a characteristic red shift of the Q bands indicating that Si was incorporated into the macrocycle.

Bands attributed to π - π^* transitions (*Q-Bands*) appear in the spectra of porphyrins between 480-720 nm as an indicator that changes of molecular structure have occurred.[299] When the porphyrin macrocycle is coordinated with elements or metals, changes will be observed for the pattern and number of Q bands. Depending on molecular symmetry, there are typically four Q bands for transitions that involve the four nitrogens of the porphyrin macrocycle. The relative intensity of Q bands is due to the position and nature of substituents on the macrocycle. In this example, the intense Soret bands between 400-450 nm were saturated.

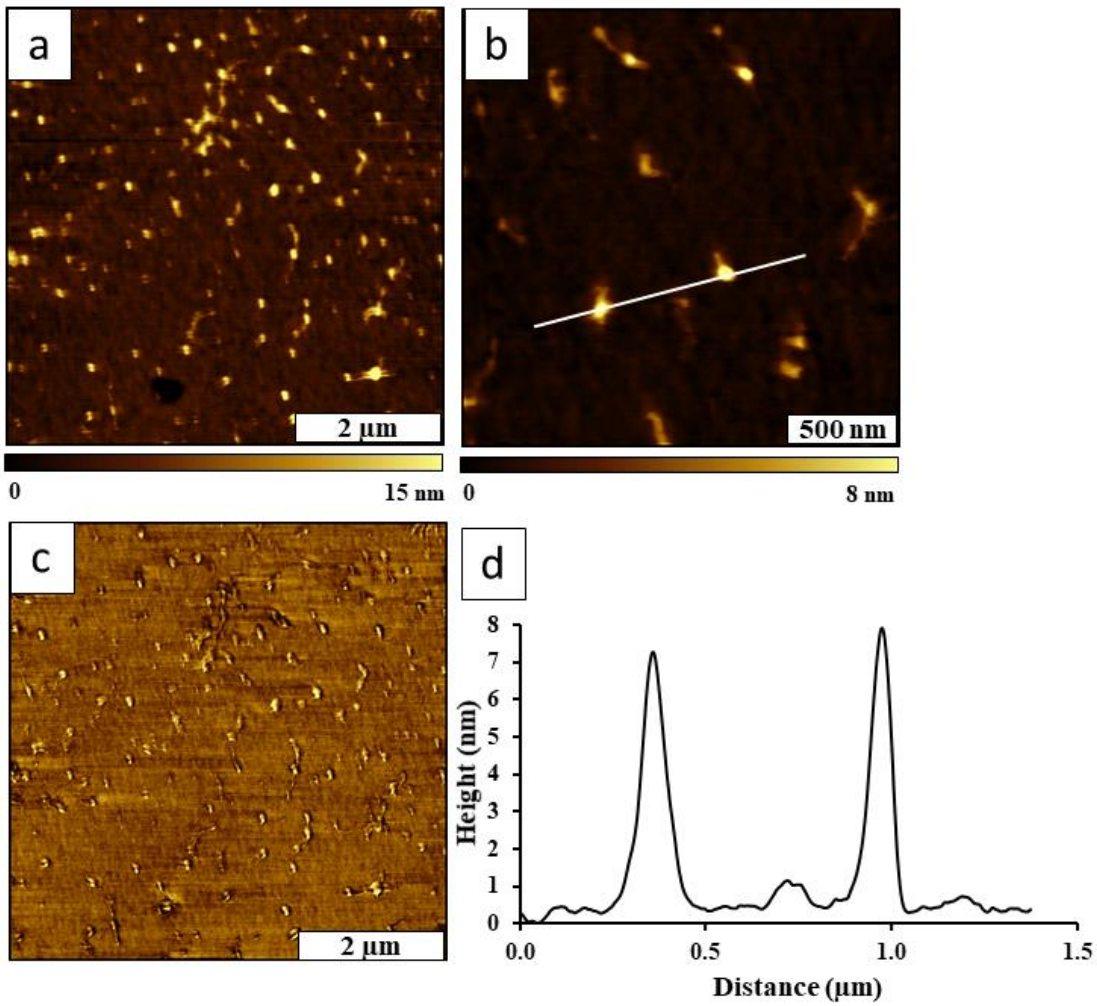

Figure E.4. Nanodots of Si-OEP assembled within nanoholes of an OTS matrix film after 24 h reaction. (a) Topography view ($6 \times 6\ \mu m^2$); (b) Zoom-in topograph ($2 \times 2\ \mu m^2$); (c) simultaneously acquired phase frame for a; (d) Cursor profile across two nanodots in *b*. Tapping-mode images were acquired in ambient air. A double-tip artifact is evident in the images which is caused by multiple asperities at the apex of the probe.

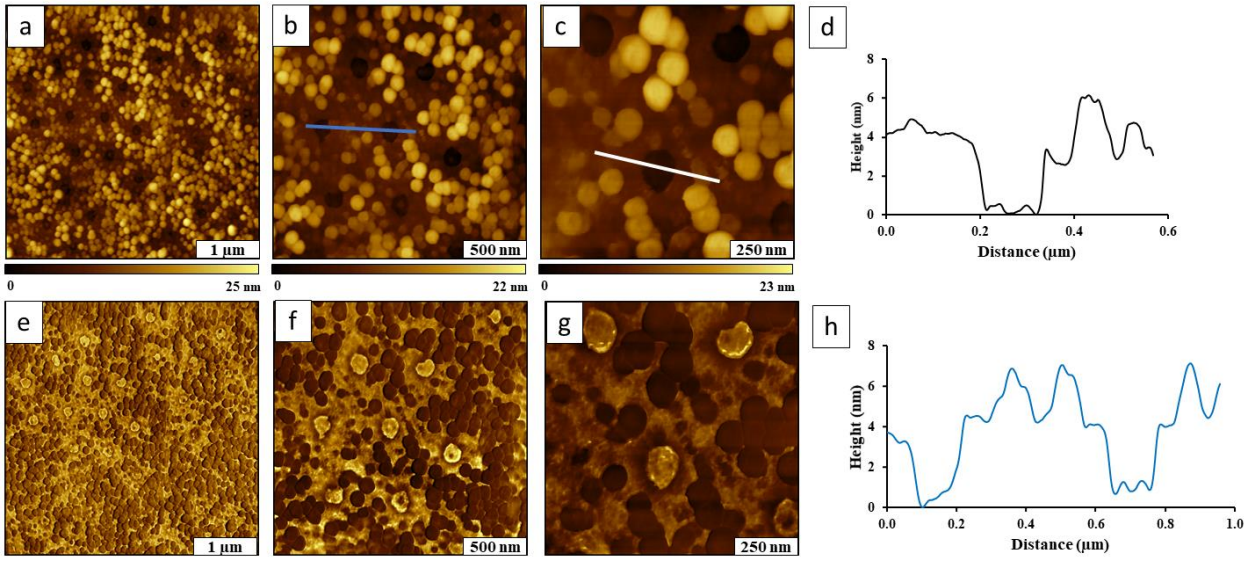

Figure E.5. Successive zoom-in views of nanoholes within a film of Si-OEP on Si(111) obtained with tapping mode. (a) to (c) Topography frames; (d) cursor profile for the line on *c*; (e) to (g) are corresponding phase images of *a*, *b* and *c* respectively; (h) cursor profile for the line drawn over two nanoholes in *b*.

An interesting morphology of nanoholes formed within Si-OEP thin films during a 24 h reaction is shown in tapping mode images in Figure E.5. The distribution of molecular domains on Si(111) is rather less homogeneous compared to the sample presented in Figure 6.2. We assume this happens due to the variations of water deposits on the surface for this sample. Amount of surface water has not been enough to facilitate a dense assembly of porphyrin skewers with complete surface coverage. The full-length growth of S-OEP strands in the vertical direction has also been limited. The average height of these films was measured 5.4± 1.4 nm (n=50).

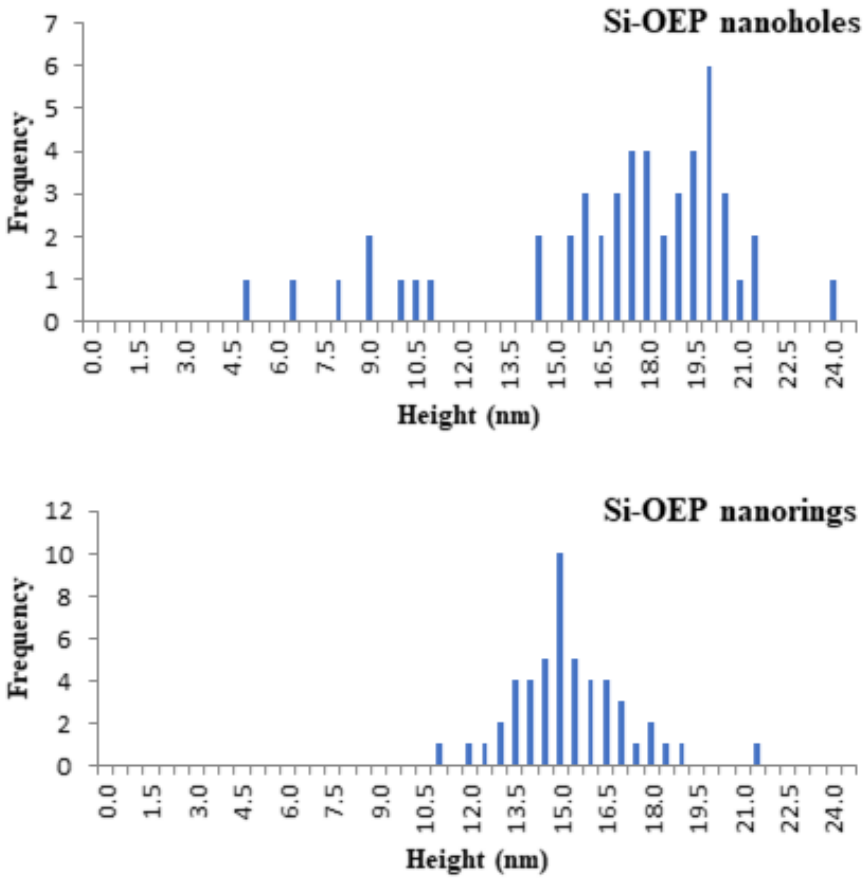

Figure E.6. The histogram comparison for height measurements of Si-OEP nanodots prepared on Si(111) for 5 h and 24 h immersion. Height was measured from individual cursor profiles across 50 nanoholes taking surrounding OTS matrix as the reference.

At the nanoscale, there is variability for the heights of the nanodots with an average value of 5.8 ± 1.3 nm for 5 h immersion and 8.7 ± 1.9 nm average height for 24 h immersion. The mean values of the two data sets (5h and 24 h) are statistically different, compared using a paired t-test at the 99.5 percentile. The variability of the heights of nanodots can be attributed to slight changes in the diameters of the nanoholes which occur naturally from variations of particle sizes of the surface.

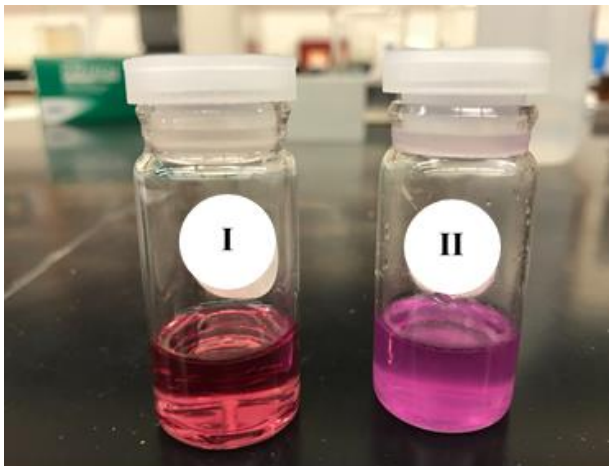

Figure E.7. Changes in the color of the OEP solution in chloroform after adding $SiCl_4$.

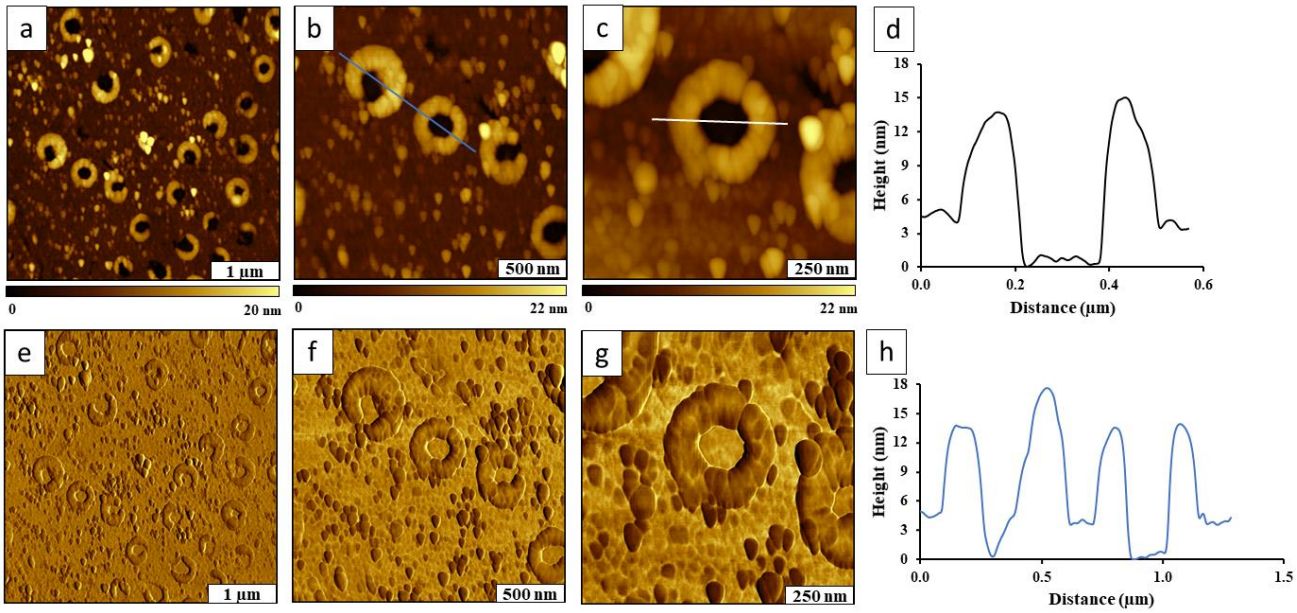

Figure E.8**.** Ring-shaped nanostructures of OEP-silane formed on Si(111) by increasing the drying period of the surface mask to 20 h in an oven at 150 ^{o}C before immersion in the reaction vessel. (a) Topography view of nanorings (4 × 4 μm^2); (b) zoom-in topograph (2 × 2 μm^2); (c) zoom-in view of a single Si-OEP nanoring (1 × 1 μm^2); (d) cursor profile of the line traced in *c*; (e), (f) and (g) are corresponding phase images of *a*, *b* and *c*; (h) cursor profile for the line on *b*. Images were acquired with tapping-mode AFM in the air.

APPENDIX F. LETTER OF PERMISSION FOR CHAPTER 6

Regarding Incident 2576421 Permission Request

support@services.acs.org
Mon 2/25/2019 8:55 PM
To: Neepa M Kuruppu Arachchige <nkurup1@lsu.edu>

Dear Dr. Kuruppu Arachchige:

Thank you for contacting ACS Publications Support.

Your permission request is granted and there is no fee for this reuse. In your planned reuse, you must cite the ACS article as the source, add this direct link (https://pubs.acs.org/doi/10.1021/acsomega.8b03204) and include a note to readers that further permissions related to the material excerpted should be directed to the ACS.

I hope this information helped. Please let me know if I can be of further assistance.

Sincerely,

Kryxie J. Ramirez
ACS Customer Services & Information
https://help.acs.org

Incident Information:

Incident #: 2576421
Date Created: 2019-02-26T07:45:24
Priority: 3
Customer: Neepa M KuruppuArachchige
Title: Permission Request
Description: Dear Editor,

I am requesting the permission to reprint the article I have co-authored and published in ACS Omega. I have decided to add it as one of my dissertation chapters. The title of the article is

"Surface Coupling of Octaethylporphyrin with Silicon Tetrachloride".

Dissertation Title: Chemical approaches for nanofabrication based on colloidal lithography with

organosilanes, nanoparticles and nickel films: the role of water in directing surface self-assembly

Article link:
https://pubs.acs.org/doi/10.1021/acsomega.8b03204

Thank you for your consideration.

Neepa

Neepa M K Kuruppu Arachchige
Ph.D. candidate
Department of Chemistry
Louisiana State University
232, Choppin Hall, Baton Rouge, LA 70803
office 225-578-8853
nkurup1@lsu.edu | lsu.edu | www.lsu.edu/science/chemistry/

APPENDIX G. FORCE MODULATION MICROSCOPY STUDY OF SPATIALLY CONFINED PHTHALOCYANINES NANOPATTERNS*

G.1. Overview

Nanopatterns of 3-aminopropyltriethoxysilane (APTES) were used as a surface template to bind zinc phthalocyanine (ZnPc) to silicon substrates. Protocols with solution immersion and particle lithography were used to direct the attachment and growth of ZnPcs on Si(111). An array of nanoholes was generated within a matrix of octadecyltri-methoxysilane (OTMS) as containers for the subsequent assembly of 3-aminopropyltriethoxysilane (APTES) molecules. Further immersion steps enabled the site-selective patterning ZnPc with designed substituents (Figure F.1). Characterizations with the force modulation microscopy (FMM) mode of AFM were used to evaluate local differences in elastic and viscoelastic properties of the nanostructures of ZnPc assembled on APTES nanodots. The FMM mode provided ultra-sensitive surface maps the elastic response of for compositional differences between areas of the surface patterns compared to the surrounding matrix film of OTMS.

G.2. Force Modulation Microscopy (FMM)

A model 5500 scanning probe microscope (Keysight Technologies, Santa Rosa, CA) was used for AFM characterizations with FMM. The nosecone assembly for contact mode which does not have metal components was attached to the scanner. Silicon SPM-sensor tips (NanoWorld, Watsonville, CA) with an average force constant of 2.8 N/m and 75 kHz of resonance frequency were used for FMM imaging in ambient conditions. A home-constructed sample stage incorporating a piezoactuator was used for FMM studies, as previously described. [357]

* The Figures in Appendix F were previously published in Colloids and Surfaces A as a research article[125] titled "Nanopatterns of zinc phthalocyanines prepared using particle lithography: Characterization of patterning steps with scanning probe microscopy" (See Appendix H).

G.3. Protocol for Nanolithography

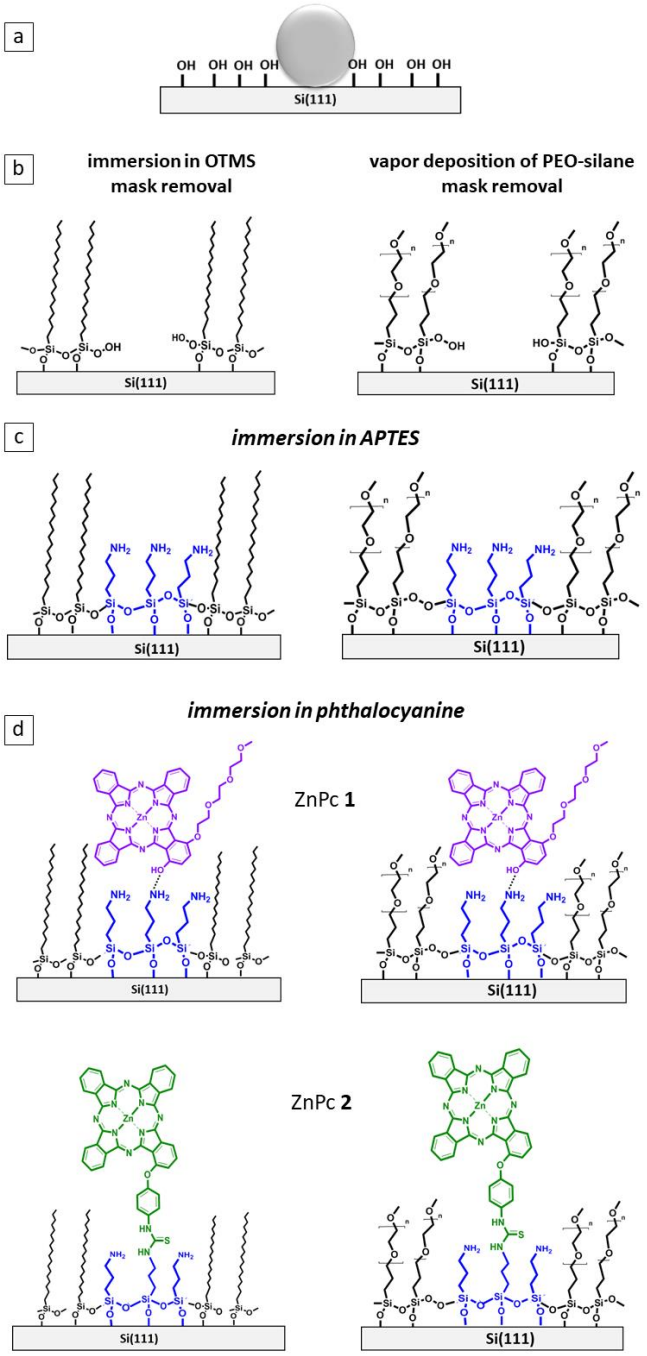

Figure G.1. Outline of the steps of colloidal lithography to prepare nanopatterns of ZnPcs. (a) A mask of latex or silica particles was dried on Si(111). (b) The masked substrate was either immersed in solution (left) or exposed to an organic vapor (right) to form a resist. (c) After rinsing away the particles, the samples were immersed in APTES solution. (c) After rinsing, the samples were then immersed in solutions of ZnPcs.

G.4. Results and Discussion

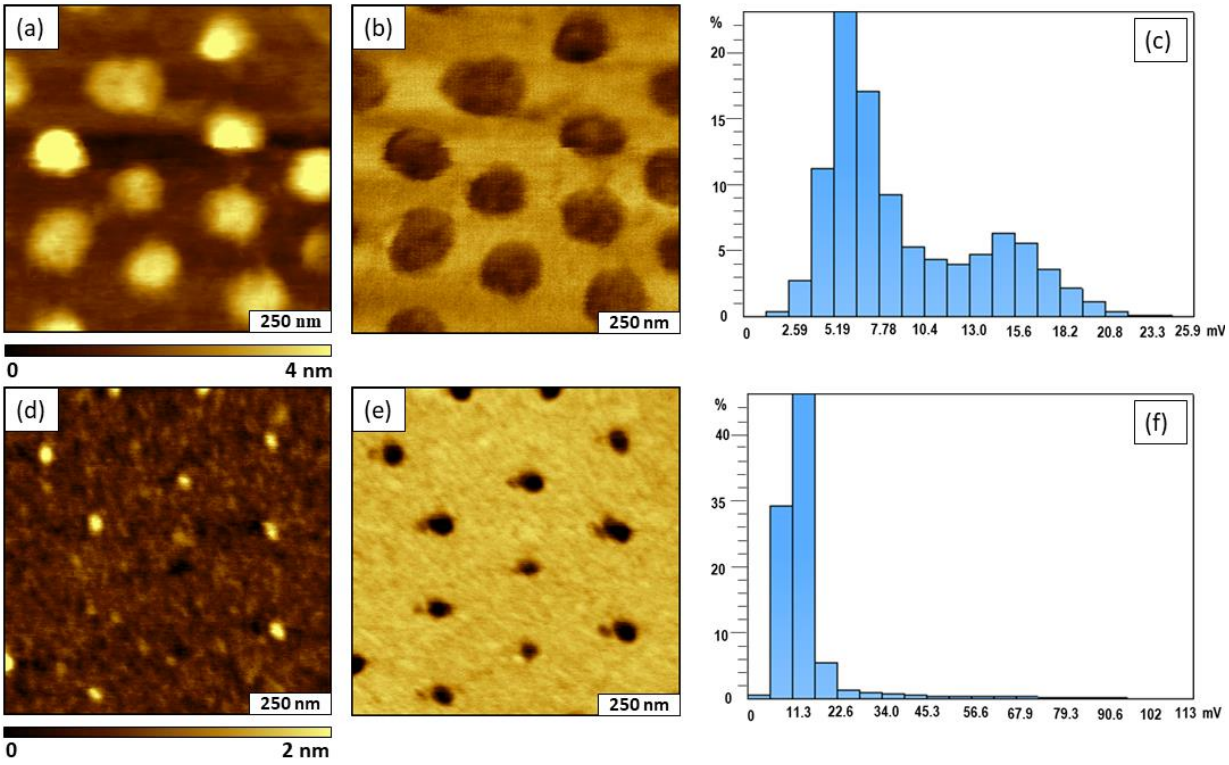

Figure G.2. Example results for ZnPc nanostructures acquired with FMM. (a) Topograph (1×1μm□2) for ZnPc 1 nanostructures acquired in ambient air; (b) simultaneously acquired amplitude frame; (c) histogram plot of amplitude signal for *b*; (d) Topography image for ZnPc 2 nanostructures; (e) corresponding amplitude channel; (f) histogram for *e*. For FMM studies, 250 nm silica spheres were used for colloidal lithography with both ZnPc 1 and ZnPc 2 using an OTMS matrix.

Characterizations with FMM were completed for nanopatterns prepared with ZnPc **1** and ZnPc **2**. Topography and concurrently acquired amplitude frames are shown for 1×1 μm^2 scans for nanopatterns of ZnPc **1** (top row) and ZnPc **2** (bottom row) of Figure G.2. In the topography frames the bright areas are the taller regions with ZnPc, surrounded by the matrix film of OTMS. The contrast is reversed in the amplitude images, showing dark spots for the areas of ZnPc nanopatterns. The AFM experiments reveal that there can be considerable variance in the diameters and shapes of nanostructures that are made with colloidal lithography. For the sphere masks used in lithography, the actual physical area of contact between the spheres with the

substrate is not always uniform between samples. The size of the contact area is influenced by capillary interactions of water as well as the deformation of the spheres. Although the patterns have regular round geometries, relatively wide nanopatterns measuring 144±36 nm (n=20) in diameter were detected for ZnPc 1 (top row, Figures G.2a and G.2b); whereas exquisitely small nanodots measuring 46±9 nm (n=20) in width were observed with ZnPc **2** (bottom panels, Figures G.2d and G.2e). The width measurements also can include significant errors due to the well-known artifact of tip-sample convolution. The AFM probe is much wider than the nanostructures which propagates significant errors in lateral measurements.

The differences in elastic response between surface domains of the matrix and nanopatterns can be discerned using FMM amplitude images. The taller, bright areas of ZnPc nanostructures in topography frames (left) coincide with the darker areas of the amplitude frames (center) in Figure G.2. Two peaks are apparent in the histogram of Figure G.2c, indicating a distinct change in softness between the nanostructures versus the matrix regions. The surface coverage of ZnPc **1** measured 32% compared to 3.5% for ZnPc **2**, calculated using the amplitude images. The topography image (Figure G.2d) can be mapped along with the amplitude frame (Figure G.2e) for ZnPc **2** as well, although the nanostructures are far smaller in diameter than with ZnPc 1. With such small areas of ZnPc **2**, there is only one-color contrast that can be resolved in the histogram of Figure G.2f. The FMM experiments show a discrete change in surface chemistry as well as softness for the ZnPcs compared to the matrix layer. The highly sensitive detection of chemical differences for tip-surface interactions plotted in FMM channels shows that there is virtually no nonspecific attachment of adsorbates on the methyl-terminated areas between nanopatterns.

Additional FMM data acquired with ZnPc **1** (top row) and ZnPc **2** (bottom row) nanopatterns are presented in Figure G.3. The color contrast between FMM amplitude and phase

channels indicate two distinct regions that correspond to ZnPc nanodots and the surrounding organosilane SAMs. The areas of ZnPc nanodots show brighter contrast in topography frame. The phthalocyanines appear to have a softer texture compared to organosilanes because a darker contrast or a smaller amplitude is apparent for ZnPc regions in amplitude frames. These results suggest that FMM is an ideal tool to investigate elastic properties of nanostructures prepared with phthalocyanine macrocycles.

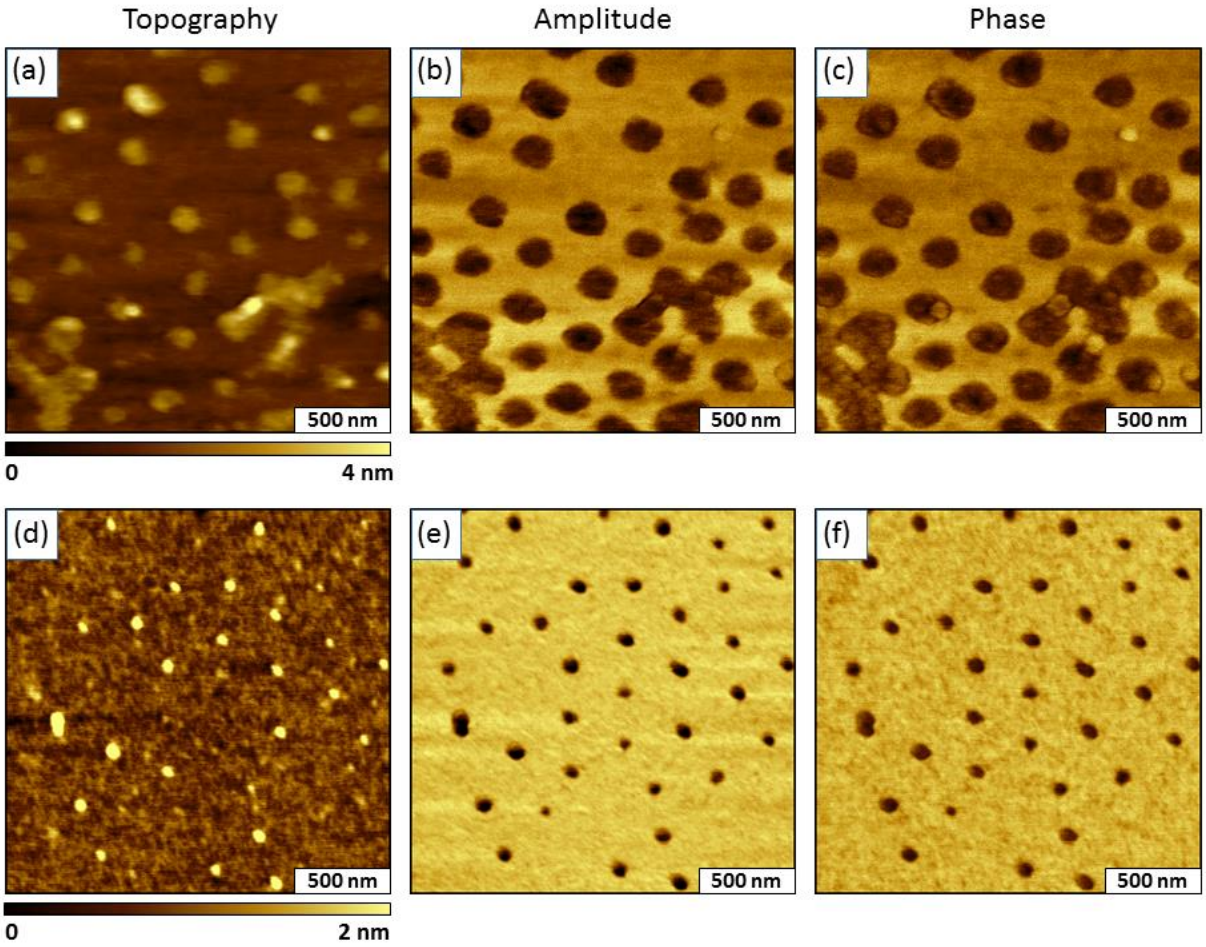

Figure G.3 Example images for FMM characterization of ZnPc nanostructures. Top row: Simultaneously acquired (a) topography; (b) amplitude; and (c) phase channels for a 2 × 2 μm^2 area of the sample with nanopatterns of ZnPc **1** formed on APTES nanodots within an OTMS matrix. Bottom panels: Concurrent frames obtained for (d) topography; (e) amplitude; and (f) phase images using FMM with a sample of ZnPc **2** attached to APTES nanodots within OTMS.

APPENDIX H. LETTER OF PERMISSION FOR APPENDIX F

Title: Nanostructures of functionalized zinc phthalocyanines prepared with colloidal lithography: Evaluation of surface orientation and dimensions using scanning probe microscopy

Author: Ashley M. Taylor,Elizabeth A. Okoth,Neepa M.K. Kuruppu Arachchige,M. Graça H. Vicente,Jayne C. Garno

Publication: Colloids and Surfaces A: Physicochemical and Engineering Aspects

Publisher: Elsevier

Date: 20 February 2019

VITA

Neepa Malsi Kumari Kuruppu Arachchige was born in Embilipitiya, Sri Lanka to her parents Mr. and Mrs. Kuruppu Arachchige. She has a younger brother named Ruchitha Kuruppu Arachchige. She was raised in the Southern Province of Sri Lanka where she graduated from Weeraketiya Central college in 2008. Neepa completed her bachelor's degree in Chemistry at University of Colombo, Sri Lanka in 2014. Then in the same year, she enrolled in graduate program in the Department of Chemistry at Louisiana State University, Baton Rouge, LA to pursue a doctoral degree in analytical chemistry. Neepa conducted her research studies in professor Jayne C. Garno's Research group with the concentration of Atomic Force Microscopy based characterization of Self-assembled monolayers, nanoparticles and organic thin films.

During her Ph.D. career, Neepa has prepared three first author manuscripts and published four co-authored journal papers. She also has three additional manuscripts in preparation for collaborative projects. Neepa has presented her research at both regional and national conferences including a talk, five first-author poster presentations and three co-authored posters. Neepa has been recognized with several awards during her time at Louisiana State University. She was awarded TA Scholar Award for outstanding Teaching Assistant Teaching CHEM 1212 & CHEM 1431 (2017), Graduate Students Travel Award (2017 and 2018), Coates Travel Award (2018) and Tom W. Dutton Award for the female graduate student for outstanding community service and leadership (2019). Neepa was also awarded James G. Traynham graduate student award for excellence in teaching and research in chemistry (2019) and James W. Robinson outstanding research in analytical sciences award (2019) by the department of chemistry. She has been an active member of the National Honor Society for Women in Chemistry and National Organization for the Black Chemists and Chemical Engineers (NOBCChE). Additionally, she has served as the

Member at Large of International Students Association at LSU (2017-2018) and Public Relations of Chemistry Graduate Student Council (2016-2017). Neepa plans to graduate in August 2019 with a doctorate in analytical chemistry.